

DISS. ETH NO. 26133

The varying activity of supermassive black holes on multiple timescales

A thesis submitted to attain the degree of

DOCTOR OF SCIENCES of ETH ZURICH

(Dr. sc. ETH Zurich)

presented by

Lia Federica Sartori

Master of Science ETH in Physics

ETH Zurich

born on October 26, 1990

citizen of Bosco/Gurin (TI), Switzerland

accepted on the recommendation of

Prof. Dr. Alexandre Refregier

Dr. Kevin Schawinski

Prof. Dr. Ezequiel Treister

2019

*Per la mia famiglia
Vargaltsgott*

Abstract

Variable emission is a ubiquitous property of active galactic nuclei (AGN). It can be observed or inferred at essentially all timescales, from hours to billions of years, and across the entire electromagnetic spectrum. Since most of the AGN luminosity originates from the accretion of matter into the central supermassive black hole (SMBH), the study of AGN variability can provide crucial information about the physics and structure of the central engine, including at spatial scales that are beyond the resolving power of most of the observing facilities for the majority of the AGN. In addition, the study of AGN variability allows us to probe the close link between SMBHs and their host galaxies by taking into account the fact that the energy injection from the AGN varies with time. In this thesis, I investigate AGN variability on multiple timescales and its effect on the host galaxy by combining multiwavelength observations, phenomenological models, and simulations. With multiwavelength observations, we can investigate AGN variability on an object-by-object basis, phenomenological models describe the general behaviour of the AGN population, while simulations of the AGN luminosity evolution with time (AGN light curves) are very valuable both for the planning of future time-domain surveys and for the interpretation of the observations.

In the first part of the thesis, I show how galaxies with extended AGN photoionised gas on the scale of the galaxy or larger ($\gtrsim 10$ kpc) can be used to constrain AGN variability and the AGN-host galaxy interaction on super-human, $\gtrsim 10^4$ yr timescales. Using new dedicated X-ray data combined with archival observations, I confirm that the AGN in IC 2497 – the prototypical system of this class of extended AGN photoionised systems – significantly dropped in luminosity and, most likely, in accretion rate in the last $\sim 10^5$ yr, although the magnitude of the drop is lower than previously thought. The analysis also hints that the fading AGN is (or was) affecting its surroundings by injecting mechanical energy into the hot gas around it, in a similar way as observed in X-ray binaries, the stellar-mass analogs of AGN. These findings highlight that even when the activity of the AGN is decreasing, the SMBH can still affect its host galaxy. Due to the spatial extent of the photoionised gas, which allows us to trace the past luminosity, such galaxies are unique systems to search for fading AGN and investigate them in detail. I present a photoionisation analysis method aimed at reconstructing historical AGN light curves using spatially resolved spectroscopy and publicly available photoionisation codes, and

apply it to the merging galaxy Mkn 463.

The results of these pilot studies are the motivation for three new large observational campaigns I am leading, aimed at obtaining a multiwavelength view of additional galaxies of this unique class. Specifically, hard X-ray observations from *NuSTAR* are needed to probe the current intrinsic AGN luminosity, spatially resolved spectroscopy from MUSE allows us to reconstruct historical AGN light curves, and radio imaging from the VLA is valuable for the investigation of the galaxies environment and the sample selection. I provide an overview of the obtained database and possible future uses.

In the second part of the thesis, I present a simple yet powerful framework to simulate AGN light curves based on the distribution of Eddington ratios among the galaxy population, therefore linking the behaviour of single AGN to the AGN population. This framework represents a novel unifying approach to AGN variability which allows us to simultaneously investigate the different variability features observed in specific objects, the general behaviour of the AGN population, as well as variability at very different timescales. The basic premise I put forward is that the variety of AGN variability features observed in different AGN arises from the fact that every AGN is a different (unique) realisation of the same underlying process, and that the observed periods (i.e. the observed light curves) are much shorter than the total AGN lifetime.

Thanks to the efficient graphics processing units (GPU) implementation, our simulation tool enables the fast production of AGN light curves reaching up to $\sim 10^8$ points. This allows us for example to cover over 1 Myr with a roughly weekly cadence, which is similar to the cadence of the upcoming time-domain surveys. The presented framework is therefore highly valuable to prepare for, and best exploit, new observational time-domain data. As I demonstrate with some early applications, it can for example be used to investigate whether any observed variability feature is consistent with the general behaviour of the AGN population (i.e. if it can be reproduced with our simple general model) and to constrain the intrinsic AGN variability from external processes and from artefacts due, for example, to sample selection and observational cadence.

The methods and results presented in this thesis provide a first important step towards *a novel unified approach to AGN variability*. This approach will be extremely valuable in the upcoming era of time-domain astronomy, in particular by linking phenomena observed in different galaxies and at very different timescales, that may appear unrelated.

Riassunto

La variabilità dell'emissione è una proprietà onnipresente nei nuclei galattici attivi (AGN, dall'inglese "active galactic nuclei") che può essere osservata o dedotta a tutte le scale temporali, da ore a miliardi di anni, e a tutte le lunghezze d'onda. Poiché la frazione principale della luminosità degli AGN è prodotta dall'accrescimento di materia da parte del buco nero supermassiccio al loro centro, lo studio della variabilità degli AGN può fornire informazioni cruciali riguardo alla fisica e alla struttura del motore centrale, anche su scale spaziali inferiori al potere risolutivo della maggioranza dei telescopi per la maggior parte degli AGN. Inoltre, permette di investigare lo stretto legame tra i buchi neri supermassicci e le galassie che li ospitano, tenendo conto del fatto che l'iniezione di energia da parte dell'AGN varia nel tempo.

Lo scopo di questa tesi è lo studio della variabilità degli AGN a diverse scale temporali e il suo effetto sulle galassie che li ospitano combinando osservazioni a diverse lunghezze d'onda, modelli fenomenologici e simulazioni. Le osservazioni a diverse lunghezze d'onda permettono di indagare la variabilità degli AGN oggetto per oggetto, i modelli fenomenologici descrivono il comportamento generale della popolazione di AGN, mentre le simulazioni dell'evoluzione temporale della loro luminosità (curve di luce) sono utili per pianificare ed interpretare osservazioni di variabilità degli AGN.

Nella prima parte della tesi discuto come galassie associate a nubi estese di gas fotoionizzato da AGN, di dimensioni pari a o maggiori della galassia stessa ($\gtrsim 10$ kpc), possono essere utilizzate per caratterizzare la variabilità degli AGN e la loro interazione con le galassie ospitanti su archi di tempo molto maggiori delle scale temporali umane ($\gtrsim 10^4$ anni). Combinando nuove osservazioni nei raggi X appositamente proposte per la galassia IC 2497 – il prototipo di questa classe di galassie – con dati d'archivio confermo che la luminosità, e molto probabilmente il tasso d'accrescimento, dell'AGN al suo centro, sono diminuiti significativamente negli ultimi $\sim 10^5$ anni, seppur meno rispetto a quanto precedentemente ipotizzato. Inoltre, l'analisi suggerisce che questo AGN, in fase di riduzione d'attività, stia influenzando (o abbia influenzato) l'ambiente circostante iniettando energia meccanica nel gas caldo che lo circonda, in maniera simile a quanto osservato per le binarie X, oggetti analoghi agli AGN ma con masse stellari. Questi risultati evidenziano il fatto che un buco nero supermassiccio può influenzare la galassia ospitante anche quando l'attività dell'AGN è in diminuzione. Grazie all'estensione spaziale del gas

fotoionizzato, che permette di tracciare la luminosità passata, queste galassie sono sistemi unici per individuare e studiare AGN in fase di riduzione d'attività. Come parte di questa tesi presento un metodo per ricostituire curve di luce storiche utilizzando dati spettroscopici spazialmente risolti e codici pubblici per l'analisi dei processi di fotionizzazione, e lo applico alla galassia in interazione Mkn 463.

I risultati di questi studi pilota sono la motivazione per tre nuove grandi campagne di osservazione che sto conducendo, volte ad ottenere una conoscenza a più lunghezze d'onda di altre galassie appartenenti a questa classe. Precisamente, osservazioni nei raggi X provenienti da *NuSTAR* sono necessarie per misurare la luminosità intrinseca dell'AGN, la spettroscopia spazialmente risolta ottenuta con MUSE permette di ricostruire le curve di luce storiche, mentre immagini in banda radio ottenute con VLA sono utili per indagare l'ambiente galattico e la selezione del campione di galassie. Fornisco una panoramica della banca dati ottenuta finora e dei possibili usi futuri.

Nella seconda parte della tesi presento un semplice ma potente concetto di lavoro (“framework” in inglese) che permette di simulare curve di luce sulla base della distribuzione del rapporto di Eddington tra la popolazione di galassie, collegando così il comportamento dei singoli AGN all'intera popolazione. Questo framework rappresenta un nuovo approccio unificante alla variabilità degli AGN che permette di indagare simultaneamente le diverse caratteristiche di variabilità osservate in oggetti specifici, il comportamento generale della popolazione di AGN, nonché la variabilità su tempi molto diversi. L'ipotesi su cui baso il framework è che la varietà di caratteristiche di variabilità osservate in differenti AGN deriva dal fatto che ogni AGN rappresenta una diversa (unica) realizzazione dello stesso processo di base, e che i periodi osservati (cioè le curve di luce ottenute tramite osservazioni) sono molto più brevi della vita totale dell'AGN.

Grazie all'efficiente implementazione su GPU (unità di elaborazione grafica, dall'inglese “graphics processing unit”), il nostro strumento di simulazione permette la rapida produzione di curve di luce costituite da fino a $\sim 10^8$ punti. Ciò consente ad esempio di coprire oltre un milione di anni con cadenza approssimativamente settimanale, simile alla cadenza dei futuri esperimenti nel dominio temporale. Questo framework ha quindi grande valore per pianificare nuovi esperimenti e sfruttare al meglio i dati da questi prodotti. Ad esempio, come dimostro attraverso alcune applicazioni preliminari, può essere utilizzato per indagare se una certa proprietà della variabilità osservata in un singolo AGN è coerente con il comportamento generale dell'intera popolazione (cioè se può essere riprodotto con il nostro semplice modello generale), e per discriminare tra variabilità intrinseca all'AGN e processi esterni o artefatti dovuti ad esempio alla selezione del campione e alla cadenza d'osservazione.

I metodi ed i risultati presentati in questa tesi costituiscono un primo importante passo verso *un nuovo approccio unificato alla variabilità degli AGN*. Questo approccio sarà estremamente prezioso nel futuro prossimo dell'astronomia nel dominio del tempo, in particolare in quanto consente di collegare fenomeni osservati in galassie diverse e a differenti scale temporali, che possono apparire non correlati tra loro.

Contents

Abstract	i
Riassunto	iii
1 Introduction	1
1.1 Supermassive black holes and active galactic nuclei	2
1.1.1 Supermassive black holes	2
1.1.2 AGN structure and emission	3
1.2 Co-evolution between black holes and host galaxies	9
1.3 Active galactic nuclei variability	11
1.3.1 Physical timescales for AGN variability	11
1.3.2 The current observational pictures	13
1.3.3 The Voorwerpjes sample	18
1.4 Organization and content of the thesis	22
2 Extended X-ray emission in IC 2497 – energy injection in the gas around a fading AGN	25
2.1 Observations	27
2.2 Analysis	28
2.2.1 Radial profile and source extension	28
2.2.2 Spectral fit and temperature profile	32
2.3 Discussion	37
2.3.1 Hot gas in IC 2497	37
2.3.2 Energy in the bubble	38
2.3.3 Accretion state changes, AGN feedback and analogy with X-ray binaries	40
2.4 Summary	41
3 Joint NuSTAR and Chandra analysis of the obscured quasar in IC 2497	43
3.1 Observations	44
3.1.1 Chandra	44
3.1.2 NuSTAR	44

Contents

3.1.3	Optical data	45
3.2	Analysis	46
3.2.1	X-ray emission	46
3.2.2	Luminosity estimation	52
3.3	Discussion	54
3.4	Summary	56
4	New observational data for the Voorwerpjes galaxies	57
4.1	MUSE: spatially resolved optical spectroscopy (IFU)	58
4.2	NuSTAR: Hard X-ray spectroscopy	62
4.3	VLA: radio imaging and spectroscopy	63
5	A model for AGN variability on multiple timescales	67
5.1	Framework and model	69
5.2	Proof of concept	71
5.2.1	Data compilation	71
5.2.2	Example model	73
5.3	Discussion	75
5.3.1	Insights and results from the structure function plot	75
5.3.2	Insights from modelling	76
6	A forward modelling approach to AGN variability – method description and early applications	77
6.1	Model and method	79
6.1.1	Simulations of Eddington ratio time series	79
6.1.2	Converting Eddington ratio time series to observables: light curves and structure function	83
6.2	Simulations	84
6.2.1	Code Implementation	84
6.2.2	Testing and characterisation of the simulations code	84
6.3	Applications	101
6.3.1	Constraining specific models with existing AGN variability data	102
6.3.2	Simulating future time-domain surveys	106
6.3.3	Extremely variable quasars and changing-look AGN	108
6.4	Summary and conclusions	115
6.A	Appendix: Definitions	118
7	Conclusions	123
7.1	Summary	123
7.2	Future prospects	126
7.2.1	Modelling the variable Universe in the time-domain era	126
7.2.2	AGN variability in the context of galaxy evolution and cosmological simulations	127

7.2.3 Cosmic black hole mass growth	128
Bibliography	129
List of symbols	163
List of abbreviations	163
Acknowledgements	167
Curriculum Vitae	171

1 Introduction

*Laudato si', mi' Signore, per sora luna e le stelle,
in celu l'ài formate clarite et pretiose et belle.*¹

Laudes Creaturarum, San Francesco D'Assisi (1224)

Supermassive black holes (SMBHs) with masses $M_{\text{BH}} \sim 10^6 - 10^9 M_{\odot}$ are hosted in the center of most of the massive galaxies in the present day Universe, including our own Milky Way (Kormendy and Richstone 1995; Schödel et al. 2003; Kormendy and Ho 2013). When the SMBH is actively growing, the nuclear region of the host galaxy is referred to as an “active galactic nucleus” (AGN), and its luminosity overcomes the emission from the stellar component over most of the electromagnetic spectrum².

The luminosity of an AGN is however not constant in time. Variable emission can be observed or inferred at essentially all timescales, from hours to billions of years, and across the entire electromagnetic spectrum. Since the AGN luminosity originates from the accretion of dust and gas (e.g. Hoyle and Fowler 1963; Salpeter 1964; Lynden-Bell 1978), the study of AGN variability can provide crucial information about the SMBH physics and central engine, including at spatial scales that are beyond the resolving power of most of the telescopes. Furthermore, it allows us to probe the close link between SMBHs and their hosts by taking into account the fact that the energy injection from the AGN varies with time (e.g. Hickox et al. 2014). AGN variability is also often employed as an efficient method to select AGN from large multi-epoch surveys (e.g. Trevese et al., 2008; Villforth et al., 2010; De Cicco et al., 2015; Sánchez-Sáez et al., 2019; De Cicco et al., 2019; Pouliaxis et al., 2019).

The aim of this thesis is to investigate AGN variability and its effect on the host galaxy by combining 1) multiwavelength observations of single AGN host galaxies, 2) phenomenological models describing the general behaviour of the AGN population, and 3) simulations of the AGN luminosity evolution with time (AGN light curves).

¹*Praised be You, my Lord, through Sister Moon and the stars, in heaven you formed them clear and precious and beautiful* (Canticle of the Sun, Saint Francis of Assisi, 1224).

²For historical reasons, luminous AGN are often referred to as quasars or quasi stellar objects (QSO). Throughout the thesis I will use these terms interchangeably.

In this Introduction I will present an overview of the current knowledge about the structure and accretion processes of AGN (Section 1.1), their (variable) emission (Section 1.3), as well as the co-evolution with their host galaxies (Section 1.2). In Section 1.4 I will summarise the main questions and the structure of the thesis.

1.1 Supermassive black holes and active galactic nuclei

1.1.1 Supermassive black holes

A black hole (BH) is a region of the spacetime exhibiting such a strong gravitational field that nothing, even light, can escape. Mathematically defined as a singularity, BHs are predicted by the theory of general relativity (Einstein 1915; Schwarzschild 1916).

In astronomy, we define supermassive as black holes (SMBHs) the BHs which are lying in the center of galaxies and have masses $M_{\text{BH}} \sim 10^6 - 10^9 M_{\odot}$. Smaller BHs, called stellar mass black holes ($\sim 10 - 100 M_{\odot}$) or intermediate mass black holes ($\sim 10^2 - 10^6 M_{\odot}$) can be found at different locations within the galaxy (e.g. Fender and Belloni 2012; Mezcua 2017). In this thesis we will concentrate on SMBHs, but some analogies with stellar mass black holes will also be discussed.

SMBHs, as well as smaller BHs, can be fully characterised by three parameters, which are critical to determine the observational features of the AGN: the mass M_{BH} , the mass accretion rate \dot{m} , and the spin a . A characteristic size related to BHs is the gravitational radius r_g :

$$r_g = \frac{GM_{\text{BH}}}{c^2} = \frac{1}{2}r_s \quad (1.1)$$

where G is the gravitational constant, c the speed of light, and r_s the Schwarzschild radius, that represents the event horizon of a non rotating BH.

When the BH is accreting, part of the accreted mass is converted to energy and luminosity is released. In the case of a steady isotropic accretion flow, accretion can only occur if the pressure generated by the luminosity does not exceed the gravitational force from the BH. This brings to the definition of the Eddington luminosity L_{Edd} , that is the maximum luminosity at which a BH can radiate without overcoming the gravitational force:

$$L_{\text{Edd}} = \frac{4\pi cGM_{\text{BH}}\mu m_p}{\sigma_T} \simeq 1.5 \times 10^{38} \frac{M_{\text{BH}}}{M_{\odot}} \text{ erg s}^{-1} \quad (1.2)$$

1.1. Supermassive black holes and active galactic nuclei

where μ is the mean molecular weight, m_p the proton mass and σ_T the Thomson cross section. Assuming an accretion rate $\dot{m} = L/\eta c^2$, where η is the efficiency of converting gravitational potential energy to electromagnetic radiation (radiative efficiency), the accretion rate required to produce L_{Edd} is:

$$\dot{m}_{\text{Edd}} = \frac{L_{\text{Edd}}}{\eta c^2} \simeq 3M_8 \left(\frac{\eta}{0.1}\right)^{-1} M_\odot \text{ yr}^{-1} \quad (1.3)$$

where M_8 is the black hole mass in units of $10^8 M_\odot$. Finally, the Eddington ratio λ_{Edd} is the ratio between the total (bolometric) luminosity L_{Bol} of the accreting BH and the Eddington luminosity:

$$\lambda_{\text{Edd}} \propto \frac{L_{\text{Bol}}}{L_{\text{Edd}}} \propto \frac{\dot{m}}{\dot{m}_{\text{Edd}}} \propto \frac{\dot{m}}{M_{\text{BH}}} \quad (1.4)$$

As we will see in the following, λ_{Edd} is one of the main properties of accreting SMBHs defining the AGN structure and behaviour.

1.1.2 AGN structure and emission

In addition to the central SMBH, AGN comprise multiple components at different spatial scales ranging from sub-pc to Mpc (Fig. 1.1). Although by definition no electromagnetic radiation is emitted by the SMBH itself, AGN are known to radiate across the entire electromagnetic spectrum, from radio up to gamma rays. This emission mostly arises from the accretion process onto the SMBH (e.g. Hoyle and Fowler 1963; Salpeter 1964; Lynden-Bell 1978), and from the interaction between the different AGN components. In the following I summarise the main AGN components and processes responsible for the observed AGN spectrum.

Accretion disc and optical/UV emission

When a BH is accreting, matter is transported inwards and angular momentum outwards, creating an accretion disc. In the case of moderately to high accreting BHs ($0.01 \lesssim \lambda_{\text{Edd}} \lesssim 0.3$), accretion discs are usually assumed to be optically thick and geometrically thin ($h/r \ll 1$, h/r where is the aspect ratio), and their properties are described by the so-called α -disc model (Shakura and Sunyaev 1973). In this model, the momentum is transported outwards due to the kinematic viscosity $\nu = \alpha c_s h$, where c_s is the local mean sound speed in the disc and α the viscosity parameter ranging between 0 (no viscosity) and 1.

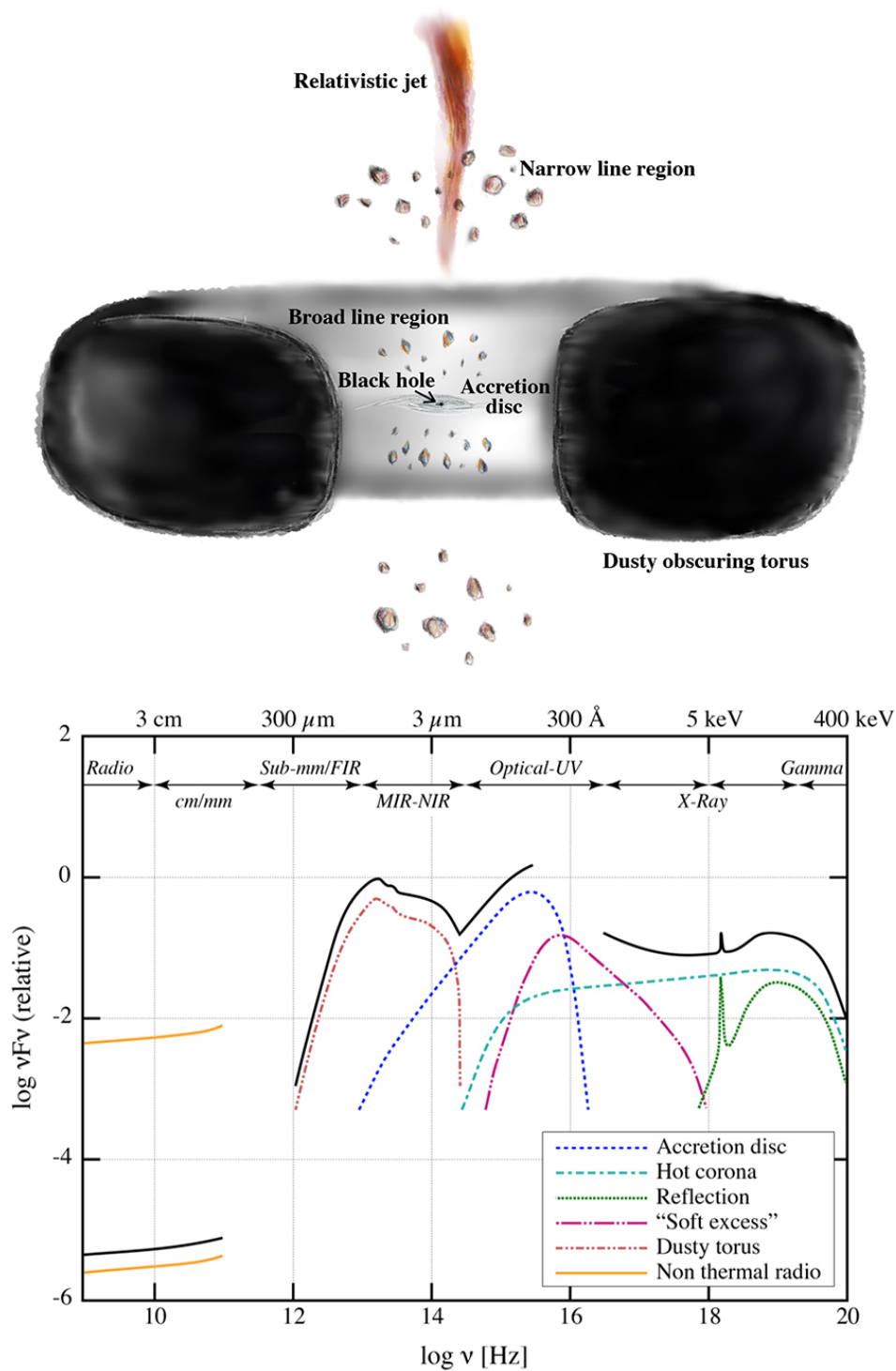


Figure 1.1: *Top:* Schematic illustration of the typical AGN structure (not to scale, adapted from [Oh 2014](#)). Not shown is the hot corona which is expected to be located close to the accretion disc. *Bottom:* Schematic representation of the AGN spectral energy distribution (SED). The black line represents the total emission while the coloured lines show the different contributions discussed in Chapter 1.1.2. The radio continuum varies between sources depending on their radio loudness (adapted from [Harrison et al. 2014](#)).

1.1. Supermassive black holes and active galactic nuclei

The thermal emission of an optically thick, geometrically thin accretion disc is generally treated as a superposition of black body emission from annuli at increasing radii and different temperature. Following [Netzer \(2013\)](#), the radial dependence of the temperature is parametrised as:

$$T(r) \sim 8.6 \times 10^6 \dot{m}^{1/4} M_8^{-1/2} f^{1/4}(r) \left(\frac{r}{r_g}\right)^{-3/4} \text{ K} \quad (1.5)$$

where M_8 and \dot{m} are the BH mass and accretion rate as defined in Section 1.1.1, and $f(r)$ a non linear function which depends on the BH spin. For typical SMBHs with $M_{\text{BH}} \sim 10^8 M_\odot$ ($M_8 \sim 1$) the maximum disc temperature is $\sim 10^5 \text{K}$, such that the disc's emission peaks at UV wavelengths. The total emission from the accretion disc, spanning the optical and UV part of the spectrum, is known as Big Blue Bump and accounts for a substantial fraction of the total AGN luminosity (e.g. [Shields 1978](#); [Malkan and Sargent 1982](#); [Netzer and Trakhtenbrot 2014](#); [Capellupo et al. 2015](#); [Castelló-Mor et al. 2016](#); [Bertemes et al. 2016](#)).

The structure and size of the accretion disc strongly depends on other parameters such as spin and λ_{Edd} , but for typical AGN it is expected to extend up to $\sim 10^{-3} \text{pc}$ from the central BH. The inner radius may depend on the BH spin, with smaller radii and therefore more emission at shorter wavelengths for rapidly rotating BHs³. In addition, there are theoretical and observational evidences that standard discs are present only at moderate to high Eddington ratios, while at $\lambda_{\text{Edd}} \lesssim 0.01$ the accretion process should transition to a radiatively inefficient, advection dominated accretion flow (e.g. [Narayan and Yi 1994](#); [Narayan et al. 1998](#); [Vasudevan and Fabian 2009](#); [Ho 2009](#); [Yuan and Narayan 2014](#)).

Hot corona and X-ray emission

X-ray emission is ubiquitous in AGN and is thought to arise from inverse Compton scattering of accretion disc photons in a compact, hot corona ($\sim 10^9 \text{K}$) in the nuclear region ([Sunyaev and Titarchuk 1980](#); [Haardt and Maraschi 1991](#); [Zdziarski 1998](#); [Jovanović and Popović 2009](#)). The exact geometry and location of the corona is still matter of debate, but it is expected to be located within a few r_g from the accretion disc (e.g. [Burlon et al. 2011](#)).

The primary X-ray emission from an AGN is well modeled as a power law with photon index $\Gamma \sim 1.8 - 2$ ([Nandra and Pounds 1994](#); [Piconcelli et al. 2005](#); [Ricci et al. 2011](#)), with an high energy cutoff at a few hundreds keV (e.g. [Ricci et al. 2017](#)). This primary emission is absorbed and reprocessed by multiple absorbers at various spatial scales,

³This is a consequence of the fact that the innermost stable circular orbit (ISCO), the smallest circular orbit at which a particle can orbit a BH, is decreasing for increasing spin. In the case of a non-spinning BH, the ISCO is located at $r_{\text{ISCO}} = 3 \times r_s$.

mostly in the broad line regions and in the dusty torus (see [Ramos Almeida and Ricci 2017](#) for an extensive review of the obscuration processes), producing the so-called Compton reflection spectrum (e.g. [George and Fabian 1991](#)). The most prominent features of the reflection spectrum are the Compton hump peaking at 20 – 40 keV, which is visible only in Compton thick sources⁴, and the iron (Fe) $K\alpha$ line at 6.4 keV which is present in both Compton thick and Compton thin AGN (e.g. [Lightman and White 1988](#); [Pounds et al. 1990](#); [Nandra and Pounds 1994](#); [Nandra 2006](#); [Ricci et al. 2014](#)). In addition, a soft excess is usually observed below 2 keV, and is thought to originate from multiple processes including blurred relativistic reflection and comptonisation of accretion disc photons in colder plasma (see [Ricci et al. 2017](#) and references therein).

As mentioned above, the observed X-ray spectrum can be strongly affected by obscuration. Photoelectric absorption is already effective at low column densities $N_{\text{H}} \sim 10^{21} \text{cm}^{-2}$ and is strongly energy dependent, affecting more the soft, low energy spectrum ($\lesssim 10$ keV). However, it does not play a significant role in Compton thin AGN at energies $\gtrsim 10$ keV. On the other hand, Compton scattering strongly affects also the spectrum of Compton thick AGN, but no significant dependence on energy is found below ~ 150 keV.

X-ray emission, especially in the hard X-ray band ($\gtrsim 10$ keV) observed by telescopes such as the Nuclear Spectroscopic Telescope Array (*NuSTAR*, [Harrison et al. 2013](#)) and the Burst Alert Telescope (BAT, [Barthelmy et al. 2005](#); [Krimm et al. 2013](#)) on board of *Swift* ([Gehrels et al. 2004](#)), provides the most complete and less biased way to select AGN to date. Indeed, in addition to being (mostly) unaffected by obscuration, hard X-ray emission is a typical signature of SMBH activity.

Broad line regions and narrow line regions

The broad line region (BLR) and narrow line region (NLR) are collections of gas clouds photoionised by the optical/UV continuum of the AGN, producing emission lines mostly in the UV, optical and IR part of the spectrum.

The BLR is found in a sub-pc scale ($\sim 10^{-2} - 1$ pc) dust free region around the accretion disc, and is composed by high column density gas clouds ($\sim 10^{23} \text{cm}^{-2}$) moving at typical velocities of $\sim 3000 \text{ km s}^{-1}$ (e.g. [Netzer 2006](#)). The emission spectrum is characterised by permitted (e.g. $H\alpha$, $H\beta$) and semi-forbidden (e.g. $\text{C III}|\lambda 1909$, $\text{O III}|\lambda 1663$) lines at UV and optical wavelengths. Because of high velocities and Doppler effect, the emission lines from the BLR are broad (hence the name BLR), with full width at half maximum FWHM $\sim 1000 - 25000 \text{ km s}^{-1}$ (e.g. [Peterson 2006](#)).

The NLR in contrast is composed by lower column density gas clouds ($\sim 10^{20} - 10^{21} \text{cm}^{-2}$) moving at lower velocities ($\sim 500 \text{ km s}^{-1}$) and at larger distances from the center (e.g. [Netzer 2006](#)). The physical extent of the NLR depends on the AGN luminosity and ranges

⁴In this thesis we define Compton thick the sources with neutral hydrogen column density $N_{\text{H}} > 10^{24} \text{ atoms cm}^{-2}$. Sources with lower N_{H} are referred to as Compton thin.

1.1. Supermassive black holes and active galactic nuclei

from ~ 100 pc to ~ 1 kpc for moderately luminous AGN (e.g. [Capetti et al. 1996](#)) or even ~ 10 kpc for the most luminous AGN (e.g. [Hainline et al. 2014](#)). Because of the lower column densities and velocities, NLR produce both permitted and forbidden emission lines at UV, optical and IR wavelengths (e.g. $\text{He II}\lambda 4686$, $[\text{O III}]\lambda 5007$, $[\text{N II}]\lambda 6583$), but with lower FWHM $\lesssim 500 \text{ km s}^{-1}$ (e.g. [Peterson 2006](#)).

The presence or absence of broad emission lines is one of the main features distinguishing Type 1 (both broad and narrow emission lines) and Type 2 (only narrow) AGN.

Dusty torus and mid-IR emission

The mid-IR emission in AGN spectra mostly arises from the reprocessing of accretion disc photons by a toroidal dust structure around the accretion disc and BLR. Although the geometric distribution of the dusty material (smooth or clumpy) is still matter of debate (see [Padovani et al. 2017](#) and references therein), it is usually referred to as torus. Since the inner radius of the torus is expected to be set by the dust sublimation temperature, which depends on the luminosity as $r \propto L^{1/2}$ (e.g. [Barvainis 1987](#); [Suganuma et al. 2006](#); [Kishimoto et al. 2011](#)), the extent of the dusty structure can be different from source to source. Recent sub-mm observations as well as mid-IR imaging and interferometry revealed structures with $0.1 - 10$ pc sizes (e.g. [Radomski et al. 2008](#); [Burtscher et al. 2013](#); [García-Burillo et al. 2016](#)).

Besides reprocessing the optical and UV emission, the torus is also collimating the same emission, and is therefore responsible for the (bi-)conical shape of the ionisation cones (e.g. [Kishimoto et al. 2011](#)), with increasing opening angle for increasing luminosities and possibly Eddington ratio ([Lawrence 1991](#); [Simpson 2005](#); [Oh et al. 2015](#)). The presence of a dusty torus, together with the different optical spectra observed in Type 1 and Type 2 AGN, plays a fundamental role in the classical AGN unification model ([Antonucci 1993](#); [Urry and Padovani 1995](#)), as will be clear in the following sections.

Radio emission and jets

Radio jets can be observed at a variety of spatial scales from close to the accretion disc up to a few Mpc (e.g. [Hada et al. 2013](#); [Solovyov and Verkhodanov 2011](#); [Clarke et al. 2017](#)), but although they have played a crucial role in the discovery of quasars ([Schmidt 1963](#)) their formation mechanism still remains unclear. It is however general consensus that the jet should be launched by processes related to the BH spin and/or the inner accretion disc (e.g. [Cai et al. 2019](#) and references therein), which extract energy and angular momentum from the central AGN engine (e.g. through magnetic fields, [Blandford and Payne 1982](#); [Lynden-Bell 2003](#)).

The radio continuum in AGN is mostly due to synchrotron radiation and is usually parametrised as a power law. AGN can be classified as radio loud or radio quiet depending on the level of radio emission, its ratio with optical luminosity, and the presence or absence

of powerful radio jets (see [Padovani et al. 2017](#) for a review). Although the definition of radio loudness is not unique in the literature, radio loud AGN make up $\sim 10 - 30\%$ of the AGN population (e.g. [White et al. 2000](#); [Mushotzky 2004](#)).

AGN unification model

As mentioned above, AGN were historically divided into Type 1 and Type 2, where Type 1 show both broad and narrow emission lines in the optical and UV part of the spectrum, while Type 2 only narrow lines. However, spectropolarimetric observations revealed that broad line components can be present also when they are not observed directly in the optical spectrum ([Antonucci and Miller 1985](#)). This led to the classical AGN Unification scheme, which states that the physical structure of every AGN is intrinsically the same, and that the different appearance of Type 1 and Type 2 AGN simply arises from the orientation of the dusty obscuring torus with respect to the observer's line of sight ([Antonucci 1993](#); [Urry and Padovani 1995](#)). Specifically, in Type 2 AGN the view of the central AGN region, including the BLR, is hindered by the torus, while in Type 1 AGN both BLR and NLR emission can be directly observed.

Although the classical Unification picture successfully explains the different emission line structure in Type 1 and Type 2 AGN, new studies suggest that this simple orientation based model is too simplistic to account for the variety of observed AGN properties. In addition to orientation, additional physical parameters may be responsible for the AGN appearance, including Eddington ratio, torus covering fraction, jet strength and host galaxy properties (see [Treister and Urry 2012](#); [Netzer 2015](#); [Padovani et al. 2017](#) for extensive reviews on this topic). In addition, as I will discuss in detail below, there are now multiple evidences that the AGN emission varies with time, both regarding its overall luminosity and emission line shapes (e.g. [MacLeod et al. 2010](#); [LaMassa et al. 2015](#); [Schawinski et al. 2015](#)), so that AGN should be treated as dynamical objects which can change their structure throughout their life.

Analogy between AGN and X-ray binaries and their limitations

As we saw above, the term AGN refers to the structure around SMBHs. However, accretion discs and jets are observed also around stellar mass black holes which are accreting material from a companion star (see [Fender and Belloni 2012](#) for an extensive review). These systems are called X-ray binaries as in this case most of the luminosity due to the accretion process is emitted in the X-rays (see e.g. Eq. 1.5).

Direct observations of X-ray binaries showed that these systems can switch from a radiatively efficient to a radiatively inefficient state⁵, with related changes in luminosity over five orders of magnitude, on timescales of days to weeks (e.g. [Chen et al. 1997](#); [Remillard and McClintock 2006](#)). The question if AGN are simply “scaled up” version of

⁵These states are known as “high-luminosity/soft-spectrum state” and “low-luminosity/hard-spectrum state” (see [Ruan et al. 2019](#) and references therein).

X-ray binaries, i.e. if the physical processes governing the accretion in X-ray binaries and AGN are the same but at timescales and energies scaled up with respect to M_{BH} (see e.g. equations in Section 1.3.1), is still matter of debate (e.g. McHardy et al. 2006; Ruan et al. 2019). We will address this point in Chapter 2 and Chapter 3.

1.2 Co-evolution between black holes and host galaxies

Although the mass of a typical SMBH is only a few percent of the mass of its host galaxy, the energy released during the accretion phase can be tens or hundreds of times higher than the binding energy of the galaxy bulge. If only a small part of the radiated energy couples with the surrounding gas, then the gas can be kept hot or blown away, therefore preventing the formations of new stars (e.g. Silk and Rees 1998; Ostriker and Ciotti 2005). On the other hand, a lack of gas supply in the central region of the galaxy can reduce the activity of the AGN which, as we saw above, is primarily powered by accretion onto the SMBH⁶ (e.g. Silk and Rees 1998; King 2003). SMBHs and their hosts could therefore be expected to co-evolve by regulating each other growth. This phenomenon is generally referred to as “AGN feedback”, and represents one of the main current areas of research in the AGN field (see e.g. Kormendy and Ho 2013; Fabian 2012; Heckman and Best 2014 for extensive reviews).

The main line of observations supporting a possible evolutionary link between SMBHs and host galaxies is the presence of tight correlations between the SMBH mass and different physical properties of the host. Indeed, M_{BH} is found to correlate, among others, with the stellar velocity dispersions σ of the galaxy bulge (this is the well known $M - \sigma$ relation, Gebhardt et al. 2000; Ferrarese and Merritt 2000; Kormendy and Ho 2013; see also Zubovas and King 2019 for a recent review and Sexton et al. 2019 for a recent study of the possible redshift evolution and sources of scatter), the bulge mass (Magorrian et al. 1998; Kormendy and Ho 2013) and the bulge luminosity (Kormendy 1993; Magorrian et al. 1998; Marconi and Hunt 2003). Furthermore, the black hole accretion rate density (BHARD) and the star formation rate density (SFRD) of the Universe show similar redshift evolutions, with a peak at $z \sim 1 - 2$ and a decrease towards $z \sim 0$ (e.g. Madau and Dickinson 2014 and references therein).

⁶We note that the SMBH growth is not limited by the amount of gas per se, as the accretion rate of a powerful quasar is on the order of $\sim 1 M_{\odot}\text{yr}^{-1}$, but rather by the efficiency at which the gas can reach the central region by losing angular momentum.

Even though these observations show that SMBHs and host galaxies grow and evolve in a “parallel” way, it is not clear yet if this co-evolution really arises from an interaction between the two, or if it is simply the result of the fact that both are growing in a similar environment. For example, [Peng \(2007\)](#) and [Jahnke and Macciò \(2011\)](#) pointed out that some correlations between M_{BH} and galaxy properties naturally emerge from the hierarchical assembly of SMBH and stellar masses during multiple galaxy mergers. This means that AGN feedback is not the only process responsible for the observed co-evolution. Nevertheless, it is now widely accepted that AGN feedback can have an impact on the star formation, at least in some galaxies, through two different modes: radiative and kinetic (see e.g. [Fabian 2012](#) and [Alexander and Hickox 2012](#) for extensive reviews).

In the radiative mode (also called quasar or wind mode), radiation pressure, AGN winds and outflows push the cold gas out of the galaxy, therefore quenching star formation⁷. This mode operates in typical bulge galaxies with SMBHs accreting close to the Eddington limit, and is expected to be most effective at $z \sim 2 - 3$, when AGN were more active (peak of quasar activity) and the galaxies were more gas rich. Indeed, most of the extended outflows have been found in galaxies hosting luminous AGN ($L_{\text{bol}} \gtrsim 10^{46} \text{ erg s}^{-1}$) at such redshifts (e.g. [Cano-Díaz et al. 2012](#); [Harrison et al. 2012](#); [Carniani et al. 2015](#)). On the other hand, the role of the kinetic mode (also called jet or maintenance mode) is to keep the galaxy empty of gas, or at least to keep the gas hot therefore preventing fragmentation which could lead to star formation. This mode mostly occurs in galaxies hosting low-Eddington, radiatively inefficient AGN with powerful radio jets. The mechanical power of the jet indeed creates bubbles or cavities in the hot gas, that are commonly seen in deep X-ray imaging of galaxy clusters with a central AGN (e.g. [Birzan et al. 2004](#); [Rafferty et al. 2006](#); [McNamara and Nulsen 2012](#); [Vantyghem et al. 2014](#)).

The examples above well illustrate the complexity of the AGN feedback phenomenon, where SMBHs with different levels of activity are expected to quench the star formation through different processes. It is also important to remember that the similarity between BHARD and SFRD does not imply that highly accreting SMBHs are always hosted in highly starforming galaxies (or viceversa), but only that the two populations evolve in a similar manner. Indeed, observational studies based on different AGN and galaxy samples found both strong (e.g. [Rafferty et al. 2011](#); [Juneau et al. 2013](#); [Yang et al. 2019](#)) and weak (e.g. [Rosario et al. 2012](#); [Shao et al. 2010](#)) correlations between SMBH accretion and star formation. As pointed out by [Hickox et al. \(2014\)](#), this discrepancy may arise from the fact that the AGN activity and luminosity varies on multiple timescales (from hours to Myr, see Section 1.3) which are much shorter than the typical timescales involved in star formation and galaxy evolution ($\gtrsim 100 \text{ Myr}$). As a consequence, understanding the variability behaviour of AGN is crucial in order to be able to interpret these different results, and therefore establish a causal link (or lack thereof) between SMBH and host

⁷There are however some observations and simulations claiming that, at least in some galaxies, AGN outflows could induce star formation instead of quenching it (e.g. [Cresci and Maiolino 2018](#)).

galaxy growth. Developing a framework aimed at modelling AGN variability on multiple timescales is one of the main goals of this thesis.

1.3 Active galactic nuclei variability

Variable emission is one of the first discovered properties of AGN (Matthews and Sandage 1963). As mentioned above, it can be observed or inferred at essentially all timescales, from hours to billions of years (e.g. Goyal et al. 2013; McHardy et al. 2004; Smith et al. 2018; MacLeod et al. 2012; Schawinski et al. 2015; Novak et al. 2011), and across the entire electromagnetic spectrum (e.g. Uttley and McHardy 2004; Paolillo et al. 2017; Caplar et al. 2017; Assef et al. 2018).

In the following I will first discuss the physical (theoretical) timescales associated to standard accretion discs which may be relevant for AGN variability. I will then provide an overview of the current picture of the AGN variability phenomenon arising from observational studies, and highlight the main caveats and open questions.

1.3.1 Physical timescales for AGN variability

Since the AGN luminosity mostly arises from the accretion process, variable emission could originate from physical processes taking place inside the accretion disc at different timescales. Indeed, there are several timescales associated to standard optically thick, geometrically thin accretion discs which may be relevant for AGN variability.

The *inflow timescale*, also called *viscous timescale*, is the time needed for a parcel of gas to drift radially from a given radius r within the accretion disc to the center. This corresponds to the timescale at which a steady state accretion disc fed from outer radii can vary in luminosity as a result of abrupt changes in the accretion rate. For the radiation-pressure dominated inner region of a standard accretion disc, LaMassa et al. (2015) parametrised this timescale as:

$$t_{\text{inff}} [\text{yr}] \sim 20 \left(\frac{\alpha}{0.1}\right)^{-1} \left(\frac{\lambda_{\text{Edd}}}{0.03}\right)^{-2} \left(\frac{\eta}{0.1}\right)^2 \left(\frac{r}{10r_g}\right)^{7/2} M_8 \quad (1.6)$$

where α is the viscosity parameter and η the efficiency of converting potential energy to radiation. Since the inflow timescale is inverse proportional to λ_{Edd}^2 , this timescale is longer for AGN “switch on” compared to AGN “switch off”. For $r \sim 10r_g$, as commonly assumed for the UV emitting region (LaMassa et al. 2015), the inflow timescale may be on the order of $\sim 50 - 100$ yr. The timescale is significantly longer for the optical wavelengths, for which $r \sim 200r_g$ (e.g. Morgan et al. 2010; Fausnaugh et al. 2016). Inflow

Chapter 1. Introduction

timescales alone are therefore not sufficient to explain the optical and UV variability observed at much shorter, days to decades timescales (see Section 1.3.2), what could question the standard thin accretion disc theory, or at least require some modification. Indeed, numerical simulations of inner accretion discs (e.g. Krolik et al. 2005) suggest that the drift velocity may be several times higher than the value predicted by the model, with consequently lower infall timescales. This would reduce the discrepancy between inflow timescales and observed timescales for AGN variability. Furthermore, additional processes such as reprocessing of UV and X-ray emission or local instabilities in the accretion disc are expected to produce rapid variability, as I will discuss in detail in the next Section. Relevant timescales for these processes include the light-crossing, dynamical and thermal timescales.

The *light-crossing timescale* is the time needed for light to cross a region of radius r . Following Netzer (2013), for a standard accretion disc this is given by:

$$t_{\text{lc}} [\text{yr}] \sim 0.016M_8 \frac{r}{r_g} \quad (1.7)$$

This timescale is relevant for irradiated discs.

The *dynamical timescale*, also called *orbital timescale* is the time needed from the accretion disc to achieve hydrostatic equilibrium:

$$t_{\text{dyn}} [\text{yr}] \sim \frac{1}{\Omega} = 0.005M_8 \left(\frac{r}{r_g} \right)^{3/2} \quad (1.8)$$

where $\Omega = (GM_{\text{BH}}/r^3)^{1/2}$ is the angular velocity (Netzer 2013). The dynamical timescale is also the shortest timescale on which it is possible to see physical changes in the disc.

Finally, the *thermal timescale* is the time needed for energy to redistribute due to dissipative and cooling processes within the disc, and it is related to t_{dyn} and viscosity:

$$t_{\text{therm}} = \frac{t_{\text{dyn}}}{\alpha} \quad (1.9)$$

Potential causes of local thermal fluctuations are e.g. an increase in the X-ray produced in the hot corona, which irradiate the inner part of the accretion disc (e.g. Shappee et al. 2013), magneto rotational instabilities (see e.g. Dexter and Agol 2011 and references

therein). As we will see in Chapter 1.3.2, recent studies pointed out that this timescale is the one which best matches observations (e.g. Ross et al. 2018; Stern et al. 2018; Noda and Done 2018; Parker et al. 2019), what implies that variability may be mostly due to rapid changes in the temperature of the accretion disc.

The timescales discussed above all relate to processes which modify the intrinsic emission of the accretion disc. However, the observed variability (both in total emission and in emission line shape) can be due to occultation events, e.g. from dust clouds outside the BLR. Following LaMassa et al. (2015), the *crossing timescale* for Keplerian orbits is:

$$t_{\text{cross}} [\text{yr}] \sim 0.07 \left(\frac{r_{\text{orb}}}{1 \text{lt} - \text{day}} \right)^{3/2} M_8^{-1/2} \arcsin \left(\frac{r_{\text{src}}}{r_{\text{orb}}} \right) \quad (1.10)$$

where r_{orb} is the radius of the Keplerian orbit and r_{src} the radius of the emitting region affected by the occultation event.

1.3.2 The current observational pictures

In the previous Section I discussed some of the physical timescales which may be relevant for AGN variability. However, such timescales are not always consistent with observations, so that the causes of the observed variability is still matter of debate. Below I will outline the main observed variability features, together with the corresponding timescales, and discuss some of the current interpretations.

X-ray variability

Due to the compact size of the X-ray emitting region, X-ray emission is expected to undergo the fastest variations among all the wavelengths (e.g. Ulrich et al. 1997; Uttley et al. 2002). Indeed, X-ray light curves from facilities such as *XMM-Newton*, *ROSAT* and *ASCA* show evidence of variability on timescales of minutes to months, with amplitude anticorrelated with luminosity (e.g. Nandra et al. 1997; Almaini et al. 2000; McHardy et al. 2004). The variability amplitude is also increasing for increasing timescales, as found by works which combined multiple observation to reach up to 20 yr baselines (e.g. McHardy et al. 2004; Middei et al. 2017).

The high quality and regular sampling of X-ray light curves, together with the availability of observational campaigns covering several decades, allows us to perform power spectral distribution (PSD⁸) analysis on individual AGN. The obtained PSD are generally well described as a power law with slope $\alpha \sim -2$, consistent with a random walk, at the highest

⁸The PSD is a measure of how the power in a time series is distributed among different frequencies, and is one of the main quantities used to quantify the variability in astronomical light curves.

probed frequencies (e.g. [Lawrence and Papadakis 1993](#); [Green et al. 1993](#)), and one or two breaks leading to shallower low-frequency PSD (e.g. [Uttley et al. 2002](#); [McHardy et al. 2007](#)). The break frequency appears to be correlated with BH mass and Eddington ratio ([McHardy et al. 2004](#); [McHardy et al. 2006](#)), but the physical reason for this correlation is still unclear (e.g. [McHardy et al. 2006](#); [González-Martín and Vaughan 2012](#)). Nevertheless, a dependency of variability on BH mass and accretion rate could explain the observed anticorrelation with luminosity ([Paolillo et al. 2017](#)). After accounting for BH mass and Eddington ratio, the same PSD shape seems to explain both local and high- z AGN (up to $z \sim 4$), suggesting that the physical mechanism responsible for X-ray variability does not evolve with redshift ([Paolillo et al. 2017](#)). Although the origin of this variability is not well understood yet, possible mechanisms include instabilities in the accretion flow, orbiting hotspots, as well as a flaring corona.

Optical and UV variability

In the past decades, different campaigns with recurrent photometry and/or spectroscopy such as the Sloan Digital Sky Survey (SDSS) Stripe 82 ([York et al. 2000](#); [Ivezić et al. 2007](#); [Sesar et al. 2007](#)), the (intermediate) Palomar Transient Factory (PTF/iPTF, [Law et al. 2009](#); [Rau et al. 2009](#)), the Palomar Observatory Sky Survey (POSS, [Minkowski and Abell 1963](#)) and the Catalina Real-Time Transient Survey (CRTS, [Drake et al. 2009](#); [Djorgovski et al. 2011](#)) have provided important insights into the optical variability behaviour of the AGN population on days to decades timescales (e.g. [de Vries et al. 2003](#); [Vanden Berk et al. 2004](#); [Sesar et al. 2006](#); [MacLeod et al. 2010](#); [MacLeod et al. 2012](#); [Morganson et al. 2014](#); [Caplar et al. 2017](#)).

Based on ensemble analysis, these works showed that the amplitude of variability is increasing with increasing timescales, with typical continuum variability of 0.2 mag over \sim months to years timescales (e.g. [MacLeod et al. 2016](#) and references therein), and investigated additional dependencies with physical AGN parameters. For a fixed timescale, the amplitude of variability is observed to anti correlate with luminosity, rest frame wavelength and Eddington ratio, while little or no dependency is found as a function of redshift (e.g. [Wilhite et al. 2008](#); [Ai et al. 2010](#); [MacLeod et al. 2010](#); [Caplar et al. 2017](#); [Rumbaugh et al. 2018](#); [Sánchez-Sáez et al. 2018](#)). The dependency on BH mass is still unclear as different studies found either positive, negative or absent correlations (e.g. [Wilhite et al. 2008](#); [Kelly et al. 2009](#); [MacLeod et al. 2010](#); [Zuo et al. 2012](#); [Caplar et al. 2017](#)).

Although a few examples of periodic variability have been found ([Graham et al. 2015a](#); [Graham et al. 2015b](#); [Charisi et al. 2016](#); but see also [Liu et al. 2015](#) and [Vaughan et al. 2016](#) for different interpretations of the periodic behaviour), the observed variability is usually assumed to be stochastic and described as a damped random walk⁹ (DRW, [Kelly](#)

⁹The damped random walk is also known as first-order CARMA model (CAR(1), [Kelly et al. 2014](#)), or Ornstein–Uhlenbeck process ([Uhlenbeck and Ornstein 1930](#)).

et al. 2009). The DRW consists on a random walk at short timescales, flattening to white noise at higher timescales. The transition timescale may correspond to the physical response time needed from the disc to suppress (dampen) the variability driven by a stochastic thermal process (e.g. Kelly et al. 2009; Lawrence 2016), but its exact value (timescale) cannot be reliably measured from current data due to the limited length of the available light curves (Kozłowski 2017a; Kozłowski 2017b). In any case, most studies find break positions at scales of $\gtrsim 100$ days (e.g. MacLeod et al. 2012; Kozłowski 2016). Although the DRW has been successful in describing the general AGN variability in surveys such as SDSS and POSS (e.g. Kelly et al. 2009; MacLeod et al. 2010; MacLeod et al. 2012; but see also Kozłowski 2016), other studies based on different photometric surveys (e.g. Zu et al. 2013; Caplar et al. 2017; Sánchez-Sáez et al. 2018) or on *Kepler* light curves (Mushotzky et al. 2011; Kasliwal et al. 2015; Smith et al. 2018) revealed steeper high-frequency PSD, suggesting that the DRW is not sufficient to fully describe the variability at \sim days timescales or less.

AGN variability is also observed as variations in the optical and UV emission lines. Appearing or disappearing broad Balmer lines have been detected in the past in several local AGN, called “changing-look AGN” (CL-AGN¹⁰, e.g. Khachikian and Weedman 1971; Tohline and Osterbrock 1976; Penston and Perez 1984; Aretxaga et al. 1999; Bischoff and Kollatschny 1999; Cohen et al. 1986; Denney et al. 2014). In the last years, repeated spectroscopy and targeted searches are revealing an increasing number of sources with appearing or disappearing broad line features on months to decades timescales also at higher redshift and luminosities, usually referred to as “changing-look quasars” (CL-QSO, e.g. LaMassa et al. 2015; Runnoe et al. 2016; Ruan et al. 2016; McElroy et al. 2016; Husemann et al. 2016; Yang et al. 2018; Mathur et al. 2018; Yang et al. 2018; Wang et al. 2018; Stern et al. 2018; Ross et al. 2018; Zetzl et al. 2018; Katebi et al. 2018; MacLeod et al. 2019; Trakhtenbrot et al. 2019). In these sources the change in lines structure is often accompanied by changes in the overall optical/UV luminosity by almost one order of magnitude or more over the same timescales, much higher compared to the mean variability observed in ensemble analysis¹¹.

Whether CL-AGN and CL-QSO are simply the tail of a continuum distribution of variability, or if they belong to a distinct class with significantly different variability properties and physical mechanisms, still remains an open question (e.g. MacLeod et al. 2016). In any case, the existence of sources switching from Type 1 to Type 2 on \sim years

¹⁰We note that the term “changing look” was first used by Matt et al. (2003) to define AGN whose repeated X-ray spectra showed a switch from Compton thick to Compton thin, or vice versa (e.g. Matt et al. 2003; Piconcelli et al. 2007; Marchese et al. 2012; Ricci et al. 2016a). The cause of such changes is usually reconducible to varying column density of the nuclear obscuring material. Despite the similar name, these “X-ray CL-AGN” are not the same class of objects as the CL-AGN discussed in the following of the thesis.

¹¹We note that extreme variability in the continuum has recently been found also in AGN which do not show a changing look behaviour, or for which no spectroscopic data are available (e.g. Graham et al. 2017; Rumbaugh et al. 2018; MacLeod et al. 2019).

timescales challenges the classical AGN unification model (e.g. [Urry and Padovani 1995](#)), where the presence and absence of broad emission lines is explained by different line of sight orientations, as the angular position of the obscuring material is not expected to vary on such short timescales. The same is true also in the case of a clumpy torus (e.g. [Nenkova et al. 2008a](#); [Nenkova et al. 2008b](#); [Mor et al. 2009](#); [Hönig and Kishimoto 2010](#); [Elitzur 2012](#)), as it is not clear which population of clouds could exist at sufficiently larger radius to rapidly modify our view of the BLR (e.g. [Goodrich 1995](#); [MacLeod et al. 2016](#)).

The rapid variability observed in the optical/UV continuum, in particular in extreme cases such as the CL-QSO, is hard to reconcile with standard accretion disc theory. Indeed, months to years timescales are much shorter compared to the viscous timescales, at which variability due to overall accretion changes would appear, which is on the order of $\sim 100 - 1000$ yr (see [Lawrence 2018](#) for a discussion of the “viscosity crisis”). The observed timescales are more consistent with thermal timescales, which are relevant for instabilities or local perturbations in the accretion disc. Such instabilities and perturbations could explain the moderate variability characteristic of the majority of the AGN, as well as produce structural changes in the inner part of the accretion disc which could lead to the extreme variability observed in CL-QSO (e.g. [Stern et al. 2018](#); [Ross et al. 2018](#); [Noda and Done 2018](#)). The possible causes of such instabilities and perturbations are still matter of debate, but they include magnetorotational instabilities (MRI, [Balbus and Hawley 1991](#); [Reynolds and Miller 2009](#)), local temperature fluctuations driven e.g. by X-ray heating ([Shappee et al. 2013](#)), instabilities in the $(\Sigma-T_{\text{eff}})$ parameter space driven by large changes in opacity ([Stern et al. 2018](#) and references therein), iron opacity ([Jiang et al. 2016](#)) as well as perturbations due to stellar mass black holes, stellar remnants and stars moving within the dense medium of the accretion disc (e.g. [Syer et al. 1991](#); [McKernan et al. 2014](#); [Bartos et al. 2017](#)). Other possible explanations are that accretion discs are magnetically elevated, what could lead to larger scale heights and shorter variability timescales compared to what is expected for standard thin accretion discs ([Dexter and Begelman 2019](#)), or that the behaviour of the accretion disc is dominated by non-local physics such as magnetic fields connecting different regions on timescales shorter than viscous timescales ([Lawrence 2018](#)). Furthermore, the simultaneous disappearance of broad emission lines and decrease in overall luminosity observed in CL-QSO is consistent with the evolutionary scenario proposed by [Elitzur et al. \(2014\)](#), who suggested that AGN evolve from Type 1 to Type 1.2/1.5 to Type 1.8/1.9 as the accretion rate decreases.

The scenarios discussed above mostly relate to processes happening inside the AGN accretion disc, and are therefore intrinsic of the AGN. However, there are various external phenomena which could affect the observed luminosity, such as starburst activity in the host galaxy ([Aretxaga et al. 1997](#)), microlensing ([Hawkins 1993](#); [Lawrence 2016](#)) and tidal disruption events (TDE, [Eracleous et al. 1995](#); [Merloni et al. 2015](#)). Variable obscuration could in principle also produce variable luminosity and line structure as observed in CL-AGN, but it was excluded for most of the sources due to lack of color changes and, as explained above, inconsistent timescales (e.g. [Katebi et al. 2018](#)). The obscuration

scenario is also disfavoured by the fact that variability observed in the mid-IR is usually echoing the optical variability with time lags expected for dust reprocessing (e.g. [Sheng et al. 2017](#)).

With the advance of large, multiwavelength time-domain surveys such as the Large Synoptic Survey Telescope (LSST, [Ivezic et al. 2008](#); [LSST Science Collaboration et al. 2009](#)), the Time-Domain Spectroscopic Survey in SDSS-V (TDSS, [Morganson et al. 2015](#); [Kollmeier et al. 2017](#)), the Zwicky Transient Facility (ZTF, [Bellm et al. 2019](#); [Graham et al. 2019a](#)), the All-Sky Automated Survey for SuperNovae (ASAS-SN, [Shappee et al. 2014](#)) and the extended ROentgen Survey with an Imaging Telescope Array (eROSITA, [Merloni et al. 2012](#)) we are entering an exciting era of time-domain astronomy which will allow us to probe the variable Universe with an unprecedented cadence (\sim days), depth, sky area, and time-span. These surveys will allow us to probe the variability properties of individual AGN, of the AGN population as a whole, as well as new types of flares and other extreme variability phenomena associated with SMBH accretion such as CL-AGN or TDE. This will provide crucial information to quantify the variability phenomena and to test various models for its origin.

Variability on super-human timescales

The variability discussed above only refers to galaxies hosting active SMBH (AGN and quasars), and to timescales which can be directly probed with observations (i.e. human timescales). However, SMBHs could alternate active and inactive phases, and variability could be present also on timescales much larger than what probed by current studies¹². Indeed, long timescales variability has been inferred for SgrA*, the SMBH in our own Milky Way. Although this SMBH is currently not active, there are multiple observations which allow us to constrain its past activity. For example, [Bland-Hawthorn et al. \(2013\)](#) suggested that the Magellanic Stream was photoionised by a strong AGN burst with $\lambda_{\text{Edd}} \sim 0.03 - 0.3$ in the Galactic center, whose luminosity decreased by 7 – 8 orders of magnitude within a time frame of $\sim 1 - 5$ Myr. This strong AGN-like episode may be responsible for the Fermi Bubbles ([Su et al. 2010](#)), which may have been inflated by an AGN jet $\sim 1 - 3$ Myr ago ([Guo and Mathews 2012](#)). In addition, X-ray reflections from molecular clouds in the Galactic center suggest that SgrA* underwent several flares in the last centuries (e.g. [Ponti et al. 2010](#); [Zhang et al. 2015](#)).

A hint of variability on super human timescales is given also by indirect arguments based on the photoionisation state of large scale gas in (and around) galaxies. Based on the number of optically elusive AGN in the *Swift*/BAT BASS sample ([Koss et al. 2017](#)), [Schawinski et al. \(2015\)](#) suggested that typical AGN phases (or AGN lifecycles) are on the order of $\sim 10^5$ yr. Since these timescales are much shorter than the total time needed

¹²As described above, the amplitude of variability is observed to increase with timescales. Although this increase cannot continue indefinitely, as it would imply infinite power at very low frequencies, it is reasonable to think that variability is present also at larger timescales than the ones probed to date.

for a SMBH to accumulate its mass through accretion ($\sim 10^7 - 10^9$ yr, [Soltan 1982](#); [Yu and Tremaine 2002](#); [Marconi et al. 2004](#)), this suggests that AGN may “flicker” on and off 100 – 1000 times during their life ([Schawinski et al. 2015](#))¹³. In a theoretical follow-up paper, [King and Nixon \(2015\)](#) showed that these timescales are consistent with chaotic accretion ([Sanders 1981](#); [Moderski et al. 1998](#); [King and Pringle 2006](#)) from very close, randomly oriented accretion discs ($r < r_{\text{sg}} \sim 0.01$ pc, where r_{sg} is the self-gravitational radius of the accretion disc). A flickering behaviour due to clumpy cold accretion arising from instabilities in the hot gas, or to the interaction between outflowing radiation and winds with the galactic gas, is found also in both high resolution simulations ([Hopkins and Quataert 2010](#); [Novak et al. 2011](#); [Bournaud et al. 2011](#); [Gabor and Bournaud 2013](#); [DeGraf et al. 2014](#); [Sijacki et al. 2015](#); [Gaspari et al. 2017](#)) and theoretical models ([Siemiginowska and Elvis 1997](#); [Sanders 1981](#); [Di Matteo et al. 2005](#); [Hopkins et al. 2005](#); [Springel et al. 2005](#); [King and Pringle 2007](#)).

A laboratory to study AGN variability on $10^4 - 10^5$ yr timescales is provided by galaxies with extended, ~ 10 kpc scale, AGN photoionised gas, as it can be found in the Voorwerpjes galaxies (see Section 1.3.3). Indeed, because of the travel time of the ionising photons, the photoionisation state of the gas at different distances from the center may allow us to estimate the past AGN luminosity, and therefore reconstruct historical AGN light curves (see Chapter 1.3.3 and Chapter 4.1).

Information about variability on still longer timescales, $10^7 - 10^9$ yr, can be inferred by the study of radio jets, where multiple lobes and remnants can be indicative of recurrent AGN activity (e.g. [Parma et al. 2007](#); [Marecki 2012a](#); [Marecki 2012b](#); [Shulevski et al. 2015b](#); [Shulevski et al. 2015a](#)).

1.3.3 The Voorwerpjes sample

The Voorwerpjes galaxies (VP) are a sample of 20 galaxies with extended AGN photoionised gas on ~ 10 kpc scale (1.2, Fig. 1.3), which were discovered by citizen scientists as part of the Galaxy Zoo project ([Lintott et al. 2008](#)).

The first and best studied example of VP is the extended emission line region (EELR) connected to the nearby postmerger galaxy IC 2497, now known as “Hanny’s Voorwerp” (HV)¹⁴ ([Lintott et al. 2009](#)). The cloud spans a projected range from 15 to 35 kpc from the galaxy nucleus, and the photoionisation state of its gas, as revealed by the optical spectrum, strongly supports the interpretation that it is illuminated by a powerful quasars with bolometric luminosity of at least $L_{\text{bol}} = 10^{46}$ erg s⁻¹ ([Lintott et al. 2009](#)). Multiwavelength observations of the center of IC 2497 confirmed the presence of an AGN,

¹³We note that, according to simulations of galaxy evolution, periodic AGN activity is also required to prevent the accumulation of cold gas in the galactic centers (see [Morganti 2017](#) and references therein).

¹⁴“Hanny’s Voorwerp” means “Hanny’s object” in dutch, from the name of the dutch citizen scientists who serendipitously discovered the system.

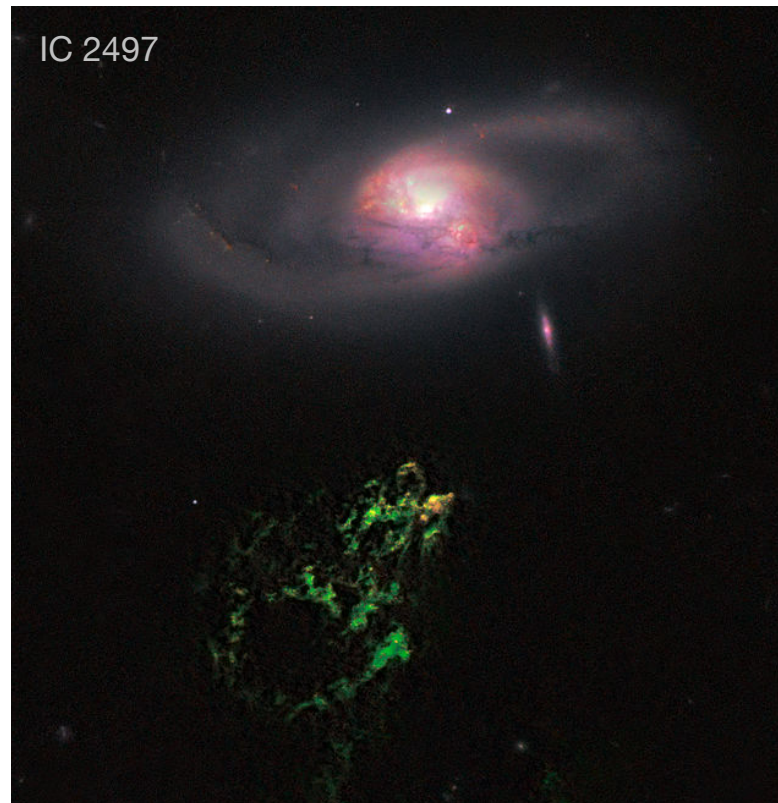


Figure 1.2: Composite image of the galaxy IC 2497 and Hanny’s Voorwerp (green cloud, $\sim 11 \times 16$ kpc in projected extent) obtained with the *HST* and WIYN telescopes (dark green: F160W *H*; dark red: F814W *I*; red: redshifted $H\alpha$; green: FR505N [O III]; blue: WIYN *B*). The green appearance of the cloud signifies that its emission is strongly dominated by [O III], as confirmed also by optical spectroscopy. Credit: NASA, ESA, W. Keel and the Galaxy Zoo team (adapted).

but not as strong as required by photoionisation balance (Lintott et al. 2009; Schawinski et al. 2010b; Keel et al. 2012b). This suggests that the AGN faded by 2 – 4 orders of magnitude in the last $\sim 10^4 - 10^5$ yr, which correspond to the travel time needed from the ionising photons to reach the cloud, and that HV is an example of ionisation echo. An analysis of the *Chandra* and *NuSTAR* X-ray spectra of IC 2497, aimed at reliably measuring the current intrinsic luminosity (and therefore the magnitude of the luminosity drop), as well as investigating the state of the hot gas in the nuclear region, are part of this thesis and presented in Chapter 2 and Chapter 3.

Systems similar to IC 2497 and HV provide a great laboratory to study AGN variability, and its effect on the host galaxy, on previously inaccessible timescales. Motivated by the discovery of HV, the Galaxy Zoo science team started a new project aimed at finding additional systems with similar properties, i.e. the VP galaxies (Keel et al. 2012a). First, citizen scientists were requested to visually inspect the composite *gri* Sloan Digital Sky

Survey (SDSS, [Abazajian et al. 2009](#)) images of ~ 20000 local ($z < 0.1$) galaxies¹⁵ to look for extended gas structures outside the galaxy plane. As a second step, the 50 top ranked candidates were followed up to obtain optical longslit spectra, and the sources were classified as AGN-photoionised based on 1) the optical [O III]/[H β] and [N II]/[H α] line ratios and their position in the spatially resolved BPT diagram ([Baldwin et al. 1981](#); [Kewley et al. 2001](#); [Kewley et al. 2013](#)); 2) the presence of prominent He II and [Ne V] lines, as can be produced only by the hard spectrum of an AGN; and 3) modest electron temperatures $T_e \lesssim 2 \times 10^4$ K to exclude cases where the ionisation is produced by shocks. This resulted in a sample of 19 sources, now known as VP galaxies. Calculations based on energy balance suggest that 8 of them host an AGN which is fading in a similar way as observed in IC 2497 ([Keel et al. 2012a](#); [Keel et al. 2017](#)).

Most of the VP galaxies are bulge dominated, and are part of merging, post merging or interacting systems ([Keel et al. 2012a](#); [Keel et al. 2015](#)). Although the *HST* images available for 8 sources show nuclear rings and loops which may be suggestive of outflow, the large scale gas is mostly rotation-dominated and outflows seem to have only a very localised role ([Keel et al. 2015](#); [Keel et al. 2017](#)). These findings suggest that the observed clouds are actually gas-rich tidal debris which are illuminated by the AGN ionisation cone but are not displaced by outflows, and therefore make them the ideal place to study long timescales AGN variability. However, due to the fact that most of the sources are in interacting or merging systems, and that in contrast to most EELRs in quasars the outflows only play a marginal role (e.g. [Stockton et al. 2006](#)), this sample is expected to be highly biased and not representative of the whole AGN population. Chapter 4 describes our effort to compile a multiwavelength dataset for the VP sample, and provide examples of how these data can be used to investigate long timescales variability as well as the properties of the host galaxies and therefore the sample selection.

The VP galaxies are not the only ionisation echoes discussed in the literature. Other examples of AGN-photoionised clouds related to nearby AGN that are currently too faint to light them up are the merger remnant NGC 7252 ([Schweizer et al. 2013](#)), the off-nuclear photoionised region in NGC 3621 ([Menezes et al. 2016](#)), the EELR associated to NGC 4151 ([Penston et al. 1990](#)) and at higher redshift and luminosities the “Green Beans” galaxies (Ly α blobs, [Schirmer et al. 2013](#); [Davies et al. 2015](#); [Schirmer et al. 2016](#); [Kawamuro et al. 2017](#)). Altogether, the analysis of these sources will provide crucial information about the general AGN variability behaviour on super human timescales.

¹⁵The initial AGN host galaxy sample for this specific project included all the SDSS galaxies with [O III]/[H β] and [N II]/[H α] line ratios consistent with AGN photoionisation ([Baldwin et al. 1981](#); [Kewley et al. 2001](#); [Kewley et al. 2013](#)), and all the galaxies in the [Véron-Cetty and Véron 2010](#) catalog falling in the SDSS DR7 area. In addition, citizen scientists were requested to look for extended gas structures in the general Galaxy Zoo project, which also includes galaxies not known to host an AGN (as the AGN may be faded).

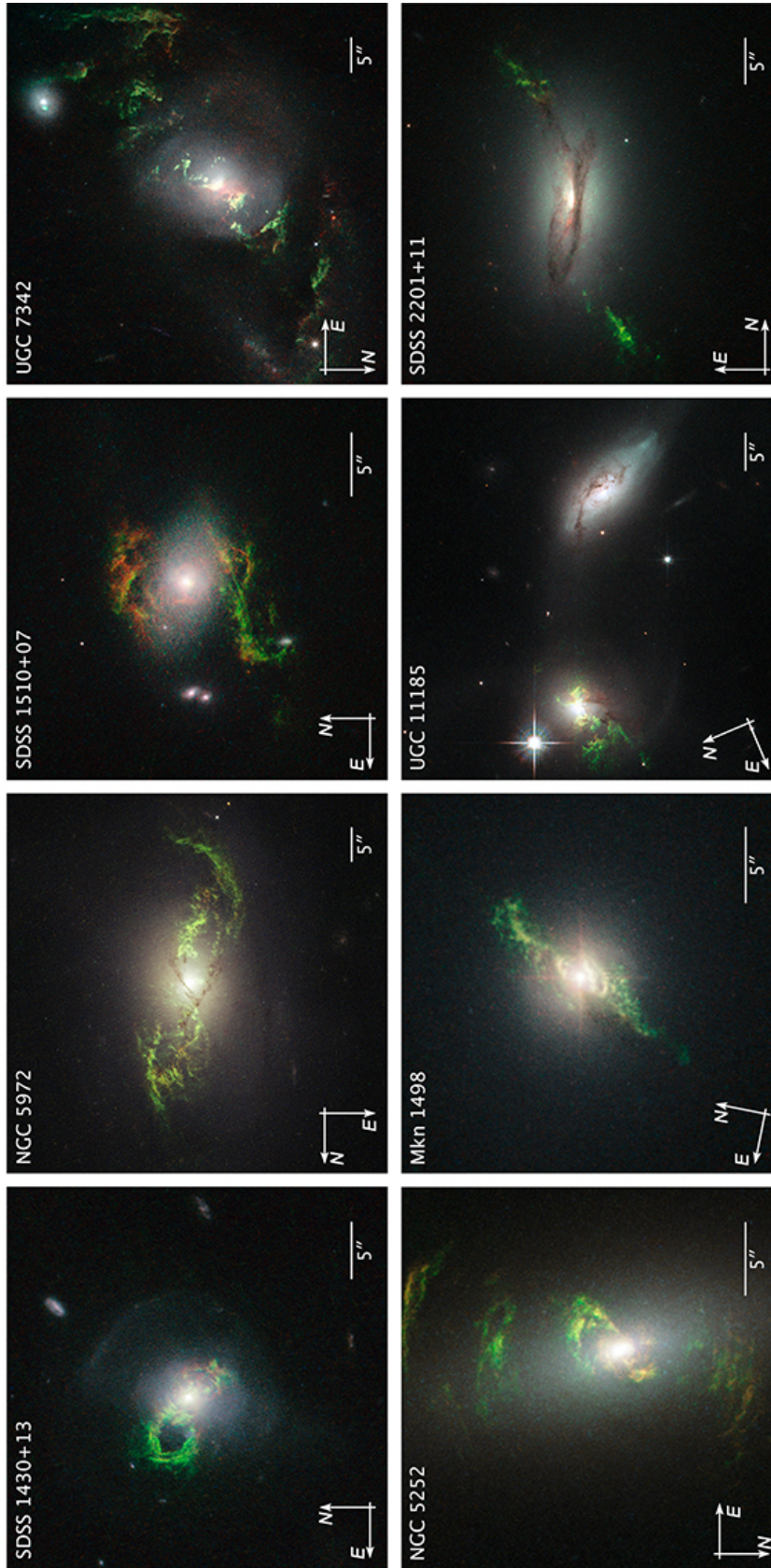


Figure 1.3: Combined *HST* images of 8 Voorwerpjes galaxies, similar to Fig. 1.2. Blue and red are the continuum images, while green corresponds to the strong [O III] line which clearly dominates the emission from the clouds. Although the geometry of the Voorwerpjes clouds differ from source to source, they all extend beyond the size of the galaxy, on ~ 10 kpc scales. Credit: NASA, ESA and W. Keel (adapted).

1.4 Organization and content of the thesis

The picture emerging from the previous chapters clearly supports the idea that the study of AGN variability is crucial for our understanding of the AGN accretion mechanism, as well as of its interaction with the host galaxy.

So far, time-domain studies mostly concentrated on characterising the amplitude of AGN variability on days to decades timescales, and on understanding the physical processes responsible for the variability at single timescales, whereas larger timescales are much less investigated. In addition, a crucial step for our understanding of SMBH activity is still missing: the link between variability features observed at very different timescales and in different objects.

As pointed out at the begin, the main goal of this thesis is to investigate AGN variability, and its effect on the host galaxy, on timescales ranging from days to Gyrs by combining multiwavelength observations of single objects, phenomenological models describing the general behaviour of the AGN population, and simulations of AGN light curves. Specifically, we want to concentrate on the following questions, the first directly related to observations, the second of more theoretical flavour:

1. Are the Voorwerpjes galaxies the right laboratory to study AGN variability on super-human timescales? If yes, what do they tell us about AGN variability and its effect on the host galaxy?
2. Is it possible to develop a (simple) framework which allows us to simultaneously model the AGN variability features observed in different galaxies at different timescales? If yes, how can it be used in the upcoming time-domain era?

Question 1 is addressed in Chapter 2, Chapter 3 and Chapter 4, while our framework to address Question 2 is presented in Chapter 5 and Chapter 6.

Specifically, in **Chapter 2** we use deep *Chandra* soft X-ray observations to study the environment of the fading AGN in IC 2497. Thanks to the high spatial resolution of *Chandra*, ~ 0.5 arcsec, we found evidence of extended X-ray emission from hot gas in the center of the galaxy, with a temperature structure suggesting the presence of a central bubble or cavity. A possible scenario is that this bubble is inflated by the fading AGN which, after changing accretion state, is now in a kinetic mode. Other possibilities are that the bubble has been inflated by the past luminous quasar, or that the temperature gradient is due to a shock front from a superwind driven by the AGN. At the end of the Chapter, we discuss the possible scenarios and the implications for the AGN-host galaxy interaction, as well as an analogy between AGN and X-ray binaries lifecycles. We speculate that an AGN could inject mechanical energy into the host galaxy at the end of

every lifecycle, and thus provide a source for mechanical feedback which may affect star formation.

In **Chapter 3** we make use of new *NuSTAR* hard X-ray observations to reliably determine the current intrinsic luminosity of the AGN in IC 2497, and therefore the magnitude of the claimed drop in luminosity. The analysis of these new data, together with soft X-ray observations from *Chandra*, optical longslit spectroscopy and narrowband imaging, as well as mid-IR photometry, shows that the AGN is highly obscured (Compton thick) and that its luminosity dropped by a factor ~ 50 in the last $\sim 10^5$ yr. These findings confirm the idea that IC 2497 hosts a fading AGN, although the magnitude of the drop in luminosity is significantly lower than previously thought. Based on repeated mid-IR and X-ray observations, and on the optical line ratios observed in the galaxy, we argue that the AGN in IC 2497 should not be classified as a CL-AGN. Rather, the measured change in Eddington ratio supports the idea that IC 2497 is entering a regime where it is switching from a radiatively efficient to a radiatively inefficient accretion state, in a similar way as observed in X-ray binaries.

The results presented in Chapter 2 and Chapter 3 confirm that at least in one VP galaxy the AGN underwent a large change in luminosity on $\sim 10^5$ yr timescales, and that hard X-ray observations are critical for the determination of the current luminosity. Therefore, VP galaxies can be used to study AGN variability on previously inaccessible timescales, provided that high quality multiwavelength data are available. In **Chapter 4** we describe our effort to compile a large multiwavelength database for these galaxies, and outline possible uses as well as a pilot study. Specifically, hard X-ray observations from *NuSTAR* are needed to probe the current intrinsic luminosity, spatially resolved spectroscopy from MUSE allows us to reconstruct historical AGN light curves, while radio imaging from VLA is valuable for investigating the environment of the VP galaxies and the sample selection.

Regarding Question 2, in **Chapter 5** we present our novel framework which links the variability of AGN over a broad range of timescales and luminosities to the observed properties of the AGN population as a whole, and particularly to the Eddington ratio distribution function (ERDF). After outlining the framework and the model, we present a compilation of variability measurements from the literature and from our own measurements covering many orders of magnitude both in time lags and variability amplitude. This compilation includes ensemble studies, which characterise the mean variability among the AGN population, as well as measurements for single objects such as the CL-AGN and the VP galaxies. We then combine the variability measurements on a structure function plot ranging from days to Gyrs, which provides a novel and valuable overview of the AGN variability phenomenon.

Finally, in **Chapter 6** we present the implementation of our framework on graphics processing unit (GPU) architecture. After extensive tests that characterise several intrinsic

and numerical aspects of the simulations, we describe some applications used for current and future time-domain surveys and for the study of extremely variable sources (e.g. CL-AGN or flaring AGN). Specifically, we define a simulation setup which reproduces the AGN variability observed in the PTF/iPTF survey and use it to forward model longer light curves of the kind that may be observed within the LSST main survey. Thanks to our efficient implementations, these simulations cover over 1 Myr with a roughly weekly cadence. This framework will become highly valuable to prepare for, and best exploit, data from upcoming time-domain surveys such as LSST and eROSITA.

A summary of the main results and achievements of this thesis, together with future prospects, is given in **Chapter 7**.

2 Extended X-ray emission in IC 2497 – energy injection in the gas around a fading AGN

*Laudato si', mi' Signore, per frate vento
et per aere et nubilo et sereno et onne tempo,
per lo quale a le tue creature dâi sustentamento.*¹

Laudes Creaturarum, San Francesco D'Assisi (1224)

This chapter is based on Sartori et al. (2016), “Extended X-ray emission in the IC 2497 - Hanny’s Voorwerp system: energy injection in the gas around a fading AGN”, MNRAS, 457:3629-3636.

IC 2497 is a massive, nearby ($z \sim 0.05$) spiral galaxy associated with Hanny’s Voorwerp (HV), an extended emission line region ($\sim 11 \times 16$ kpc in projected extent) located at ~ 20 kpc in projection from the core of the galaxy and closely matching its redshift. HV was discovered by Hanny van Arkel² a citizen scientist participating in the Galaxy Zoo project (Lintott et al. 2008, 2009). The optical spectrum of HV is dominated by [O III] $\lambda\lambda 4959, 5007\text{\AA}$ emission, and the presence of emission lines from high ionisation species such as [Ne V] $\lambda\lambda 3346, 3426\text{\AA}$ and He II $\lambda 4616\text{\AA}$ suggests that the cloud is photoionised by the hard continuum of an active galactic nucleus (AGN) in IC 2497 rather than star formation (Lintott et al. 2009). Moreover, the relatively quiet kinematics (line widths < 100 km/s) and low electron temperature ($T_e = 13500 \pm 1300\text{K}$) exclude the possibility of ionisation from shocks (Lintott et al. 2009).

¹*Praised be You, my Lord, through Brother Wind, and through the air, cloudy and serene, and every kind of weather through which You give sustenance to Your creatures* (Canticle of the Sun, Saint Francis of Assisi, 1224).

²Hanny’s Voorwerp means Hanny’s object in dutch.

Chapter 2. Extended X-ray emission in IC 2497 – energy injection in the gas around a fading AGN

Large scale radio observations of the system revealed an extended HI structure ($M = 8.5 \pm 2.1 \times 10^{10} M_{\odot}$) with irregular kinematics around the southern part of IC 2497, which suggests a tidal origin (Józsa et al. 2009). These observations also show a kpc-scale structure which may be a jet coming from the AGN. HV lies where the jet meets the HI reservoir and corresponds to a local decrement of HI column density which may be due to photoionisation. At smaller scales, Rampadarath et al. (2010) found a radio AGN in the core of IC 2497, and a second nuclear source which may be a jet hotspot in the large scale jet reported by Józsa et al. (2009).

In order to produce sufficient ionising photons to power the observed [O III] emission in HV, the quasar in IC 2497 has to have a bolometric luminosity of at least $L_{\text{bol}} = 10^{46} \text{ erg s}^{-1}$. However, the optical nuclear spectrum shows only very weak emission lines, so that the ionising source is classified as LINER or low-luminosity Seyfert galaxy (Lintott et al. 2009; Keel et al. 2012b). The two possible explanations to reconcile observed and expected emission are:

1. The quasar is obscured only along our line of sight but not in the direction of HV (Józsa et al. 2009; Rampadarath et al. 2010).
2. IC 2497 hosts a faded AGN (Lintott et al. 2009; Schawinski et al. 2010a; Keel et al. 2012b).

This second option would mean that the quasar dropped in luminosity within the last ~ 200 kyr, the travel time needed from the photons to reach the cloud (Keel et al. 2012b), but HV still remains lit up because of this travel time. Support for the fading scenario was given by Schawinski et al. (2010a) who analysed the IR data from IRAS and X-ray data from *XMM* and *Suzaku* obtained for IC 2497. First, as already reported in Lintott et al. (2009) the IR data show no evidence of the reprocessed luminosity expected from an obscured strong quasar. In addition, the *XMM* spectrum is best fitted with an unobscured power-law with photon index $\Gamma = 2.5 \pm 0.7$, as expected from an unobscured AGN, and a component for the hot gas in the galaxy. The quality of the fit is not improved if additional absorption and obscuration are taken into account. This model implies a bolometric luminosity of the AGN $L_{\text{bol}} = 4.2 \times 10^{42} \text{ erg s}^{-1}$, which is ~ 4 orders of magnitude lower than what expected from HV. In addition, *Suzaku* observations show only a marginal detection with the 15-30 keV PIN camera (hard X-ray detector). If these counts are real, this would mean that the AGN is strongly obscured and we are observing the reemission instead of the AGN power-law, but the obtained luminosity would still be ~ 2 orders of magnitude below what expected from HV. Also the *HST* observations presented by Keel et al. (2012b) argue against the hypothesis of a luminous, strongly obscured AGN. WFC3 images show a complex dust structure near the nucleus of the galaxy, but the view of the nucleus is not hindered by absorbing features, so that obscuration cannot be the explanation of the lack of strong AGN features. Moreover, there is no high-ionisation gas near the nucleus, suggesting that the current radiative output from the AGN is low.

The observations described above suggest that the quasar in IC 2497 dropped in luminosity by at least 2 orders of magnitude in the last $\sim 10^5$ years. The system composed by HV and its galaxy is therefore a great laboratory to study AGN variability on previously inaccessible timescales. The analysis of the galaxy allows us to study the present state of the AGN and the AGN-host galaxy interaction in this “post quasar” phase, while HV provides information about the past state of the AGN. Finally, the distance between the two provides information about timescales.

In this Chapter we present the analysis of new, deep *Chandra* X-ray observations of IC 2497. The Chapter is organised as follows. In Section 5.2 we describe the X-ray observations and the data reduction. In Section 2.2 we describe the performed imaging and spectroscopic analysis. Because of the good spatial resolution reached by *Chandra*, this analysis allows us not only to measure the overall X-ray flux from the galaxy, but also to (partially) resolve its emission. In Section 2.3 we discuss the results and possible consequences for the AGN-host galaxy interaction as well as the analogy between AGN and X-ray binaries.

2.1 Observations

We observed IC 2497 with the *Chandra* Advanced CCD Imaging Spectrometer (ACIS) on 2012 January 8 (ObsID 13966, 59.35 ks) and 2012 January 11 (ObsID 14381, 53.4 ks; PI Kevin Schawinski, Cycle 13). We took the data with the S-array (ACIS-S) in very faint (VFaint) time-exposure (TE) mode. We performed a standard data reduction starting from the level 1 event files using the CIAO 4.7 software (Fruscione et al., 2006) provided by the *Chandra* X-ray Center (CXC). We ran the script CHANDRA_REPRO with the latest CALDB 4.6.8 set of calibration files, applied subpixel position using the Energy Dependent Subpixel Event Repositioning algorithm (PIX_ADJ=EDSER; Tsunemi et al. 2001; Li et al. 2003, 2004), and flagged the background events most likely associated with cosmic rays by running the task ACIS_PROCESS_EVENTS (CHECK_VF_PHA=YES in CHANDRA_REPRO). We analysed the background light curves with the CIAO routine LC_SIGMA_CLIP() and found no interval of unusually strong background flaring. Because of the low count rate the observations show no evidence of pileup.

In order to correct for the offset in the relative astrometry of the two observations, we first rebinned the reprocessed event files to 1/4 pixel resolution (0.125 arcsec) using the CIAO DMCOPY routine with binning factor 0.25. We then ran the CIAO DMSTAT routine on the rebinned images to get the centroid of the emission from IC 2497. In the following we will consider the centroid as the center of the emission in the respective observation.

We extracted the spectra and generated the response files using the CIAO tool SPECEXTRACT (see Chapter 2.2 for more details about the extraction regions). For the background estimation we considered three source-free circular regions with a 5 arcsec radius ~ 20

Chapter 2. Extended X-ray emission in IC 2497 – energy injection in the gas around a fading AGN

arcsec away from the source. We then grouped each spectrum with a minimum of 3 counts per bin using the HEASOFT tool GRPPHA.

We simulated the PSF images needed for the analysis using MARX 5.1 (Davis et al., 2012). First, we created a model of the emission using XSPEC and SHERPA (see Chapter 2.2 for details about the assumed models). We then used MARX³ to run the raytrace simulation and project the ray-tracings onto the ACIS-S detector. Since we are interested on the sub-pixel regime we ran the simulations with PIXADJ=EDSER and ASPECT-BLUR=0.19 arcsec (telescope pointing uncertainty). We also included the telescope dithering (DITHERMODEL=INTERNAL, DITHERAMP_RA=8, DITHERAMP_DEC=8) and corrected for SIM drift and offset.

2.2 Analysis

2.2.1 Radial profile and source extension

We compute the 0.5 - 6.0 keV background-subtracted surface brightness profiles of the two observations starting from the reprocessed event files. We use the CIAO tool DMEXTRACT to extract the counts in four concentric annuli centered on the centroid of each exposure, and with outer radius 0.5, 1.0, 1.5 and 4.0 arcsec (Fig. 2.1, first panel). For the background we consider a source-free annulus with internal radius 4 arcsec and external radius 7 arcsec. The obtained radial profiles, normalized to the total number of counts in a 4 arcsec aperture, are shown in Fig. 2.2. The error bars correspond to the 1σ confidence interval (68.23%). For the annuli with more than 25 counts ($N > 25$) we compute the 1σ error of the total counts (not background subtracted) using Gaussian statistic, $\sigma = \sqrt{N}$. For $N \leq 25$ we use the Gehrels approximation $\sigma = 1 + \sqrt{N + 0.75}$ (Gehrels 1986; this actually corresponds to the 84.13% upper limit for a Poisson distribution). The profiles of the two observations are consistent within 1σ (2σ in the last annulus), showing no evidence of variability.

The emission from an AGN is expected to be point-like. However, the radial profile suggests that the emission in IC 2497 is extended. Moreover, the spectrum extracted from a 4 arcsec aperture is best-fit with a combination of two models: a power-law model for the AGN emission, and a collisionally ionised diffuse gas model (APEC) representing the hot gas in the galaxy, which can be expected to be extended (Fig. 2.3, Table 2.1). This is true both performing a simultaneous fit of the two observations, or considering them separately (the best-fit parameters are always consistent within the 90% confidence level, see more details about spectral fit in Chapter 2.2.2). In order to understand if the observed extension is physical, and not only due to the PSF, we compare the radial profile of the observations with the expected PSF profile. We simulate the PSF image as

³For details on simulating a PSF image using MARX see http://cxc.harvard.edu/chart/threads/marx_sim/

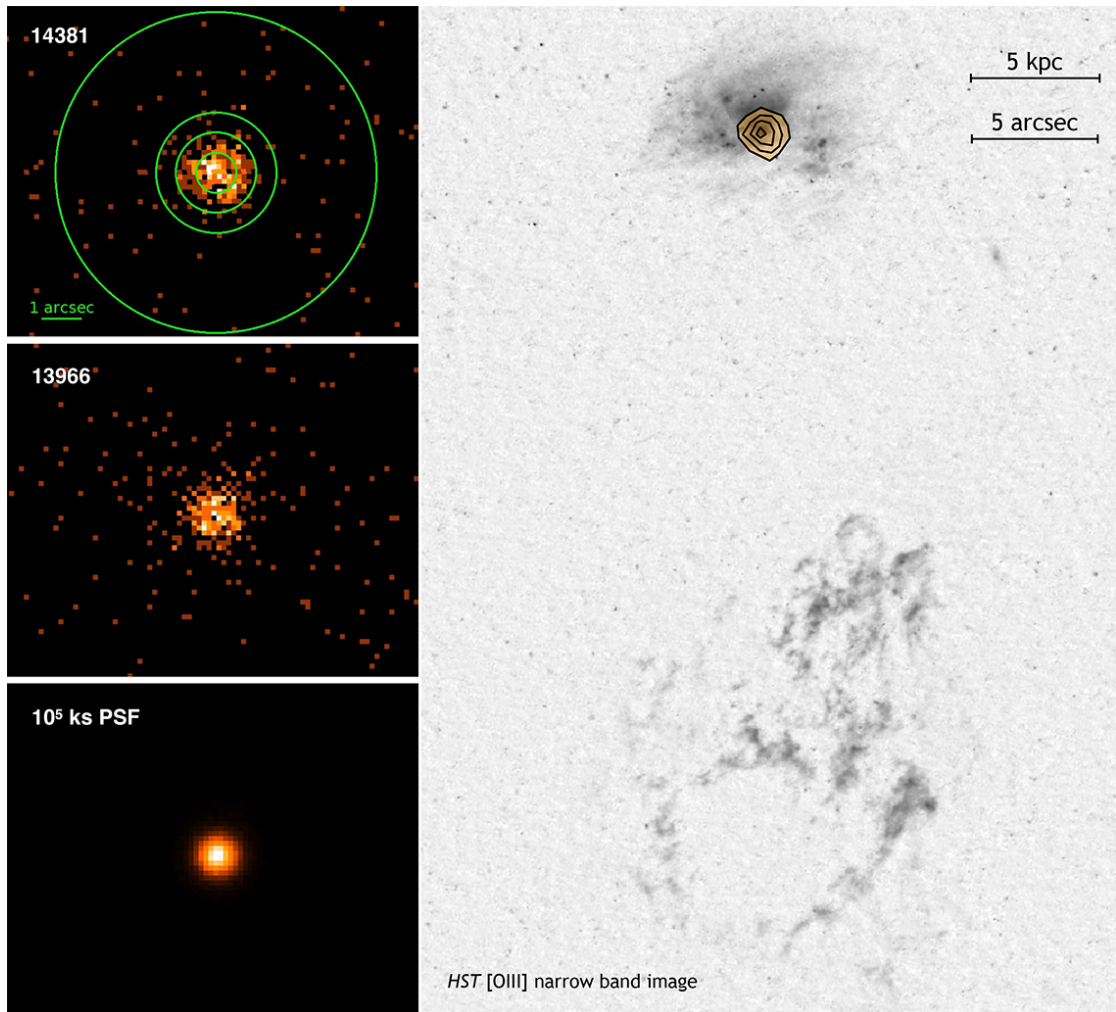


Figure 2.1: Left: *Chandra* X-ray images for ObsID 14381 (53.4 ks), ObsID 13966 (59.35 ks), and simulated 10^5 ks PSF. The green annuli show the regions from which we extract the spectra and compute the brightness profile. The spatial scale is the same for each image. The colour scale is linear (0-5 counts for the observations, 0-1800 counts for the 10^5 ks PSF). Right: *Chandra* X-ray contours overlaid on the *Hubble* [O III] narrow band image of IC 2497 (top) and Hanny’s Voorwerp (bottom; from [Keel et al. 2012b](#)).

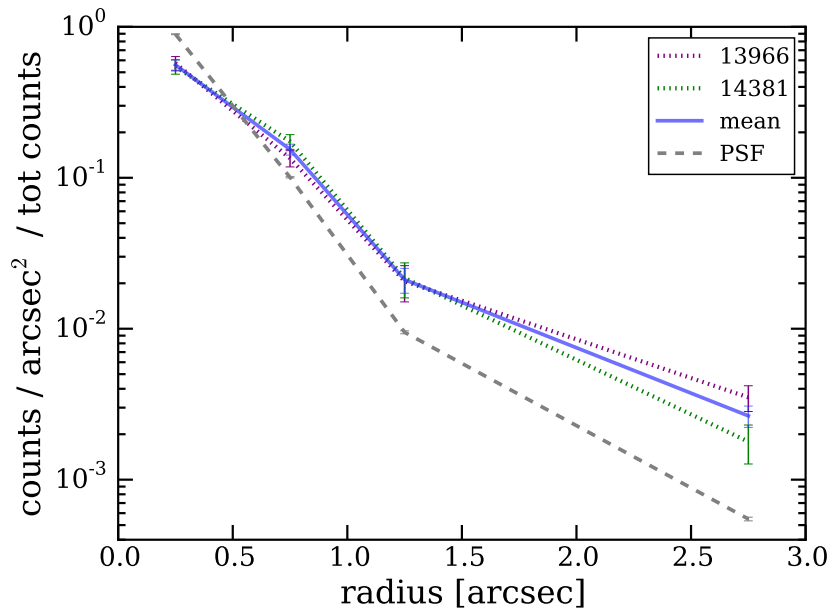


Figure 2.2: Normalized surface brightness profiles of the *Chandra* images and of the simulated PSF. ObsID 13966 and 14381 are shown in purple and green, respectively, while the blue line shows the mean between the two observations. The profiles of the two observations are consistent within 1σ (2σ in the last annulus). The gray line shows the profile of the simulated point spread function (PSF). The PSF profile is steeper toward the center than the source’s profile. This confirms that the source is extended.

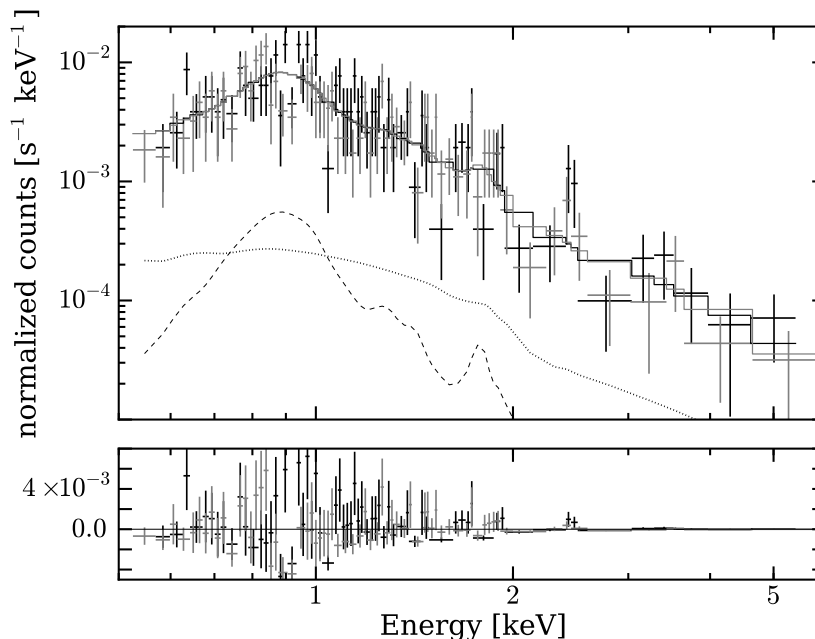


Figure 2.3: *Chandra* 0.5 - 6.0 keV X-ray spectrum of IC 2497 (total emission, $r = 4$ arcsec) for ObsID 14381 (black) and ObsID 13966 (gray). The spectra are binned so that each bin contains at least 3 counts. The lines correspond to the best fit model $\text{PHABS} \times (\text{ZPOW} + \text{APEC})$, where ZPOW corresponds to the AGN emission and APEC to the emission from a hot diffuse gas (see text). The absorption is fixed to the Galactic value. The residuals of the fit are shown in the bottom panel. The dotted and dashed lines correspond to the $\text{PHABS} \times \text{ZPOW}$ and $\text{PHABS} \times \text{APEC}$ models, respectively, both normalised by a factor 10 for illustrative purposes.

described in Chapter 5.2, starting from the fit to the total emission. We first create a model of the total emission using XSPEC and SHERPA, and the spectral model described above, where we also consider Galactic absorption ($\text{PHABS} \times (\text{ZPOW} + \text{APEC})$), and then use MARX to run the ray trace simulation and project the ray-tracings onto the ACIS-S detector. In order to get a good sampling of the PSF, and thus understand its analytic shape, we increase the exposure time to 10^5 ks. We compute the PSF brightness profile in the same way as described for the real observations. Since the PSF profile should in principle depend on the input spectrum and on the source position on the ACIS-S detector we repeat the simulations for both observations separately. However, due to the similarity of model spectra and positions (both observations are nearly on-axis) the normalized PSF brightness profiles are the same.

Fig. 2.2 shows the comparison between the normalized brightness profile of the source (two observations and mean value) and of the PSF. The PSF profile is steeper toward the center than the source's profiles. This confirms that the source is extended.

2.2.2 Spectral fit and temperature profile

For both observations we use `SPEXTRACT` to extract the spectrum of the total X-ray emission in IC 2497 from an aperture with $r = 4$ arcsec centered on the centroid. We fit the spectra in the 0.5 – 6.0 keV energy range with `XSPEC` using Cash statistic (Gehrels, 1986) as fit statistic, and Chi-Square statistic as test statistic. Since there is no variability in the observations and between the observations at the 90% level we fit the spectra from the two data sets simultaneously. The source is best fitted as a sum of two components: a power-law model representing the AGN emission (ZPOW model, $\Gamma = 2.33^{+0.15}_{-0.16}$), and a model for the hot gas emission at the redshift of the host galaxy, with abundance fixed at solar value (APEC model, $kT = 0.953^{+0.048}_{-0.054}$ keV)⁴. The absorption component (PHABS) is fixed at the Galactic value ($N_{\text{H}} = 1.31 \times 10^{20}$ cm⁻², as given by the Colden Calculator with the NRAO dataset⁵). All the best fit parameters are listed in Table 2.1. The power-law component is consistent with a low luminosity AGN with $L_{2-10\text{keV}} = 5.8 \times 10^{40}$ erg s⁻¹.

In order to understand the properties of the extended emission we attempt a spatially resolved spectral analysis. For each observation we use `SPEXTRACT` to extract the spectrum from a circular aperture of radius 0.5 arcsec centered on the centroid, and 3 annuli with outer radius 1.0, 1.5 and 4.0 arcsec. Since we will account for the PSF during the fit, as described in details in the following, we set `CORRECTPSF=NO`. We then fit the spectra in the same way as described for the total emission. The best fit parameters are listed in Table 2.1, while the spectra and fits are shown in Fig. 2.4.

The AGN emission is expected to be point-like and the ZPOW component should in principle be present in the nuclear spectrum only. However, because of the PSF some AGN contribution is present also in the external annuli. We therefore perform the following analysis, where we fix the AGN component in the fit such that the normalization and the power-law slope are PSF-dependent, and let only the APEC model free to vary. First, we simulate a PSF in the same way as described in Section 5.2 and Section 2.2 but for a ZPOW model only, extract the spectra from the annuli considered for the analysis, and fit them using the response files (RMF and ARF files) obtained for the real spectra⁶. Since the number of counts in the simulated spectra is high, we group them with a minimum of 25 counts per bin and use Gaussian statistic. In each annulus the spectrum is consistent with a power-law at the redshift of the galaxy (ZPOW). However, since the PSF also depends on the energy, the power-law slope (PHOINDEX) varies with radius, as

⁴Since IC 2497 is a massive galaxy, the assumption of solar abundance should be appropriate. However, we also performed the fits considering metallicities of 0.2 and 0.5 solar, and the differences in the measured temperatures are only at the < 10% level. This is true both for the total emission and for the annuli described in the next paragraphs

⁵<http://cxc.harvard.edu/toolkit/colden.jsp>

⁶By assuming the same RMF and ARF files as the observations we treat the simulated spectra as similar as possible to the real spectra. We repeated the analysis also using simulated RMF and ARF files, but the fit parameters do not differ significantly.

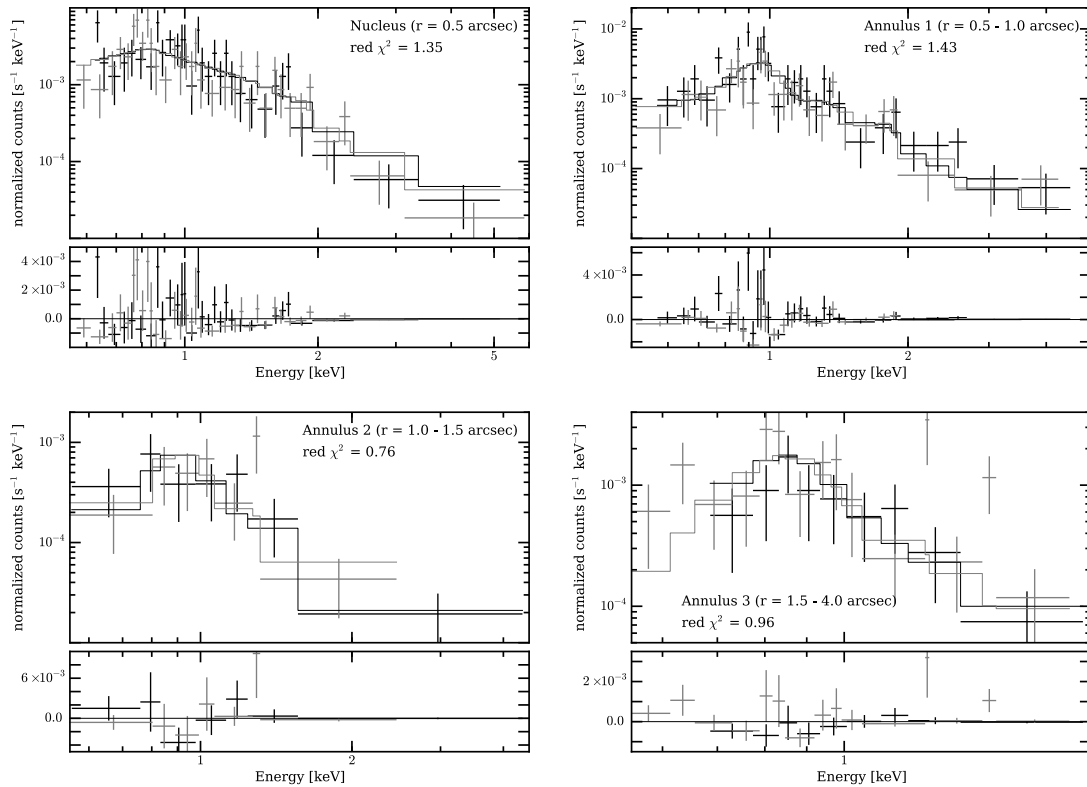


Figure 2.4: *Chandra* X-ray spectra extracted from the nuclear region and from the three annuli, for ObsID 14381 (black) and ObsID 13966 (gray). The spectra are binned so that each bin contains at least 3 counts. The lines correspond to the best fit model $\text{PHABS} \times (\text{ZPOW} + \text{APEC})$, where ZPOW corresponds to the AGN emission and APEC to the emission from a hot diffuse gas (see text). The absorption is fixed to the Galactic value. The residuals of the fit are shown in the bottom panel.

Chapter 2. Extended X-ray emission in IC 2497 – energy injection in the gas around a fading AGN

described in Table 2.1. We therefore fit the real spectra with the $\text{PHABS}\times(\text{ZPOW}+\text{APEC})$ model described above, where for each annulus we fix the power-law slope at the value obtained from the PSF simulation. In order to fix the power-law normalisation, we first fit the total emission (0.0 – 4.0 arcsec), and assume that in each annulus the normalisation scales in the same way as seen in the PSF simulation:

$$\text{NORM_PL}_i = \frac{\text{NORM_PSF}_i}{\text{NORM_PSF}_{\text{tot}}} \times \text{NORM_PL}_{\text{tot}} \quad (2.1)$$

where NORM_PL_i and $\text{NORM_PL}_{\text{tot}}$ are the normalisation of the power-law component in the real spectra extracted from the i -th annulus and from the total aperture (0.0-4.0 arcsec), while NORM_PSF_i and $\text{NORM_PSF}_{\text{tot}}$ are the same but for the PSF simulation.

In Fig. 2.5 we show the projected temperature profile (from the APEC parameter kT). We find a hint of increasing temperature from the center toward the first and second annuli with a statistical significance above 1σ . We discuss possible implications of the found temperature gradient in Chapter 2.3. In order to understand if this gradient is due to systematics in the fits we perform a Monte Carlo simulation: first we use the XSPEC function `FAKEIT` to simulate spectra similar to the observed ones (similar power-law slope and normalisation) with a given temperature profile. We then fit the simulated spectra using the same procedure as for the real data. Our simulations show that we can recover the input profile within 1σ , and thus the gradient is not due to systematics. We also investigate the possibility that the gradient is artificially introduced by our fitting procedure. We repeat the fit of the real data without fixing the power-law slope and normalisation. Also in this case we find a temperature gradient consistent at the 90% confidence level with the one showed in Fig. 2.5. Finally, we investigate the possibility that the temperature gradient is due to a PSF effect. We simulate a PSF with the same model as the total emission ($\text{PHABS}\times(\text{ZPOW}+\text{APEC})$) and measure the temperature in the same annuli as used for the real source. As we can see in Fig. 2.5 (gray shadow), the measured temperature does not show the gradient seen in the real data, what again confirms that the gradient is not due to the PSF.

The temperature increase showed in Fig. 2.5 could be symmetric, or due to a feature in a preferred direction. In order to investigate these possibilities we repeat the analysis dividing the first annulus (0.5 – 1.0 arcsec) into 4 semi annuli of 90 deg each. The results are listed in Table 2.1. Because of the lower number of counts in each region, these fits are less reliable than the one to the total annulus. However, the temperature gradient seems to be present in each direction, although it is more important in the southern part. This seems to rule out the possibility of a single feature with significantly higher temperature.

It is important to note though that the low number of counts in our spectra do not

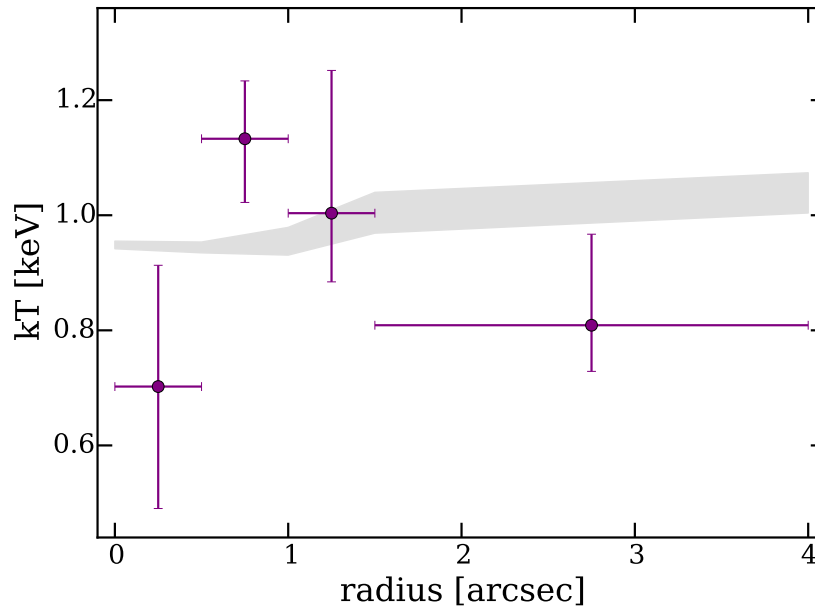


Figure 2.5: Projected temperature profile from the spatially resolved spectral analysis. Each bin corresponds to one annulus defined in Fig. 2.1. The purple points correspond to the real data. There is a hint of a temperature gradient from the center to the first two annuli with a statistical significance above 1σ , which could indicate the presence of a bubble powered by the central AGN. The gray shaded area corresponds to the temperature profile measured in the simulated PSF (see Chapter 2.2.2 for more details). This temperature does not show the gradient seen in the real data, which confirms that the gradient is not due to the PSF.

allow us to deproject the emission from the different shells, so that the reported gas temperatures and normalisations are projected values along the line of sight. A deeper ~ 1 Ms *Chandra* exposure will allow us to obtain a minimum of 200 counts in all region of interest, and thus properly deproject the emission and carefully measure the intrinsic gas parameters.

Region	Net Counts	PL slope	PL norm [10^{-7}]	Temperature kT [keV]	APEC norm [10^{-7}]
Total emission (0.0 – 4.0 arcsec)	620	$2.33^{+0.15}_{-0.16}$	$67.486^{+9.453}_{-9.162}$	$0.953^{+0.048}_{-0.054}$	$38.735^{+6.558}_{-6.381}$
Nucleus (0.0 – 0.5 arcsec)	262	2.47	46.708	$0.702^{+0.211}_{-0.212}$	$5.193^{+1.941}_{-1.823}$
Annulus 1 (0.5 – 1.0 arcsec)	221	2.31	15.387	$1.133^{+0.100}_{-0.111}$	$21.143^{+4.293}_{-3.974}$
Annulus 2 (1.0 – 1.5 arcsec)	52	1.89	2.019	$1.003^{+0.248}_{-0.120}$	$5.023^{+1.077}_{-1.130}$
Annulus 3 (1.5 – 4.0 arcsec)	84	1.65	1.213	$0.809^{+0.158}_{-0.080}$	$10.013^{+1.425}_{-1.315}$
Semi-annulus 1 (45 – 135 deg)	54	2.28	3.709	$1.064^{+0.249}_{-0.123}$	$5.185^{+2.893}_{-1.277}$
Semi-annulus 2 (135 – 225 deg)	56	2.37	3.881	$0.920^{+0.105}_{-0.139}$	$5.316^{+1.343}_{-1.180}$
Semi-annulus 3 (225 – 315 deg)	55	2.27	3.709	$1.575^{+und.}_{-0.343}$	$7.933^{+7.583}_{-3.163}$
Semi-annulus 4 (315 – 405 deg)	55	2.29	3.886	$1.283^{+0.386}_{-0.185}$	$7.401^{+4.406}_{-2.173}$

Table 2.1: Best fit parameters for each region considered in this analysis (nucleus, three annuli, four semi-annuli). The assumed model is PHABS×(ZPOW+APEC). In the nucleus all the fit parameters are free. The power-law slope and normalisation are fixed according to the PSF simulation (see text for details). Abundance is fixed at Solar value and absorption at Galactic value ($N_{\text{H}} = 1.31 \times 10^{20} \text{ cm}^{-2}$).

2.3 Discussion

We detect extended soft X-ray emission in the nucleus of IC 2497, in addition to the point-like power-law emission expected from an AGN. We associate this emission with a hot, diffuse gas. The projected temperature profile (Fig. 2.5) shows a resolved cold center. The temperature gradient may be interpreted as a bubble or cavity in the hot gas which is kinematically inflated by the AGN. Alternatively, the temperature gradient could indicate a shock front, e.g. from an AGN-driven superwind. The different hypothesis, and the consequences for the AGN-host galaxy interaction, are described in the following subsections.

The current analysis also supports the idea that IC 2497 hosts a fading AGN, as suggested by [Lintott et al. \(2009\)](#), [Schawinski et al. \(2010a\)](#) and [Keel et al. \(2012b\)](#). In fact, by scaling the quasar spectral energy distribution (SED) templates from [Elvis et al. \(1994\)](#) to match the measured X-ray luminosity, $L_{2-10\text{keV}} = 5.8 \times 10^{40} \text{ erg s}^{-1}$, we obtain a bolometric luminosity $L_{\text{bol}} \sim 10^{42} \text{ erg s}^{-1}$, which is ~ 4 orders of magnitude below what is needed in order to power Hanny's Voorwerp ([Lintott et al. 2009](#); [Schawinski et al. 2010a](#)). This result is consistent with what reported by [Schawinski et al. \(2010a\)](#). As reported by [Schawinski et al. \(2010a\)](#), if the AGN is Compton thick, this would mean that it is strongly obscured and we are observing the reemission instead of the AGN power-law, and the bolometric luminosity would be $L_{\text{bol}} \sim 10^{44} \text{ erg s}^{-1}$ (see Introduction of the Chapter). This is still ~ 2 orders of magnitude below what is needed in order to power Hanny's Voorwerp. Hard X-ray observation from *NuSTAR* are now crucial in order to understand if the AGN is obscured and measure the real magnitude of the shutdown, as we will show in Chapter 3.

2.3.1 Hot gas in IC 2497

The projected temperature observed in the gas in IC 2497 is in the range $kT \sim 0.7-1.1 \text{ keV}$ ($T \sim 0.8 - 1.2 \times 10^7 \text{ K}$). This relatively high temperature may indicate that the emission from the hot gas is not due to photoionisation, as seen in other Seyfert galaxies (e.g. [Bianchi et al. 2006](#), [Greene et al. 2014](#)). On the other hand, the projected temperature measured in the center and in the external annulus are consistent with what found in ultraluminous infrared galaxies (ULIRGs, [Grimes et al. 2005](#)). The high projected temperature, especially in the two central annuli, may be an indication that we are observing a shock front, e.g. from an AGN-driven superwind. Models of AGN-driven superwinds suggest a temperature of $T \sim 10^{10} - 10^{11} \text{ K}$ for the inner reverse shock and $T \sim 10^7 \text{ K}$ for the forward shock, and the expanding medium can persist also after the AGN has switched off ([Zubovas and King 2012](#)). The observed temperatures are consistent with the forward shock, but too low for the inner shock. Is the AGN in IC 2497 too faint to produce such a high temperature? Or is the observed shock front a residual of a wind driven by the AGN during the past quasar phase? Deeper X-ray observations (leading

Chapter 2. Extended X-ray emission in IC 2497 – energy injection in the gas around a fading AGN

to X-ray spectra with more counts) will allow us to deproject the emission and carefully constrain the intrinsic temperature, density and X-ray luminosity of the gas in each shell around the AGN. This will allow us to estimate the velocity of the shock and the ratio between X-ray and mechanical luminosity (e.g. [Chu and Mac Low 1990](#)), and therefore probe the superwind hypothesis and constrain between the two scenarios.

Another possible interpretation of the observed projected temperature gradient is that the AGN is, or was, blowing away the hot gas around it by injecting kinetic energy, therefore creating a bubble or cavity. If the hypothesis of a bubble inflated by a fading AGN is confirmed, this would give us new insights into the AGN-host galaxy interaction in the “post-quasar” phase, as described below. As mentioned above though that the low number of counts in our spectra do not allow us to deproject the emission from the different shells, so that the reported gas temperatures and normalisations are projected values along the line of sight. Again, a deeper ~ 1 Ms *Chandra* exposure will allow us to obtain a minimum of 200 counts in all region of interest, and thus properly deproject the emission and carefully measure the gas parameters. In this way we will be able to further test the bubble hypothesis.

2.3.2 Energy in the bubble

In order to understand the effect of the AGN on the surrounding medium we need to estimate the energy in the bubble, i.e. the energy required to create it. The uncertainties in this calculation are quite high due to the uncertainties in the spectral fitting and the unknown shape of the bubble and hot gas. Therefore, the obtained energy should be seen as an order of magnitude estimation. One possible way to approach the problem is to consider an analogy with the cavities observed in galaxy clusters (e.g. [Bîrzan et al. 2004](#), [Rafferty et al. 2006](#), [McNamara and Nulsen 2012](#), [Vantyghem et al. 2014](#)). In this case the energy needed to create the bubble can be expressed as:

$$E_{\text{bub}} = \frac{\gamma}{\gamma - 1} p V_{\text{bub}} \quad (2.2)$$

where p is the pressure of the gas surrounding the bubble, V_{bub} is the bubble’s volume, and γ is the heat capacity ratio of the gas inside the bubble ($\gamma = 4/3$ for a relativistic gas, $\gamma = 5/3$ for a non-relativistic, monoatomic gas). For our estimation we consider a spherical bubble with radius $r = 1$ arcsec, corresponding to $r = 987$ pc at the redshift of the source. The pressure p can be expressed as:

$$p = n(kT) \quad (2.3)$$

where n and kT are the number density and temperature of the gas outside the bubble, as derived from the spectral fit to the third annulus (1.5 – 4.0 arcsec). For a fully ionised

gas with 10% He we can assume $n_e \sim n_H$ and $n \sim 2n_e$, so that n can be derived from the APEC normalisation:

$$\text{NORM} = \frac{10^{-14}}{4\pi D_A^2 (1+z)^2} \int n_e n_H dV \quad (2.4)$$

where we consider the normalisation obtained in the third annulus, while the volume corresponds to a napkin ring for a sphere with $r = 4$ arcsec and a cylinder with $r = 1.5$ arcsec (i.e. the volume of the external shell which is projected into the third annulus). In this way we obtain $n \sim 0.02 \text{cm}^{-3}$ and $p \sim 2.5 \times 10^{-11} \text{erg cm}^{-3}$, so that the energy in the bubble is $E_{\text{bub}} \sim 10^{54} - 10^{55}$ erg.

Now we will carry out comparisons to test what these numbers can tell us about the bubble itself and the effect of the AGN on the host galaxy. The energy in the bubble is $\sim 3 - 4$ orders of magnitude higher than what expected from a supernova explosion, so that the bubble cannot be inflated by supernovae. Keel et al. (2012b) found a ring of ionised gas on the northern part of the nucleus of IC 2497. The ring has a radius $r \sim 250$ pc which can be seen in both *HST* $\text{H}\alpha$ and [O III] continuum images, and with a kinematic age $< 7 \times 10^5$ yr (see Figure 5 in Keel et al. 2012b). The kinetic energy in this ring is $\sim 3 \times 10^{51}$ erg, $\sim 3 - 4$ orders of magnitude lower than what found in our bubble, and also the spatial extent is different. This is an indication that additional components need to be considered, probably happening at the same time, near the nucleus of IC 2497. Finally, the binding energy of IC 2497 is $E_{\text{bind}} \sim 10^{60}$ erg, which means that the present-day AGN is not able to blow away the whole ISM. However, Schawinski et al. (2015) recently suggested that AGN “flicker” on and off 100 – 1000 times alternating high-Eddington bursts and lower-Eddington troughs points, with a typical AGN phase lasting $\sim 10^5$ yrs. If what we observe in IC 2497 is typical to each burst, i.e. the AGN injects $\sim 10^{55}$ erg in each cycle, the sum of the energy injected in each cycle could start having some effect on the gas reservoir (although alone it would probably be insufficient to totally unbind it). Finally, if we assume that the bubble is inflated by the fading AGN after the quasar drop in luminosity (i.e. in the last $\sim 2 \times 10^5$ yr), the AGN should inject at least $\sim 10^{42}$ erg/s in kinetic form, and the bubble should expand with a velocity $v_{\text{exp}} \sim 5000$ km/s.

2.3.3 Accretion state changes, AGN feedback and analogy with X-ray binaries

As explained above, one possible interpretation of the bubble is that it is inflated by the fading AGN after the quasar dropped in luminosity, and we are witnessing a state change in the accretion mode of the quasar. After dropping in accretion rate, the low-Eddington AGN moved from a radiative mode to a kinetic mode, and now puts out part of its energy in kinetic form. In this way, it can do a feedback on the galaxy, e.g. by inflating a bubble in the surrounding gas or launching the radio jets. The hypothesis of a state change in IC 2497 is consistent with the analysis done by [Keel et al. \(2012b\)](#). In fact, the *HST* STIS spectra and images indicate the presence of an outflow from the nucleus which suggests that some of the energy output from the AGN switched from radiative to kinetic form.

The idea of a bubble inflated by an AGN undergoing a state change fits naturally into the general picture of unifying BH accretion physics from X-ray binaries (XRB) to AGN. Rapid state transitions, on timescales of days to weeks, are often observed in XRB, and are connected to a change in radiative output (e.g. [Fender et al. 2003](#), [Coriat et al. 2011](#), [Eckersall et al. 2015](#)). The luminous soft state is radiatively efficient and the accretion can be described by an optically thick, geometrically thin accretion disc ([Shakura and Sunyaev 1973](#)). On the other hand, the hard state is radiatively inefficient and the accretion is due to an advection dominated (ADAF; [Narayan and Yi 1995](#)) or jet dominated accretion flow (JDADF; [Falcke et al. 2004](#)), so that most of the energy output from the accreting BH is in kinetic form. The hypothesis of a state switch connected to the drop in luminosity is consistent also with [Done et al. \(2007\)](#) which show that, as the Eddington ratio decreases, the radiative power of an XRB decreases while the mechanical/kinetic power increases. [Alexander and Hickox \(2012\)](#) suggested that this is true also for AGN. In this framework, low-luminosity AGN correspond to the hard XRB state, while the quasars correspond to the soft state. Different studies showed that the AGN accretion discs can indeed change their state from a classical radiatively-efficient quasar state to a radiatively inefficient accretion flow in a similar way as observed in X-ray binaries. However, since the dynamical and viscous timescales involved in the accretion state changes increase with BH mass, the timescales expected for AGN are significantly longer (e.g. [Narayan and Yi 1995](#), [Maccarone et al. 2003](#), [McHardy et al. 2006](#), [Körding et al. 2006](#), [Schawinski et al. 2010a](#)). As an example, the analogous of a state transition lasting several days in an X-ray binary with a $\sim 10M_{\odot}$ BH will last $\sim 10^4$ yr in an AGN with a $\sim 10^7M_{\odot}$ SMBH. These timescales are consistent with what is seen in IC 2497.

2.4 Summary

In this Chapter we have presented new, deep *Chandra* X-ray observations of IC 2497. This galaxy is associated with the extended emission line cloud called Hanny's Voorwerp and hosts a fading AGN. The X-ray data show extended hot gas around the very low-luminosity unobscured AGN ($L_{2-10\text{keV}} \sim 10^{40} \text{ erg s}^{-1}$). Moreover, the data suggest a temperature gradient in the hot gas which may be interpreted as an expanding bubble ($r_{\text{bub}} \sim 1 \text{ kpc}$, $E_{\text{bub}} \sim 10^{54} - 10^{55} \text{ erg}$). One hypothesis is that this bubble is inflated by the AGN that, after changing accretion state and dropping in luminosity, is now in a kinetic mode. As a consequence, the right place to search for and study mechanical AGN feedback could be galaxies hosting fading AGN (i.e. the Voorwerpjes, [Keel et al. 2012a](#), [Keel et al. 2014](#)). The idea of an AGN doing mechanical work at the end of its radiatively efficient phase also fits into the general picture of unifying black hole accretion physics from X-ray binaries to AGN. Follow-up deeper *Chandra* observations will allow us to confirm the presence of the bubble and better constrain its properties and its effect on the host galaxy.

3 Joint NuSTAR and Chandra analysis of the obscured quasar in IC 2497

*Laudato si', mi' Signore, per frate focu,
per lo quale ennallumini la nocte, et ello è bello
et iocundo et robustoso et forte.*¹

Laudes Creaturarum, San Francesco D'Assisi (1224)

This chapter is based on Sartori et al. (2018a), "Joint NuSTAR and Chandra analysis of the obscured quasar in IC 2497 - Hanny's Voorwerp system", MNRAS, 474:2444–2451.

The discovery of Hanny's Voorwerp (HV) by a citizen scientist taking part in the Galaxy Zoo project (Lintott et al. 2008, 2009) opened the field for studying AGN variability on $10^4 - 10^5$ yr timescales, as already discussed in the previous chapters. However, despite intensive efforts, previous works were not able to reliably measure the intrinsic current luminosity of the AGN in IC 2497 and therefore the magnitude of the claimed drop in luminosity (see Section 2.3).

In this Chapter we present new dedicated hard X-ray observations (P.I. Lia Sartori) obtained with the Nuclear Spectroscopic Telescope Array (*NuSTAR*, Harrison et al. 2013). Due to the high sensitivity and the hard X-ray coverage of *NuSTAR* (3 – 79 keV) we are able, for the first time, to put strong constraints on the current intrinsic AGN luminosity and to test directly the fading and obscuration scenarios discussed at the begin of Chapter 2. Indeed, hard X-ray observations are the only true probe of the AGN luminosity also in the case of high obscuration, which would hinder our view of the central source at other wavelengths.

¹*Praised be You, my Lord, through Brother Fire, through whom you light the night and he is beautiful and playful and robust and strong* (Canticle of the Sun, Saint Francis of Assisi, 1224).

Chapter 3. Joint NuSTAR and Chandra analysis of the obscured quasar in IC 2497

Obs. #	Observatory	Observation date	Observation ID	Net exposure
1	<i>Chandra</i>	2012 Jan 8	13966	59.35 ks
2	<i>Chandra</i>	2012 Jan 11	14381	53.4 ks
3	<i>NuSTAR</i>	2016 Sep 29	60201017002	31.4 ks

Table 3.1: X-ray observations log for the data analysed in this Chapter. The archival *Chandra* observations cover the soft part of the X-ray spectrum (0.5 – 8.0 keV) while the newly obtained *NuSTAR* observations probe the hard part of the spectrum (3 – 24 keV).

The Chapter is organised as follows. In Section 3.1 we present the data and data reduction. In Section 3.2 we describe the performed analysis and how we estimate the past and current AGN bolometric luminosity. The results are discussed in Section 3.3.

3.1 Observations

We present the analysis of new *NuSTAR* observations of IC 2497 (3 – 24 keV, see Section 3.1.2), together with previously obtained *Chandra* X-ray observations of the galaxy (0.5 – 8.0 keV), and optical longslit spectroscopy and narrowband imaging of both the galaxy and HV. Details about the *Chandra* and *NuSTAR* observations are listed in Table 3.1.

3.1.1 Chandra

Chandra (Weisskopf et al., 2000) observations of IC 2497 were obtained with the Advanced CCD Imaging Spectrometer S-array (ACIS-S; Garmire et al. 2003) in very faint (VFaint) time-exposure (TE) mode on 2012 January 8 (ObsID 13966, 60 ks) and 2012 January 11 (ObsID 14381, 55 ks; PI K. Schawinski, Cycle 13). We performed standard data reduction starting from the level 1 event files using the CIAO 4.7 software (Fruscione et al., 2006) provided by the *Chandra* X-ray Center (CXC). For both exposures we extracted the spectra and generated the response curves from a circular aperture with 4 arcsec radius around the centroid of the emission using the CIAO task SPECEXTRACT. For the background we considered three source-free apertures ~ 20 arcsec away from the target. We grouped the spectra with a minimum of 3 photons per bin using the HEASOFT task GRPPHA. Details about the *Chandra* data, data reduction and spectral extraction are provided in Chapter 2.

3.1.2 NuSTAR

NuSTAR observations of IC 2497 were obtained on 2016 September 29 (ID 60201017002, 39 ks; program 02041, PI L. Sartori, GO cycle-2). We processed the raw event files

	FPMA	FPMB	FPMA + FPMB
Source net counts	$59.9^{+12.4}_{-11.4}$	$84.6^{+13.2}_{-12.2}$	$144.5^{+17.7}_{-16.7}$
Background counts	$63.1^{+16.6}_{-15.9}$	$58.4^{+17.8}_{-17.1}$	$121.5^{+24.1}_{-23.3}$

Table 3.2: Source net counts and background counts in the 8 – 24 keV band, for each *NuSTAR* focal plane.

using the *NuSTAR* Data Analysis Software package (NUSTARDAS version 1.6.0²) and the calibration files from CALDB version 20160922. Because of the slightly elevated background event rates around the SAA we processed the data with the parameters SAAMODE=STRICT and TENTACLE=YES as recommended by the *NuSTAR* Science Operations Center. We extracted the source and background spectra using the NUPRODUCTS task included in the NUSTARDAS package with the appropriate response and ancillary files. For each focal plane module we extracted the source spectra using a circular aperture with 45 arcsec radius. We checked that no additional bright sources are detected by *Chandra* within this region. For the background we considered two source-free apertures with 60 arcsec radius on the same detector chip as the source. Similar to the *Chandra* spectra, we grouped the *NuSTAR* spectra with a minimum of 3 photons per bin using the HEASOFT task GRPPHA. The obtained net counts and background counts are listed in Table 3.2. For the analysis we limited the *NuSTAR* spectrum to 3-24 keV instead of 3-79 keV because of the drop in sensitivity and the heightened background above 24 keV (e.g. Wik et al. 2014).

3.1.3 Optical data

Optical longslit spectra passing through both the nucleus of IC 2497 and HV were obtained with the double-spectrograph system at the 4.2m William Herschel Telescope (WHT) on La Palma and with the 3m Shane telescope at the Lick Observatory. All the spectra were obtained with a 2 arcsec slit width and nearly identical position on the sky. Details about observations and data reduction are given in Lintott et al. (2009).

Narrowband H α images obtained with the *HST* using the tunable ramp filters on the Advanced Camera for Surveys (ACS). Both data and data processing are described in Keel et al. (2012b) and Keel et al. (2017).

²http://heasarc.gsfc.nasa.gov/docs/nustar/analysis/nustar_swguide.pdf

3.2 Analysis

The goal of this analysis is to measure the level of obscuration and the current intrinsic bolometric luminosity of the AGN in IC 2497. A comparison of the obtained current luminosity with the past luminosity inferred from the photoionisation state of HV will allow us to probe if the quasar really dropped in luminosity within the last $\sim 10^5$ yr as suggested by previous studies, and the magnitude of the drop.

3.2.1 X-ray emission

We fit the obtained spectra using XSPEC (Arnaud, 1996) with Cash statistics (Gehrels, 1986), and estimate best fit parameters and errors using the MCMC routine implemented in XSPEC. Because of the low signal to noise of the *NuSTAR* observations, we first examine the *Chandra* observations alone. We then perform combined fits considering different models for the hard X-ray part of the spectrum, which is expected depend on the amount and structure of the obscuring material around the AGN. We verified that no significant variability is present between the observations but allow a 10% offset to account for different responses of the *Chandra* and *NuSTAR* detectors and uncertainties in the cross-calibrations. Errors for the best fit parameters are quoted at the 90% confidence level. All the fit results are summarised in Table 3.3.

Chandra observations

The 0.5–8.0 keV *Chandra* spectrum is best fit (C-stat/dof = 181.9/132) by an unabsorbed power-law ($\Gamma = 2.14_{-0.28}^{+0.27}$), as expected for an unobscured AGN or for the Thomson-scattered emission of an obscured AGN, plus an APEC component representing the hot gas in the galaxy ($kT = 0.93_{-0.11}^{+0.07}$ keV). We notice that the power-law component may also be partially attributed to emission from star formation and X-ray binaries, as discussed below. The total absorption component is fixed to the Galactic value ($N_{\text{H}} = 1.31 \times 10^{20} \text{ cm}^{-2}$, as given by the Colden Calculator with the NRAO dataset³). A similar value for the photon index ($\Gamma = 2.23_{-0.38}^{+0.57}$) is obtained also when excluding the counts below 1.5 keV in order to avoid contamination by the hot gas. By fitting the 3.0–8.0 keV spectrum with a simple power-law we obtain a photon index $\Gamma = -0.76_{-0.05}^{+1.45}$. This low value is an indication that the source is heavily obscured and that the power-law observed in the soft X-ray spectrum corresponds to the scattered component. However, due to the narrow energy interval considered, adding an obscured component to our fiducial model for the *Chandra* data does not improve the quality of the fit significantly, so that a combined fit with *NuSTAR* is needed to determine the real amount of obscuration.

³<http://cxc.harvard.edu/toolkit/colden.jsp>

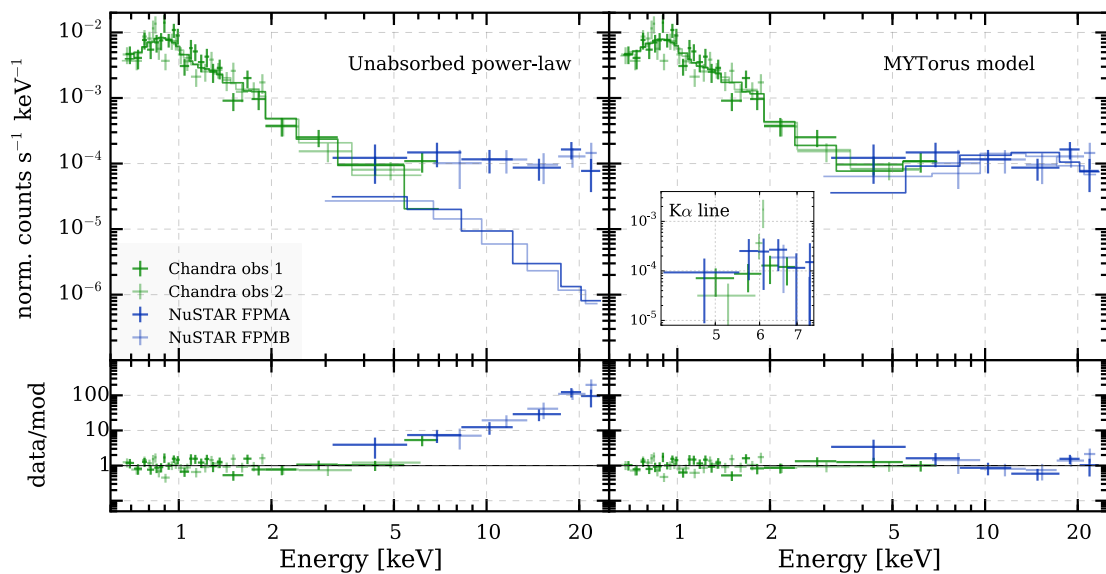


Figure 3.1: Broadband X-ray spectrum from *Chandra* (green) and *NuSTAR* (blue). The crosses correspond to the data while the lines show the models. For plotting clarity we rebinned the spectrum with a minimum of 9 counts per bin. *Left*: The fit corresponds to the best fit to the *Chandra* data only, that is an unabsorbed power-law with an APEC component, with extrapolation to higher energies. This model clearly underpredicts the hard X-ray counts observed with *NuSTAR*. *Right*: The fit corresponds to the MYTORUS model with $\theta_i = 90^\circ$. This model is a better match to the data, and indicates that the source is obscured. The box shows a zoom-in on the iron Fe K α line region with a different binning (minimum of 3 counts per bin).

Possible contribution from star formation

IC 2497 is a luminous infrared galaxy (LIRG) with far-IR (FIR) luminosity $L_{\text{FIR}} = 6.6 \times 10^{44} \text{ erg s}^{-1}$. Assuming the FIR - star formation rate relation of [Kennicutt \(1998\)](#), this corresponds to a star formation rate $SFR \sim 30 M_{\odot} \text{ yr}^{-1}$. Using the relations of [Ranalli et al. \(2003\)](#) or [Lehmer et al. \(2016\)](#), the expected 2 – 10 keV luminosity is $L_{2-10\text{keV}} \sim 1.5 \times 10^{41} \text{ erg s}^{-1}$, which is comparable (within the large scatter of the correlations) to the observed 2 – 10 keV luminosity measured from the *Chandra* and *NuSTAR* spectra (we stress that all the used relations have a large scatter, so that the results have to be considered as an order of magnitude estimation). In addition, the low $W1 - W2$ color, $W1 - W2 = 0.3$, suggests that the mid-IR emission is dominated by stellar emission (see Section 3.2.2 for a discussion of the mid-IR emission). Altogether, this points to a scenario where star formation provides an important contribution to the soft part of the X-ray spectrum. We will consider this component in the analysis below.

Phenomenological model

Applying the unabsorbed power-law model described above to the 0.5 – 24.0 keV spectrum significantly underpredicts the hard X-ray counts observed with *NuSTAR*, especially in the 10.0 – 20.0 keV range (see Fig. 3.1, left). This again is an indication that the source is highly obscured (e.g. [Koss et al. 2016](#); [Ricci et al. 2016b](#)). To infer the intrinsic column density N_{H} and the X-ray luminosity of the source we first fit the 0.5 – 24.0 keV spectrum with a phenomenological model which includes:

1. An absorbed power-law representing the intrinsic emission of the AGN, where we consider both photoelectric absorption and Compton scattering.
2. A second unabsorbed power-law representing the scattered AGN component and the contribution from star formation.
3. The unabsorbed reflected X-ray emission from neutral material above the accretion disc (the PEXRAV model, [Magdziarz and Zdziarski 1995](#)).
4. A Gaussian representing the narrow Fe $K\alpha$ line usually detected in AGN (e.g. [Nandra and Pounds 1994](#); [Shu et al. 2010](#); [Ricci et al. 2014](#)), with fixed energy $E = 6.4\text{keV}$ and sigma $\sigma = 10\text{eV}$.
5. An APEC model for the hot gas in the galaxy.

In XSPEC this model can be defined as:

$$\text{PHABSGAL} \times (\text{ZPHABS} \times \text{CABS} \times \text{ZPOW} + \text{PEXRAV} + \text{ZPOW} + \text{ZGAUSS} + \text{APEC}).$$

The photon index of the intrinsic power-law is fixed at $\Gamma = 1.9$ as expected for average AGN (e.g. [Nandra and Pounds 1994](#); [Piconcelli et al. 2005](#); [Ricci et al. 2015](#)), while the photon index of the unabsorbed power-law is let free to vary. The best fit results in a column density $N_{\text{H}} = 1.87^{+1.27}_{-0.21} \times 10^{24} \text{ cm}^{-2}$ and an intrinsic 2-10 keV luminosity (intended as the luminosity of the intrinsic power law) $L_{2-10\text{keV}} = 2.3 \times 10^{43} \text{ erg s}^{-1}$. We note that the reflection parameter R is an upper limit and the best fit parameters do not change significantly if we fix $R = -1 \times 10^{-10}$. This suggests that the reflection component is not statistically significant.

In order to estimate the equivalent width (EW) of the narrow Fe $K\alpha$ line we fit the *Chandra* and *NuSTAR* data in the 3.0 – 24.0 keV range simultaneously with a simplified model: ZPOW + ZGAUSS. We obtained EW $1.74^{+0.86}_{-0.72} \text{ keV}$, which is again consistent with heavy obscuration (e.g. [Matt et al. 1996](#)).

BNtorus model

A more physically motivated model for highly obscured sources is the BNTORUS model developed by [Brightman and Nandra \(2011\)](#), which considers both absorbed and reprocessed emission of an intrinsic power-law from a torus. In order to fit the whole 0.5 – 24.0 keV spectrum simultaneously we add a scattered power-law component with same photon index as the intrinsic one and an APEC model in a similar way as described above:

$$\text{PHABSGAL} \times (\text{BNTORUS} + \text{ZPOW} + \text{APEC}).$$

In order to obtain a good fit we need to fix the inclination angle of the torus to the maximum permitted value $\theta_i = 87.1^\circ$. Varying the opening angle of the torus between $\theta_{\text{oa}} = 40^\circ$ and $\theta_{\text{oa}} = 80^\circ$ provides fit parameters which are consistent within the uncertainties and statistically indistinguishable. For $\theta_{\text{oa}} = 60^\circ$ the fit implies $N_{\text{H}} = 2.10^{+1.05}_{-0.57} \times 10^{24} \text{ cm}^{-2}$ and $L_{2-10\text{keV}} = 1.0 \times 10^{43} \text{ erg s}^{-1}$.

MYtorus model

A second physically motivated model for highly obscured AGN is the MYTORUS model developed by [Murphy and Yaqoob \(2009\)](#), which includes three components: the intrinsic absorbed power-law continuum (MYTORUSZ), the scattered continuum (MYTORUSS) and the line emission (MYTORUSL). In order to avoid artifacts present in the MYTORUS model at low energies we cut the spectrum at 0.65 keV instead of 0.5 keV. As before, we add a scattered power-law and an APEC component so that the total model is:

$$\text{PHABSGAL} \times (\text{MYTORUSZ} \times \text{ZPOW} + \text{MYTORUSS} + \text{MYTORUSL} + \text{ZPOW} + \text{APEC}).$$

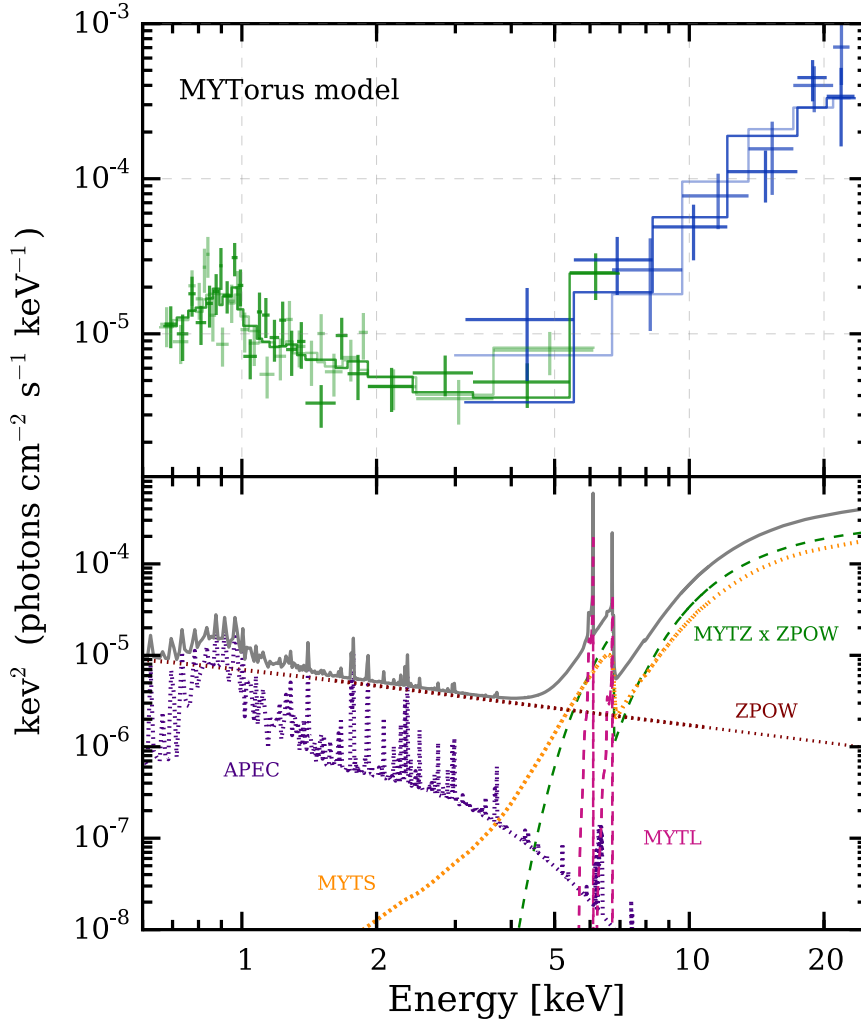


Figure 3.2: *Top*: same as Fig. 3.1, right, but for the unfolded spectrum. *Bottom*: unfolded model components for the best-fit MYTORUS model with $\theta_i = 90^\circ$.

As in the previous models, the photon index of the intrinsic power-law is fixed at $\Gamma = 1.9$ while the photon index of the unabSORBED power-law is let free to vary. The power-law parameters of the MYTORUS components are tied together. Due to the low signal to noise of the spectrum, the column density and normalisations of the different MYTORUS components are considered to be the same, as the available data do not allow to constrain a different normalisation of the scattered and line components with respect to the zeroth-order continuum represented by MYTORUSZ. In addition, we fix the inclination angle to $\theta_i = 90^\circ$ (Fig. 3.1, right, and Fig. 3.2) and $\theta_i = 75^\circ$. The fits return $N_H \sim 2 \times 10^{24} \text{ cm}^{-2}$ and $L_{2-10\text{keV}} \sim 1.2 \times 10^{43} \text{ erg s}^{-1}$ (see Table 3.3 for the values corresponding to the individual fits).

Phenomenological model		
Column density N_{H} (10^{24} cm^{-2})	$1.87_{-0.21}^{+1.27}$	
Reflection parameter R	≤ 0.02	
Plasma temperature kT (keV)	$0.95_{-0.08}^{+0.1}$	
Soft Γ	$2.32_{-0.14}^{+0.5}$	
C-stat/dof	246.8/222	
intrinsic 2-10 keV luminosity $L_{2-10\text{keV}}$ (erg s^{-1})	$(2.3_{-0.8}^{+4.4}) \times 10^{43}$	
bolometric luminosity L_{bol} (erg s^{-1})	$(4.9_{-2.1}^{+14.9}) \times 10^{44}$	
BNtorus model		
Column density N_{H} (10^{24} cm^{-2})	$2.10_{-0.57}^{+1.05}$	
Inclination angle $\theta_{\text{i}}^{(1)}$	87.1°	
Torus opening angle $\theta_{\text{oa}}^{(1)}$	60°	
Plasma temperature kT (keV)	$1.00_{-0.1}^{+0.15}$	
Soft Γ	$2.86_{-0.33}^{+0.12}$	
C-stat/dof	245.3/217	
intrinsic 2-10 keV luminosity $L_{2-10\text{keV}}$ (erg s^{-1})	$(1.0_{-0.4}^{+0.4}) \times 10^{43}$	
bolometric luminosity L_{bol} (erg s^{-1})	$(1.9_{-0.8}^{+1.0}) \times 10^{44}$	
MYtorus model		
	$\theta_{\text{i}} = 90^\circ$	$\theta_{\text{i}} = 75^\circ$
Column density N_{H} (10^{24} cm^{-2})	$1.81_{-0.36}^{+0.70}$	$2.09_{-0.49}^{+1.03}$
Plasma temperature kT (keV)	$0.98_{-0.10}^{+0.23}$	$1.01_{-0.14}^{+0.15}$
Soft Γ	$2.62_{-0.32}^{+0.34}$	$2.90_{-0.33}^{+0.09}$
C-stat/dof	239.8/213	241.9/213
intrinsic 2-10 keV luminosity $L_{2-10\text{keV}}$ (erg s^{-1})	$(1.3_{-0.5}^{+1.1}) \times 10^{43}$	$(1.2_{-0.4}^{+0.6}) \times 10^{43}$
bolometric luminosity L_{bol} (erg s^{-1})	$(2.4_{-1.0}^{+2.8}) \times 10^{44}$	$(2.1_{-0.8}^{+1.4}) \times 10^{44}$

Table 3.3: Summary of the joint *Chandra* and *NuSTAR* X-ray spectral analysis. Details about the different models are given in the text.

⁽¹⁾ Frozen parameters. The errors on the fit parameters correspond to the 90% confidence range. The intrinsic 2-10 keV luminosities are intended as the luminosity of the intrinsic power-law only.

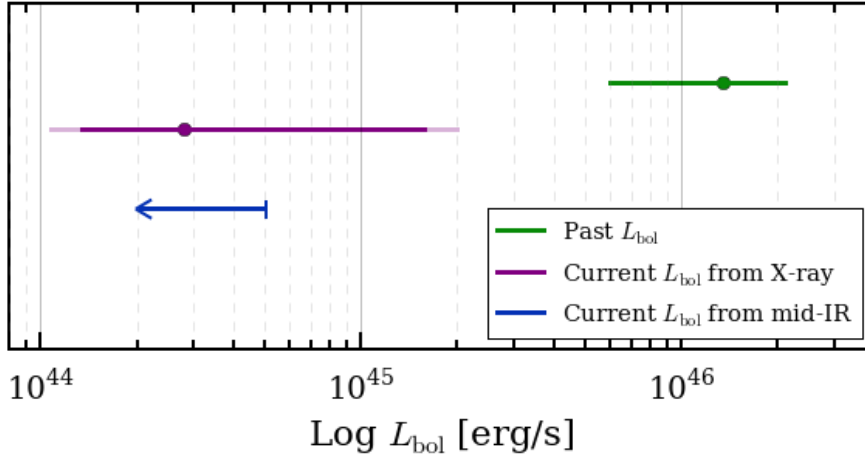


Figure 3.3: Past and current bolometric luminosity ranges as estimated from optical (green), X-ray (purple) and mid-IR (blue) data. The past luminosity range corresponds to the range between the minimum and maximum values obtained from optical data. The current bolometric luminosity range from X-ray data corresponds to the range obtained using the 68% (strong purple) and 90% (light purple) confidence intervals on the intrinsic power-law normalisation. The mid-IR data allows to compute an upper limit for the current bolometric luminosity. See Section 3.2.2 for more details.

3.2.2 Luminosity estimation

In this section we estimate the current bolometric luminosity from the X-ray fits and from mid-IR data, and the past bolometric luminosity ($\sim 10^5$ yr ago) using optical spectroscopy. The results are summarised in Fig. 3.3.

Current bolometric luminosity from the X-ray spectrum

The simultaneous *Chandra* and *NuSTAR* analysis of the 0.5–24.0 keV spectrum of IC 2497 suggests that the source is highly obscured, $N_{\text{H}} = 1.8 - 2.1 \times 10^{24} \text{ cm}^{-2}$, with intrinsic 2-10 keV luminosity (luminosity of the intrinsic power-law) $L_{2-10\text{keV}} = 1 - 2.3 \times 10^{43} \text{ erg s}^{-1}$. Assuming the luminosity dependent X-ray to bolometric conversion from Marconi et al. (2004), the measured 2-10 keV luminosity corresponds to a bolometric luminosity $L_{\text{bol}} = 1.9 - 4.9 \times 10^{44} \text{ erg s}^{-1}$.

Fig. 3.3 shows the range covered by the estimated bolometric luminosity considering also the uncertainties on the intrinsic power-law. For every model we compute the 2-10 keV luminosity for the best fit normalisation and for the minimum and maximum value allowed from the 90% and 68% confidence regions. We then infer the bolometric luminosity as explained above. In the plot we show the mean value obtained from the best-fit parameters, and the minimum and maximum values for the two confidence levels measured with the different models.

Current bolometric luminosity from mid-IR emission

The *WISE* observations (Wright et al., 2010) of IC 2497 allow us to compute an upper limit to the current bolometric luminosity of the obscured quasar. First, the $W1 - W2$ color is low, $W1 - W2 = 0.3^4$, which suggests that the mid-IR flux is dominated by stellar emission (e.g. Stern et al. 2005; Jarrett et al. 2011; Stern et al. 2012). Moreover, the emission detected with $W3$ and $W4$ (12 and 22 μm , respectively) appears effectively not to be absorbed e.g. by dust also in the case of highly obscured quasars (e.g. Gandhi et al. 2009; Asmus et al. 2015), so that the observed luminosity corresponds to the intrinsic one. Assuming a radio quiet quasar SED template from Elvis et al. 1994 and normalising it to the lowest non absorbed *WISE* point, i.e. $W3$, we obtain an upper limit for the bolometric luminosity $L_{\text{bol}} = 5.0 \times 10^{44} \text{ erg s}^{-1}$. This value is consistent with that obtained from the X-ray analysis.

Past bolometric luminosity from optical emission

A detailed analysis of the optical longslit spectra, which allow the computation of the lower and upper limits to the AGN output needed to photoionise HV, is presented in Lintott et al. (2009). Here we provide a brief summary of their findings. A lower limit for the required AGN output is obtained from simple recombination balance, i.e. by assuming that the number of ionisations is equal to the number of recombinations, and that the number of ionising photons is high enough to power the observed recombination lines. The integrated $H\beta$ luminosity of HV is $L_{H\beta} = 1.4 \times 10^{41} \text{ erg s}^{-1}$. Assuming typical nebular conditions and a flat ionising continuum ($F_\nu \propto \nu^{-1}$) this corresponds to a lower limit for the ionising luminosity $L_{\text{ion}} > 1 \times 10^{45} \text{ erg s}^{-1}$. On the other hand, the ionisation parameter obtained from the $[\text{OII}]\lambda 3727/[\text{OIII}]\lambda 5007$ ratio of HV is $\log(U) = -2.2$ while the $[\text{SII}]\lambda 6717/6731$ doublet ratio provides an upper limit for the electron density $n_e < 50 \text{ cm}^{-3}$. This provides an upper limit for the ionising photon density $n_{\text{phot}} < 0.32 \text{ cm}^{-3}$. Assuming a flat ionising continuum and the mean projected separation between IC 2497 and HV, $d = 20 \text{ kpc}$, the obtained photon density corresponds to an upper limit for the ionising luminosity $L_{\text{ion}} < 3.2 \times 10^{45} \text{ erg s}^{-1}$.

A similar analysis was performed also in Keel et al. (2017). Based on *HST* narrow-band $H\alpha$ images and photoionisation balance, they infer a lower limit (because of possible dust obscuration and/or clumpy gas structure) for the isotropic emission rate of ionising photons $Q_{\text{ion}} \sim 3 \times 10^{55} \text{ photons s}^{-1}$ for almost the whole time range probed by the photoionised cloud, which again corresponds to a lower limit for the ionising luminosity $L_{\text{ion}} > 1.1 \times 10^{45} \text{ erg s}^{-1}$.

Altogether, these observations point to a past ionising luminosity in the range $L_{\text{ion}} = 1 - 3.2 \times 10^{45} \text{ erg s}^{-1}$. By scaling a radio quasar template from Elvis et al. 1994 to

⁴We checked that no variability is present between *WISE* and *NEOWISE* (Mainzer et al. 2011).

match the estimated ionising luminosity between 1 and 4 Ryd, we infer a past bolometric luminosity $L_{\text{bol}} = 0.6 - 2.1 \times 10^{46} \text{ erg s}^{-1}$.

3.3 Discussion

We used new hard X-ray *NuSTAR* observations of IC 2497, together with archival *Chandra* observations and *WISE* fluxes, to investigate the current state of its quasar. The data rule out the possibility that the quasar is currently radiating at a rate $L_{\text{bol}} \sim 10^{46} \text{ erg s}^{-1}$ as required by the photoionisation state of Hanny’s Voorwerp, and suggest a drop in luminosity by a factor ~ 50 in the last $\sim 10^5$ yr. In addition, the newly obtained observations suggest that the source is Compton thick with $N_{\text{H}} \sim 2 \times 10^{24} \text{ cm}^{-2}$. However, obscuration alone cannot explain the discrepancy between the needed and observed levels of AGN emission; this suggests that significant AGN variability is required to explain the properties of this system. These findings also support the idea first proposed by [Lintott et al. \(2009\)](#) that Hanny’s Voorwerp is a quasar ionisation echo, although the magnitude of the drop in luminosity is significantly lower than previously thought, i.e. a factor ~ 50 instead of > 100 , assuming the mean current and past luminosities obtained with our analysis.

Assuming a stellar mass $M_{\star} \sim 1.7 \times 10^{11} M_{\odot}$ and the $M_{\star} - M_{\text{BH}}$ relation in [Jahnke et al. \(2009\)](#), as well as the mean current and past luminosities obtained with our analysis, the measured drop in bolometric luminosity corresponds to a drop in Eddington ratio (ER) from $\lambda_{\text{Edd}} \sim 0.35$ to $\lambda_{\text{Edd}} \sim 0.007$. The ER found for luminous AGN is typically $\lambda_{\text{Edd}} \sim 0.01 - 1$ (e.g. [Panessa et al. 2006](#); [Kollmeier et al. 2006](#)). An ER $\lambda_{\text{Edd}} \sim 0.007$ is more consistent with the predictions for a radiatively inefficient (RIAF) or advection dominated accretion flow (ADAF, e.g. [Narayan and Yi 1995](#); [Narayan et al. 1998](#); [Ho 2009](#)), where most of the energy is radiated in kinetic form. The drop in ER could therefore suggest that IC 2497 is entering a regime where we might expect a change from a radiatively efficient to a radiatively inefficient accretion state (e.g. [Done et al. 2007](#); [Alexander and Hickox 2012](#)). This hypothesis is supported also by the fact that IC 2497 and its quasar show other characteristics common to ADAF sources, such as the presence of a compact radio source or jet, and the prevalence of low-ionisation nebular conditions (e.g. [Terashima et al. 2002](#); [Ptak et al. 2004](#); [Ho 2009](#)).

Accretion state changes are common in X-ray binaries. In these systems the switch from radiatively efficient to radiatively inefficient state is often linked to changes in the jet activity, and provides a source of mechanical feedback (e.g. [Done et al. 2007](#); [Pakull et al. 2010](#)). As observed by [Józsa et al. \(2009\)](#) and [Rampadarath et al. \(2010\)](#), IC 2497 shows a large scale radio jet which connects the galaxy to Hanny’s Voorwerp, and a jet hotspot ~ 300 pc away from the AGN which may correspond to a jet launched after the quasar started dropping in luminosity. A hypothesis is that the nuclear jet is connected to the current accretion state change, in analogy to what is observed in X-ray binaries,

while the large scale radio jet was launched during a previous AGN phase. In fact, as suggested by [Schawinski et al. \(2015\)](#) and discussed in Chapter 2, AGN may “flicker” on and off 100 – 1000 times, with a typical AGN phase lasting $\sim 10^5$ yr, so that the host galaxy may present signatures related to different AGN phases. The idea of the AGN currently doing mechanical feedback on the galaxy is supported also by the presence of a nuclear outflow and a nuclear ring of expanding gas observed in the optical *HST* images ([Keel et al. 2012b](#)) and of a bubble expanding in the hot gas around the AGN seen in the *Chandra* data ([Sartori et al. 2016](#), see also Chapter 2). The analogy between IC 2497 and what is observed in X-ray binaries provides further indication of a possible unification of black hole accretion physics from stellar mass BHs to SMBHs. However, it is important to notice that different timescales have to be taken into account since the dynamical and viscous timescales increase with black hole mass. If we assume the underlying physics for black hole accretion to be the same, the analogous of a state transition lasting ~ 1 h for a $\sim 10M_{\odot}$ BH would last $\sim 10^{4-5}$ yr for a $\sim 10^9M_{\odot}$ SMBH.

Other examples of AGN variability are given by the so-called *changing-look AGN*, which present a change in the AGN type (e.g. from Type 1 to Type 1.9) due to broadening or narrowing of the Balmer lines⁵ ([Denney et al. 2014](#); [LaMassa et al. 2015](#); [Ruan et al. 2016](#); [MacLeod et al. 2016](#); [Runnoe et al. 2016](#); [Husemann et al. 2016](#); [McElroy et al. 2016](#); [Gezari et al. 2017](#); [Stern et al. 2018](#)). The appearance or disappearance of broad emission lines is often accompanied by a change in luminosity of a factor ~ 10 over ~ 10 yr timescales. As described above, these timescales are much shorter compared to timescales expected for accretion state changes (e.g. [Sobolewska et al. 2011](#); [Hickox et al. 2014](#)), and possible alternative explanations of the changing-look behaviour are variable absorption due to a clumpy torus (e.g. [Elitzur 2012](#)), transient events, e.g. tidal disruption of a star by the central black hole (e.g. [Eracleous et al. 1995](#); [Merloni et al. 2015](#)), or major changes in the photoionisation balance. The magnitude of the drop in luminosity measured in IC 2497 is at least a factor ~ 2 higher than what has been observed in changing-look AGN. Moreover, the *Chandra* and *NuSTAR* data do not show significant variability, and the upper limits obtained from archival *WISE*, *NEOWISE* and *IRAS* data seem to exclude that the total drop in luminosity happened within the last decades. For these reasons, we argue that the AGN in IC 2497 should not be classified as a changing-look AGN. On the other hand, we suggest that changing-look AGN correspond to a short-time ($\sim 10 - 100$ yr) variability which is superimposed on the long-term ($\sim 10^{5-6}$ yr) AGN phases suggested by this work and other observations (e.g. [Schawinski et al. 2015](#)), high resolution simulations ([Hopkins and Quataert 2010](#); [Novak et al. 2011](#); [Bournaud et al. 2011](#); [Gabor and Bournaud 2013](#); [DeGraf et al. 2014](#); [Sijacki et al. 2015](#)) and theoretical models ([Siemiginowska and Elvis 1997](#); [Sanders 1981](#); [Di Matteo et al. 2005](#); [Hopkins et al. 2005](#); [Springel et al. 2005](#); [King and Pringle 2007](#); [King and Nixon 2015](#)).

⁵In this chapter we refer to optical changing-look AGN, while other studies describe systems where the X-ray changing-look behaviour, from Compton thick to Compton thin or viceversa, is due to a change in the obscuration (e.g. [Risaliti et al. 2005](#); [Ricci et al. 2016a](#))

3.4 Summary

In this Chapter we present new *NuSTAR* observations of IC 2497, the galaxy associated with Hanny's Voorwerp. The analysis of these new data, together with archival *Chandra* X-ray observations, optical longslit spectroscopy and narrowband imaging, and *WISE* mid-IR photometry, shows that the AGN in IC 2497 is Compton thick, and its luminosity dropped by a factor ~ 50 within the last $\sim 10^5$ yr. These findings support the idea that Hanny's Voorwerp is an ionisation echo, although the magnitude of the quasar's drop in luminosity is significantly lower than previously thought. On the other hand, the observed change in Eddington ratio, from $\lambda_{\text{Edd}} \sim 0.06$ to $\lambda_{\text{Edd}} \sim 0.001$, suggests that the quasar in IC 2497 is entering a regime where it is switching from a radiatively efficient to a radiatively inefficient accretion state, in a similar way as observed in X-ray binaries.

4 New observational data for the Voorwerpjes galaxies

*Laudato sie, mi' Signore, cum (...) messor lo frate sole,
lo qual è iorno, et allumini noi per lui.
Et ellu è bellu e radiante cum grande splendore.*¹

Laudes Creaturarum, San Francesco D'Assisi (1224)

Part of this chapter is based on different observing proposals written by L. Sartori for the Voorwerpjes galaxies.

To date, the Voorwerpjes (VP) sample represents one of the best laboratories to date to study AGN variability on super-human, $\gtrsim 10^4$ yr timescales. Since AGN variability on such timescales is poorly understood yet, the study of these galaxies is crucial to constrain the total AGN variability behaviour, as it will become clear in the next chapters. In addition, these galaxies allow us to investigate the close relation between the AGN and its host galaxy, in particular by observing how it affects the gas in and around it.

In this Chapter I will describe the major observing programs I am leading aimed at obtaining a multiwavelength view of the VP sample. Although the analysis of the obtained data is not part of this Ph.D. thesis, the work performed in planning and obtaining this data compilation is very valuable for future studies, and represents an important achievement of the thesis. The aim of this Chapter is to provide an overview of the available data and suggest possible uses. A summary of the galaxies observed as part of the different programs is given in Table 4.1.

¹*Be praised, my Lord, through (...) my lord Brother Sun, who brings the day; and you give light through him. And he is beautiful and radiant in all his splendour* (Canticle of the Sun, Saint Francis of Assisi, 1224).

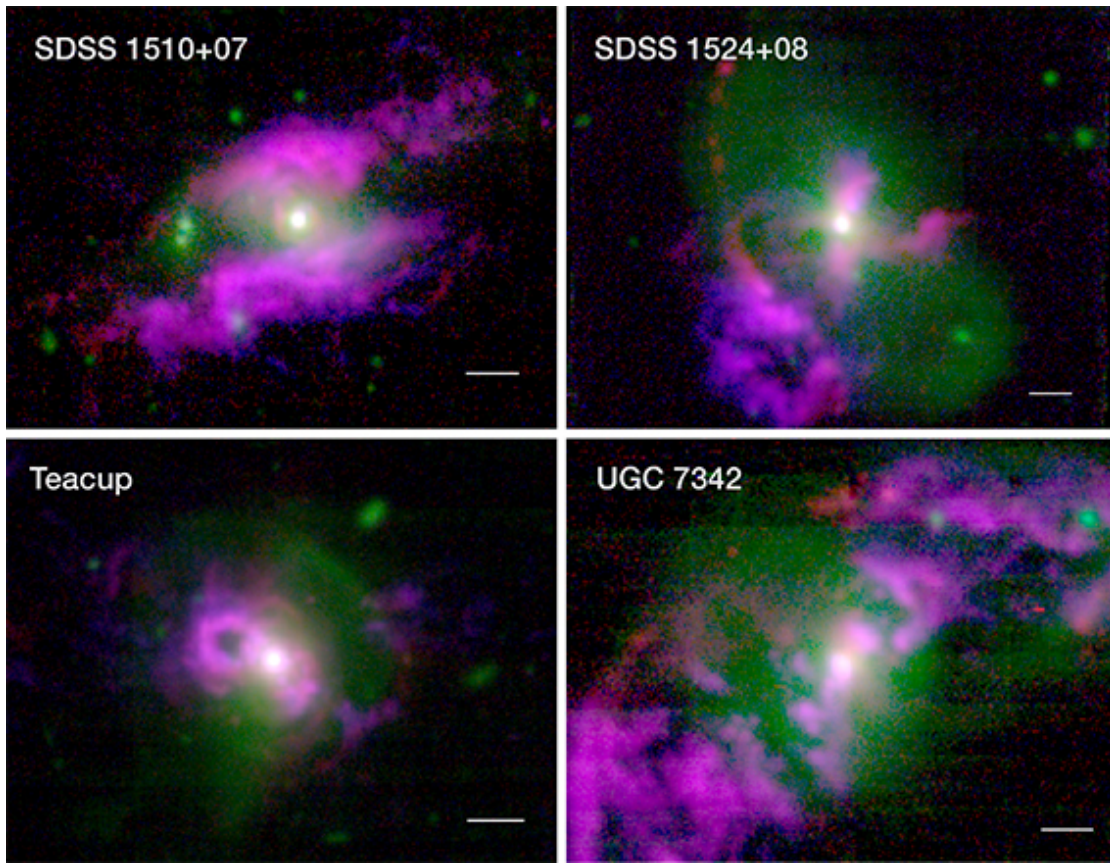


Figure 4.1: Preliminary MUSE composite images for four VP galaxies observed as part as our program. The $[\text{O III}]$ emission is shown in blue, while red and green correspond to $\text{H}\alpha$ emission and stellar continuum respectively. As expected, extended photoionised gas is detected in all the galaxies, what will allow us to reconstruct the historical AGN light curves. The scale bar corresponds to 5 arcsec ($\sim 4 - 8$ kpc depending on the galaxy).

4.1 MUSE: spatially resolved optical spectroscopy (IFU)

Instrument: Multi Unit Spectroscopic Explorer (MUSE)

Program: ESO program 0102.B-0107(A), ESO period 102A

Title: Probing the lifecycle of supermassive black holes on 10-100 kyr timescales using spatially resolved spectroscopy

Principal Investigator: Lia Sartori

Target galaxies: UGC 7342, Teacup, SDSS 1510+07, SDSS 1524+08, NGC 5972

Total time: 13 hours (priority A)

4.1. MUSE: spatially resolved optical spectroscopy (IFU)

The Multi Unit Spectroscopic Explorer (MUSE, [Bacon et al. 2010](#)) is a second generation integral field units (IFU) instrument at the ESO Very Large Telescope (VLT). Thanks to its large field of view (~ 1 arcmin) and the broad spectral coverage ($\sim 4800 - 9300 \text{ \AA}$) it is the best suited instrument to investigate the photoionisation state of the large scale gas in the VP galaxies. The main goal of this program is to constrain AGN variability from $\lesssim 10^3 \text{ yr}$ to $\sim 10^{4-5} \text{ yr}$ timescales in five VP galaxies. The preliminary MUSE composite images for four galaxies observed as part of the program are shown in [Fig. 4.1](#). Specifically, the extracted emission line maps, spanning from $\text{He II } \lambda 4686 \text{ \AA}$ to $[\text{S II}] \lambda 6731 \text{ \AA}$, will allow us to:

1. Obtain spatially resolved BPT diagrams (optical emission lines diagnostic from $\text{H}\alpha$, $\text{H}\beta$, $[\text{O III}] \lambda 5007 \text{ \AA}$, $[\text{N II}] \lambda 6584 \text{ \AA}$, $[\text{O I}] \lambda 6300 \text{ \AA}$ and $[\text{S II}] \lambda 6716, 6731 \text{ \AA}$; e.g. [Baldwin et al. 1981](#); [Kewley et al. 2001](#); [Kauffmann et al. 2003](#); [Schawinski et al. 2007](#)) to **define regions where the interstellar medium is photoionised by the AGN** (e.g. [Belfiore et al. 2015](#)). Although the available longslit spectra already confirmed the AGN photoionisation nature of the VP clouds ([Keel et al. 2012a](#)), IFU observations are needed to reliably define the spatial boundaries of these regions, and to investigate the photoionised gas distribution throughout the galaxy. A single slit may indeed cross some peculiar gas region which is not representative of the gas at a given distance from the galaxy nucleus. This is crucial in order to trace the AGN variability by decoupling changes in photoionising flux (intrinsic AGN variability) from local variations in the gas density or nuclear obscuration, which could also mimic a variation in the luminosity.
2. **Investigate the physical conditions of the AGN-photoionised gas.** Thanks to the wavelength coverage and the high spectral resolution, the obtained line maps will allow us to estimate the electron density n_e and temperature T_e at different spatial positions (from $[\text{N II}] \lambda 5755 \text{ \AA}$, $[\text{N II}] \lambda 6548, 6584 \text{ \AA}$ and $[\text{S II}] \lambda 6717, 6731 \text{ \AA}$), derive the dust extinction maps from the Balmer decrement $\text{H}\alpha/\text{H}\beta$ (e.g. [Caplan and Deharveng 1986](#); [Calzetti et al. 2000](#); [Lee et al. 2009](#)), and measure the gas metallicities (from $\text{H}\beta$, $[\text{O III}] \lambda 4959, 5007 \text{ \AA}$, $\text{H}\alpha$ and $[\text{N II}] \lambda 6548, 6584 \text{ \AA}$). In addition, the $\text{H}\beta/\text{He II } \lambda 4686 \text{ \AA}$ ratio will provide information about the shape of the ionising continuum (e.g. [Kraemer et al. 1994](#)).
3. **Trace the AGN luminosity history from $\lesssim 10^3 \text{ yr}$ to $\sim 10^{4-5} \text{ yr}$,** by comparing the emission line features observed at different position within the VP clouds to photoionisation models (e.g. CLOUDY, [Ferland et al. 2013](#)). Photoionisation models can indeed provide information about the AGN photon flux “seen” by the gas at different distances from the galaxy nucleus ([Fig. 4.2](#)). Specifically, these models allow us to simultaneously constrain the ionisation parameter U and the hydrogen volume density n_{H} which, for a fixed distance d between ionising source and ionised gas, are linked to the number of ionising photons emitted by the AGN

per unit of time Q through:

$$U = \frac{Q}{4\pi d^2 n_{\text{H}} c} \quad (4.1)$$

The AGN luminosity corresponding to the obtained Q can then be computed by assuming a template AGN SED (e.g. from [Elvis et al. 1994](#); [Vanden Berk et al. 2001](#); [Richards et al. 2006](#)). Because of the travel time needed from the ionising photons to reach the different positions within the gas clouds, this will allow us to estimate the AGN luminosity at different times in the past and construct the AGN lightcurves, as illustrated in [Fig. 4.2](#).

Pioneering work in this direction has been performed by [Gagne et al. \(2014\)](#) on the Teacup galaxy (see also [Villar-Martín et al. 2018](#); [Lansbury et al. 2018](#)). This analysis suggests that the source dropped in luminosity by more than 2 orders of magnitude in the last $\sim 5 \times 10^4$ yr. However, the spatial resolution, $\gtrsim 2$ arcsec, does not allow a precise definition of the timescales as it will be possible with MUSE, as MUSE will allow a 10 times increase in spatial resolution. [Keel et al. \(2017\)](#) also performed a similar analysis based on $\text{H}\alpha$ narrow band *HST* imaging of 8 VP galaxies. Based on this work, these AGN underwent drops in luminosity of 1.5 – 3 orders of magnitude in the last $\sim 10^5$ yr, but the use of a single emission line does not allow us to determine the gas density, and therefore fully distinguish between changes in ionising flux and changes in the line emitting region properties (i.e. changes in the local gas density).

More recently, [Treister et al. \(2018\)](#) presented a multiwavelength study of the VP merger galaxy Mkn 463. As part of this work, I successfully developed and applied the photoionisation analysis method aimed at determining the past AGN luminosity, and therefore reconstructing the long timescales AGN light curves, described above (point 3). Specifically, as we described extensively in [Treister et al. \(2018\)](#), we tested both matter-bound case (3 free parameters: ionisation parameter U , hydrogen volume density n_{H} , and hydrogen column density N_{H}) and radiation-bound case (2 free parameters: U and n_{H}). In both cases we parametrised the ionising AGN spectrum as a power-law $L_{\nu} \propto \nu^{\alpha}$, with $\alpha = -0.5$ for $h\nu < 13.6$ eV, $\alpha = -1.5$ for 13.6 eV $< h\nu < 0.5$ keV, and $\alpha = -0.8$ for $h\nu > 0.5$ keV (e.g. [Kraemer et al. 2009](#)). By comparing the optical line ratios measured in the VP cloud to the obtained photoionisation models from CLOUDY ([Ferland et al. 2013](#)) we determined that the AGN dropped in luminosity by a factor of 3 – 20 over the last $\sim 4 \times 10^4$ yr.

Besides being an important contribution to the published study, the analysis performed on Mkn 463 provides a proof of concept for my AGN light curve reconstruction technique. In addition, this pilot work shows that MUSE is the ideal instrument to perform the proposed AGN variability analysis.

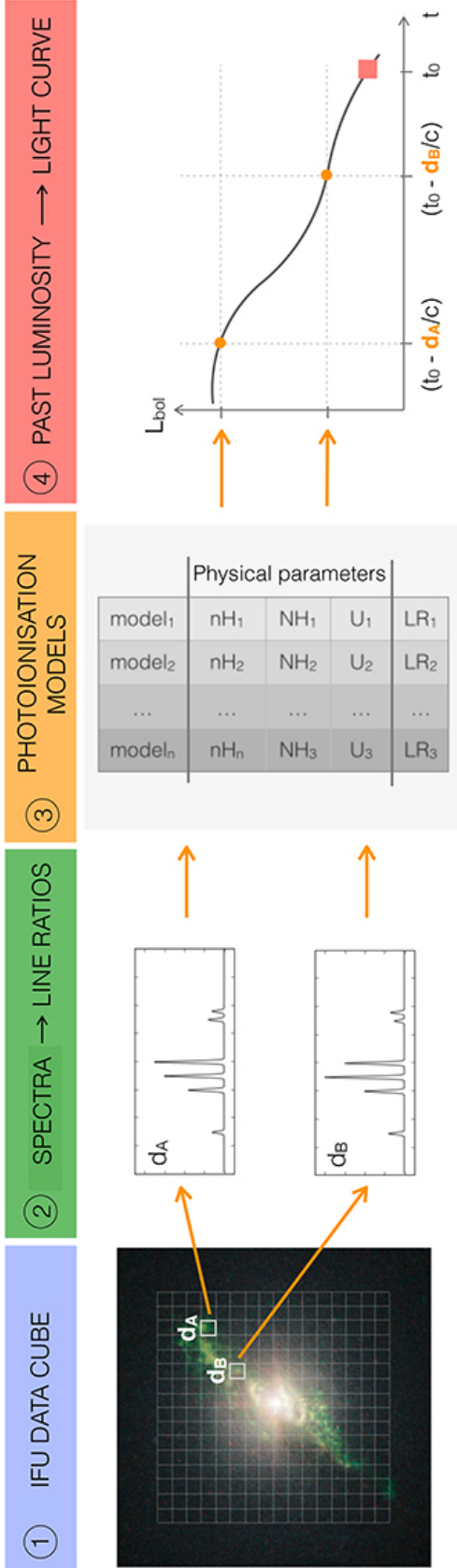


Figure 4.2: Schematic of the proposed method to extract AGN light curves from IFU and X-ray observations of galaxies with extended AGN photoionised gas (e.g. the Voorwerpijjes galaxies). **1-2)** Extract spectra from multiple positions in the AGN photoionised region and measure the emission line fluxes for the detected lines; **3)** Compare the intrinsic line ratios with photoionisation models to determine physical parameters such as the hydrogen density n_H and the ionisation parameter U . Combining U , n_H and distance d it is possible to estimate the number of ionising photons Q emitted by the AGN per unit of time and therefore the AGN bolometric luminosity L_{bol} “seen” by the gas at every position. Because of the travel time of the ionising photons, this corresponds to $L_{bol}(t_0 - d/c)$, where t_0 is the time of the observations (in the galaxy’s system); **4)** By repeating the procedure for different d we can probe the historical AGN light curve (orange points). In addition, X-ray observations allow us to constrain the current luminosity $L_{bol}(t_0)$ also in the case of high obscuration (red square).

4.2 NuSTAR: Hard X-ray spectroscopy

Instrument: Nuclear Spectroscopic Telescope Array (NuSTAR)

Program: NuSTAR GO cycle-3 program 03045

Title: Probing the lifecycle of supermassive black holes on 10-100 kyr timescales

Principal Investigator: Lia Sartori

Target galaxies: UGC 7342, SDSS 1510+07, NGC 5972, SDSS 2201+11

Total time: 190 ksec (priority A)

Motivated by the results obtained for IC 2497 (Chapter 3), I started an observational campaign aimed at acquiring additional hard X-ray observations for the VP galaxies. These new observations complement the archival soft and hard X-ray observations already available (from *Chandra*, *XMM*, *NuSTAR*, and *Swift*-BAT), leading to an X-ray coverage of 17 out of the 20 galaxies in the sample.

Since most of the VP galaxies are found in merger or post-merger galaxies (e.g. [Keel et al. 2012a](#), [Keel et al. 2015](#), [Keel et al. 2017](#)), their centers are expected to be highly obscured (e.g. [Barnes and Hernquist 1991](#); [Bekki and Shioya 2000](#); [Stierwalt et al. 2013](#)). Hard X-ray observations are therefore crucial in order to reliably measure the current intrinsic luminosity (as shown in Chapter 3) which, together with the past luminosities obtained from spatially resolved spectroscopy, is needed to fully constrain the historical AGN light curves (see Chapter 4.1).

Besides measuring the present day intrinsic AGN luminosity (both in the soft and in the hard X-ray bands, as well as bolometric), the analysis of these data will allow us to characterise the VP sample in terms of nuclear obscuration, Eddington ratio and spectral shape. Comparing these results to the properties observed in the BAT AGN Spectroscopic Survey (BASS, [Koss et al. 2017](#); see also e.g. [Ricci et al. 2017](#); [Trakhtenbrot et al. 2017](#); [Lamperti et al. 2017](#); [Oh et al. 2018](#)), the largest unbiased sample of local AGN available to date, will allow us to test if AGN host galaxies with extended AGN photoionised regions differ in some way from the mean AGN population, and to investigate a possible link between AGN variability and other AGN parameters.

4.3 VLA: radio imaging and spectroscopy

Instrument: Karl G. Jansky Very Large Array (VLA)

C and D configurations, C- and L-band

Programs: VLA/15B-145, VLA/16A-023, VLA/17A-004

Title: Characterisation of Voorwerpjes with the VLA: probing the environment of fading AGN

Principal Investigators: Kevin Schawinski (15B, 16A), Lia Sartori (17A)

Target galaxies: 1510+07, SDSS 1524+08, SDSS 2201+11, NGC 5972, UGC 11185, SDSS 1005+28, Mkn 463, Mkn 1498, Mkn 883

Allocated time: 84 hours (priority C)

Observed time: 39 hours

Radio imaging and spectroscopy are very valuable to investigate the environment of AGN, in particular by detecting the presence of large gas reservoirs and of radio jets at all spatial scales (e.g. [Józsa et al. 2009](#); [Rampadarath et al. 2010](#)).

Although the data has never been published, some of the VP galaxies were already observed in the past using the Westerbork Synthesis Radio Telescope (WSRT, e.g. [Muller 1969](#)) and the (enhanced) Multi Element Remotely Linked Interferometer Network (e-MERLIN, e.g. [Muxlow 2003](#)). The preliminary analysis of these data revealed very interesting features. As an example, Mkn 1498 was found to be a bright radio source with a well-defined core (visible in both C- and L-band images) and Mpc jets (visible only in the L-band image), culminating in large and well-defined lobes with multiple hotspots. The jets are misaligned with respect to the ionisation cone, probably because of a recent major merger which influenced the orientation of both dust and gas streams. In addition, the small-scale loops seen in the [O III] λ 5007 maps ([Keel et al. 2017](#)) are aligned with the jets, what suggests that they may be excited by the jets itself. NGC 5972 also shows misaligned radio jets, with Mpc-scale radio lobes and hotspots. In addition, the jets are S-shaped and there is evidence of jet precession, as the position angle changes with frequency. One interesting possible explanation of the observed features is that this galaxy hosts two black holes, one responsible for the radio jet and one for the ionisation cone, while the interaction between the two causes the distorted S-shape.

Radio studies of other VP galaxies can be found in the literature (e.g. [Allison et al. 2014](#); [Harrison et al. 2014](#)). One of the most spectacular cases is the Teacup galaxy, where the VP is seen as a 13 kpc filamentary loop of ionised gas. VLA observations by [Harrison et al. \(2014\)](#) and our own e-MERLIN data of this galaxy revealed two radio bubbles, probably inflated by the AGN, one of which is co-spatial with the VP, a bright core and

a diffuse radio emission. Although the galaxy is classified as radio quiet, there is evidence of a radio jet or quasar wind interacting with the ISM at large scales ($\gtrsim 10$ kpc, [Harrison et al. 2014](#)). This highlights that radio emission can be very valuable to investigate AGN feedback also in the case of radio quiet sources.

Motivated by these findings, I started an observational VLA campaign aimed at obtaining C band continuum images as well as L band spectroscopic and continuum observations of the VP galaxies. The high sensitivity and large angular size (field of view) provided by the most compact VLA configurations (C and D) are in fact needed to detect and study extended and faint radio structures and HI signatures. The obtained data can be used to:

1. Measure the radio spectral index for any central AGN and therefore **determine whether the VP is illuminated by a currently (radio) active AGN** (e.g. [Shulevski et al. 2017](#) and references therein). This would be a complementary test of the AGN light curve reconstruction technique based on optical and X-ray observations described in Chapter 4.1 and Chapter 4.2.
2. **Look for faint large-scale structures which may be signature of jets** much fainter than the ones seen in WSRT, therefore understanding if jets are a common feature in the VP galaxies.
3. **Measure the overall radio flux** which will help planning higher-resolution radio and sub-mm observations, e.g. with the Atacama Large Millimeter/submillimeter Array (ALMA), the Very Long Baseline Interferometry (VLBI) and other VLA configurations.
4. Detect, or get strong limits on, the HI streams directly associated with the extended emission line regions, and therefore **quantify the presence of an hydrogen reservoir at large scales**.

Alltogether, these radio data will allow us to better investigate the environment of the VP galaxies, and therefore possible biases in the sample selection (e.g. driven by the presence of large scale gas, see Chapter 1.3.3). The preliminary L- and C-band maps for three of the observed galaxies are shown in Fig. 4.3.

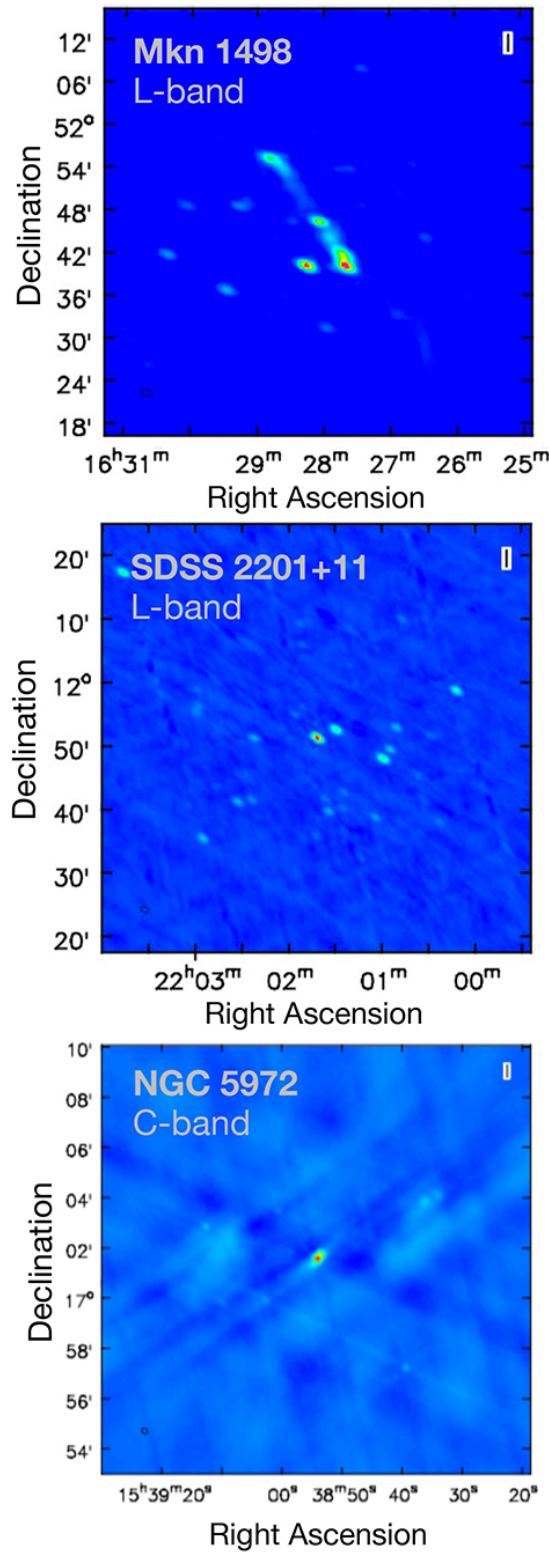


Figure 4.3: Preliminary L-band maps for Mkn 1498 and SDSS 2201+11 and C-band map for NGC 5972 (from the program 15B-145). The beam size is indicated on the bottom left. All the three galaxies are well detected. Mkn 1498 and NGC 5972 also present large structures on Mpc scale, as already observed with WSRT.

	RA		Dec	redshift	MUSE	NuSTAR	VLA	
	RA	Dec					L-band	C-band
IC 2497	9:41:04.09	+34:43:57.8	0.0502		40 ksec			
UGC 7342	12:18:19.28	+29:15:13.2	0.0477	3 h	50 ksec			
Teacup	14:30:29.88	+13:39:12.0	0.0852	2 h				
SDSS 1510+07	15:10:04.01	+07:40:37.2	0.0458	3 h	50 ksec	1 h	45 min	
SDSS 1524+08	15:24:12.58	+08:32:41.3	0.0371	3 h		2 h	45 min	
NGC 5972	15:38:54.17	+17:01:34.3	0.0297	2 h	40 ksec	70 min	1.5 h	
SDSS 2201+11	22:01:41.64	+11:51:24.4	0.0296		50 ksec	7 h	45 min	
UGC 11185	18:16:11.55	+42:39:37.2	0.0412		21 ksec	35 min		
Mkn 463	13:56:02.88	+18:22:19.5	0.0504	2 h	23 ksec	45 min	45 min	
Mkn 1498	16:28:04.06	+51:46:31.4	0.0547		23 ksec	1.5 h	45 min	
Mkn 883	16:29:52.89	+24:26:38.4	0.0368			75 min	1.5 h	
SDSS 1005+28	10:05:07.88	+28:30:38.6	0.0517			30 min	80 min	
NGC 5252	13:38:15.96	+04:32:33.3	0.0228		19 ksec			
IC 2637	11:13:49.75	+09:35:10.7	0.0292		30 ksec			
NGC 4388	12:25:46.74	+12:39:43.5	0.0086		21 ksec			
Mkn 273	13:44:42.11	+55:53:12.6	0.0373		70 ksec			

Table 4.1: Overview of the VP galaxies observed as part of our MUSE, *NuSTAR* and VLA programs (black), and archival observations obtained with the same instruments (gray). In some cases, the reported times correspond to the time requested in the proposal, which may be longer than the real observation due to observing conditions and/or overheads. See text for details about the different programs.

5 A model for AGN variability on multiple timescales

*Laudato si', mi' Signore, per sora nostra matre terra,
la quale ne sustenta et governa,
et produce diversi fructi con coloriti flori et herba.*¹

Laudes Creaturarum, San Francesco D'Assisi (1224)

This chapter is based on Sartori et al. (2018b), "A model for AGN variability on multiple timescales", MNRAS, 476:L34–L38.

The previous chapters well illustrate that AGN variability can be observed or inferred at all timescales, from days to $>10^4$ yr. It is likely to be driven by physical processes originating at different spatial scales, from the nuclear region up to the size of the galaxy or larger.

As discussed in details in Chapter 1.3, variability on days to decades timescales likely arises from accretion disc instabilities, mostly observed in the optical and UV bands. The AGN behaviour on these timescales has been studied through ensemble analysis (e.g. Sesar et al. 2006; MacLeod et al. 2010; Caplar et al. 2017). Years to decades timescales are observed also for the so-called “changing look AGN” or “changing look quasars”², where a change in AGN type is often accompanied by a change in luminosity (CL-AGN, e.g. LaMassa et al. 2015; Ruan et al. 2016; MacLeod et al. 2016; Runnoe et al. 2016; McElroy et al. 2016; Gezari et al. 2017). Possible explanations for this phenomenon include changes in accretion rate (e.g. Marin 2017). On longer timescales, $>10^4$ yr, AGN variability is probed through extended AGN photoionised emission line regions (EELR)

¹*Praised be You, my Lord, through Sister Mother Earth, who sustains us and governs us and who produces varied fruits with coloured flowers and herbs* (Canticle of the Sun, Saint Francis of Assisi, 1224).

²We note that the terms “changing look AGN” and “changing look quasars” are used inconsistently throughout the literature, and can refer to changes both in emission line width or obscuration, as well as in luminosity.

such as the *Voorwerpjes* (VP, e.g. [Lintott et al. 2009](#); [Gagne et al. 2011](#); [Keel et al. 2012a](#); [Keel et al. 2017](#); [Sartori et al. 2016](#); [Sartori et al. 2018a](#)) or ionisation and radio structures in our own Milky Way (e.g. [Su et al. 2010](#); [Bland-Hawthorn et al. 2013](#)). Such timescales may be linked to dramatic changes in the AGN accretion state, as suggested by the viscous radial inflow timescales in standard thin accretion discs (e.g. [Shakura and Sunyaev 1973](#); [LaMassa et al. 2015](#)), which might happen in an analogous way to X-ray binaries (e.g. [Sobolewska et al. 2011](#)). The variability features observed at different timescales, corresponding to modulation of AGN luminosity during the active phase of supermassive black holes (SMBH) growth, may then be superimposed to longer AGN phases. [Schawinski et al. \(2015\)](#) suggested that SMBHs can switch on and off 100 – 1000 times with typical AGN phases lasting $\sim 10^5$ yr, as supported also by some models and statistical arguments (e.g. [Martini and Schneider 2003](#); [Novak et al. 2011](#); [Gabor and Bournaud 2013](#); [King and Nixon 2015](#)).

The variability features described above span many orders of magnitude both in amplitude and timescales. In this Chapter we concentrate on the optical-UV emission from AGN accretion discs, which also illuminates gas far from the nucleus. Variability may therefore be mostly attributed to non-uniform SMBH fuelling, which can arise from physical mechanisms in place at different spatial scales. First, major galaxy mergers can trigger the fuelling of a gas reservoir through the central region (e.g. [Barnes and Hernquist 1991](#)). Internal galaxy dynamics and gas temperature can then affect how and when this gas enters the accretion disc (e.g. [Hopkins and Hernquist 2006](#)). Finally, the conversion of gravitational potential to luminosity depends on physical properties of the disc (e.g. structure and viscosity), as well as the system’s reaction to perturbations (e.g. [Shakura and Sunyaev 1973](#)).

In this Chapter we propose a simple phenomenological model to link and describe the variability features of actively accreting SMBHs observed at different timescales. We assume that the observed variability is mostly driven by changes in SMBH fuelling, which near the nucleus can lead to changes in accretion rate and Eddington ratio (L/L_{Edd}). The link is motivated by general galaxy population properties, such as the L/L_{Edd} distribution function (ERDF) and the power spectral density (PSD) of the L/L_{Edd} evolution with time. This framework allows us to test if and how variability in individual AGN can be linked to and explained by the distribution of L/L_{Edd} among the galaxy population.

We note that the aim of this Chapter is to illustrate the general idea of our new framework, while an extensive description of the implementation and testing, as well as some early applications, is given in Chapter 6.

5.1 Framework and model

AGN variability is generally considered to be a stochastic process (e.g. Kelly et al. 2011). Therefore, every light curve can be interpreted as a realisation of an underlying set of statistical properties. In this context, Emmanoulopoulos et al. (2013) proposed an algorithm to generate light curves based on a probability density function (PDF) describing the distribution of fluxes, and a power spectral density (PSD) describing the distribution of time frequencies.

Motivated by these ideas, we propose that AGN variability due to changes in SMBH fuelling can be modeled starting from the PDF and the PSD of the L/L_{Edd} evolution with time. In the following, we will refer to the time series representing the L/L_{Edd} evolution with time as “ L/L_{Edd} time series”. A summary of the proposed approach is illustrated in Fig. 5.1. By assuming that over long enough time periods every AGN should span the same L/L_{Edd} range as a static snapshot of the whole AGN population, the PDF shape may be inspired by the ERDF. On the other hand, the PSD of the L/L_{Edd} time series is likely to have a broken power-law shape, similar to what is observed for the light curves on timescales of hours to years (although we note that such light curves are expressed in magnitude). The bending may also be expected since variability power cannot increase indefinitely, as accretion is bounded by physical processes. Following the algorithm in Emmanoulopoulos et al. (2013), the input PSD and PDF are used to generate L/L_{Edd} time series which, assuming a radiative efficiency and a description for the BH mass growth, are converted into light curves. Following a forward modelling approach, the light curves can then be used to compute observables (e.g. SF points or magnitude differences) to be compared to real observations.

In this Chapter we provide a simplified proof of concept, motivated by and compared to some data available in the literature (Section 5.2). We will present an elaborate investigation of this model, including numerical and other tests, as well as extensive comparison with data, in Chapter 6. Our hypothesis is that a single ERDF+PSD set, or a limited number of them, should be able to reproduce observed light curves (in a statistical sense), that are consistent with the variability features observed both at short (\sim days) and long ($>10^4$ yr) timescales. This simple model effectively links the variability of individual AGN to the underlying, and more accessible, properties of the entire population.

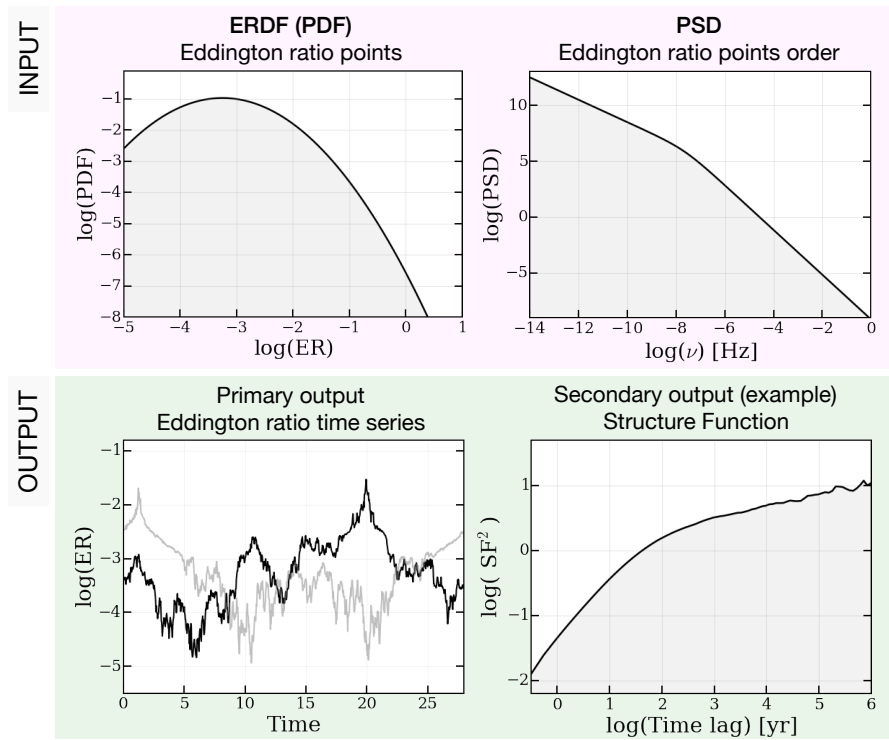


Figure 5.1: Schematic summary of the L/L_{Edd} time series simulations. The input quantities, ERDF and PSD, provide information about the L/L_{Edd} values allowed in the L/L_{Edd} time series (ERDF) and how these points are ordered (PSD). The output L/L_{Edd} time series (primary output; grey and black lines correspond to two different realisations) is then converted into a light curve and used to produce observables to be compared to observations (secondary output, e.g. structure function). Plots are for illustrative purpose only.

5.2 Proof of concept

To show how our model can be used to link and describe AGN variability on different timescales, we compile a set of variability measurements in terms of magnitude differences (Δm) at a given time lag, motivated by the definition of the structure function (SF). In this work, the SF² of the light curve $m(t_i)$ at a time lag τ is defined as:

$$\text{SF}^2(\tau) = \frac{1}{P} \sum_{i,j>i} [m(t_i) - m(t_j)]^2 = \langle [m(t) - m(t + \tau)]^2 \rangle \quad (5.1)$$

where P is the number of magnitude pairs $\{m(t_i), m(t_j)\}$ with $t_j - t_i = \tau$, and the units are [mag²]. The SF can be computed directly from a single AGN light curve, or using an ensemble approach (e.g. MacLeod et al. 2010). From Eq. 6.14, $(\Delta m)^2$ measurements for single objects at given timescales can be directly compared to SF² values. This formalism therefore allows us to compare, on a single plot, the general AGN variability behaviour at different timescales, as well as with specific variability features (e.g. CL-AGN).

In the following we describe how we compiled the rest-frame SF and Δm measurements shown in Fig. 5.2. We stress that all the measurements refer to galaxies currently hosting *actively accreting* SMBH (although EELR may in principle allow us to find galaxies hosting currently inactive SMBHs), and that the reported time lags correspond to the time probed by the observations, as opposed to model predictions or timescales inferred from observed occurrence rates. Since sources generally exhibit chromatic variability properties (e.g. Vanden Berk et al. 2004), it would be preferable to compare SF and Δm in the same band. However, since the goal of the present work is to compile a wide range of observations covering different timescales we are forced to consider measurements obtained for various spectral regimes, although we mainly concentrate on optical and UV data, which are linked to accretion disc physics and SMBH fuelling. This will not affect our main findings, as the differences among optical and UV bands are generally lower than the level of precision required for our current analysis.

5.2.1 Data compilation

Ensemble quasar variability

Ensemble SFs for time lags between days and multiple decades are often described as a damped random walk, an exponential or a broken power law (e.g. MacLeod et al. 2012; Caplar et al. 2017). In Fig. 5.2 we show the r -band SF points from the PTF/iPTF survey (Caplar et al. 2017) and the g -band SF points from POSS (Sesar et al. 2006). We also overplot example fits to the PTF/iPTF SF points (Caplar et al. 2017) and to SDSS and

POSS (MacLeod et al. 2012) with extrapolation to longer timescales. When needed we converted SF measurements and fits to agree with the formulation in Eq. 6.14.

Changing look AGN

We obtained Δm values for single CL-AGN from the literature, starting from the reported changes in magnitude or accretion rate (LaMassa et al. 2015; Ruan et al. 2016; Runnoe et al. 2016; McElroy et al. 2016). In addition we computed a mean $(\Delta m)^2$ value for the SDSS CL-AGN in MacLeod et al. 2016. For the time lags we considered the shortest reported time difference between observations that bracket the AGN class change (as defined in the correspondent literature), converted into rest-frame. We note that some of these timescales may be upper limits.

Extended emission line regions - Voorwerpjes

We computed the Δm values for the VP galaxies in two different ways. For 8 galaxies with available narrow-band *HST* imaging (Keel et al. 2015) we considered the difference between the observed nuclear emission and that required to account for the AGN-like emission in the most distant, AGN-photoionised region (assuming a constant spectral energy distribution shape; see Keel et al. 2017 for the ionisation history reconstruction). For 7 galaxies we estimated the present day AGN luminosities from the fit to the *XMM-Newton* and *NuSTAR* X-ray spectra and a conversion factor to bolometric luminosity (Marconi et al. 2004), and compared them to the past luminosities inferred from the ionising luminosity reported in Keel et al. (2012a) (see also Chapter 2 for a similar analysis on IC 2497). The timescales therefore correspond to the difference between the times probed by the observations. We note that since the measured distances are projected distances, the reported time lags are lower limits. Because of the complexity of photoionisation physics and bolometric corrections, and the uncertainties in the travel time estimation, we caution that the obtained Δm values and time lags have to be treated as order of magnitude estimates. We also stress that, because of the sample selection, the VP sample is biased towards AGN exhibiting large luminosity drops..

Hydrodynamic simulations

Most simulations that trace SMBH growth provide a history of BH accretion rates, which in turn can be converted into (bolometric) light curves. By assuming that the bolometric luminosity varies in the same way as the optical luminosity, the simulated light curves can be used to compute SFs to be compared with observations. In Fig. 5.2 we show the SFs obtained from the simulations in Novak et al. (2011) and from F. Bournaud (private communication). We note that simulations are currently the only possible way to investigate AGN variability on timescales longer than 10^5 yr.

5.2.2 Example model

To illustrate a possible application of our model we simulate L/L_{Edd} time series with three different input PSD and PDF, and compute their SF in magnitude space. The obtained SF can then be compared to the values in Fig. 5.2 to test if the input PSD and PDF can explain the observed variability.

We chose a lognormal PDF with the same parameters as the ERDF proposed in Weigel et al. (2017). For the PSD we considered three different broken power-laws with different slopes and break frequency (BPL 1: $\alpha_{\text{low}} = 0$, $\alpha_{\text{high}} = -2$, $\nu_{\text{break}} = 10^{-8}\text{Hz} \sim 3\text{yr}$; BPL 2: $\alpha_{\text{low}} = -1$, $\alpha_{\text{high}} = -2$, $\nu_{\text{break}} = 10^{-8}\text{Hz} \sim 3\text{yr}$; BPL 3: $\alpha_{\text{low}} = -1$, $\alpha_{\text{high}} = -2$, $\nu_{\text{break}} = 2 \times 10^{-10}\text{Hz} \sim 160\text{yr}$). We then assumed a linear conversion between L/L_{Edd} and luminosity (M_{BH} is not expected to increase significantly during the considered timescales) and computed the SF in magnitude space with Eq. 6.14. The resulting SF, arbitrarily renormalised to be consistent with the PTF/iPTF SF, are shown in Fig. 5.2. The origin of the normalisation mismatch will be addressed in the next Chapter.

We caution that because of computational limits and uncertainties due e.g. to the conversion from L/L_{Edd} to luminosity³, these example simulations have illustrative purposes only. The details of the simulation approach, as well as the comparison with the data, will be addressed in detail in Chapter 6. The aim of the current proof of concept is not to fit the data, but rather to qualitatively illustrate what different PSDs lead to.

³The conversion from L/L_{Edd} to either bolometric or monochromatic luminosities is not fully understood yet, especially at low L/L_{Edd} regimes ($\text{ER} \ll 0.01$) where we expect a change from radiative efficient to radiative inefficient accretion (e.g. Ho 2009).

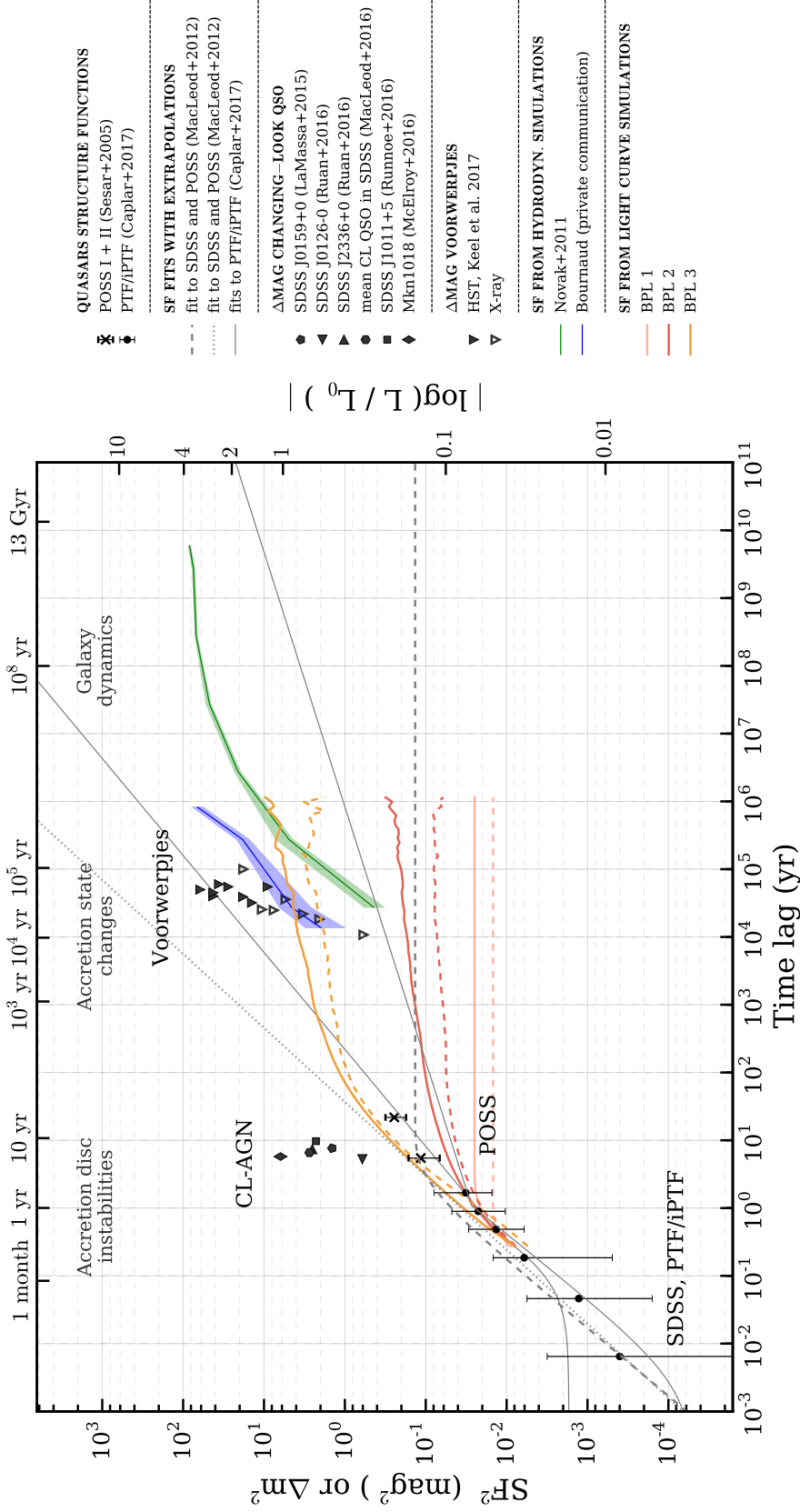


Figure 5.2: Rest-frame SF and Δm plot summarising variability data from the literature and from our own estimates (black points), fits to the SF points (grey lines) as well as simulations results (coloured lines). The SF from light curve simulations are computed both considering all the simulated points (solid line) or only the points with $L/L_{\text{Edd}} > 10^{-3}$ (dashed line) to mimic observational biases. See Section 5.2 for details and references.

5.3 Discussion

5.3.1 Insights and results from the structure function plot

The SF² and $(\Delta m)^2$ plot in Fig. 5.2 summarises all the observed variability measurements described in Section 5.2. The SF corresponding to the short timescales probed by ensemble analysis implies an increase in variability with increasing time lags, and hints at a flattening at $\tau \sim 10^1 - 10^2$ yr. Extrapolating the fits to these SF measurements to longer timescales leads to disagreement. They are therefore not sufficient to predict variability at longer, $>10^4$ yr, timescales.

The position of the VP galaxies on the plot provides further support for a flattening of the SF at time lags exceeding the regime probed by ensemble analysis. We stress that some of the VP galaxies were preselected to show large luminosity drops. Since VP are rare among general AGN population, the ensemble SF at these timescales may be much lower. The *observed* flattening of the SF is also a natural consequence of the fact that, at long time lags, a single power law SF would predict Δm that are too large to be observed due to sensitivity limits and AGN selection criteria. Indeed, AGN with very low L/L_{Edd} ($\sim 10^{-4}$ or lower) are almost undetectable with current facilities, unless they are found in nearby galaxies with high quality data. Such selection biases can be included in our modelling approach. We will therefore be able to test if a single ERDF+PSD set, or a limited number of them, can reproduce the observed flattening and variability features.

The $(\Delta m)^2$ values observed in some CL-AGN are at least one order of magnitude higher than the mean values given by the SF measured using the ensemble approach, in agreement with the results reported in many of the aforementioned CL-AGN studies. Similar to what is observed for the VP, CL-AGN are likely rare based on large searches (Ruan et al. 2016; MacLeod et al. 2016) and possibly related to other processes with higher variability. modelling the AGN light curves and the $(\Delta m)^2$ distributions may help understand if these objects are the extreme tail of the AGN phenomena, or if they represent a separate process (see Rumbaugh et al. 2018, Graham et al. 2017 for a discussion about extreme variability in QSO).

The variability properties predicted by hydrodynamic simulations are strongly dependent on their spatial resolution and on the applied accretion and feedback recipes. This is consistent with the fact that the BH fueling, and thus variability in emission, is ultimately dominated by circumnuclear processes, on scales that are seldom addressed by simulations. Current hydrodynamic simulations are therefore not suited to investigate AGN variability. Fig. 5.2 illustrates the challenges that simulations are facing (e.g. Negri and Volonteri 2017), and provides an additional way to test how closely future simulations will reflect observations.

5.3.2 Insights from modelling

In Section 5.2.2 we outlined an example application of our method. We considered three different ERDF+PSD sets. The first results suggest that a broken power-law shaped PSD may be able to explain the gross variability features observed. However, further investigation — e.g. of the input definition and conversion from L/L_{Edd} time series to observables — is needed to get more constraining results. This will be addressed in detail in Chapter 6.

We hypothesize that a single ERDF+PSD set, or a limited number of them, should be able to produce L/L_{Edd} time series, and therefore accretion rate and light curves, which are consistent with the observed variability features both at short ($\sim\text{yr}$) and long ($>10^4\text{ yr}$) timescales. This assumption may be justified by the fact that the ERDF appears to be universal (Weigel et al. 2017), and by the BH accretion physics (e.g. Shakura and Sunyaev 1973). Since there is no obvious reason that accretion disc physics should evolve with time (the same physics is expected in local galaxies and in $z \sim 7$ quasars), the short timescale variations connected to the accretion disc ought to be redshift independent. On the other hand, the long-timescale variability linked to cosmology may evolve with redshift (e.g. redshift-dependent gas accretion or merger rate, Lotz et al. 2011). In any case, since the observations in Fig. 5.2 are mostly for luminous quasars in low to intermediate redshift galaxies, we cannot probe the evolution with redshift with the current data. We also note that, as suggested by some ensemble studies (e.g. Caplar et al. 2017; Rumbaugh et al. 2018), short timescale variability could depend on L/L_{Edd} , luminosity and black hole mass M_{BH} . However, the data analysed here do not seem to require a model dependent on these quantities.

If our hypothesis is correct, the underlying PSD would be the temporal analogue in AGN physics to the matter power spectrum in cosmology: similarly to how a single matter power spectrum is responsible for multiple matter assemblages (e.g. Frenk and White 2012), from large cosmic structures down to dwarf galaxies, the AGN power spectrum may be responsible for AGN variability over many orders of magnitude in time. If this is true, our model will allow us to link and describe AGN variability at different timescales. Our framework will allow us to test this hypothesis and to constrain the shape of the underlying PSD, providing novel insights into the AGN variability phenomenon.

6 A forward modelling approach to AGN variability – method description and early applications

*Laudato si', mi' Signore, per sor'aqua,
la quale è multo utile et humile et pretiosa et casta.*¹

Laudes Creaturarum, San Francesco D'Assisi (1224)

This chapter is based on Sartori et al. (submitted), “A forward modelling approach to AGN variability – method description and early applications”, submitted to ApJ.

As discussed in the Introduction, variability is one of the first discovered properties of AGN, and has been extensively studied in the past. However, well sampled light curves are available only for a limited number of objects, and the majority of the studies relies on sparse measurements and/or ensemble approaches, what complicates our understanding of the variability phenomenon.

In the near future, new large, multiwavelength time-domain surveys such as LSST (Ivezic et al. 2008; LSST Science Collaboration et al. 2009), TDSS (Morganson et al. 2015), SDSS-V (Kollmeier et al., 2017), ZTF (Bellm et al. 2019; Graham et al. 2019a), ASAS-SN (Shappee et al., 2014) and *eROSITA* (Merloni et al. 2012) will allow us to probe the variable Universe with unprecedented cadence (\sim days), depth, sky area, and time coverage. These surveys will allow us to probe the variability properties of millions of AGN individually, as well as of the AGN population as a whole. In addition, it will be possible to better characterise and understand new types of flares and other extreme

¹*Praised be You, my Lord, through Sister Water, which is very useful and humble and precious and chaste* (Canticle of the Sun, Saint Francis of Assisi, 1224).

Chapter 6. A forward modelling approach to AGN variability – method description and early applications

variability phenomena associated with SMBH accretion such as changing-look AGN (CL-AGN; e.g. LaMassa et al. 2015; Ruan et al. 2016; MacLeod et al. 2016; Runnoe et al. 2016; McElroy et al. 2016; Gezari et al. 2017), tidal disruption events (TDE; e.g., Rees 1988; van Velzen et al. 2011; Gezari et al. 2012; Arcavi et al. 2014; Chornock et al. 2014; Hung et al. 2017; Auchettl et al. 2017) and extreme variable quasars (e.g. Lawrence et al. 2016; Graham et al. 2017; Rumbaugh et al. 2018).

The data obtained in this new exciting time-domain era will provide crucial information to quantify the variability phenomena and to test various models for its origin. However, challenges for modelling and characterisation of the observed light curves will be important. These are due to the finite time resolution and length of the obtained light curves (e.g. Uttley et al. 2002; Emmanoulopoulos et al. 2010), as well as sample selection and observational biases inherent to each survey. A careful study of AGN variability therefore requires sophisticated statistical analysis methods as well as computationally expensive modelling and simulations.

In Chapter 5 we proposed that the AGN variability observed at optical/UV wavelengths may be modelled based on the distribution of the Eddington ratio (L/L_{Edd}) among the (observed) AGN population. In fact, the emission at such wavelengths mainly arises from the accretion process (Shakura and Sunyaev 1973) and can therefore be modulated by changes in L/L_{Edd} , although other processes such as reprocessing of high energy photons from the hot corona may as well affect the observed luminosity at short timescales (e.g. Uttley et al. 2003). Specifically, we suggest that AGN light curves can be fully simulated starting from two statistical functions: the Eddington ratio distribution function (ERDF, representing the L/L_{Edd} probability density function PDF, see Section 6.1.1) defining the possible L/L_{Edd} values in the simulation, and a power spectral density (PSD, see Section 6.1.1) describing the variability and therefore the time ordering of the L/L_{Edd} points. The obtained L/L_{Edd} time-series can then be converted to (optical/UV) light curves in the observed band in question following commonly-used conversion factors (i.e. reciprocal bolometric corrections). In this framework, every AGN light curve is therefore one realisation of the underlying variability process described by the assumed ERDF+PSD set, and represents the entire AGN population (following the ergodic hypothesis). A forward modelling approach allows us to compare the predictions of our models to observations to test if and how the observed variability features can be reproduced with this simple model and, if this is the case, constrain the underlying ERDF and PSD. In addition, given a model, it is possible to produce light curves that would be observed by specific facilities. We also stress that what proposed in Chapter 5 allows us to link and discuss, in the same framework, AGN variability observed at very different timescales.

In this Chapter we present a new simulations setup aimed at producing AGN light curves following the framework proposed in Chapter 5, based on the algorithm presented in Emmanoulopoulos et al. (2013) (E13 hereafter), and discuss possible applications. The Chapter is structured as follows. In Section 6.1 we describe the model and method. An

extensive description of the simulations code and of the tests to characterise both intrinsic and numerical behaviours of the simulations is given in Section 6.2. Finally, in Section 6.3 we discuss some early application of our framework based on the observed variability in the PTF/iPTF survey and aimed at interpreting extremely variable SMBHs in the LSST era.

6.1 Model and method

The goal of our framework is to statistically model the (observed) AGN variability due to changes in accretion (thus, variability in Eddington ratio, L/L_{Edd}), by simulating L/L_{Edd} time series based on the distribution of L/L_{Edd} among the (active) galaxy population. Specifically, we simulate L/L_{Edd} time series whose PDF is inspired by the ERDF, and with variability behaviour described by a chosen input PSD. The next sections outline the methods used to simulate the L/L_{Edd} time series and to convert them to (observed) AGN light curves, while details about the code are given in Section 6.2. We note that, although the framework presented here and the algorithm are optimised for AGN and L/L_{Edd} time series, they can be adapted to investigate other variable processes such as, e.g. stellar variability (e.g. [Catelan and Smith 2015](#) and references therein; [Labadie-Bartz et al. 2017](#)) or star formation histories ([Caplar and Tacchella 2019](#)).

6.1.1 Simulations of Eddington ratio time series

To simulate L/L_{Edd} time series we start from the time series generating algorithm proposed by [E13](#). This algorithm, which is based on previous algorithms presented in [Timmer and Koenig \(1995\)](#) (TK95 hereafter) and [Schreiber and Schmitz \(1996\)](#) (S96 hereafter), produces time series whose PDF and PSD are consistent with the desired (input) ones. These input PDF and PSD can be taken from real observations (e.g. to reproduce multiple observations with the same variability behaviour as an observed light curve), or from models which have to be tested against the data. The first step consists of creating a time series of the desired length (e.g., in years) and time resolution, whose periodogram scatters around the underlying input PSD (TK95 algorithm), therefore determining the variability in the data. A second time series with the desired number of steps and PDF corresponding to the input one is then obtained through a random draw. Finally, the two time series are combined following the iterative amplitude adjusted Fourier transform algorithm described [S96](#) to produce a time series with both PDF and PSD consistent with the input ones (see Fig. 1 in [E13](#)). We stress that although this algorithm can be used to generate the time evolution of any given quantity (e.g., count rates, fluxes, or magnitudes), in our framework it is only employed to directly simulate L/L_{Edd} time series, while the conversion from L/L_{Edd} to other observed quantities is performed in post processing.

Chapter 6. A forward modelling approach to AGN variability – method description and early applications

In our framework, we assume that the PDF of the L/L_{Edd} time series corresponds to the ERDF of the AGN population (as discussed in Section 6.1.1). We therefore implemented the algorithm in such a way that it allows us to choose between different ERDF shapes proposed in the literature, such as a broken power-law or log-normal distributions (see, e.g., Caplar et al. 2015; Weigel et al. 2017; Caplar et al. 2018). We note that our fundamental assumption that the PDF corresponds to the ERDF is physically acceptable only if the simulation is long enough for the AGN to span the whole ERDF. Although the current knowledge about AGN variability does not allow us to constrain this timescale yet, we assume that it should be on the order of $\sim 10^6$ yr (see Section 6.3.1). On the other hand, in order to compare the predictions to observations, the simulations require a time resolution of years, and preferably even shorter timescales. As a consequence, we need to simulate light curves with $> 10^7$ steps. This makes the simulations extremely challenging from a computational point of view. In order to maximise the performance and the length of the simulated light curves we thus implemented our entire algorithm to run on an architecture of graphical processing units (GPUs; Section 6.2.1).

The Eddington ratio distribution function as the variability PDF

As mentioned above, we propose to use the Eddington ratio distribution function (ERDF) as the PDF of the AGN (population) variability. By construction, the ERDF describes the distribution of L/L_{Edd} among the galaxy population, i.e. the fraction of galaxies in a given L/L_{Edd} range, for a given sample of galaxies at a given redshift range². Assuming that the ERDF shape does not vary significantly during the considered time span, and that all the galaxies in the considered sample have the same variability properties, the ERDF can also be interpreted as the distribution of L/L_{Edd} that a galaxy can have during this time span (up to a normalisation factor): a galaxy moves across the ERDF, spending more time at L/L_{Edd} states corresponding to higher ERDF values³.

Many studies attempted to infer the ERDF directly from observations (e.g. Kollmeier et al. 2006; Kauffmann and Heckman 2009; Schulze and Wisotzki 2010; Aird et al. 2012; Kelly and Shen 2013; Schulze et al. 2015; Jones et al. 2016). However, directly measuring the ERDF is challenging mainly due to selection effects and difficulties in measuring black hole masses M_{BH} for statistically significant samples (e.g. Trakhtenbrot and Netzer 2012; Shen 2013; Peterson 2014; Mejía-Restrepo et al. 2016). Caplar et al. (2015) and Weigel et al. (2017) (W17 hereafter) proposed a different approach, where they assume a simple ERDF shape and apply forward modelling to deduce the parametrisation of the ERDF by deconvolving the AGN luminosity function. Specifically, W17 determined the the ERDF for local AGN, while Caplar et al. (2018) showed that the typical L/L_{Edd} of the (broken

²We note that in many empirical studies the ERDF is determined for the AGN population instead of the total galaxy population.

³In a monotonically declining ERDF, this translates to spending more time at lower L/L_{Edd} values than at higher ones.

power-law) ERDF increases with redshift following $\lambda^*(z) \propto (1+z)^{2.5}$ (at least to $z \sim 2$).

Different parametrisations have been proposed in the literature to describe the observed ERDF. The most common are the broken power-law (e.g. Caplar et al. 2015; Bongiorno et al. 2016; W17; Caplar et al. 2018) and the log-normal distributions (Kollmeier et al. 2006; Conroy and White 2013; Kauffmann and Heckman 2009). Since the aim of our study is to reproduce the *observed* AGN variability, and therefore the behaviour of (mainly) radiatively efficient AGN, we consider as local ($z \sim 0$) PDF the (normalised) ERDF inferred by W17⁴ (see below). In later stages of the present work, we will use the analysis of Caplar et al. (2018) to evolve the ERDF to higher redshift. We stress again that these assumptions can be made only if the length of the simulated light curve is comparable to the time needed for the AGN to span the whole ERDF, and if the ERDF is not expected to vary significantly on these timescales.

Following W17, the broken power-law ERDF for local AGN is parameterised as:

$$\xi(\lambda) = \frac{dN}{d \log \lambda} = \xi^* \times \left[\left(\frac{\lambda}{\lambda^*} \right)^{\delta_1} + \left(\frac{\lambda}{\lambda^*} \right)^{\delta_2} \right]^{-1} \quad (6.1)$$

with parameter values $\log \lambda^* = -1.84$, $\delta_1 = 0.47$, $\delta_2 = 2.53$ and $\log \xi^* = -1.65$. On the other hand, the log-normal parameterisation is:

$$\xi(\lambda) = \frac{dN}{d \log \lambda} = \frac{\xi^*}{\tilde{\sigma} \sqrt{2\pi}} \times \exp \left(\frac{-(\log \lambda - \log \lambda^*)^2}{2\tilde{\sigma}^2} \right) \quad (6.2)$$

where $\log \lambda^* = -3.25$, $\tilde{\sigma} = 0.64$, $\log \xi^* = -0.77$.

It is important to note that the two parameterisations are almost equivalent for the L/L_{Edd} range probed in W17, i.e. $\log(\lambda) \approx (-4) - (+1)$. However, the currently available data do not allow us to constrain the ERDF shapes at lower ER values where the two parameterisations differ significantly, with the log normal distribution leading to fewer low L/L_{Edd} AGN (Fig. 6.1). A drop at low L/L_{Edd} is however expected since the ERDF cannot increase indefinitely at the lower end. We also note that in our simulations we will sample the PDF uniformly in linear space (as opposed to logarithmic space). Therefore, we will consider $dN/d\lambda$ instead of $dN/d \log \lambda$ (see 6.2.1 for more details).

⁴In the present work we are considering the values for radiatively efficient AGN.

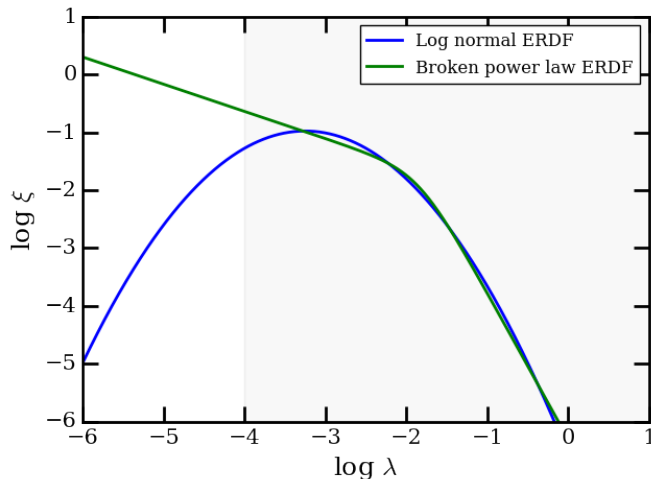


Figure 6.1: Eddington ratio distribution functions for local AGN, from W17, described either as a lognormal (blue) or broken power-law (green) distribution. The two descriptions are essentially indistinguishable for the $L/L_{\text{Edd}}(\lambda)$ range probed in that work, i.e. $\log(\lambda) \approx -4 - 1$ (lightly shaded region). We note that while here we present $\xi(\lambda) = dN/d\log \lambda$ (i.e., space density per logarithmic unit in L/L_{Edd}), as parameterised in Eqs. 6.1 and 6.2, our implementation uses a linear scaling, i.e. $dN/d\lambda$.

Power Spectral Density

The second statistical function needed from our simulations is the PSD that describes the time variability of L/L_{Edd} . The total PSD can be interpreted as a superposition of different physical processes driving the variability at different timescales, and therefore at different frequencies, and its overall shape is not yet fully understood. Multiple studies have performed detailed investigations of the PSD on hours to decades timescales derived from light curves in the X-rays (in counts units, e.g. Markowitz et al. 2003; McHardy et al. 2004; González-Martín and Vaughan 2012; Paolillo et al. 2017) or optical/UV (in magnitude units, e.g. C17; Smith et al. 2018). Specifically, in the case of X-rays, the PSD is generally well described as a power law with slope approximately $\alpha = 2$, consistent with a random walk, at the highest probed frequencies (e.g. Lawrence and Papadakis 1993; Green et al. 1993), and one or two breaks leading to shallower low-frequency PSD (e.g. Uttley et al. 2002; McHardy et al. 2007). The break frequency appears to be correlated with BH mass and L/L_{Edd} (McHardy et al. 2004; McHardy et al. 2006), but the physical reason of this correlation is still unclear (e.g. McHardy et al. 2006; González-Martín and Vaughan 2012). On the other hand, studies based on different optical/UV photometric surveys (e.g. Zu et al. 2013; Caplar et al. 2017) or on *Kepler* light curves (Mushotzky et al. 2011; Kasliwal et al. 2015; Smith et al. 2018) revealed steeper high-frequency PSD, strongly varying between different AGN.

The studies mentioned above all refer to PSDs in counts or magnitude units, while to the best of our knowledge no measurement or prediction for the PSD in L/L_{Edd} units is present in the literature. However, for the sake of simplicity, and inspired by the results above, we assume that also the PSD of L/L_{Edd} has a broken power-law shape. In this scenario, the bending may be associated to some specific physical process which suppresses the variability on progressively short frequencies, e.g. the response of the accretion disc to instabilities (e.g. [Suberlak et al. 2017](#) and references therein).

Through the Chapter, we adopt the following parameterisation of a broken power-law:

$$PSD(f) = A \times \left[\left(\frac{f}{f_{\text{br}}} \right)^{\alpha_{\text{low}}} + \left(\frac{f}{f_{\text{br}}} \right)^{\alpha_{\text{high}}} \right]^{-1} \quad (6.3)$$

where f_{br} is the break frequency, and α_{low} and α_{high} are the slopes at lower and higher frequencies, respectively (longer and shorter timescales, respectively). This parameterisation can however be modified to add additional breaks if needed. In addition, we do not consider any evolution of the variability behaviour, and therefore of the PSD, with redshift, as supported by some observations (e.g. [C17](#); [Paolillo et al. 2017](#)). We stress that throughout the Chapter we will often refer to the periodogram, which is the statistical estimator of the PSD. The periodogram can be directly computed from a time series, and scatters around the underlying PSD (see Appendix [6.A](#)).

6.1.2 Converting Eddington ratio time series to observables: light curves and structure function

As discussed in the Introduction and at the beginning of this section, the primary output of our simulations are time series in units of L/L_{Edd} . In order to compare the simulations to observations, or to make predictions for future surveys, the simulated L/L_{Edd} time series have therefore to be converted to observables. First, the simulated L/L_{Edd} time series can be converted to light curves in luminosity or magnitude units at the same wavelength range as the observations we want to compare to. The forward modelling approach allows us to test different conversion recipes, e.g. by considering constant or luminosity dependent bolometric corrections (e.g. [Marconi et al. 2004](#) and references therein), as well as introducing flux limits or other observational biases proper of every observation. The obtained light curves can then be treated as real observations and used to compute other quantities characterising the AGN variability behaviour. Specifically, in this work we concentrate on the (ensemble) structure function (SF), which quantifies the characteristic amount of variability for light curve (or in general time series) measurements separated by a given time interval τ . A detailed definition and discussion of the SF is given in Appendix [6.A](#) (see in particular Eq. [6.14](#)).

6.2 Simulations

6.2.1 Code Implementation

We implemented the algorithm proposed by E13 to be executed on GPUs. Specifically, we wrote our implementation in C++ within the CUDA programming framework⁵, with the libraries cuFFT⁶, cuRAND⁷ and Thrust⁸. This platform choice allows us to maximise the length (in steps) of the simulations, and is therefore more suited to our science goal than other available implementations based on, e.g., MATLAB (E13) or Python (Connolly 2015). This is particularly due to the fact that the algorithm requires multiple (inverse) discrete Fourier transform (DFT) and sorting operations⁹, which are time consuming especially on arrays of the lengths considered in our work (up to $\sim 10^8$ points), and are being optimised on this platform.

We note that the current implementation is optimised for broken power-law and log-normal PDFs, and for single- or broken power-law PSDs. Specifically, for the random draw step we apply slice sampling (Neal 2003) from a normalised ERDF that is parameterised as in Eqs. 6.1 and 6.2. This choice of PDF and PSD shape is motivated by the observed ERDF and PSD, as discussed in Section 6.1.1. However, additional functional forms can be added if needed. As mentioned in Section 6.1.1, we are sampling the PDF uniformly in linear space.

6.2.2 Testing and characterisation of the simulations code

We tested and optimised our code for the TITAN X (Pascal) NVIDIA GPU. In the following we describe a series of tests that we performed to characterise both numerical effects and intrinsic behaviour of the simulations.

Distortions in the Timmer & König algorithm

The first step of the E13 algorithm consists in running the TK95 algorithm to create a time series of the desired length with a periodogram consistent with the input PSD. The PDF of the output time series should asymptotically approach a normal distribution for increasing number of steps (e.g., E13). However, we found that this is not true for power-law PSDs with steep slopes, $\alpha \gtrsim 1.5$ (PSD $\propto \nu^{-\alpha}$). We illustrate these distortions for several choices of α in Fig. 6.2. We conducted a number of simple tests in an attempt to understand the origin of these distortions. We found that the deviation from a normal

⁵Version 9.0, <https://developer.nvidia.com/cuda-downloads>

⁶<https://docs.nvidia.com/cuda/cufft/index.html>

⁷<https://docs.nvidia.com/cuda/curand/index.html>

⁸<https://docs.nvidia.com/cuda/thrust/index.html>

⁹As an example, 1 simulation with N_{steps} iterations requires $O(N)$ DFT, $O(N)$ IDFT and $O(N)$ sorting operations. See also Section 6.2.2)

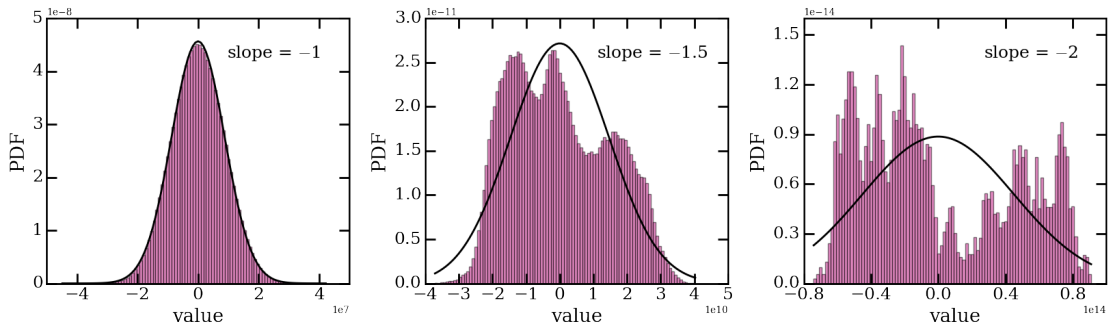


Figure 6.2: Example *output* PDFs of simulated time series based on the TK95 algorithm and on single power-law PSDs with various slopes (as indicated in each panel). In each panel, the black lines show normal distributions which match the output PDFs in mean values and in standard deviations. For step PSDs, the resulting PDF deviates from a normal distribution. We note that, differently from the text, for this image we assume $\text{PSD} \propto \nu^\alpha$ instead of $\text{PSD} \propto \nu^{-\alpha}$.

PDF does not depend on the number of steps, and is therefore not a consequence of the finite simulation length. We also found that the same behaviour is present in simulations performed with other open codes (e.g., astroML, Ivezić et al. 2014; Vanderplas et al. 2012; DELCgen, Connolly 2015) and is therefore not an artefact of our specific implementation. Since our simulations only rely on the PSD of the TK95 output, and not on its PDF, this discrepancy between claimed and observed PDF does not affect our results. However, the TK95 algorithm is extensively used in the literature, and this aspect should be further investigated. We therefore decided to report it here for future reference.

Iterations and convergence

The algorithm that produces the time series is iterative in nature (E13), and so has to converge in order to be robust. Here, convergence means that the output time series does not change (significantly) after a given iterative step, that is the ordering of the time series values stays essentially fixed. The exact number of iterations needed for the algorithm to converge to the final time series depends on the total number of steps, the assumed PDF and PSD, as well as the seed used for the random draw process. E13 proposed a convergence test where, at each step, the periodogram of the resulting time series is fitted with the same functional form as the input PSD, and the convergence of the fit parameters with respect to the input ones is considered. However, due to the significantly larger number of steps used in our simulations – more than 3 orders of magnitude larger than what considered in previous applications of the algorithm – this convergence test would be too time consuming to implement in our case. We therefore decided to base our convergence criterion on the ratio between the time series obtained from two consecutive iterations. Specifically, at every iteration i we consider the following

Chapter 6. A forward modelling approach to AGN variability – method description and early applications

distance measurement δ_i between time the series $x_i(t)$ and $x_{i-1}(t)$:

$$\delta_i = \text{rms} \left[\log \left(\frac{x_i(t_n)}{x_{i-1}(t_n)} \right) \right], \quad n = 1, \dots, \text{num. steps} \quad (6.4)$$

The use of logarithm is motivated by the large dynamical range of the values in time series that are simulated using our observationally-motivated ERDF as PSD. The threshold corresponding to convergence strongly depends on the input PSD and PDF, and should therefore be chosen by the user depending on the performed simulations.

Performance

The maximum number of steps per simulation allowed in the current implementation is 2^{27} ($\sim 10^8$), which is set by memory limitations¹⁰. In the astrophysical context of the present study, this may correspond to, e.g., a ~ 13 Gyr long simulation with ~ 100 yr resolution, or a $\sim 10^6$ yr long simulation with \sim day resolution.

The running time is currently limited by the random draw and sorting steps of the algorithm (steps *ii* and *iv* in Fig. 1 of E13, respectively). On the other hand, using `cuFFT` ensures that the (inverse) Fourier transform steps are performed in the most efficient way. Since the running time is mostly determined by the random draw step, it can vary depending on the assumed PDF shape. However, typical running times for 1 simulation with 200 iterations on TITAN X (Pascal) NVIDIA GPU machines do not exceed a few / several minutes.

Dependencies on input parameters, combining and dividing light curves

In this subsection we discuss how the final L/L_{Edd} time series, PDF, periodogram and SF shapes depend on the following input quantities:

- t_{bin} : time separation between consecutive steps
- N_{steps} : number of steps
- T : simulation length in the same units of time as t_{bin} . This quantity combines t_{bin} and N_{steps} , i.e. $T = t_{\text{bin}} \times N_{\text{steps}}$.
- μ : the mean of the simulated L/L_{Edd} time series. For large N_{steps} this corresponds to the mean of the input PDF.

¹⁰The number of steps is defined in powers of 2 to maximise the simulation speed, in particular with regard to the discrete Fourier and inverse discrete Fourier transforms. All the arrays involved in the simulations are allocated in shared memory for the CPU and GPU using `cudaMallocManaged`.

- σ : the standard deviation of the simulated L/L_{Edd} time series. For N_{steps} that is large enough this corresponds to the standard deviation of the input PDF.

In addition, we look at the effect of combining or dividing light curves obtained from different simulations. Indeed, given the challenge to run long simulations (see previous section), a naive approach would have been to consider “stitching” together separate shorter simulations. On the other hand, understanding the behaviour of subsamples is critical for the interpretation of observed light curves, which actually span only a short time window of the hole AGN life (or, in the case of these simulations, of the time needed for the AGN to span the whole ERDF). We note that in this sub-Section we refer to quantities computed in L/L_{Edd} units, while a discussion of the actual observables, i.e. magnitudes, is given later in this chapter.

For these tests we considered multiple simulations with broken power-law PDFs inspired by the ERDF from W17 (see Eq. 6.1) and a broken power-law PSD as in Chapter 5 (BPL3), but different choices of t_{bin} and N_{steps} . A summary of the input parameters for the different simulations is given in Table 6.1. Specifically, we consider L/L_{Edd} time series simulated assuming different combinations of t_{bin} , N_{steps} and T (ER_sim_1 - ER_sim_6 in Table 6.1, we will refer to these simulations as “direct simulations”), as well as L/L_{Edd} time series obtained by dividing (ER_sim_2_cut) or stitching together (ER_sim_1_comp) direct simulations. We note that although some of the observed features depend on the specific adopted PSD and PDF, the main conclusions from these tests are valid also for different simulation setups.

Shape of the L/L_{Edd} time series

For the considered PSD and PDF set, the shape (global behaviour) of the L/L_{Edd} time series obtained from direct simulations (ER_sim_1 - ER_sim_6 in Table 6.1) is similar and does not depend on t_{bin} , N_{steps} and T . Specifically, in this particular case all the simulations show one main prolonged period of elevated L/L_{Edd} (a “burst” or “switch on”), and a few additional, shorter “spikes”. This is a direct consequence of the fact that each of the simulations spans the entirety of the same PDF, and of the (bent) power-law shape of the periodogram, which gives more power to the lowest frequencies (longer time separations).

The composite simulation (ER_sim_1_comp) shows more bursts, and therefore a higher level of variability on short timescales, compared to a direct simulation of same length (ER_sim_2, see Fig. 6.3). In fact, in the composite simulation every subsample has similar characteristic features (e.g. burst and spikes) as the direct simulation, although at different timescales. This means that stitching together shorter L/L_{Edd} time series will not conserve the variability behaviour proper of the input PSD (see also discussion

Chapter 6. A forward modelling approach to AGN variability – method description and early applications

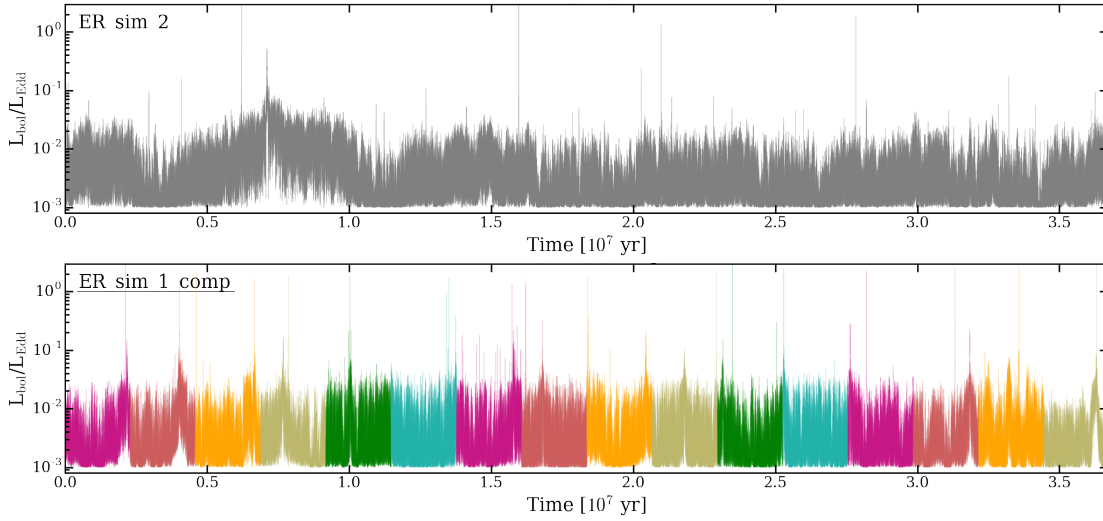


Figure 6.3: Testing the prospects of simulating increasingly long time-series. *Top:* L/L_{Edd} time series from a single simulation spanning the entire PDF (i.e., the entire ERDF; `ER_sim_2`). *Bottom:* composite L/L_{Edd} time series obtained by “stitching” together multiple shorter simulations (different colours), each of them also spanning the entire PDF (`ER_sim_2_comp`). Evidently, although both example data-sets span the same physical length (in yr) and L/L_{Edd} range, the direct (top) and composite (bottom) simulations present different features. Specifically, the composite simulations show multiple peaks (periods of elevated L/L_{Edd}), approximately one per short simulation, while the single simulation only has one such peak (around 0.75×10^7 yr). This can be naturally understood given that each of the short simulations is forced to cover the entire ERDF. As a consequence, stitching together light curves is not a feasible solution to obtain a realistically long L/L_{Edd} time series (with a given computational setup), since it will not preserve the L/L_{Edd} time series shape

below). As a consequence, simulating and stitching together shorter light curves, although computationally cheaper, is not a feasible way to obtain longer L/L_{Edd} time series with both L/L_{Edd} values and variability properties consistent with the assumed PDF and PSD.

Cutting a long simulation into subsamples (`ER_sim_2_cut`) also returns L/L_{Edd} time series with different shapes compared to direct ones with same final length (`ER_sim_3`, `ER_sim_4`). These are in general smoother as they are not covering the whole L/L_{Edd} range allowed by the PDF, but only a (consecutive) part of it.

In summary, combining or cutting simulations returns L/L_{Edd} time series with different shapes and variability features compared to direct simulations with same final length. This effect is visible also in the PDF and periodogram, as discussed below.

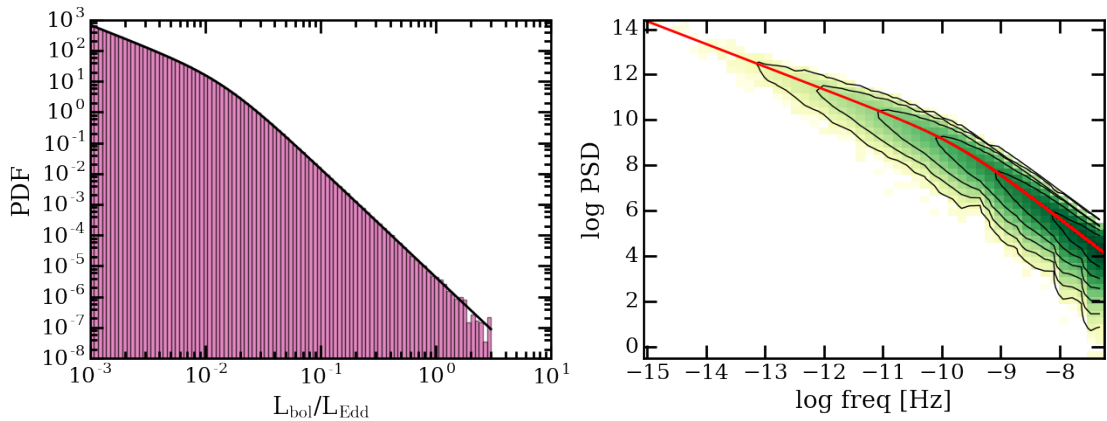


Figure 6.4: Comparison of input and output for a realistic choice of PDF (i.e., ERDF) & PSD (i.e., broken power-laws). *Left*: the PDF of the `ER_sim_2` simulation (purple) compared with the input PDF (black line). By construction, the PDF (i.e., ERDF) of the simulated time-series is statistically consistent with the input one. As expected, the sampling of the PDF becomes more accurate with increasing N_{steps} , as is particularly evident at the high L/L_{Edd} end, where the sampling probability decreases. *Right*: the periodogram of the same simulation. The red line illustrates the input PSD, normalised according to μ , σ , t_{bin} and N_{steps} of the simulation (see Eqs. 6.12 and 6.13). Here, too, the output periodogram is statistically consistent with the input PSD.

Probability density function

By construction, the PDF of every direct simulation (`ER_sim_1`-`ER_sim_6`), and of the composite simulation (`ER_sim_1_comp`), is statistically consistent with the input PDF (e.g. Fig. 6.4, left). In addition, as expected, the sampling of the PDF is more accurate for high values of N_{steps} , especially at the increasingly high L/L_{Edd} end, which is sampled increasingly rarely. The lack of points with high L/L_{Edd} for low N_{steps} simulations has to be taken into account when looking at specific features in the L/L_{Edd} time series, which may ultimately be interpreted as extreme variability events (e.g., changing-look AGN).

On the other hand, the different subsamples (`ER_sim_2_cut`) also show PDFs which are (mostly) continuous in the L/L_{Edd} space, but these do not overlap in any way/range with the input PDF (Fig. 6.5, top). Specifically, most of the subsamples span a narrower L/L_{Edd} range. This is due to the fact that the L/L_{Edd} time series values are not randomly distributed (in time) but follow an order defined by the PSD. As a consequence, the PDF of light curves corresponding to different times during the AGN life can be significantly different.

	Name	t_{bin} [ks]	N_{steps}	T [10^6 yr]	Comment
Initial simulation	ER_sim_1	8'640	$2^{23} \sim 8 \times 10^6$	~ 2.30	
Longer simulation but with same t_{bin}	ER_sim_2	8'640	$2^{27} \sim 10^8$	~ 36.75	$16\times$ longer in yr
Append simulations	ER_sim_1_comp	8'640	$2^{27} \sim 10^8$	~ 36.75	Append 16 realisations of ER_sim_1
Cut long simulation	ER_sim_2_cut	8'640	$2^{23} \sim 8 \times 10^6$	~ 2.30	Cut ER_sim_2 in $16\times$ pieces with same length and binning as ER_sim_1
Change t_{bin} and N_{steps}, same T	ER_sim_3	4'320	$2^{24} \sim 2 \times 10^7$	~ 2.30	$2\times N_{\text{steps}}, 0.5\times t_{\text{bin}}$
	ER_sim_4	2'160	$2^{25} \sim 3 \times 10^7$	~ 2.30	$4\times N_{\text{steps}}, 0.25\times t_{\text{bin}}$
Change t_{bin} and T, same N_{steps}	ER_sim_5	2'160	$2^{23} \sim 8 \times 10^6$	~ 0.60	$0.25\times t_{\text{bin}}$ and T
	ER_sim_6	34'560	$2^{23} \sim 8 \times 10^6$	~ 9.20	$4\times t_{\text{bin}}$ and T

Table 6.1: Summary of simulations for the tests in Section 6.2.2. As a reference, 8'640 ks corresponds to 100 days.

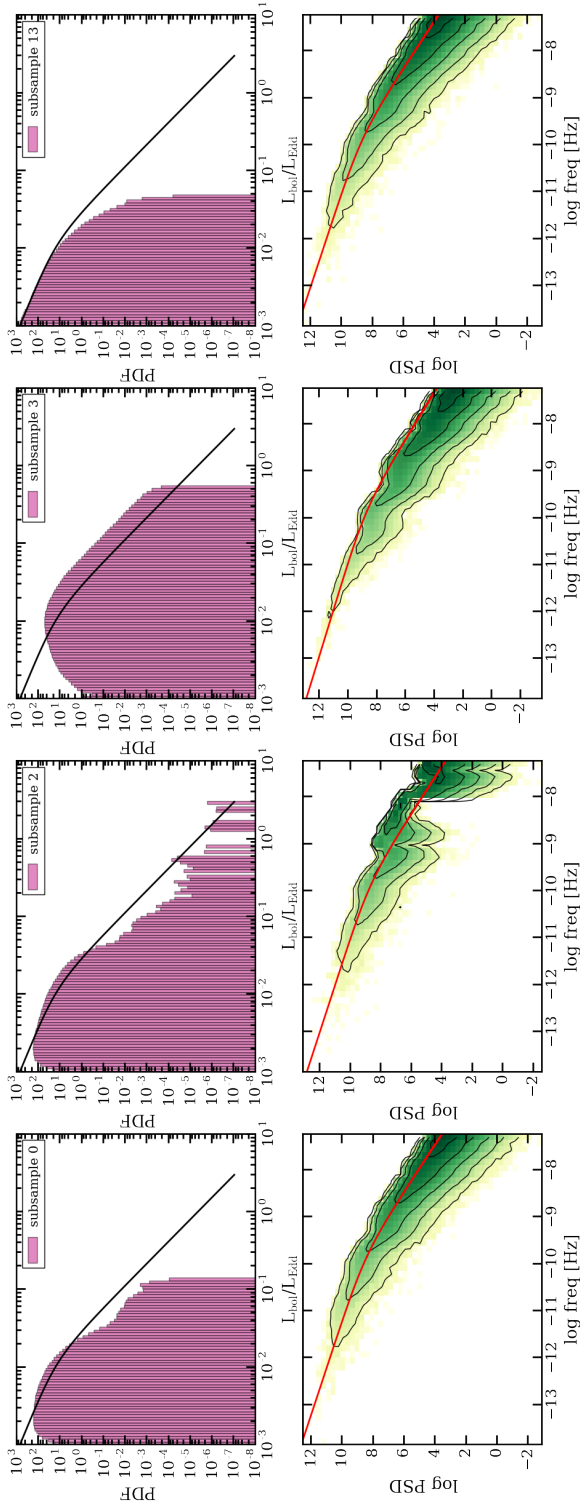


Figure 6.5: Same as Fig. 6.4 but for four sub-samples of `ER_sim_2` (from `ER_sim_2_cut`; that is, shorter simulations). The PDFs of the sub-samples do not match well the input PDF, as the simulated time-series are not sufficiently long to cover the entire PDF. Moreover, the periodogram show distortions, which are more important for subsamples covering a broader L/L_{Edd} range. See text for discussion.

Chapter 6. A forward modelling approach to AGN variability – method description and early applications

Periodogram

By construction, all the periodograms computed for the direct simulations (`ER_sim_1` - `ER_sim_6`) have shapes consistent with the input PSD (e.g. Fig. 6.4, right). As described in Appendix 6.A, the normalisation of the output periodogram differs from the input one, and depends on all the other aforementioned parameters, as well as on the covered frequency range. We verified that the normalisations of the periodograms computed for direct simulations are consistent with the expected value.

The periodograms computed for the subsamples (`ER_sim_2_cut`) show some distortions compared to the input PSD which are more important for subsamples with larger dynamical range in L/L_{Edd} (Fig. 6.5). A detailed discussions of these distortions, including both well known spectral distortions and effects related to the simulations, is given in the following of this chapter. On the other hand, the periodogram of the composite simulation (`ER_sim_1_comp`) also shows some distortion which in this case may be explained by a suppression of variability at long timescales (every subsample has same L/L_{Edd} values, therefore not allowing the formation of a single peak as observed in the direct simulation, Fig. 6.3 top) and an increase of variability at short timescales (every subsample spans the whole PDF, Fig. 6.3 bottom).

Structure function

We construct SFs following Eq. 6.14 and Chapter 5. All the SF computed for direct L/L_{Edd} time series (`ER_sim_1`-`ER_sim_6`) show a broken power-law shape, which seems to reflect the PSD shape. Indeed, the two slopes coincide asymptotically (for $\tau \rightarrow 0$ and $\tau \rightarrow \infty$) to the prediction of the Wiener-Khinchin theorem¹¹ and the break is broadly consistent with $\tau_{\text{br}} \sim 1/\nu_{\text{br}}$.

In the case of composite and divided L/L_{Edd} time series (`ER_sim_1_comp`, `ER_sim_2_cut`), the SFs show a similar behaviour as described above for the periodogram, again confirming a relation between the two quantities. Specifically, distortions of the PSD at high frequencies are reflected to distortions of the SF at low τ .

The normalisation of the SF differs between our various simulations. For a fixed PSD, it depends on the total length of the simulation (T), as well as on the standard deviation of the time series (σ). Specifically, for pure power-law PSD we empirically found that the

¹¹The Wiener-Khinchin theorem states that a power-law PSD with slope $-\alpha$, $1 < \alpha < 3$ should corresponds to a power-law SF with slope $\beta = (\alpha - 1)/2$ (under specific assumptions; see also [Emmanoulopoulos et al. 2010](#)).

normalisation has the following proportionality:

$$\text{norm}_{\text{SF}} \propto \frac{\sigma}{(t_{\text{bin}} \times N_{\text{steps}})^{\beta}}, \quad (6.5)$$

where $\beta = (\alpha - 1)/2$ is the same exponent as in the Wiener-Khinchin theorem, i.e. the exponent expected for the SF (in an ideal case). For broken power-law PSD, the difference between SFs obtained from different simulation setups (i.e. different T and σ) is less well defined, as the ratio between two SFs changes as a function of τ (i.e., the SF have slightly different shapes). Although we were not able to find an analytical description of the normalisation in this case, we see similar dependencies: the overall SF is higher for increasing σ or decreasing T , although the dependency on T is more important for steeper PSD. This can be understood as follows. By construction, the time series obtained with our simulations span the entire PDF (i.e., the ERDF). If the simulation length is shorter, this means that the PDF has to be covered faster, which translates to an overall higher level of variability and thus a higher SF. Similarly, a larger σ corresponds to a broader PDF, which, for fixed T has to be again covered faster. This dependency of the SF normalisation on T and σ has to be considered when comparing simulations to observations, as discussed in detail in Section 6.3.1. Specifically, the length of the simulation has to be chosen such that the normalisation of the output SF (i.e., the SF of the simulated time series) matches the observed one. Moreover, we note that the normalisation does not depend on t_{bin} or N_{steps} separately, but on the combination of the two (i.e. simulations with different t_{bin} and N_{steps} but same T have the same normalisation).

Mean variability behaviour from multiple realisations

Since we are working with stochastic processes, every simulated ER curve will have a different periodogram and SF, i.e. they fluctuate around the input PSD and SF. By construction, at every frequency the periodogram scatters around the intrinsic PSD as defined by the Timmer & König algorithm (see Section 3 in Timmer and Koenig 1995 or Appendix A2 in E13 for more details). On the other hand, the SF of different realisations have similar shapes but different normalisations. Both effects are illustrated in Fig. 6.6.

In order to compare the simulated SF to observations as proposed in Chapter 5, we need to define a representative SF and properly take into account the scatter among the different realisations. To get a representative SF for a given input set, $\text{SF}(\tau)_{\text{rep}}$, we therefore repeat the simulation N_{sim} times ($N_{\text{sim}} > 50$; see discussion below), and compute the mean of the obtained $\text{SF}(\tau)^2$ (see also C17):

$$\text{SF}_{\text{rep}}(\tau)^2 = \langle \text{SF}(\tau)^2 \rangle = \frac{1}{N_{\text{sim}}} \sum_{i=1}^{N_{\text{sim}}} \text{SF}_i(\tau)^2 \quad (6.6)$$

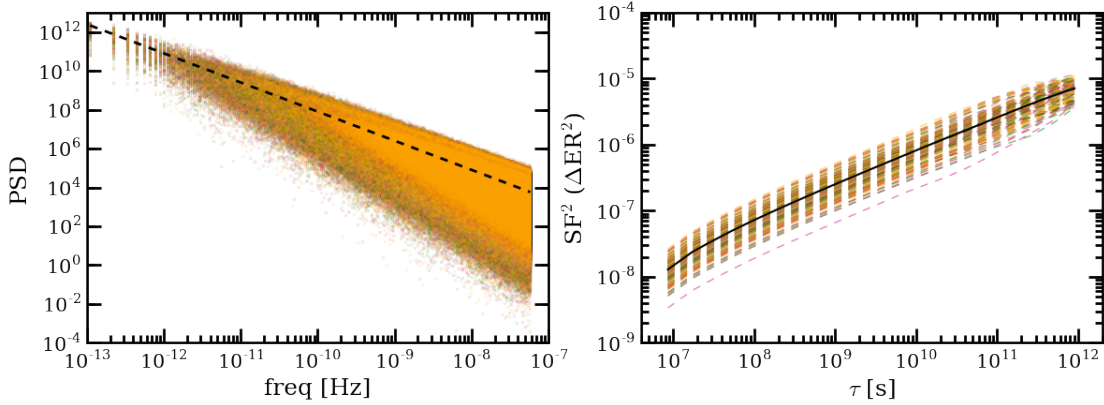


Figure 6.6: Scatter and robustness in repeated realisations of a time-series simulation. *Left:* periodograms for 200 realisations of the same simulation input with simple power-law PSD (slope $\alpha = 1.5$; coloured crosses). The black line traces the input PSD (renormalised, see Appendix 6.A for discussion about PSD normalisation). As expected, the periodograms measured from the simulated time-series scatter around the intrinsic (input) PSD. *Right:* SF^2 for the same simulations (dashed colour lines). The SF^2 measurements for different simulations have a similar shape, but different normalisations. The representative (mean) SF^2 , defined following Eq. 6.6, is shown in black.

The standard error on $SF(\tau)_{\text{rep}}$ at every τ can then be estimated using the scatter in the set of calculated $SF_i(\tau)^2$. Uttley et al. (2002) used a similar procedure to determine the intrinsic PSD from multiple light curves, and claimed that > 50 realisations are needed in order to reliably estimate the standard errors on the simulated periodograms. The same seems to also hold for the SF, but more testing should be done for every specific input set.

We note that in general the time span probed by observations are much shorter compared to the simulated ones. In order to probe that the observed SF can be directly compared to the representative one (i.e., there is no distortion or different normalisation), we first simulated 200 time series with $\sim 10^6$ points each and computed the representative SF (Fig. 6.6, right). From every time series we then randomly selected a (consecutive) subsample of 1000 points, obtained the corresponding SF, and then computed the representative SF (Fig. 6.7A). Although the shorter SFs show a larger dispersion, the representative SF for the subsamples overlaps with the representative SF of the long simulations. This means that the representative SF can be directly compared to SF computed taking into account only subsamples (see also 6.2.2). We confirmed that holds by considering various input PSD shapes, and by computing the SF in magnitude units instead of L/L_{Edd} units.

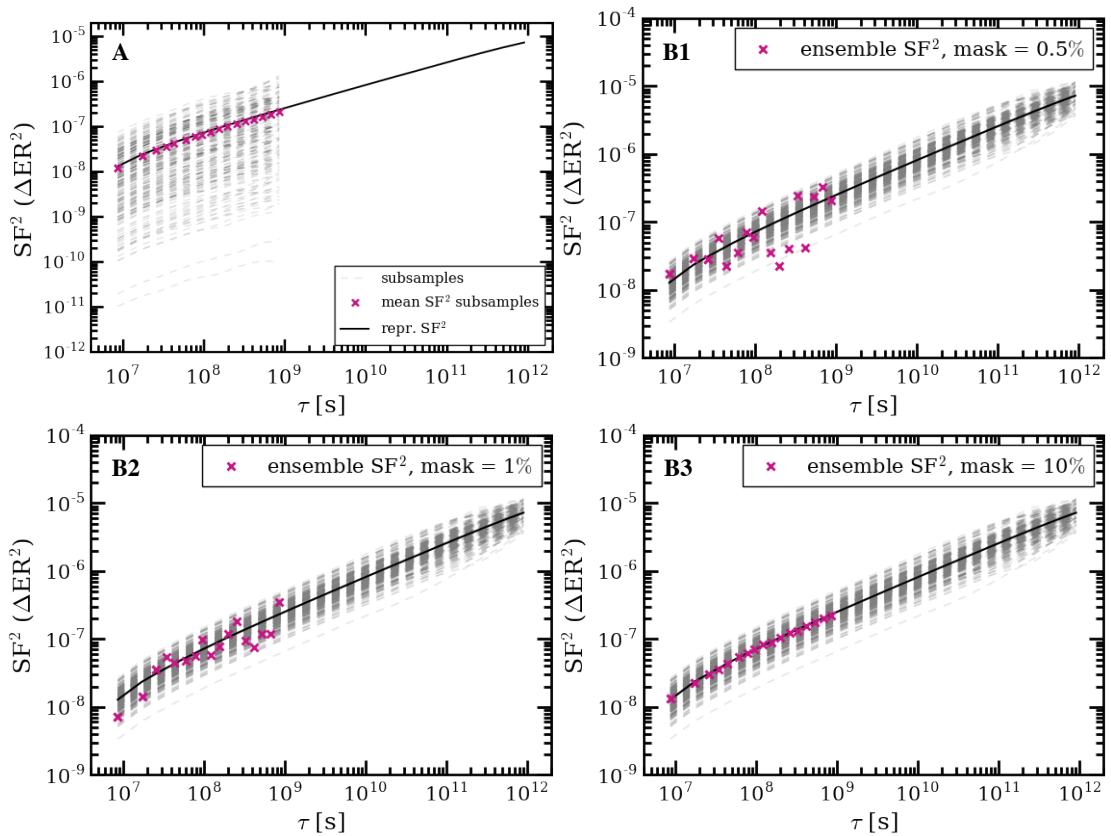


Figure 6.7: *A*: Robustness of the representative structure function. The SF^2 for the random sub-samples of the simulations shown in Fig. 6.6 (gray dashed lines, see text for more details). The representative SF^2 of the sub-samples (purple crosses) overlaps with the representative SF^2 of the long simulations (black line). *B*: Ensemble structure functions for sub-samples of the simulated time-series – similar to Fig. 6.6 (right) and *A*, but for ensemble analysis. Here the purple crosses show the ensemble SF obtained by considering only 0.5% , 1% , and 10% of the simulated data points in every sub-sample, (*B1*, *B2*, and *B3*, respectively; randomly selected points). The ensemble SF always scatters around the representative SF , but the scatter decreases significantly with increasing number of considered points.

Ensemble analysis

Since the SF is a statistical measurement, it is possible to compute it for a single source only in the case of a well sampled light curve (e.g. [Suberlak et al. 2017](#) and references therein). However, for sparsely sampled light curves, the SF is usually computed in an ensemble way (e.g. [Sesar et al. 2006](#); [MacLeod et al. 2012](#); [C17](#)). In this case, it is assumed that all the sources in the considered sample have the same variability behaviour, and that the SF at a given time lag τ is computed with Eq. 6.14, by considering simultaneously all the pairs of data points separated by a corresponding time lag, in all the sources under question.

In order to test if SFs computed in an ensemble way (i.e. considering subsamples of different light curves) are consistent with SFs computed directly from individual simulations, we performed a test similar to what is described at the end of the previous section. First, we ran 1000 simulations with $\sim 10^6$ points each and selected a (consecutive) subsample of 1000 data points from each simulation. For every simulation, we then masked the subsamples to mimic sparse measurements and computed the ensemble SF. As an example, Fig. 6.7B shows the ensemble SF obtained by considering only 0.5%, 1% and 10% of every subsample, respectively (randomly selected points). As expected, the ensemble SF always scatters around the representative SF, but the scatter significantly decreases with increasing number of considered points. This means that the mean shape and the normalisation of the SF are conserved with ensemble analysis, but the accuracy strongly depends on the number of measurements.

We stress that what reported in the test above is only indicative of a trend. In fact, the scatter in the ensemble analysis strongly depends on the number of considered sources, and on the length and sampling of the light curves measured for each source. Therefore, in order to determine how well an ensemble SF computed for a given survey represents the intrinsic one (i.e. if we can compare the ensemble SF with our simulations), the test above should be repeated by assuming the same source numbers observational cadence as in the considered survey.

Spectral distortions: red noise leak and aliasing

The periodograms computed for finite, discrete light curves are subject to spectral distortions known as red noise leak and aliasing (see below for a definition, and [Uttley et al. 2002](#) for a detailed discussion). In fact, measuring a light curve $l(t)$ with a time sampling given by the window function $w(t)$, where $w(t) = 1$ during the observations and 0 elsewhere, corresponds to convolving the Fourier transform of the underlying light curve $F(f)$ with the Fourier transform of the window function $W(f)$:

$$l_{\text{obs}}(t) = l(t) \times w(t) \quad \Rightarrow \quad F_{\text{obs}}(f) = F(f) * W(f) \quad (6.7)$$

Since the periodogram is computed from $F_{\text{obs}}(f)$ (see Appendix 6.A), a distortion due to a window function is reflected as a distortion in the periodogram. Specifically, red noise leak (e.g. Deeter and Boynton 1982; Deeter 1984) appears when the length of the observed light curve is significantly shorter than the length of the intrinsic light curve, so that significant power is present at frequencies shorter than the ones probed with the observations. In this case, trends in the light curve due to frequencies below the observed limit (timescales longer than the light curve total length) are not distinguishable from trends at higher frequencies, and power is transported from low to high frequencies. This effect is more pronounced for steep PSDs (see Uttley et al. 2002 and references therein). On the other hand, aliasing (e.g. van der Klis 1997) appears when the time sampling does not allow us to probe variability at high frequencies f , and in this case there is a fold-back of power from $f_{\text{Nyq}} + \Delta f$ to $f_{\text{Nyq}} - \Delta f$, where f_{Nyq} is the Nyquist frequency (see Appendix 6.A). This effect is more pronounced for shallow PSD.

Both red noise leak and aliasing cause a flattening of the measured periodogram, at a level that depends on the shape of the underlying PSD. Studies comparing simulated periodograms to observed ones should therefore include such distortions in the simulations. The standard way to do it is to simulate longer light curves (e.g. 100 times longer, for red noise leak) with higher sampling (e.g. 10% of the observed sampling, for aliasing), and then randomly select a subsample with length and sampling as in the observations (e.g. Uttley et al. 2002).

Distortions of the Structure Function

While the spectral distortions discussed in the previous section can significantly modify the computed periodogram, the SF is commonly thought to be less affected by finite, irregularly sampled light curves. However, Emmanoulopoulos et al. (2010) showed that spurious breaks can appear in the SF of single light curves even in the case of a power-law PSD (i.e. no intrinsic characteristic time-scales), with unpredictable behaviour at timescales longer than the break. The position of the break increases with light curve length and PSD steepness (see Fig. 5 in Emmanoulopoulos et al. 2010), so that the effect is less important in long light curves with steep PSDs. In addition, he showed that windowing of the light curve may also affect the precise SF shape (although the general behaviour is conserved). As can be seen e.g. in Fig. 6.7A, some distortions at the longest probed times scales are present also in our simulations, although they are not as extreme as reported in Emmanoulopoulos et al. (2010). However, these distortions smooth out when considering the representative or ensemble SF, so that these distortions do not significantly affect statistical studies (see also Kozłowski 2017b; Guo et al. 2017), as it is the case in the applications presented in Section 6.3.

Although the distortions described in Emmanoulopoulos et al. (2010) do not affect ensemble studies, other distortions can be seen in our simulations and should be taken

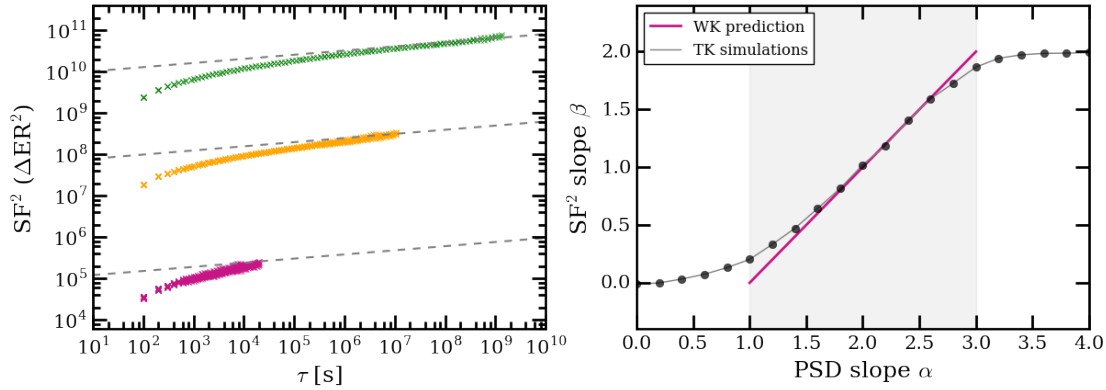


Figure 6.8: *Left:* Structure functions computed for [TK95](#) simulation with PSD with a slope $\alpha = 1.1$, a fixed time step but different lengths. The grey dashed lines have slopes as expected from the Wiener-Khinchin theorem for this PSD (arbitrarily normalised). All the simulated SFs show a downturn at the shortest probed timescales, which is independent of the simulation length. *Right:* resulting SF slopes as a function of input PSD slope (black points). Each point was obtained by fitting a line to 100 [TK95](#) simulations (for every PSD slope). Here $SF \propto \tau^\beta$ and $PSD \propto \nu^{-\alpha}$. The results deviate from expectation from Wiener-Khinchin theorem (purple) as the PSD slopes deviates from $\alpha = 2$, with higher (lower) mean SF slopes for decreasing (increasing) PSD slopes.

into account. According to the Wiener-Khinchin theorem, a power-law PSD with slope $-\alpha$, $1 < \alpha < 3$, should corresponds to a power-law SF with slope $\beta = (\alpha - 1)/2$ (under specific assumptions, see also [Emmanoulopoulos et al. 2010](#)). However, as can be seen in Fig. 6.8, for $\alpha \lesssim 1.5$ ($\gtrsim 2.5$) the obtained SF is steeper (shallower) than expected from the theorem. For a given time resolution, this effect is more pronounced for short timeseries, as the difference between the predicted and observed SF slope is higher at the lowest probed tau τ , independently on the total number of steps (see Fig. 6.8 for [TK95](#) simulations). The main reason of this discrepancy is that the observed and simulated light curves are not infinite and continuous in time, as required by the theorem. In addition, for steep PSDs we often see a distortion at the highest probed τ even in the representative SF. The main reason of these distortions is that the number of pairs for a given τ decreases with increasing τ , and therefore the SF, which is a statistical measure, cannot be reliably computed for large τ .

The discussed issues strongly illustrate why one should be cautious when considering the highest τ SF measurements of any simulation, as these are essentially unreliable. The actual threshold above which the SF becomes unreliable depends on light curve sampling and length, as well as on the PSD shape. As a rule of thumb, in our analysis we are considering SFs only up to 1/10 of the total light curve length (e.g. [C17](#)). We stress, however, that for the PSD slopes expected from observations (see Section 6.3), and for ensemble studies, we do not expect our results to be biased by these distortions.

PSD and SF collapse

For some choices of PSD and PDF sets, the algorithm returns time series whose periodograms “collapse” towards utterly unrealistic PSD shapes. As an example, a PDF as described in W17 with $\lambda_{\min} = 10^{-5}$, $\lambda_{\max} = 10$ combined with a broken power-law PSD with a low-frequency end $\alpha_{\text{low}} \gtrsim 1.5$ leads to a collapse of the final periodogram to a line with negligible scatter and a slope close to $\alpha = 1$ (pink noise). This effect is observed for both lognormal and broken power-law PDFs, and the final shape mostly depends on the initial random seed (and not on other parameters such e.g. the input slope). An example of this collapse for 3 simulations with power-law PDF and 3 different slopes, $\alpha_{\text{low}} = 1.6, 1.8$ and 2.0 , is given in Fig. 6.9. We note that a distortion of the periodogram at high (low) frequencies is usually reflected in a distortion of the SF at short (long) τ .

The observed collapse in the periodogram, as well as the distortions in the SF, disappear in the following circumstances (see example in Fig. 6.10):

1. The overall slope is shallower. This will very likely always be the case in most of our analysis, since a steep low-frequency end would mean a steep long-timescale SF, and this seem not to be allowed by the observations;
2. The dynamical range $[\lambda_{\min}, \lambda_{\max}]$ for the PDF is narrower (e.g. 2 dex instead of 6 dex);
3. We only consider a subsample of the LC, e.g. 10%. We note that in most cases this also corresponds to a smaller dynamical range (as the time series does not have enough time to traverse the entire PDF);
4. We consider the SF in magnitude units instead of L/L_{Edd} . We note that, since $\Delta\text{mag} \propto \Delta \log L \propto \Delta \log L/L_{\text{Edd}}$ (see below), working in magnitude instead of L/L_{Edd} results in a reduced dynamical range (i.e., a PDF covering 4 dex in L/L_{Edd} would be mapped to 10 magnitudes).

These conditions suggest that the observed distortions are due to a numerical issue (that is, the LC intrinsically have the right PSD and SF, but we are not able to compute it) instead of being intrinsic of the LC. Specifically, since the SF is computed by looking at the differences between two different points, it is numerically harder to compute it carefully when the dynamical range of the time series is larger (i.e. a roundoff error). In addition, it is possible that some choices of PSD+PDF sets are not allowed for mathematical reasons (as an extreme, a very sharp PDF would not allow almost any variability). Although we are not investigating this issue further, we acknowledge this effect and exclude PSD+PDF sets which lead to collapse from our analysis, or we only consider the magnitude (i.e., logarithmic) version of the SF (which is indeed the version used for comparison with observations).

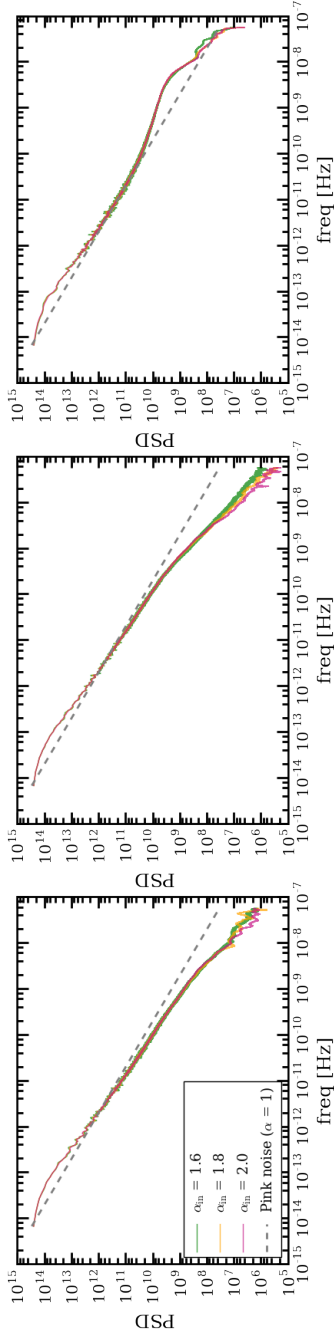


Figure 6.9: Example of the periodogram “collapse”. We show three sets of simulations with broken power-law PDFs, and power-law PSDs with slopes of $\alpha = 1.6$, 1.8 , and 2.0 (green, orange, and purple, respectively). The three panels correspond to three initial random number generator seeds. The periodograms collapse to a line with negligible scatter and slope close to $\alpha = -1$ (pink noise), whose specific shape mostly depends on the initial random seed.

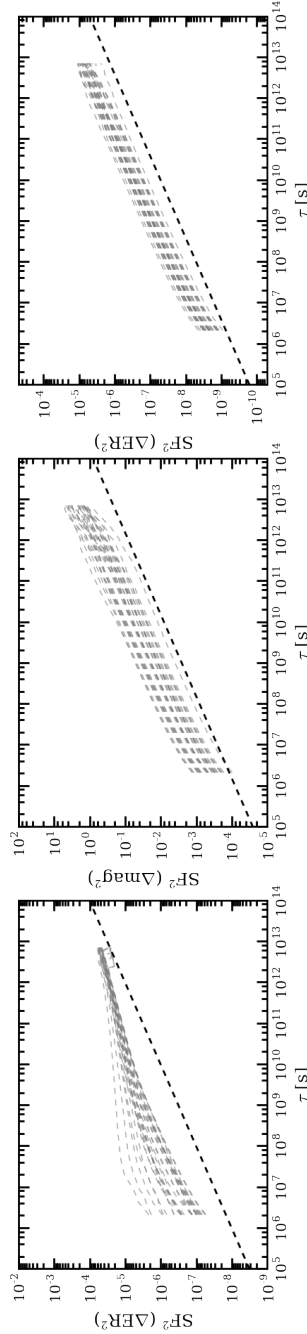


Figure 6.10: Distortions of the structure function due to dynamic range of the PDF. *Left*: SF computed for 30 L/L_{Edd} time series simulated with the same input parameters (grey dashed lines), i.e. a power-law PSD with slope $\alpha = 1.5$ and a broken power-law PDF spanning 6 dex in L/L_{Edd} . The SFs are distorted compared to the predictions of the Wiener-Khinchin theorem (black dashed line, arbitrarily normalised). The distortions are clearly reduced if the SF is computed in magnitude instead of L/L_{Edd} (*centre*), or if the PDF covers a narrower dynamical range (*right*, here 1 dex).

Structure function in Eddington ratio vs. structure function in magnitude

As we mentioned in Section 6.1.2, the primary output of our simulations are L/L_{Edd} time series which, in order to be compared to observations, have to be converted to light curves. Specifically, most of the ensemble studies considered in this work compute SFs in *magnitude* units, SF_{mag} (e.g. de Vries et al. 2003; Sesar et al. 2006; MacLeod et al. 2010; MacLeod et al. 2012; C17). A description of how to convert from L/L_{Edd} to luminosity curves is given in Section 6.1.2. However, in the simplest case where the luminosity $L(t)$ in the considered band is proportional to the Bolometric luminosity $L_{\text{bol}}(t)$ ¹², the magnitude difference needed to compute the SF_{mag} (eq. 6.14) can be directly derived from the L/L_{Edd} time series following:

$$\begin{aligned} m(t_2) - m(t_1) &= -2.5 \log \left[\frac{L(t_2)}{L(t_1)} \right] = -2.5 \log \left[\frac{L_{\text{bol}}(t_2)}{L_{\text{bol}}(t_1)} \right] \\ &= -2.5 \log \left[\frac{\lambda_{\text{Edd}}(t_2)}{\lambda_{\text{Edd}}(t_1)} \right] \end{aligned} \quad (6.8)$$

where $\lambda_{\text{Edd}}(t)$ is the Eddington ratio at time t (L/L_{Edd} throughout the text).

By inspecting multiple simulations we found that, if no distortions are present in $\text{SF}_{L/L_{\text{Edd}}}$ (see previous section), then for the same simulation the SF_{mag} computed following equations 6.14 and 6.8 would have a similar shape, but different normalisation, compared to $\text{SF}_{L/L_{\text{Edd}}}$. On the other hand, for the cases where $\text{SF}_{L/L_{\text{Edd}}}$ shows distortions due to, e.g., a large dynamical range of the PDF (ERDF), these distortions disappear for SF_{mag} . The true underlying reason for this is not yet clear.

6.3 Applications

In the previous sections we presented our framework to simulate AGN light curves starting from the distribution of L/L_{Edd} among the galaxy population. In the following we illustrate some early science applications for the framework, and describe how this framework (and, hopefully, similar studies pursued by the community) will become increasingly important to best exploit new observational data and surveys.

We note that the observational data available to date, and in particular the lack of observational constraints on super-human timescales, do not allow us to fully apply our framework to constrain the underlying PDF+PSD driving AGN variability (or to probe its existence). However, new IFU observations of galaxies with extended AGN photoionised gas (e.g. the *Voorwerpjes* galaxies, Lintott et al. 2009; Keel et al. 2012a; Keel et al. 2012b; Schawinski et al. 2010a; Gagne et al. 2014; Sartori et al. 2016; Keel et al. 2017; Sartori et al. 2018a) will allow us to reconstruct historical AGN light curves (e.g. Treister et al. 2018) and gain new information about AGN variability on $> 10^4$ yr timescales.

¹²We assume that the BH mass is not increasing significantly during the time probed by the simulations.

Chapter 6. A forward modelling approach to AGN variability – method description and early applications

This will be crucial to constrain our models including data at timescales which are still poorly understood. In addition, new time-domain surveys, such as the upcoming LSST, will provide light curves for millions of sources (LSST Science Collaboration et al. 2009) which will allow us to better investigate the variable behaviour of single AGN, as well as compare it to the ensemble behaviour of the general AGN population (e.g. MacLeod et al. 2010; MacLeod et al. 2012; C17).

6.3.1 Constraining specific models with existing AGN variability data

The goal of this section is to provide an example of how existing AGN variability data, in this case the optical SF measurements from the PTF/iPTF survey (Bellm 2014) presented in C17, can be used to constrain the input model parameter space for the kind of simulations enabled by our framework. Specifically, we want to find a simulation setup such that the derived 4000 Å (*R*-band) SF is consistent with the observed one, presented in C17.

As described in Section 6.2.2, the shape and normalisation of the simulated SF depend on the input PSD and PDF, while the simulation’s length in physical units (T , e.g. yr) also influences the overall normalisation (in particular for steep PSDs). Since different normalisations correspond to different variability behaviours, it is crucial to choose physically motivated assumptions for these input parameters in order to obtain realistic SFs to use for our analysis. In addition, observational biases such as flux limits and sample selection can influence the shape and normalisation of the observed SF, and therefore have to be included as additional steps in the simulation process¹³. In the following we outline how to use available observations to define a reference simulation setup consistent with the PTF/iPTF SF, and which will be used for other example applications in the next sections.

The PTF/iPTF structure function

C17 presented the ensemble 4000 Å SFs for a homogeneous sample of $\sim 28,000$ quasars selected from SDSS-DR7 (Shen et al. 2011) divided into 64 $M_{\text{BH}} - z - L_{\text{bol}}$ bins (median $z \sim 1.3$, median $\log(M_{\text{BH}}) = 9.1$; see Fig. 4 in C17). In order to obtain a representative SF for the whole PTF/iPTF sample, we divided the SF values C17 in 6 time bins and took the mean of all SF² measurements in that bin (see Fig. 6.12, black points). In the following we will refer to this representative SF as the PTF/iPTF structure function, $\text{SF}_{\text{PTF,C17}}$.

¹³We stress that the simulations presented and discussed in the previous sections did not consider sample selection or flux limits.

The input PDF and PSD

Following Section 6.1.1, we defined the input PDF as a broken power-law with slopes as in W17 (see Section 6.1.1) and $\lambda^* = 0.11$ as expected for $z \sim 1.3$ and the redshift evolution in Caplar et al. (2018). For these simulations we fixed $\log(\lambda_{\max}) = 0.5$ in order to allow for short periods of super-Eddington accretion (and thus, super-Eddington sources). On the other hand, we chose $\log(\lambda_{\min}) = -3.75$ such that the active fraction, defined as the fraction of time the AGN spends above $\lambda = 0.01$, is $\sim 10\%$ (this is broadly consistent with observations, e.g. Aird et al. 2018). We stress that different definitions of the active fraction are present in the literature, and that its value is not fully constrained yet, as it may depend on multiple parameters such as black hole mass, luminosity and redshift.

While the PDF can be motivated by observational constraints (e.g. ERDF, AGN fraction), the shape of the PSD is well less defined (see discussion in 6.1.1). However, inspired by the PSD obtained e.g. in mag or flux units we assumed a broken power-law shape with slopes and break to be determined through forward modelling, i.e. by comparing the SFs obtained through our suite of simulations to the observed one, $\text{SF}_{\text{PTF,C17}}$.

Creating mock ensemble structure functions

For every input PDF and PSD set (see Section 6.3.1 for the assumed inputs, including total simulation length), we ran 300 simulations (i.e. 300 realisations of the same input set) and created a mock ensemble SF to be compared to $\text{SF}_{\text{PTF,C17}}$ as follows. First, for every simulation we looked for one subsample with similar length as the PTF survey (assumed here to simply be 2000 days in the observed frame), and similar observational biases and sample selection as the sample selection in C17, following the procedure below:

1. *SDSS selection*: select a random point in the L/L_{Edd} time series and convert L/L_{Edd} to the observed SDSS i -band magnitude assuming $z = 1.3$ and $\log(M_{\text{BH}}) = 9.1$. Specifically, we convert L_{bol} to observed magnitude by assuming the Vanden Berk et al. (2001) quasar composite UV-optical SED, shifted to $z = 1.3$, sampled at 3000 \AA (rest frame) and applying a bolometric correction of $L_{\text{bol}}/\lambda L_{\lambda}(3000) = 3.25$ (e.g. Trakhtenbrot and Netzer 2012). Whenever the flux exceeds the SDSS main quasar sample flux limit, $i < 19.1$, we proceed to step (ii); otherwise, we select another random point and repeat the calculation. This step assures that the mock AGN would have been selected within the main SDSS quasar sample, and therefore part of the initial sample used in C17.
2. *PTF sample*: take a 2000 days long subsample starting 5 yrs after the SDSS point¹⁴.
3. *PTF masking*: convert L/L_{Edd} to the observed PTF R -band magnitude (following

¹⁴We chose 5 yr as representative of the gap between SDSS and PTF observations but we tested that varying this gap by a couple of years does not significantly affect our results.

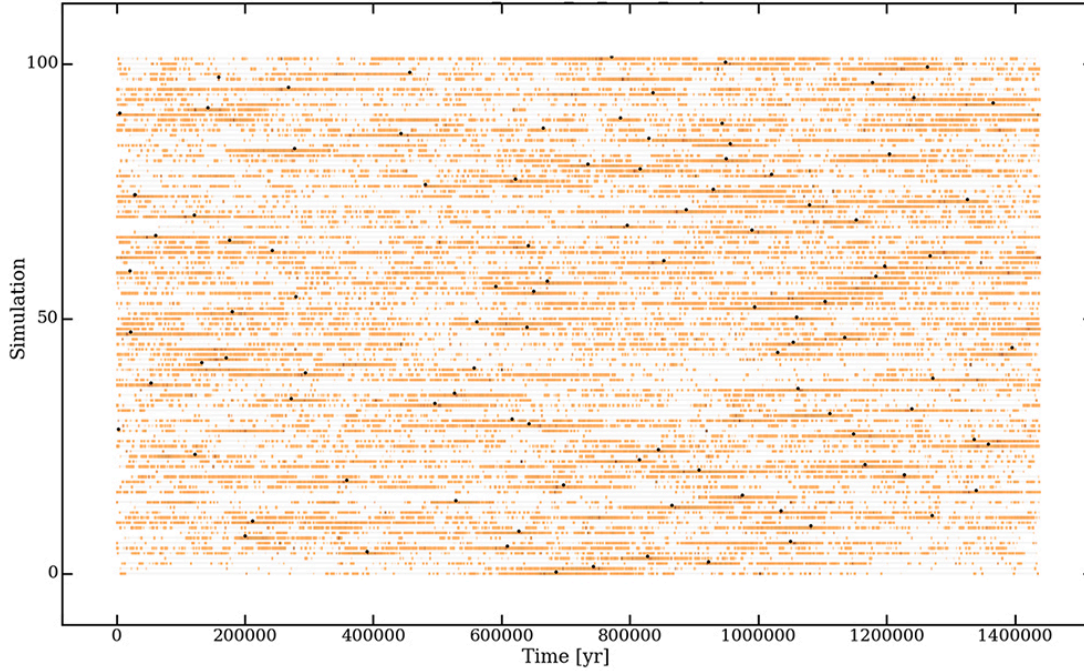


Figure 6.11: Identifying the PTF quasar sample in simulated light curves. This figure illustrates the regions above the PTF limit for 100 of the 300 reference simulations (orange; see Section 6.3.1), as well as the position of a possible PTF-observed region, selected following the procedure outlined in Section 6.3.1 (black points). Only $\sim 1.7\%$ of the points in every light curve meet the PTF selection (mainly the SDSS+PTF flux limits). This fraction may appear to be higher in this illustration due to the limited image resolution (see, e.g., Fig. 6.14, top panel). Evidently, there is no preferential position within the ~ 1.4 Myr covered by the simulation where the the points that could be associated with the PTF quasars sample are clustered.

the same conversions as in step (i) above) and apply a mask such that 1) all the points with $R < 20$ are observed, 2) all the points with $R > 21$ are not observed, and 3) the points with $20 < R < 21$ have a probability to be observed which is a linear interpolation in mag between 20 and 21. This step aims at reproducing the observational limits in the PTF sample with a simple prescription.

4. *PTF selection*: if the median of the masked subsample is $R < 19.1$, accept the subsample as a legitimate mock PTF light curve, otherwise go back to step (i). This magnitude cut reproduces the specific sample selection applied in C17. We note that at the considered redshift ($z = 1.3$) and BH mass ($\log(M_{\text{BH}}/M_{\odot}) = 9.1$), the $R = 19.1$ magnitude cut corresponds to an L/L_{Edd} cut of roughly $\log(L/L_{\text{Edd}}) = -1.2$, which is consistent with what seen in the C17 sample. As an illustration, Fig. 6.11 shows the regions above the PTF limit for 100 of the 300 simulations, as well as the position of a possible PTF region.

We then computed the ensemble *observed* SF, in magnitudes, from the 300 mock PTF light curves (i.e., observed *R*-band magnitudes), and converted it to *intrinsic* 4000 Å SF using Eq. 4 in C17. For every choice of input parameter set (i.e. every PDF and PSD set), we repeated this procedure 500 times (i.e. we computed 500 ensemble SF, each time using different subsamples), and computed the representative SF_{PTF} following Eq. 6.6. We note that this is essentially equivalent to computing the ensemble SF for $300 \times 500 = 150'000$ AGN.

The reference simulation

In principle, what described in Section 6.3.1 should be repeated following an MCMC approach by stepping over a grid of input parameters (i.e., PSD break and slopes, and simulation length), in order to find the best possible model for the data. However, as pointed out above, the current data are not sufficient to fully constrain the PSD, especially due to the lack of measurements beyond human timescales. Therefore, for now we can only use a forward modelling approach to test if a given set of input parameters is consistent with the observed ensemble analysis. For the PDF described in 6.3.1, we found that a PSD with $\alpha_{\text{low}} = 1$, $\alpha_{\text{high}} = 2$, and $f_{\text{br}} = 1 \times 10^{-9}$ (~ 30 yr), and a simulation length of 1.4 Myr is consistent with the observations, as shown in Fig. 6.12. The reference simulation setup is summarised in Table 6.2, and will be used in the next Sections.

We stress that timescales on the order of the PSD break (~ 30 yr in intrinsic frame) or longer are not directly probed by the subsamples used for the ensemble analysis, as the iPTF/PTF data span only 5.5 yr. However, they *are* probed by the total light curves from which the subsamples are selected. Therefore, they indirectly affect also the timescales probed in the ensemble analysis. Specifically, in this case we saw that the break position influences the SF normalisation at the timescales that are probed by the observed data. In addition, we notice that a simulation length of ~ 1 Myr is long enough for the AGN to realistically span the whole ERDF, but advanced computational setup allowing simulations with $> 10^8$ points (see Section 6.2.2) will allow us to probe even longer timescales.

We also note that a break position of ~ 30 yr is longer compared to the breaks reported in the literature for both ensemble SF or PSD, which are on the order of several years (e.g. MacLeod et al. 2012; Simm et al. 2016 C17). However, as discussed in Kozłowski (2017a), break timescales directly computed from observed SFs may be considerably underestimated due to the finite length of the AGN light curves, which is not sufficient to fully probe the variability behaviour at timescales longer than the claimed break (that is, the surveys do not satisfy $T \gg \tau_{\text{br}}$). Moreover, PSD analyses almost always refer to *individual* AGN and find break frequencies which vary from source to source (e.g. Simm et al. 2016). Such short timescales breaks could therefore be “washed out” when averaged over an ensemble of sources, and could therefore not be robustly identified in the intrinsic

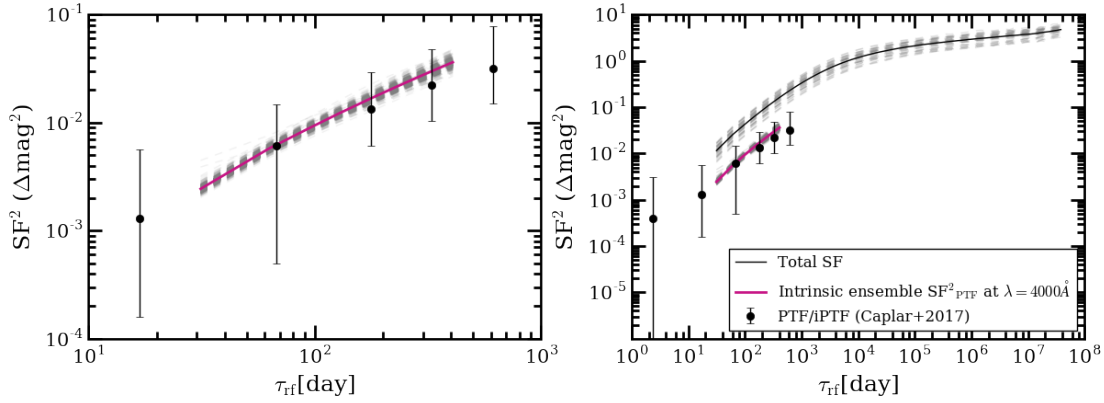


Figure 6.12: Matching the observed PTF/iPTF structure function with our reference simulation. *Left*: black points denote the ensemble PTF/iPTF SF, taken from C17; the gray lines trace 500 ensemble SF from light curves obtained with the reference simulation setup. The indigo line traces the final, representative ensemble SF for the best model, computed from the 500 intrinsic ones. *Right*: Same as left but showing also the total SF obtained directly from the best model simulations without applying any cut or sample selection (black line). We note that the ensemble SF obtained as discussed in Section 6.3.1 has a lower normalisation compared to the intrinsic one.

PSD of the AGN population. Finally, we stress that the observed SF and PSD always refers to specific samples (e.g. with a magnitude limit), such that the observed variability features do not always correspond to the intrinsic ones. As an example, Fig. 6.12 also shows a comparison between the simulated ensemble SF and the total SF obtained from the same simulations without applying any flux cut or sample selection (i.e., the intrinsic SF). The ensemble SF obtained in Section 6.3.1 has a lower normalisation compared to the intrinsic one, suggesting that the sample selected in PTF/iPTF has an overall lower variability compared to the total sample of AGN at the same redshift and BH mass. Since the sample selection mostly relies on the AGN luminosity, including only the most luminous sources (see Section 6.3.1), this effect is consistent with works suggesting the variability to be inverse proportional to luminosity and L/L_{Edd} (e.g. MacLeod et al. 2010; C17; Rumbaugh et al. 2018).

6.3.2 Simulating future time-domain surveys

With the advance of large, multiwavelength time-domain surveys such as the Large Synoptic Survey Telescope (LSST, Ivezić et al. 2008; LSST Science Collaboration et al. 2009), the Time-Domain Spectroscopic Survey in SDSS-IV (TDSS, Morganson et al. 2015), the Zwicky Transient Facility (ZTF, Bellm 2014), and the extended ROentgen Survey with an Imaging Telescope Array (eROSITA, Merloni et al. 2012), we are entering an era of time-domain astronomy which will allow us to probe the variable Universe with an unprecedented time resolution and time-span for very large statistical samples

PDF	Broken power-law (Eq. 6.1) $\lambda^* = 0.11$ $\delta_1 = 0.47$ $\delta_2 = 2.53$ $\log(\lambda_{\min}) = -3.75$ $\log(\lambda_{\max}) = 0.5$
PSD	Broken power-law (Eq. 6.3) $\alpha_{\text{low}} = 1$ $\alpha_{\text{high}} = 2$ $f_{\text{br}} = 10^{-9}$ (~ 30 yr)
Simulation length	$\sim 1.4 \times 10^6$ yr
Eddington ratio cut	$\log(\lambda_{\text{cut}}) = -1.2$

Table 6.2: Summary of reference simulation setup for a sample with $z \sim 1.3$, $\log(M_{\text{BH}}) = 9.1$, consistent with the PTF/iPTF sample in C17.

(\sim millions of objects). Thanks to the high observing cadence, these surveys will allow us to probe for the first time the variability properties of *individual* AGN in a large sample, and to compare them to what was found in ensemble analyses, therefore gaining new insights on the diversity of variability behaviours among the galaxy population.

Based on current observed light curves, which show a variety of features among different AGN (e.g. Smith et al. 2018), one would expect the light curves from the new surveys to be very diverse. In our framework, this diversity arises from the fact that 1) every AGN corresponds to a different realisation of the underlying statistical process, and 2) that the observed time-span (\sim decades) is significantly shorter than the AGN life, and therefore only probe a small part of it. Indeed, we assume that the AGN variability behaviour is (statistically) the same for every AGN only “integrated” over the time needed for the AGN to span the entire ERDF, which for our reference simulation is on the order of $\sim 10^6$ yr. As a consequence, peculiar variability features lasting only for short times (i.e. rare events) will be observed only in a few galaxies, although they may be present in all of them.

To illustrate this point, Fig. 6.13 shows some example AGN light curves which may be expected to arise from LSST assuming the reference simulation setup defined in Section 6.3.1. First, we simulated a $\sim 10^6$ yr long (intrinsic frame) L/L_{Edd} time series based on the reference PSD and PDF (from Section 6.3.1) with a 9 days resolution in *observed* frame (3.9 days in intrinsic frame at $z \sim 1.3$), which is comparable to the LSST resolution (~ 3 days, Ivezić et al. 2008). We then converted it to bolometric luminosity and LSST *i*-band magnitude in a similar way as discussed in Section 6.3.1, and extracted 10 yr long “snapshots” to mimic LSST light curves. As is clearly visible in Fig. 6.13, every

Chapter 6. A forward modelling approach to AGN variability – method description and early applications

short light curve, i.e. every mock observed time series, shows a different variability behaviour. Specifically, the example shown in Fig. 6.13 well illustrates how the AGN can experience a variety of variability features, such as “switch on”, “switch off”, and a sharp, year-long “flare”, as well as periods of much more subtle variability (see the different panels in Fig. 6.13. We caution that this plot is for illustrative purpose only. A more precise analysis which takes into account the survey’s specifics as well as the other computational effects have to be performed in order to compare the observations to the features found in the simulations). Naturally, not all these features will be observed in every AGN because of the limited observation length, as well as magnitude limits and host galaxy contamination (as will be discussed below). This framework therefore allows us to investigate the occurrence rate of specific variability features by considering both the intrinsic AGN behaviour as well as observational limitations (e.g. the fact that we are observing every AGN only for a short time). In addition, the framework proposed in this Chapter will be highly valuable for constraining the true (intrinsic) AGN variability from artefacts and distortions due to the fact that we are not continuously probing the whole AGN light curve (see Section 6.2.2), as well as other observational biases.

One additional advantage of the new and upcoming surveys is the deeper flux limit, which will allow us to detect and investigate the variability properties of fainter AGN. As an example, LSST will reach a magnitude limit $i = 24$ ¹⁵, which is almost 5 magnitudes deeper than SDSS and PTF. Given these deep flux limits, it is however important to consider the possible effect of host galaxy contamination to the observed AGN light curves. To illustrate this, we again simulated a $\sim 10^6$ yr long (intrinsic frame) L/L_{Edd} time series as described above (Fig. 6.14 top, gray light curve). We then computed the i -band magnitude for a galaxy at $z \sim 1.3$ hosting a $\log(M_{\text{BH}}) = 9.1$ BH (as in the PTF sample) by assuming the Bruzual & Charlot templates at 1 Gyr and solar metallicity (Bruzual and Charlot 2003), initial mass function (IMF) from Chabrier 2003, and the $M_{\text{BH}}-M_{\text{bulge}}$ relation from Kormendy and Ho 2013. This gives an host galaxy magnitude $i = 22.2$. The green light curve in Fig. 6.14 (top) corresponds to the the total light curves which considers bot AGN and galaxy contributions. The magnitude change due to host galaxy contribution is of ~ 0.06 mag for sources at the PTF limit, and ~ 2 mag at the LSST limit. Adding the galaxy contribution therefore causes an increase in total flux of $\sim 6\%$ at the PTF limit and of a factor $\sim 6\times$ at the LSST limit. Although the effect is almost negligible for PTF, it should be considered when analysing faint LSST observations.

6.3.3 Extremely variable quasars and changing-look AGN

In the last years, quasars exhibiting extreme variability behaviour (i.e. large magnitude changes over months-years timescales) have been found in increasingly high numbers, both serendipitously (e.g., LaMassa et al. 2015; Runnoe et al. 2016; McElroy et al. 2016; Husemann et al. 2016; Stern et al. 2018; Ross et al. 2018; Katebi et al. 2018; Trakhtenbrot

¹⁵This corresponds to the 5σ detection limit for a point source in a single visit (Kahn 2018).

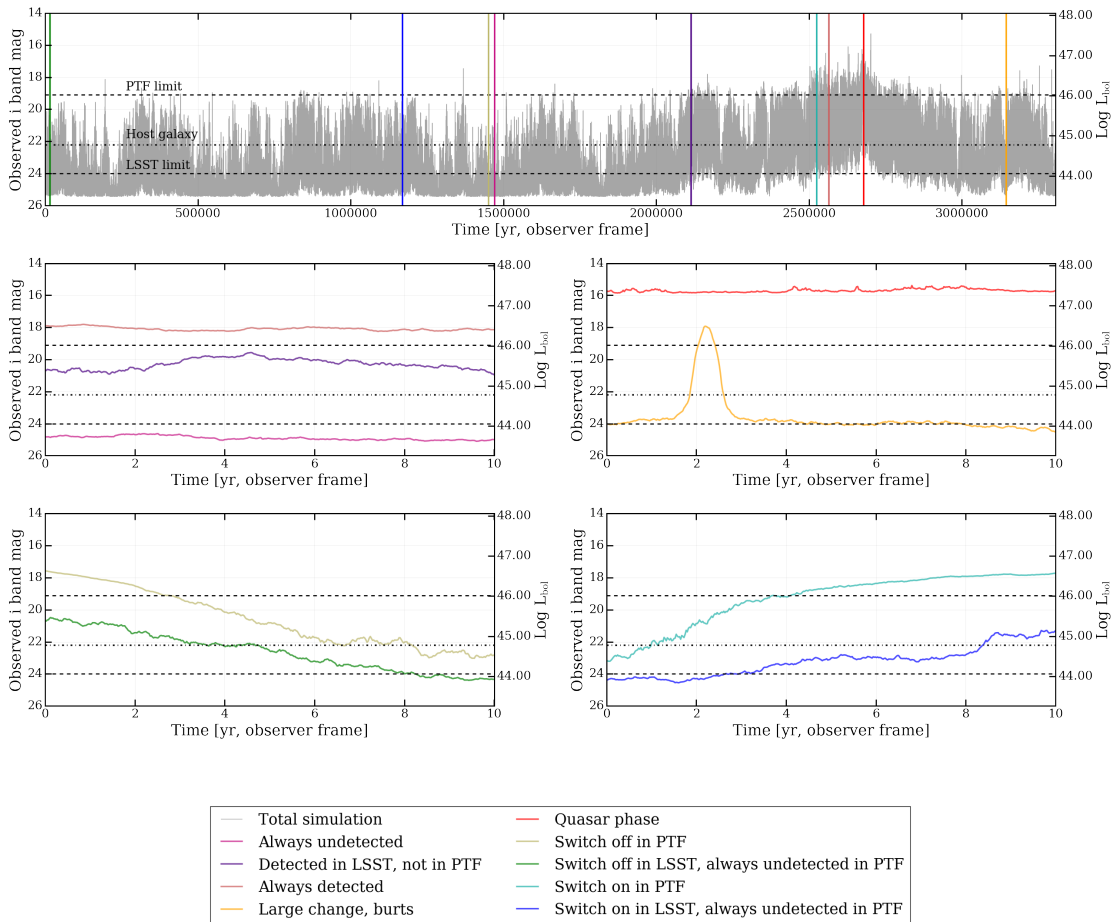


Figure 6.13: Simulating AGN variability as observed within the LSST. The top panel shows an example AGN light curve, simulated using the reference setup (described in Section 6.3.1), and a resolution of 9 days in the observed frame – comparable to the LSST cadence. The horizontal lines mark the PTF and LSST flux limits (dashed lines) and the fiducial host galaxy emission (dash-dotted line). In the panels below we show several 10 yr long “snapshots” (in the observed frame) which mimic AGN light curves that may possibly be observed within the LSST main survey. This figure illustrates how observing AGN at different moments during their life can show significantly different variability features, namely: “switch on”, “switch off” and “flaring” events, in addition to much more subtle AGN variability. We caution that this figure is for illustrative purpose only. A more complete analysis which takes into account the specifics of the surveys as well as other computational effects (see text) have to be performed in order to compare specific observations to the simulated features.

Chapter 6. A forward modelling approach to AGN variability – method description and early applications

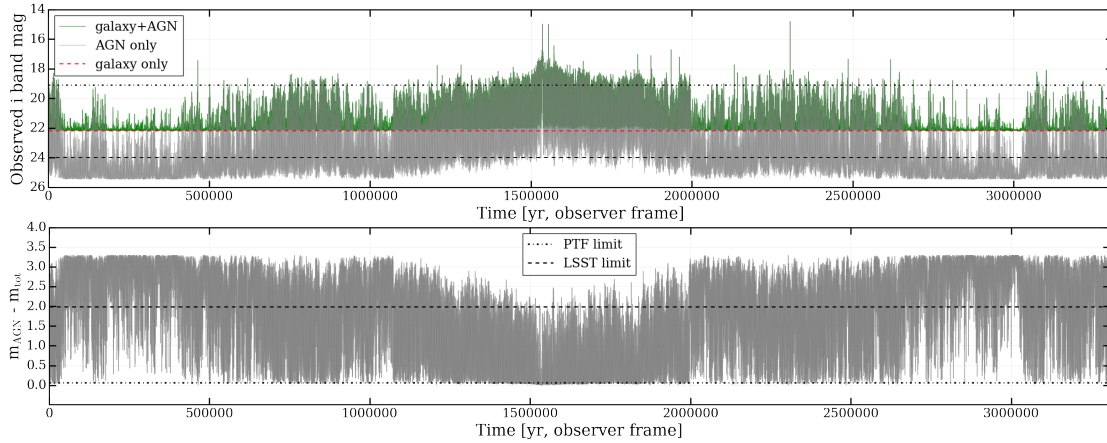


Figure 6.14: The effect of host galaxy contamination on realistic AGN light curve simulations. *Top*: in grey we show the same total AGN light curve as in the top panel of Fig. 6.13, but for a different realisation of the simulation (i.e., identical input parameters). This light curve corresponds solely to the AGN emission. In green we show the light curve derived when adding the contribution of the host galaxy (at $i \simeq 22$; see text for details). Since the host is fainter than the PTF flux limit, the magnitude change due to host light is only ~ 0.06 mag for sources above the PTF flux limit (i.e., $i \lesssim 19.1$). However, it grows to ~ 2 mag for the LSST limit ($i < 24$). *Bottom*: the magnitude difference due to the addition of the galaxy contribution.

et al. 2019) or through systematic searches in surveys such as the SDSS (Ruan et al. 2016; MacLeod et al. 2016; MacLeod et al. 2019; Rumbaugh et al. 2018), PanSTARRS-1 (Lawrence et al. 2016) or CRTS (Graham et al. 2017). One example of extreme variability is observed in CL-AGN which – in addition to changes in emission line structure – show changes in luminosity of an order of magnitude or more on years-decades timescales. Future time-domain surveys will allow us to find and follow up in a systematic way these extreme variable objects.

Although multiple explanations for extreme variability have been put forward (e.g., Graham et al. 2017; Stern et al. 2018; Ross et al. 2018; Lawrence 2018; Rumbaugh et al. 2018), it is not yet clear if these sources are driven by physical processes that are distinct from what drives “normal” AGN variability, or if their extreme variable behaviour is simply the tail of a continuous distribution characterising the overall AGN variability phenomenon (see e.g. Sartori et al. 2018b; MacLeod et al. 2019). Our framework provides an alternative way to address these questions, by comparing the observed numbers (or rates) of variable sources with the prediction from our simulations. Indeed, our framework allows us to quantify the probability of observing a given magnitude change given a model for the underlying AGN variability (i.e. the input of the simulations) and specifics of the survey (such as flux limit, cadence and length).

As an illustration, Fig. 6.15 shows the probability P of an AGN undergoing a change

in magnitude $|\Delta m| > \Delta m_{\text{ref}}$ between two epochs separated by τ , within our reference simulation (as specified in Section 6.3.1). Specifically, for a given simulated light curve, $P(|\Delta m_{\text{obs}}| > \Delta m_{\text{ref}})$ is defined as the ratio between the number of pairs separated by τ with $|\Delta m_{\text{obs}}| > \Delta m_{\text{ref}}$, and the total number of pairs separated by τ . As expected, the probability of undergoing a large magnitude change drops significantly with increasing Δm_{ref} , but increases with increasing τ ¹⁶. This is a direct consequence of the assumed general PSD shape, which gives more power to low frequencies (long τ).

Since the PDF assumed in this example spans the range $\log(L/L_{\text{Edd}}) \in [-3.75, 0.5]$, the maximum possible $|\Delta m|$ that can be found in the simulated light curves is $|\Delta m| \sim 10.6$ mag, which corresponds to a change in luminosity of more than 4 orders of magnitude (4.24 dex). As can be clearly seen in Fig. 6.15, such extreme variability can be found at all timescales probed by our simulations, although the probability for such changes is extremely low. As an example, the probability for the simulated AGN to undergo a magnitude change $|\Delta m| > 10$ mag within $\tau = 1$ yr is $P \sim 10^{-8}$. Since such large $|\Delta m|$ over such short timescales are very unlikely to be physically explainable (see e.g. Katebi et al. 2018 and references therein for a discussion of possible timescales linked to AGN variability), this feature could arise from the fact that the assumed model (both for the PSD and for the L/L_{Edd} to magnitude conversion) is too simplistic, as the SED shape could change drastically (Trakhtenbrot et al. 2019). However, the probability of these features is low enough that it does not affect the main results presented in this Chapter, and we only acknowledge this issue to be investigated in future studies.

It is important to stress that Fig. 6.15 shows the probability of a simulated AGN to *undergo* a certain change in emission, which does not directly correspond to the probability of *observing* or *detecting* such a change. In fact, given the flux limit of any reasonable considered survey, combined with the contamination from the host galaxy, low L/L_{Edd} sources are (usually) not observed (or not identified as AGN), which limits the range of $|\Delta m|$ that may be observable.

To address this limitation, in Fig. 6.16 we show a similar analysis to that shown in Fig. 6.15, but now assuming different magnitude limits discussed in the previous sections: the PTF magnitude limit $r = 19.1$, the LSST magnitude limit $i = 24$, as well as the host galaxy contamination, at $i = 22.2$. Specifically, for a given survey depth (magnitude limit) m_{cut} , we first substitute all the points with $m > m_{\text{cut}}$ with an upper magnitude limit $m_{\text{ul}} = m_{\text{cut}}$, and then compute the probabilities as in the previous test, however now considering only the pairs of data points in which at least one point is above the detection limit. As expected, the probability of detecting large magnitude changes over a given timescale decreases for higher flux limits (shallower surveys). As an example, for the considered simulation the probability of detecting a magnitude change of $|\Delta m| = 2.5$

¹⁶We caution that the trend observed at the highest probed Δm_{ref} , where the probability appears to decrease for $\tau > 30$ yr, may be due to the fact that the number of corresponding pairs within the simulated light-curves is not large enough to reliably sample this low-probability regime.

Chapter 6. A forward modelling approach to AGN variability – method description and early applications

(1 dex change in luminosity) over 10 years is $P \sim 10^{-2}$ assuming the LSST depth, and $P \sim 10^{-4}$ for the PTF. We stress that the probabilities showed in Fig. 6.15 and Fig. 6.16 are not directly comparable since they are computed using different assumptions for the total number of considered pairs (total number of pairs versus number of pairs where at least one point is detected), and since Fig. 6.16 also includes upper limits. We caution that all the numbers reported above are for illustrative purpose only. A more precise analysis which takes into account both the specifics of the considered survey as well as other computational effects in the simulations should be performed in order to directly compare the observed (or expected) rates to the simulation results.

If our hypothesis of an underlying common PSD+PDF set is correct, and the reference simulation defined in Section 6.3.1 realistically describes the AGN population, then, for sources with comparable redshifts and BH masses as the PTF quasar sample, we would expect to detect a level of variability in LSST consistent with the predictions from our simulations (after accounting for sample selection biases in a similar way to what is discussed in Section 6.3.1). Finding different values would however also be informative. For example, detecting a lower than expected number of highly variable quasars may indicate that the L/L_{Edd} changes do not directly translate to luminosity changes, but the variability is suppressed due e.g. to a luminosity dependent bolometric correction (that is, luminosity-dependent SED shape; see, e.g., Vignali et al. 2003; Marconi et al. 2004; Just et al. 2007), and to the fact that the AGN may become radiatively inefficient at low L/L_{Edd} (Narayan et al. 1998; Panessa et al. 2006; Ho 2009). On the other hand, an higher detection rate may be expected if additional external processes, such as microlensing (e.g. Lawrence et al. 2016), dust obscuration (e.g. Maiolino et al. 2010; Ricci et al. 2016a) or supernovae also contribute to the observed luminosity changes. Other possible explanations of high variability proposed in the literature are stellar mass binary black hole mergers within the dense gas of the AGN accretion disc (e.g. McKernan et al. 2014; Bartos et al. 2017) or tidal disruption events (TDEs, e.g. Gezari et al. 2012; Arcavi et al. 2014; Hung et al. 2017; Aucht et al. 2017). Although these events may contribute to the instantaneous emission changes seen in the concerned galaxy, their appearance is not expected to have the same probability in every galaxy (see e.g. Arcavi et al. 2014; French et al. 2016; Law-Smith et al. 2017 for the host galaxy dependence of TDEs). Therefore, such bursts of “external” origin are not expected to be present in our simulations, which are aiming at reproducing the intrinsic stochastic AGN behaviour only.

Systematic searches for CL-AGN are require large multi-epoch spectroscopic surveys, and of elaborate spectral fitting analysis to determine the changes in emission line structure (e.g. MacLeod et al. 2016). Therefore, current studies aimed at systematically searching for highly variable objects are concentrating on changes in the overall luminosity. As an example, starting from a sample of $\sim 900,000$ quasars in CRTS, Graham et al. (2017) found 51 sources with $|\Delta m| > 1$ (V -band) over ~ 900 days, which corresponds to a fraction of $\sim 5 \times 10^{-5} = 0.005\%$. On the other hand, Rumbaugh et al. (2018) detected of variability $|\Delta m| > 1$ (g -band) over a 15 yr period in $\sim 10\%$ of sources among a quasar sample

drawn from SDSS and DES (Flaugher et al. 2015), and further estimate that this fraction would increase to $\sim 30 - 50\%$ accounting for selection effects. Furthermore, Lawrence et al. (2016) performed a joint analysis of SDSS and PanSTARRS-1 and estimated the fraction of AGN showing $|\Delta m| > 1.5$ in the g -band to lie between $10^{-5} - 10^{-3}$. A direct comparison between the results of these studies is impossible, due to the different sample selection criteria and the analysis methodology (see Rumbaugh et al. 2018 for details). Similarly, a comparison between these observational results and the predictions from simulations would require a whole analysis aimed at reproducing the sample selection and observational biases in a similar way as showed in Section 6.3.1 for PTF, which is beyond the scope of this Chapter. We stress that the proposed framework will be very valuable for testing if the results from different studies can be reproduced starting from the same simple model, i.e. if the observed differences are only attributable to different sample selections and analysis methods, or if different works are finding intrinsically different classes of objects. Indeed, this framework allows us to start from the intrinsic AGN variability predicted by simple models, and forward model all the observational effects which may be affecting the observed variability.

It is also important to note that, although CL-AGN usually show a change in the overall luminosity $|\Delta m| > 1$, not all the highly variable sources also present changes in the line structure. For example, MacLeod et al. (2019) report that only 10 – 50% of the quasars with $|\Delta g| > 1$ in the SDSS and PanSTARRS 1 surveys also show CL-AGN behaviour in the optical spectrum. By combining upcoming photometric and spectroscopic time-domain surveys such as LSST and SDSS-V it will be possible to better constrain this fraction. Together with the predictions from the simulations enabled by our framework, this will allow us to investigate the relation between changes in accretion rate and changes in the broad line structure, and in general of the AGN structure, therefore gaining new insights into the interplay between accretion disc and broad line regions (e.g. Marin 2017).

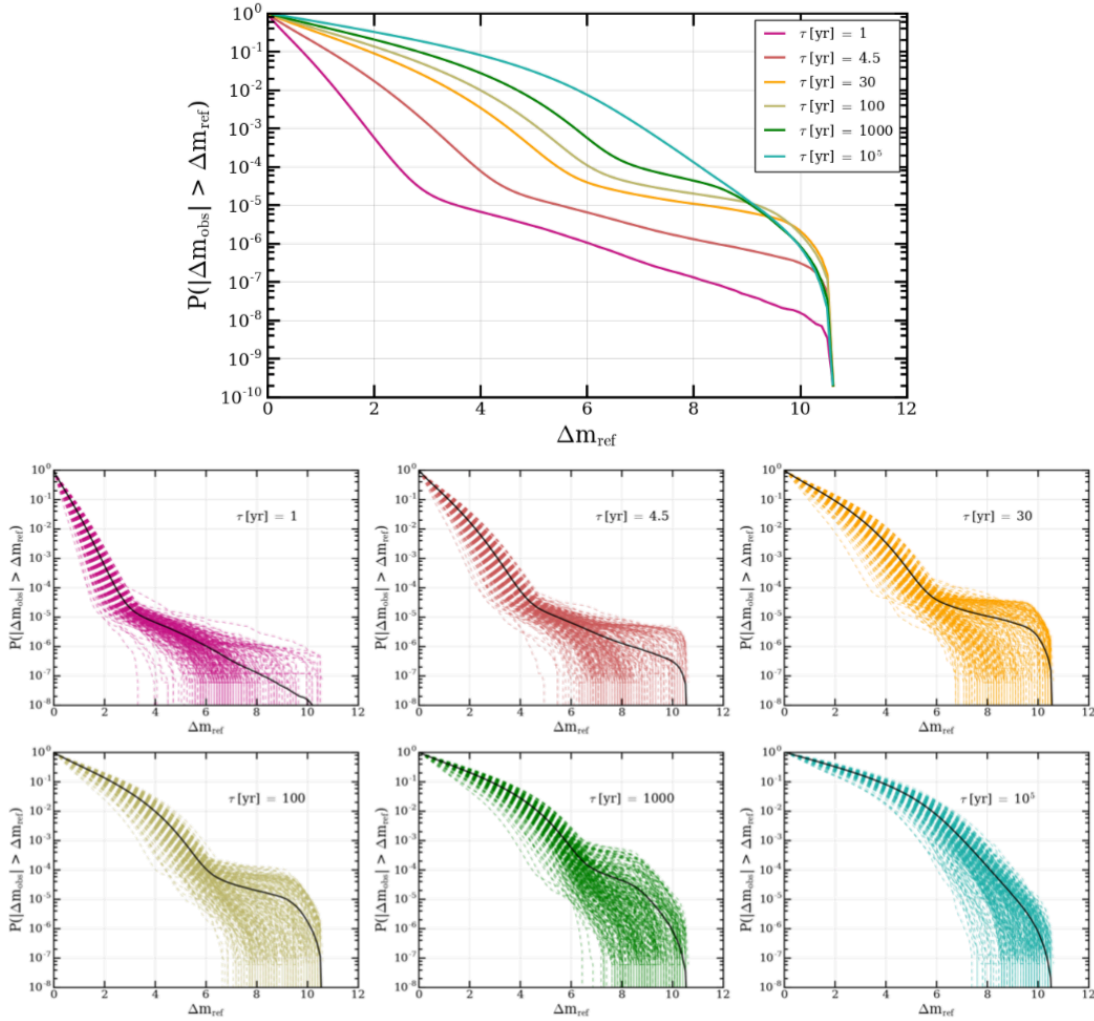


Figure 6.15: Expected distributions of AGN flux variability. We show the calculated probability of a simulated quasar, drawn from our reference simulation, to undergo a change in magnitude $|\Delta m| > \Delta m_{\text{ref}}$ between two epochs separated by τ (in the intrinsic/rest frame; see Section 6.3.1 and Section 6.3.2). The small panels below show the analysis for the different τ separately, where the coloured lines are the different realisations and the black lines show the mean trends. The large panel summarises the mean trends for all the considered τ . We note that at the redshift assumed for the reference simulation, $z = 1.3$, an intrinsic $\tau_{\text{int}} = 4.5$ yr corresponds to an observed $\tau_{\text{obs}} \sim 10$ yr, i.e. the foreseen length of the LSST main survey. Since in general the probability of the AGN undergoing a given $|\Delta m|$ decreases with decreasing τ , for every possible τ probed by LSST the probability of the AGN to undergo a given $|\Delta m|$ is lower than what found for $\tau_{\text{int}} = 4.5$ yr. We caution that this figure is for illustrative purpose only. A more complete analysis which takes into account the specifics of the surveys as well as other computational effects (see text) have to be performed in order to compare the observed rates to the simulations.

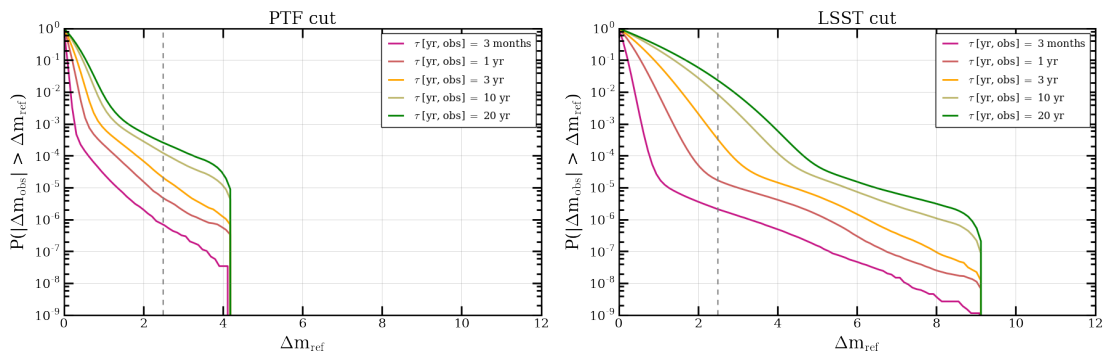


Figure 6.16: Similar to Fig. 6.15, but here τ is given in the observer frame, and taking into account different magnitude cuts (left: PTF flux limit, right: LSST limit). The grey dashed lines mark a change of $\Delta m_{\text{ref}} = 2.5$ (i.e., a $\times 10$ change in flux or luminosity).

6.4 Summary and conclusions

We presented a framework designed to model AGN variability over a broad range of timescales and in different objects, based on the observed Eddington ratio distribution among the AGN population. The framework was initially proposed in Chapter 5. In this Chapter we discuss in detail the fundamental assumptions of the framework; its implementation using GPU architecture; and various simulations that test and characterise both the intrinsic and numerical behaviour of our implementation. We then demonstrate several possible applications of the framework, based on the observed variability in the PTF/iPTF survey, with the aim to interpret the light curves expected to be observed with the LSST, and the prospects of discovering extremely variable AGN in up-coming time-domain surveys.

The central points of our framework can be summarised as follows:

- We propose that AGN light curves can be modeled starting from the distribution of the L/L_{Edd} among the galaxy population. Specifically, we assume that the distribution of L/L_{Edd} covered by an AGN during his lifetime is consistent with the ERDF of the galaxy population, and that the variability behaviour is described by a PSD which is similar for all the AGN.
- This implies that the variety of AGN variability features observed in different AGN arises from the fact that every AGN is a different realisation of the same underlying process (here described by the PSD and the ERDF), and that the observed period is much shorter than the AGN lifetime¹⁷.
- The primary output of our simulations are L/L_{Edd} time series, which can be con-

¹⁷This can be thought of as following the ergodic hypothesis for test particles.

Chapter 6. A forward modelling approach to AGN variability – method description and early applications

verted to light curves and other observables in post processing. This requires taking into account both the AGN physics (e.g. different bolometric corrections) as well as properties of the observations (e.g. flux limits and sample selection).

In order to perform the simulations we implemented the iteration algorithm from [E13](#) to run on a GPU architecture:

- Thanks to the CUDA environment, our GPU implementation allows us to maximise the performance both in terms of length of the simulation (up to $\sim 10^8$ points) and speed (\sim minutes for the longest simulations).
- The code is optimised for broken power-law or log-normal PDFs and broken power-law PSDs, however different functional forms can be added.
- By construction, the PDF and the periodogram of the final light curves are consistent with the input PDF and PSD. On the other hand, the normalisation of the correspondent SF depends on the physical length (e.g. in yr) of the simulated light curve.

As an example application, we looked for a model (i.e. input set) consistent with the variability behaviour observed in the PTF/iPTF sample ([C17](#)), and used it to simulate possible light curves, of the kind that are expected to be observed with LSST:

- After taking into account sample selection and flux limit, we found that the PTF/iPTF ensemble SF is consistent with simulations performed assuming the ERDF proposed in [W17](#) and [C17](#), and a broken power-law PSD characterised by a random walk at low frequencies and a break at ~ 30 yr. In this case, the time needed for the AGN to span the entire ERDF is ~ 1.4 Myr.
- We showed that the ensemble SF computed by including only light curve points above the PTF flux limit has a lower normalisation (and therefore a lower overall variability) compared to the SF computed by considering the entire simulated light curve. This is consistent with observations showing that the amplitude of variability is anti-correlated with the AGN luminosity and/or Eddington ratio (e.g. [MacLeod et al. 2010](#); [C17](#); [Rumbaugh et al. 2018](#))
- The simulated LSST light curves show that the same AGN can experience a variety of rather extreme variability features as “switch on”, “switch off”, and year-long “flares”, in addition to prolonged periods of much more subtle variability. Naturally, since the foreseen observations span much shorter periods than the AGN life-time, not all these features are observed for each AGN.

- We expect that the framework presented here would become highly valuable for understanding whether any observed variability feature is consistent with the general behaviour of the AGN population (i.e. if it can be reproduced with our general model), and for constraining the intrinsic variability from artefacts due to, e.g., sample selections and observational cadence.
- Our framework provides a forward-modelling approach that can be used to compare results of different time-domain surveys, for “normal” AGN variability, extreme variability events, and, with suitable adaptations, for the variability of other astrophysical sources.

6.A Appendix: Definitions

In this Appendix we define some important quantities used in our analysis, and discuss how they are related: time series, power spectral density, periodogram and structure function.

A time series corresponds to a single realisation of an underlying power spectral density (PSD) and probability density function (PDF). Given a time series $x(t_k)$, $k = 1, 2, \dots, N$, the statistical estimator of the underlying PSD is called periodogram $P(f_j)$ and is computed based on Fourier analysis.

Let's assume a time series $x(t_k)$, $k = 1, 2, \dots, N$, with N_{steps} equidistant observations with sampling period $t_k - t_{k-1} = t_{\text{bin}}$. Depending on the study, the quantity x can correspond e.g. to luminosity, magnitude, counts rate or Eddington ratio. The discrete Fourier transform (DFT) of $x(t_k)$ is given by:

$$DFT(f_j) = \sum_{k=1}^N x(t_k) e^{2\pi i(k-1)j/N} \quad (6.9)$$

where f_j , $j = 0, 1, \dots, N - 1$, are the Fourier frequencies which depend on the parity of N_{steps} :

N_{steps} even

- $f_j^+ = j/(Nt_{\text{bin}})$ for $j = 1, \dots, N/2 - 1$
- $f_{N/2} = f_{\text{Nyq}} = 1/(2t_{\text{bin}})$ for $j = N/2$
- $f_j^- = -(N - j)/(Nt_{\text{bin}})$ for $j = N/2 + 1, \dots, N - 1$

N_{steps} odd

- $f_j^+ = j/(Nt_{\text{bin}})$ for $j = 1, \dots, (N - 1)/2$
- $f_j^- = -(N - j)/(Nt_{\text{bin}})$ for $j = (N + 1)/2, \dots, N - 1$

The periodogram $P(f_j)$ is then computed from the DFT (up to a normalisation constant depending on the convention used):

$$P(f_j) = \frac{2}{N^2} \{ \text{Re} [DFT(f_j)]^2 + \text{Im} [DFT(f_j)]^2 \} \quad (6.10)$$

where $j = 0, 1, \dots, N/2$ for even N_{steps} and $j = 0, 1, \dots, (N - 1)/2$ for odd N_{steps} .

The units of the PSD, and consequently of its estimator $P(f_j)$, are [power/Hz], so that the integral of the PSD is proportional to the total power in the process:

$$\text{total power} \propto \int_0^\infty \text{PSD}(f)df \quad (6.11)$$

For a given frequency f_i , $\text{PSD}(f_i)$ is therefore proportional to the power of variations with frequency f_i .

One of the most widely used PSD normalisations is the fractional rms normalisation defined by [van der Klis \(1997\)](#) (see also [Miyamoto et al. 1991](#); [Vaughan et al. 2003](#)):

$$P_{\text{rms}}(f_j) = \frac{2t_{\text{bin}}}{\mu^2 N} \{ \text{Re} [DFT(f_j)]^2 + \text{Im} [DFT(f_j)]^2 \} \quad (6.12)$$

where μ is the mean value of the time series. With this normalisation the integral of the underlying PSD_{rms} between two frequencies f_i and f_j , $i < j$ corresponds to the contribution of the frequency window $[f_i, f_j]$ to the total rms squared variability σ^2/μ^2 . The total rms squared variability can be obtained by integrating between f_1 and f_{max} , where $f_{\text{max}} = f_{N/2} = f_{\text{Nyq}}$ for even N_{steps} and $f_{\text{max}} = f_{(N-1)/2}$ for odd N_{steps} :

$$\frac{\sigma^2}{\mu^2} = \int_{f_1}^{f_{\text{max}}} \text{PSD}_{\text{rms}}(f)df. \quad (6.13)$$

An alternative way to characterise the variability in a given time series is to construct the structure function (SF), which quantifies the amount of variability in the data for a given timescale. We stress that different definitions are present in the literature (e.g. [MacLeod et al. 2012](#); [Kozłowski 2016](#)), so that caution has to be used when comparing SF obtained in different studies. In this work, for a time series $x(t_k)$ as defined above and a given time lag τ , we adopt the following SF formulation:

$$SF(\tau)^2 = \frac{1}{P} \sum_{i,j>i} [x(t_i) - x(t_j)]^2 = \langle [x(t) - x(t + \tau)]^2 \rangle \quad (6.14)$$

Chapter 6. A forward modelling approach to AGN variability – method description and early applications

where $t_j - t_i = \tau$ and P is the number of $\{x(t_i), x(t_j)\}$ pairs, mostly in L/L_{Edd} or mag units ($x(t_k)$ are the observed or simulated L/L_{Edd} and light curves).

In the case of a zero mean stationary time series with f varying between 0 and ∞ , a power-law PSD with slope $-\alpha$, $1 < \alpha < 3$, corresponds to a power-law SF with slope $\beta = (\alpha - 1)/2$, where $\tau = 1/f$ (e.g. [Emmanoulopoulos et al. 2010](#)). This is a direct consequence of the Wiener-Khinchin theorem. However, the analytical relationship between PSD and SF for the general case is not clear yet.

7 Conclusions

*Laudato sie, mi' Signore, cum tucte le tue creature.*¹

Laudes Creaturarum, San Francesco D'Assisi (1224)

7.1 Summary

The work presented in this thesis combines multiwavelength observations of single active galactic nuclei (AGN) host galaxies, phenomenological models describing the general behaviour of the AGN population, and simulations of AGN light curves, to investigate AGN variability on multiple timescales.

The thesis is composed by two different but related parts, one more focussed on observational data analysis, the other aimed at developing a novel unifying framework to address AGN variability related questions.

In the first part (Chapter 2 and Chapter 3) we concentrated on AGN variability on very long, $\gtrsim 10^4$ yr timescales. Specifically we wanted to investigate the questions: **Are the Voorwerpjes galaxies the right laboratory to study AGN variability on super-human timescales? If yes, what do they tell us about AGN variability and its effect on the host galaxy?**

Using new dedicated hard X-ray data (P.I. L. Sartori) combined with archival observations, we confirmed that the AGN in IC 2497, the prototypical Voorwerpjes system, significantly dropped in luminosity and, most likely, in accretion rate, in the last $\sim 10^5$ yr, and is currently at the end of an accretion phase. This makes it an interesting system to study long timescales variability (Sartori et al. 2016; Sartori et al. 2018a). Our analysis also suggests that the fading AGN is (or was) affecting its surroundings by injecting mechanical energy and producing a bubble or cavity in the hot gas around it, in a similar way as observed both in X-ray binaries, the stellar-mass analogues of AGN (e.g. Pakull et al. 2010, see Chapter 1.1.2), as well as, at much larger spatial scales, in galaxy clusters (e.g. Birzan et al. 2004). These findings support the idea that AGN may behave like

¹*Be praised, my Lord, through all your creatures* (Canticle of the Sun, Saint Francis of Assisi, 1224).

Chapter 7. Conclusions

a scaled-up version of X-ray binaries (e.g. [Ruan et al. 2019](#)), i.e. that the physics of accreting black holes is similar over a wide range of black hole masses (from $\sim 10 M_{\odot}$ to $\sim 10^9 M_{\odot}$), and that the difference in timescales at which X-ray binaries and AGN vary is mostly due to the different masses that affect e.g. the viscous timescales.

Although the mechanical energy currently associated to the bubble in IC 2497 is not enough to overcome the galaxy’s binding energy, a repeated injection due to multiple AGN accretion phases, as proposed in [Schawinski et al. \(2015\)](#), could affect the nuclear hot gas reservoir, therefore reducing nuclear star formation and affecting the host galaxy evolution. The study of galaxies hosting fading AGN is therefore crucial for our understanding of the AGN-host galaxy interaction, as it is in this phase that the AGN may exert mechanical work on his host. Voorwerpjes galaxies hosting switching off AGN, as found in IC 2497, are therefore unique systems to study the AGN-host galaxy interaction in the interesting “post quasar phase”, as the extended gas is the only probe of the past quasar activity (as opposed to X-ray binaries where the cycles can be followed on human timescales).

The studies that we performed on IC 2497 confirmed that the Voorwerpjes galaxies are the right laboratory to investigate long timescales AGN variability and its effect on the host galaxy, but also highlight how multiwavelength (and multi-instrumental) observations are crucial to reach these results. Motivated by these findings, we started three large observational programs (P.I. L. Sartori and K. Schawinski) aimed at obtaining a multiwavelength dataset for the Voorwerpjes sample. Specifically, hard X-ray observations from *NuSTAR*, combined with archival soft X-ray spectra e.g. from *Chandra* and *XMM-Newton* are needed to probe the current intrinsic AGN luminosity; spatially resolved (IFU) spectroscopy from MUSE allows us to constrain the effect of the AGN on the photoionisation state of the gas at different distances from the center, and therefore reconstruct historical AGN light curves; finally, radio imaging from the VLA is valuable for investigating the environment of the Voorwerpjes galaxies (e.g. the presence of large scale gas reservoirs) and the sample selection. In Chapter 4 we presented an overview of the obtained data, together with a pilot study for the light curve reconstruction technique (from [Treister et al. 2018](#)) and an outline of other possible uses of this very rich and valuable dataset.

It is important to stress that, despite confirming its relevance in the study of long timescales AGN variability, the AGN in IC 2497 turned out to be not as extreme as previously thought. Indeed, previous studies claimed drops in luminosity up to four orders of magnitude (e.g. [Lintott et al. 2009](#); [Schawinski et al. 2010a](#)), while our new analysis constrained the drop to be of a factor ~ 50 . Nevertheless, in the second part of the thesis we showed that the Voorwerpjes systems will be crucial to constrain the general AGN variability behaviour using our new unifying approach, as they provide the only (indirect) observational probe of long timescales variability, which is still poorly understood but needed to link variability at different timescales. They are therefore important in a more general (population) sense.

In the second part of the thesis we addressed the questions: **Is it possible to find a (simple) model which allows us to simultaneously explain the AGN variability features observed in different galaxies at different timescales? If yes, how can it be used to plan and best exploit the upcoming time-domain era?**

In Chapter 5 we presented a simple framework aimed at simulating AGN light curves based on the distribution of Eddington ratios among the galaxy population, therefore linking the behaviour of single AGN to the AGN population. In this context, we proposed that the variety of AGN variability features observed in different AGN arises from the fact that every AGN is a *different (unique) realisation of the same underlying process*, and that the observed periods (i.e. the length of the observed light curves) are much shorter than the AGN lifetimes. Indeed, in Chapter 6 we showed that, assuming a model consistent with the ensemble variability behaviour observed in the PTF/iPTF sample (from Caplar et al. 2018), we are able to simulate AGN light curves which, throughout their lifetime, experience both rather extreme variability events such as “switch on”, “switch off”, and year-long “flares”, as well as prolonged periods of much more subtle variability. Which of these features is recorded in the observed light curves finally depends on the time and length of the observations. This framework therefore represents a novel “unifying” approach to AGN variability which, differently from the majority of studies in the literature, allows us to simultaneously investigate the different variability features observed in specific objects, the general behaviour of the AGN population, as well as variability at very different timescales.

Although the algorithm used for our light curve simulations is quite simple, the need of producing very long AGN light curves (i.e. spanning the whole AGN lifetime with a resolution comparable to real observations) required a significant computational effort. In Chapter 6 we presented our GPU implementation, which allows us to reach very long timescales (\sim Myr) with a resolution comparable to future time-domain surveys (\sim days). The code will be made public, and will be very valuable both for future AGN studies as well as, with suitable adaptations, for studies of other variable processes such as e.g. stellar variability (e.g. Catelan and Smith 2015; Labadie-Bartz et al. 2017) or star formation histories (e.g. Caplar and Tacchella 2019).

Finally, with the upcome of new time-domain surveys such as e.g. LSST (Ivezic et al. 2008; LSST Science Collaboration et al. 2009), TDSS (Morganson et al. 2015), ZTF (Bellm 2014; Graham et al. 2019a) and eROSITA (Merloni et al. 2012) we are entering an exciting time-domain era which will provide multiwavelength light curves for millions of AGN with unprecedented time resolution and length, allowing us to uncover the details of the AGN physics and accretion process. However, in order to fully exploit these new and rich data, it is important to be able to model the observed variability behaviour, in particular by taking into account the AGN stochasticity as well as observational limitations and setups (e.g. cadence, target selection, flux limit and other observational biases). Our framework is the ideal tool to address these issues, as it allows us to forward model AGN

light curves by taking into account both the AGN intrinsic (stochastic) properties and physics as well as observational biases. This will be highly valuable for the astronomy community both for planning future observing campaigns, as well as for interpreting the observations (as demonstrated in Chapter 6).

In summary, the methods and results presented in this thesis provide a first important step towards *a novel unified approach to AGN variability*. This new approach will be extremely valuable in the upcoming era of time-domain astronomy, in particular as it allows us to link and simultaneously investigate phenomena observed in different galaxies and at very different timescales, that may appear unrelated.

7.2 Future prospects

In Chapter 4 we described how the new data obtained for the Voorwerpjes sample can be used to constrain AGN variability on super-human timescales. These measurements, together with observations arising from new time-domain surveys, will allow us to constrain our AGN variability models, and therefore produce physically motivated AGN light curves to be used for further studies. In the last part of this thesis we outline some future prospects for our framework.

7.2.1 Modelling the variable Universe in the time-domain era

As explained in the previous chapters, our framework will be extremely valuable for forward modelling, and therefore interpreting, AGN light curves observed in future time-domain surveys. Some early applications in this regard are already presented in Chapter 6. The potential of this framework is however very rich.

As an example, our simulations can be used to disentangle the transient behaviour due to tidal disruption events (TDE) from the intrinsic stochastic AGN variability, and investigate the TDE contribution to the total variability and BH growth. By adding TDE-like flares (e.g. Rees 1988; Hung et al. 2017) to simulated light curves (from stochastic behaviour) it will be possible to quantify the effect of a given frequency of TDE on the observed structure function and/or power spectral density, therefore constraining the possible frequency of these events. Moreover, by comparing the light curves of TDE candidates to the ones simulated taking into account the stochastic behaviour only, it will be possible to understand if the observed feature is consistent with being a flare expected from the intrinsic AGN variability behaviour, or if it is a real transient event of external nature (in this case a TDE).

Our simulations will also provide an alternative approach to investigate the relation between optical/UV variability and X-ray variability. Specifically, this could be done by first simulating light curves consistent with observations in one band (e.g. optical/UV

from LSST) and then testing different recipes to convert them to light curves consistent with the ones observed at other wavelengths (e.g. X-ray from eROSITA). By considering different physical assumptions such as bolometric corrections, reprocessing models and reprocessing timescales, this analysis will provide significant insights into the interplay between different AGN component, e.g. between the accretion disc seed photons and the postulated X-ray emitting corona.

Finally, as outlined in Chapter 6, it will be possible to investigate if changing-look AGN (CL-AGN) constitute a separate population, or if their large flux change on short timescales is expected by the general variability behaviour of the AGN population. With our model it will be possible to predict the distribution of flux changes at a given timescale, by taking into account both the intrinsic AGN behaviour as well as observational biases. By comparing the numbers of observed sources in a sample undergoing a given flux change (e.g. the CL-AGN in TDSS) with the numbers predicted by our models, it will be possible to understand if CL-AGN are a separate AGN class. This information will be valuable for our understanding of the AGN variability phenomenon, as well as for (theoretical) studies of accretion disc physics. Indeed, if every AGN may in principle experience a changing-look phase (or changing-*state* phase, as recently proposed by [Graham et al. 2019b](#)), then the same accretion disc should allow both “standard” AGN variability as well as the extreme variability observed in CL-AGN.

7.2.2 AGN variability in the context of galaxy evolution and cosmological simulations

As explained in Chapter 1.2, the study of AGN feedback is complicated by the fact that the energy injection from the AGN varies on timescales which are much shorter than the timescales needed for the galaxy to react (e.g. [Hickox et al. 2014](#)). This means that the traditional approach of studying the AGN-host galaxy relations by taking a sample of AGN host galaxies and comparing its properties (e.g. star formation rate, SFR) to these of a sample of quiescent galaxies will not succeed as the current AGN may not be responsible for e.g. the current SFR in the galaxy.

A complementary way to study the effect of AGN on the host galaxies is through simulations, where the evolution of the SMBH is traced at the same time as the host galaxy properties, while accounting for the needed “reprocessing” timescales. However, current hydrodynamical (and other) simulations only implement limited accretion recipes, and additionally do not have the high spatial resolution needed to reliably model the AGN variability (e.g. [Negri and Volonteri 2017](#)).

One of the products of our framework are “physically motivated” light curves. It will therefore be possible to include the obtained AGN light curves in existing galaxy evolution simulations (e.g. from RAMSES, [Teyssier 2002](#)) to investigate the effect of a variable

AGN on the host galaxy, depending on both the AGN variability behaviour and the galaxy properties. Specifically, we propose to include our AGN light curves in hydrodynamical simulations to simulate e.g. the spatially resolved AGN photoionisation as a function of time. By using different galaxy snapshots (i.e. different gas distributions) as initial conditions, this study will allow us to investigate questions such as: how does the photoionisation front expand for different AGN light curves and galaxy conditions? Can we predict in which galaxies we expect to detect AGN undergoing a given variability behaviour (e.g. switching on/off AGN or CL-AGN)? Can we reproduce the large scatter found e.g. in the relations between X-ray and [O III] luminosities ($L_{X\text{-ray}} - L_{[\text{O III}]}$, e.g. [Berney et al. 2015](#)) or between [O III] luminosity and NLR size ($L_{[\text{O III}]} - R_{\text{NLR}}$, e.g. [Bennert et al. 2002](#)) by taking into account the fact that the AGN is varying in time? Or also, when and how does the AGN affect the SFR?

7.2.3 Cosmic black hole mass growth

Active SMBHs have been found up to $z \sim 7.5$, which corresponds to less than ~ 1 Gyr after the Big Bang (e.g. [Mortlock et al. 2011](#); [Bañados et al. 2018](#)). It is however still not clear how their mass is accumulated during cosmic time. As an example, the often assumed exponential growth models, which imply a constant Eddington ratio and radiative efficiency (e.g. [Trakhtenbrot et al. 2016](#)), are not able to reproduce the fast growth at high-redshift and slow growth at low-redshift expected e.g. from the shape of the black hole accretion rate density, which peaks at $z \sim 1 - 2$ and decreases towards $z \sim 0$ (e.g. [Madau and Dickinson 2014](#) and references therein, Chapter 1.2).

Our framework may be very valuable for simulating and investigating the evolution of BH mass during cosmic time starting from the AGN variability behaviour. Indeed, the primary output of our simulations are Eddington ratio time series which, under some assumption about the radiative efficiency η and the initial BH mass, can be converted to mass accretion curves $\dot{m}_{\text{BH}}(t)$ and BH mass curves $M_{\text{BH}}(t)$.

It is important to stress that our current framework is optimised for a constant (in time) ERDF, which is a sensible assumption for simulations spanning $\sim \text{Myr}$ or less (as it is the case in our early applications). However, as showed e.g. in [Caplar et al. \(2018\)](#), the ERDF is expected to evolve with redshift (at least up to ~ 2), with higher λ^* at higher redshift. Including this redshift dependence is a promising future extension of our framework, which will allow us to simulate the ~ 10 Gyr long light curves needed to trace SMBH growth across cosmic time.

In addition to improving our understanding of the AGN variability for linking AGN variability to the overall SMBH growth, and therefore investigate the evolution of SMBHs over cosmic time in a novel way.

Bibliography

- K. N. Abazajian, J. K. Adelman-McCarthy, M. A. Agüeros, et al. The Seventh Data Release of the Sloan Digital Sky Survey. *apjs*, 182:543, June 2009. doi: 10.1088/0067-0049/182/2/543.
- Y. L. Ai, W. Yuan, H. Y. Zhou, et al. Dependence of the Optical/Ultraviolet Variability on the Emission-line Properties and Eddington Ratio in Active Galactic Nuclei. *ApJ*, 716:L31–L35, June 2010. doi: 10.1088/2041-8205/716/1/L31.
- J. Aird, A. L. Coil, J. Moustakas, et al. PRIMUS: The Dependence of AGN Accretion on Host Stellar Mass and Color. *ApJ*, 746:90, Feb. 2012. doi: 10.1088/0004-637X/746/1/90.
- J. Aird, A. L. Coil, & A. Georgakakis. X-rays across the galaxy population - III. The incidence of AGN as a function of star formation rate. *ArXiv e-prints*, Oct. 2018.
- D. M. Alexander, & R. C. Hickox. What drives the growth of black holes? *New A Rev.*, 56:93–121, June 2012. doi: 10.1016/j.newar.2011.11.003.
- J. R. Allison, E. M. Sadler, & A. M. Meekin. A search for H I absorption in nearby radio galaxies using HIPASS. *MNRAS*, 440:696–718, May 2014. doi: 10.1093/mnras/stu289.
- O. Almaini, A. Lawrence, T. Shanks, et al. X-ray variability in a deep, flux-limited sample of QSOs. *MNRAS*, 315:325–336, June 2000. doi: 10.1046/j.1365-8711.2000.03385.x.
- R. Antonucci. Unified models for active galactic nuclei and quasars. *araa*, 31:473–521, 1993. doi: 10.1146/annurev.aa.31.090193.002353.
- R. R. J. Antonucci, & J. S. Miller. Spectropolarimetry and the nature of NGC 1068. *apj*, 297:621–632, Oct. 1985. doi: 10.1086/163559.
- I. Arcavi, A. Gal-Yam, M. Sullivan, et al. A Continuum of H- to He-rich Tidal Disruption Candidates With a Preference for E+A Galaxies. *ApJ*, 793:38, Sept. 2014. doi: 10.1088/0004-637X/793/1/38.
- I. Aretxaga, R. Cid Fernandes, & R. J. Terlevich. QSO variability: probing the starburst model. *MNRAS*, 286:271–283, Apr. 1997. doi: 10.1093/mnras/286.2.271.

Bibliography

- I. Aretxaga, B. Joguet, D. Kunth, J. Melnick, & R. J. Terlevich. Seyfert 1 Mutation of the Classical Seyfert 2 Nucleus NGC 7582. *ApJ*, 519:L123–L126, July 1999. doi: 10.1086/312114.
- K. A. Arnaud. XSPEC: The First Ten Years. In G. H. Jacoby, & J. Barnes, editors, *Astronomical Data Analysis Software and Systems V*, volume 101 of *Astronomical Society of the Pacific Conference Series*, page 17, 1996.
- D. Asmus, P. Gandhi, S. F. Hönic, A. Smette, & W. J. Duschl. The subarcsecond mid-infrared view of local active galactic nuclei - II. The mid-infrared-X-ray correlation. *MNRAS*, 454:766–803, Nov. 2015. doi: 10.1093/mnras/stv1950.
- R. J. Assef, J. L. Prieto, D. Stern, et al. Mid-IR Variability of Quasars and A Luminous Transient Event in A WISE-Selected AGN. *ArXiv e-prints*, July 2018.
- K. Auchettl, E. Ramirez-Ruiz, & J. Guillochon. Comparison of the X-ray emission from Tidal Disruption Events with those of Active Galactic Nuclei. *ArXiv e-prints*, Mar. 2017.
- E. Bañados, C. Carilli, F. Walter, et al. A Powerful Radio-loud Quasar at the End of Cosmic Reionization. *ApJ*, 861:L14, July 2018. doi: 10.3847/2041-8213/aac511.
- R. Bacon, M. Accardo, L. Adjali, et al. The MUSE second-generation VLT instrument. In *Ground-based and Airborne Instrumentation for Astronomy III*, volume 7735 of *Proc. SPIE*, page 773508, July 2010. doi: 10.1117/12.856027.
- S. A. Balbus, & J. F. Hawley. A powerful local shear instability in weakly magnetized disks. I - Linear analysis. II - Nonlinear evolution. *ApJ*, 376:214–233, July 1991. doi: 10.1086/170270.
- J. A. Baldwin, M. M. Phillips, & R. Terlevich. Classification parameters for the emission-line spectra of extragalactic objects. *pasj*, 93:5–19, Feb. 1981. doi: 10.1086/130766.
- J. E. Barnes, & L. E. Hernquist. Fueling starburst galaxies with gas-rich mergers. *ApJ*, 370:L65–L68, Apr. 1991. doi: 10.1086/185978.
- S. D. Barthelmy, L. M. Barbier, J. R. Cummings, et al. The Burst Alert Telescope (BAT) on the SWIFT Midex Mission. *Space Sci. Rev.*, 120:143–164, Oct. 2005. doi: 10.1007/s11214-005-5096-3.
- I. Bartos, B. Kocsis, Z. Haiman, & S. Márka. Rapid and Bright Stellar-mass Binary Black Hole Mergers in Active Galactic Nuclei. *ApJ*, 835:165, Feb. 2017. doi: 10.3847/1538-4357/835/2/165.
- R. Barvainis. Hot dust and the near-infrared bump in the continuum spectra of quasars and active galactic nuclei. *ApJ*, 320:537–544, Sept. 1987. doi: 10.1086/165571.

- K. Bekki, & Y. Shioya. On the degree of dust extinction in major galaxy mergers with dusty starburst. *A&A*, 362:97–104, Oct. 2000.
- F. Belfiore, R. Maiolino, K. Bundy, et al. P-MaNGA Galaxies: emission-lines properties - gas ionization and chemical abundances from prototype observations. *MNRAS*, 449: 867–900, May 2015. doi: 10.1093/mnras/stv296.
- E. Bellm. The Zwicky Transient Facility. In P. R. Wozniak, M. J. Graham, A. A. Mahabal, & R. Seaman, editors, *The Third Hot-wiring the Transient Universe Workshop*, pages 27–33, 2014.
- E. C. Bellm, S. R. Kulkarni, M. J. Graham, et al. The Zwicky Transient Facility: System Overview, Performance, and First Results. *PASP*, 131(1):018002, Jan. 2019. doi: 10.1088/1538-3873/aacbe.
- N. Bennert, H. Falcke, H. Schulz, A. S. Wilson, & B. J. Wills. Size and Structure of the Narrow-Line Region of Quasars. *ApJ*, 574:L105–L109, Aug. 2002. doi: 10.1086/342420.
- S. Berney, M. Koss, B. Trakhtenbrot, et al. BAT AGN spectroscopic survey-II. X-ray emission and high-ionization optical emission lines. *MNRAS*, 454:3622–3634, Dec. 2015. doi: 10.1093/mnras/stv2181.
- C. Bertemes, B. Trakhtenbrot, K. Schawinski, C. Done, & M. Elvis. Testing the completeness of the SDSS colour selection for ultramassive, slowly spinning black holes. *MNRAS*, 463:4041–4051, Dec. 2016. doi: 10.1093/mnras/stw2207.
- S. Bianchi, M. Guainazzi, & M. Chiaberge. The soft X-ray/NLR connection: a single photoionized medium? *A&A*, 448:499–511, Mar. 2006. doi: 10.1051/0004-6361:20054091.
- L. Birzan, D. A. Rafferty, B. R. McNamara, M. W. Wise, & P. E. J. Nulsen. A Systematic Study of Radio-induced X-Ray Cavities in Clusters, Groups, and Galaxies. *ApJ*, 607: 800–809, June 2004. doi: 10.1086/383519.
- K. Bischoff, & W. Kollatschny. Strong optical line variability in MKN 110. *A&A*, 345: 49–58, May 1999.
- J. Bland-Hawthorn, P. R. Maloney, R. S. Sutherland, & G. J. Madsen. Fossil Imprint of a Powerful Flare at the Galactic Center along the Magellanic Stream. *ApJ*, 778:58, Nov. 2013. doi: 10.1088/0004-637X/778/1/58.
- R. D. Blandford, & D. G. Payne. Hydromagnetic flows from accretion discs and the production of radio jets. *MNRAS*, 199:883–903, June 1982. doi: 10.1093/mnras/199.4. 883.
- A. Bongiorno, A. Schulze, A. Merloni, et al. AGN host galaxy mass function in COSMOS. Is AGN feedback responsible for the mass-quenching of galaxies? *A&A*, 588:A78, Apr. 2016. doi: 10.1051/0004-6361/201527436.

Bibliography

- F. Bournaud, A. Dekel, R. Teyssier, et al. Black Hole Growth and Active Galactic Nuclei Obscuration by Instability-driven Inflows in High-redshift Disk Galaxies Fed by Cold Streams. *ApJ*, 741:L33, Nov. 2011. doi: 10.1088/2041-8205/741/2/L33.
- M. Brightman, & K. Nandra. An XMM-Newton spectral survey of 12 μm selected galaxies - I. X-ray data. *MNRAS*, 413:1206–1235, May 2011. doi: 10.1111/j.1365-2966.2011.18207.x.
- G. Bruzual, & S. Charlot. Stellar population synthesis at the resolution of 2003. *mnras*, 344:1000–1028, Oct. 2003. doi: 10.1046/j.1365-8711.2003.06897.x.
- D. Burlon, M. Ajello, J. Greiner, et al. Three-year Swift-BAT Survey of Active Galactic Nuclei: Reconciling Theory and Observations? *ApJ*, 728:58, Feb. 2011. doi: 10.1088/0004-637X/728/1/58.
- L. Burtscher, K. Meisenheimer, K. R. W. Tristram, et al. A diversity of dusty AGN tori. Data release for the VLTI/MIDI AGN Large Program and first results for 23 galaxies. *A&A*, 558:A149, Oct. 2013. doi: 10.1051/0004-6361/201321890.
- Z. Cai, Y. Sun, J. Wang, et al. New clues to jet launching: The inner disks in radio loud quasars may be more stable. *Science China Physics, Mechanics, and Astronomy*, 62: 69511, June 2019. doi: 10.1007/s11433-018-9330-4.
- D. Calzetti, L. Armus, R. C. Bohlin, et al. The Dust Content and Opacity of Actively Star-forming Galaxies. *ApJ*, 533:682–695, Apr. 2000. doi: 10.1086/308692.
- M. Cano-Díaz, R. Maiolino, A. Marconi, et al. Observational evidence of quasar feedback quenching star formation at high redshift. *A&A*, 537:L8, Jan. 2012. doi: 10.1051/0004-6361/201118358.
- D. M. Capellupo, H. Netzer, P. Lira, B. Trakhtenbrot, & J. Mejía-Restrepo. Active galactic nuclei at z 1.5 - I. Spectral energy distribution and accretion discs. *MNRAS*, 446:3427–3446, Feb. 2015. doi: 10.1093/mnras/stu2266.
- A. Capetti, D. J. Axon, F. Macchetto, W. B. Sparks, & A. Boksenberg. Radio Outflows and the Origin of the Narrow-Line Region in Seyfert Galaxies. *ApJ*, 469:554, Oct. 1996. doi: 10.1086/177804.
- J. Caplan, & L. Deharveng. Extinction and reddening of H II regions in the Large Magellanic Cloud. *A&A*, 155:297–313, Feb. 1986.
- N. Caplar, & S. Tacchella. Stochastic modeling of star-formation histories I: the scatter of the star-forming main sequence. *arXiv e-prints*, Jan. 2019.
- N. Caplar, S. J. Lilly, & B. Trakhtenbrot. AGN Evolution from a Galaxy Evolution Viewpoint. *ApJ*, 811:148, Oct. 2015. doi: 10.1088/0004-637X/811/2/148.

- N. Caplar, S. J. Lilly, & B. Trakhtenbrot. Optical Variability of AGNs in the PTF/iPTF Survey. *ApJ*, 834:111, Jan. 2017. doi: 10.3847/1538-4357/834/2/111.
- N. Caplar, S. J. Lilly, & B. Trakhtenbrot. AGN Evolution from the Galaxy Evolution Viewpoint. II. *ApJ*, 867:148, Nov. 2018. doi: 10.3847/1538-4357/aae691.
- S. Carniani, A. Marconi, R. Maiolino, et al. Ionised outflows in $z \sim 2.4$ quasar host galaxies. *A&A*, 580:A102, Aug. 2015. doi: 10.1051/0004-6361/201526557.
- N. Castelló-Mor, H. Netzer, & S. Kaspi. Super- and sub-Eddington accreting massive black holes: a comparison of slim and thin accretion discs through study of the spectral energy distribution. *MNRAS*, 458:1839–1858, May 2016. doi: 10.1093/mnras/stw445.
- M. Catelan, & H. A. Smith. *Pulsating Stars*. Mar. 2015.
- G. Chabrier. Galactic Stellar and Substellar Initial Mass Function. *PASP*, 115:763–795, July 2003. doi: 10.1086/376392.
- M. Charisi, I. Bartos, Z. Haiman, et al. A population of short-period variable quasars from PTF as supermassive black hole binary candidates. *MNRAS*, 463:2145–2171, Dec. 2016. doi: 10.1093/mnras/stw1838.
- W. Chen, C. R. Shrader, & M. Livio. The Properties of X-Ray and Optical Light Curves of X-Ray Novae. *ApJ*, 491:312–338, Dec. 1997. doi: 10.1086/304921.
- R. Chornock, E. Berger, S. Gezari, et al. The Ultraviolet-bright, Slowly Declining Transient PS1-11af as a Partial Tidal Disruption Event. *ApJ*, 780:44, Jan. 2014. doi: 10.1088/0004-637X/780/1/44.
- Y.-H. Chu, & M.-M. Mac Low. X-rays from superbubbles in the Large Magellanic Cloud. *ApJ*, 365:510–521, Dec. 1990. doi: 10.1086/169505.
- A. O. Clarke, G. Heald, T. Jarrett, et al. LOFAR MSSS: Discovery of a 2.56 Mpc giant radio galaxy associated with a disturbed galaxy group. *A&A*, 601:A25, May 2017. doi: 10.1051/0004-6361/201630152.
- R. D. Cohen, R. J. Rudy, R. C. Puetter, T. B. Ake, & C. B. Foltz. Variability of Markarian 1018 - Seyfert 1.9 to Seyfert 1. *ApJ*, 311:135–141, Dec. 1986. doi: 10.1086/164758.
- S. Connolly. A Python Code for the Emmanoulopoulos et al. [arXiv:1305.0304] Light Curve Simulation Algorithm. *ArXiv e-prints*, Mar. 2015.
- C. Conroy, & M. White. A Simple Model for Quasar Demographics. *ApJ*, 762:70, Jan. 2013. doi: 10.1088/0004-637X/762/2/70.
- M. Coriat, S. Corbel, L. Prat, et al. Radiatively efficient accreting black holes in the hard state: the case study of H1743-322. *MNRAS*, 414:677–690, June 2011. doi: 10.1111/j.1365-2966.2011.18433.x.

Bibliography

- G. Cresci, & R. Maiolino. Observing positive and negative AGN feedback. *Nature Astronomy*, 2:179–180, Feb. 2018. doi: 10.1038/s41550-018-0404-5.
- R. L. Davies, M. Schirmer, & J. E. H. Turner. The ‘Green Bean’ Galaxy SDSS J224024.1-092748: unravelling the emission signature of a quasar ionization echo. *MNRAS*, 449: 1731–1752, May 2015. doi: 10.1093/mnras/stv343.
- J. E. Davis, M. W. Bautz, D. Dewey, et al. Raytracing with MARX: x-ray observatory design, calibration, and support. In *Society of Photo-Optical Instrumentation Engineers (SPIE) Conference Series*, volume 8443 of *Society of Photo-Optical Instrumentation Engineers (SPIE) Conference Series*, page 1, Sept. 2012. doi: 10.1117/12.926937.
- D. De Cicco, M. Paolillo, G. Covone, et al. Variability-selected active galactic nuclei in the VST-SUDARE/VOICE survey of the COSMOS field. *A&A*, 574:A112, Feb. 2015. doi: 10.1051/0004-6361/201424906.
- D. De Cicco, M. Paolillo, S. Falocco, et al. Optically variable active galactic nuclei in the 3 yr VST survey of the COSMOS field. *arXiv e-prints*, May 2019.
- W. H. de Vries, R. H. Becker, & R. L. White. Long-Term Variability of Sloan Digital Sky Survey Quasars. *AJ*, 126:1217–1226, Sept. 2003. doi: 10.1086/377486.
- J. E. Deeter. Techniques for the estimation of red power spectra. II Evaluation of alternative methods. *ApJ*, 281:482–491, June 1984. doi: 10.1086/162122.
- J. E. Deeter, & P. E. Boynton. Techniques for the estimation of red power spectra. I - Context and methodology. *ApJ*, 261:337–350, Oct. 1982. doi: 10.1086/160345.
- C. DeGraf, A. Dekel, J. Gabor, & F. Bournaud. Black hole growth and AGN feedback under clumpy accretion. *ArXiv e-prints*, Dec. 2014.
- K. D. Denney, G. De Rosa, K. Croxall, et al. The Typecasting of Active Galactic Nuclei: Mrk 590 no Longer Fits the Role. *ApJ*, 796:134, Dec. 2014. doi: 10.1088/0004-637X/796/2/134.
- J. Dexter, & E. Agol. Quasar Accretion Disks are Strongly Inhomogeneous. *ApJ*, 727: L24, Jan. 2011. doi: 10.1088/2041-8205/727/1/L24.
- J. Dexter, & M. C. Begelman. Extreme AGN variability: evidence of magnetically elevated accretion? *MNRAS*, 483:L17–L21, Feb. 2019. doi: 10.1093/mnrasl/sly213.
- T. Di Matteo, V. Springel, & L. Hernquist. Energy input from quasars regulates the growth and activity of black holes and their host galaxies. *Nature*, 433:604–607, Feb. 2005. doi: 10.1038/nature03335.
- S. G. Djorgovski, A. J. Drake, A. A. Mahabal, et al. The Catalina Real-Time Transient Survey (CRTS). *arXiv e-prints*, Feb. 2011.

- C. Done, M. Gierliński, & A. Kubota. Modelling the behaviour of accretion flows in X-ray binaries. Everything you always wanted to know about accretion but were afraid to ask. *A&A Rev.*, 15:1–66, Dec. 2007. doi: 10.1007/s00159-007-0006-1.
- A. J. Drake, S. G. Djorgovski, A. Mahabal, et al. First Results from the Catalina Real-Time Transient Survey. *ApJ*, 696:870–884, May 2009. doi: 10.1088/0004-637X/696/1/870.
- A. J. Eckersall, S. Vaughan, & G. A. Wynn. Evidence for changes in the radiative efficiency of transient black hole X-ray binaries. *MNRAS*, 450:3410–3417, July 2015. doi: 10.1093/mnras/stv739.
- A. Einstein. Die Feldgleichungen der Gravitation. *Sitzungsberichte der Königlich Preussischen Akademie der Wissenschaften (Berlin)*, Seite 844-847., 1915.
- M. Elitzur. On the Unification of Active Galactic Nuclei. *ApJL*, 747:L33, Mar. 2012. doi: 10.1088/2041-8205/747/2/L33.
- M. Elitzur, L. C. Ho, & J. R. Trump. Evolution of broad-line emission from active galactic nuclei. *MNRAS*, 438:3340–3351, Mar. 2014. doi: 10.1093/mnras/stt2445.
- M. Elvis, B. J. Wilkes, J. C. McDowell, et al. Atlas of quasar energy distributions. *ApJS*, 95:1–68, Nov. 1994. doi: 10.1086/192093.
- D. Emmanoulopoulos, I. M. McHardy, & P. Uttley. On the use of structure functions to study blazar variability: caveats and problems. *MNRAS*, 404:931–946, May 2010. doi: 10.1111/j.1365-2966.2010.16328.x.
- D. Emmanoulopoulos, I. M. McHardy, & I. E. Papadakis. Generating artificial light curves: revisited and updated. *MNRAS*, 433:907–927, Aug. 2013. doi: 10.1093/mnras/stt764.
- M. Eracleous, M. Livio, J. P. Halpern, & T. Storchi-Bergmann. Elliptical accretion disks in active galactic nuclei. *ApJ*, 438:610–622, Jan. 1995. doi: 10.1086/175104.
- A. C. Fabian. Observational Evidence of Active Galactic Nuclei Feedback. *ARA&A*, 50: 455–489, Sept. 2012. doi: 10.1146/annurev-astro-081811-125521.
- H. Falcke, E. Körding, & S. Markoff. A scheme to unify low-power accreting black holes. Jet-dominated accretion flows and the radio/X-ray correlation. *A&A*, 414:895–903, Feb. 2004. doi: 10.1051/0004-6361:20031683.
- M. M. Fausnaugh, K. D. Denney, A. J. Barth, et al. Space Telescope and Optical Reverberation Mapping Project. III. Optical Continuum Emission and Broadband Time Delays in NGC 5548. *ApJ*, 821:56, Apr. 2016. doi: 10.3847/0004-637X/821/1/56.
- R. Fender, & T. Belloni. Stellar-Mass Black Holes and Ultraluminous X-ray Sources. *Science*, 337:540, Aug. 2012. doi: 10.1126/science.1221790.

Bibliography

- R. P. Fender, E. Gallo, & P. G. Jonker. Jet-dominated states: an alternative to advection across black hole event horizons in ‘quiescent’ X-ray binaries. *MNRAS*, 343:L99–L103, Aug. 2003. doi: 10.1046/j.1365-8711.2003.06950.x.
- G. J. Ferland, R. L. Porter, P. A. M. van Hoof, et al. The 2013 Release of Cloudy. *Rev. Mexicana Astron. Astrofis.*, 49:137–163, Apr. 2013.
- L. Ferrarese, & D. Merritt. A Fundamental Relation between Supermassive Black Holes and Their Host Galaxies. *apjl*, 539:L9–L12, Aug. 2000. doi: 10.1086/312838.
- B. Flaugher, H. T. Diehl, K. Honscheid, et al. The Dark Energy Camera. *AJ*, 150:150, Nov. 2015. doi: 10.1088/0004-6256/150/5/150.
- K. D. French, I. Arcavi, & A. Zabludoff. Tidal Disruption Events Prefer Unusual Host Galaxies. *ApJ*, 818:L21, Feb. 2016. doi: 10.3847/2041-8205/818/1/L21.
- C. S. Frenk, & S. D. M. White. Dark matter and cosmic structure. *Annalen der Physik*, 524:507–534, Oct. 2012. doi: 10.1002/andp.201200212.
- A. Fruscione, J. C. McDowell, G. E. Allen, et al. CIAO: Chandra’s data analysis system. In *Society of Photo-Optical Instrumentation Engineers (SPIE)*, volume 6270 of *Society of Photo-Optical Instrumentation Engineers (SPIE) Conference Series*, page 1, June 2006. doi: 10.1117/12.671760.
- J. M. Gabor, & F. Bournaud. Simulations of supermassive black hole growth in high-redshift disc galaxies. *MNRAS*, 434:606–620, Sept. 2013. doi: 10.1093/mnras/stt1046.
- J. Gagne, D. M. Crenshaw, W. C. Keel, & T. C. Fischer. Optical Spectra of the Teacup AGN. In *American Astronomical Society Meeting Abstracts #217*, volume 43 of *Bulletin of the American Astronomical Society*, page 142.12, Jan. 2011.
- J. P. Gagne, D. M. Crenshaw, S. B. Kraemer, et al. Spatially Resolved Spectra of the “Teacup” Active Galactic Nucleus: Tracing the History of a Dying Quasar. *ApJ*, 792:72, Sept. 2014. doi: 10.1088/0004-637X/792/1/72.
- P. Gandhi, H. Horst, A. Smette, et al. Resolving the mid-infrared cores of local Seyferts. *A&A*, 502:457–472, Aug. 2009. doi: 10.1051/0004-6361/200811368.
- S. García-Burillo, F. Combes, C. Ramos Almeida, et al. ALMA Resolves the Torus of NGC 1068: Continuum and Molecular Line Emission. *ApJ*, 823:L12, May 2016. doi: 10.3847/2041-8205/823/1/L12.
- G. P. Garmire, M. W. Bautz, P. G. Ford, J. A. Nousek, & G. R. Ricker, Jr. Advanced CCD imaging spectrometer (ACIS) instrument on the Chandra X-ray Observatory. In J. E. Truemper, & H. D. Tananbaum, editors, *X-Ray and Gamma-Ray Telescopes and Instruments for Astronomy*, volume 4851 of *Proc. SPIE*, pages 28–44, Mar. 2003. doi: 10.1117/12.461599.

- M. Gaspari, P. Temi, & F. Brighenti. Raining on black holes and massive galaxies: the top-down multiphase condensation model. *MNRAS*, 466:677–704, Apr. 2017. doi: 10.1093/mnras/stw3108.
- K. Gebhardt, R. Bender, G. Bower, et al. A Relationship between Nuclear Black Hole Mass and Galaxy Velocity Dispersion. *apjl*, 539:L13–L16, Aug. 2000. doi: 10.1086/312840.
- N. Gehrels. Confidence limits for small numbers of events in astrophysical data. *ApJ*, 303:336–346, Apr. 1986. doi: 10.1086/164079.
- N. Gehrels, G. Chincarini, P. Giommi, et al. The Swift Gamma-Ray Burst Mission. *ApJ*, 611:1005–1020, Aug. 2004. doi: 10.1086/422091.
- I. M. George, & A. C. Fabian. X-ray reflection from cold matter in active galactic nuclei and X-ray binaries. *MNRAS*, 249:352–367, Mar. 1991. doi: 10.1093/mnras/249.2.352.
- S. Gezari, R. Chornock, A. Rest, et al. An ultraviolet-optical flare from the tidal disruption of a helium-rich stellar core. *Nature*, 485:217–220, May 2012. doi: 10.1038/nature10990.
- S. Gezari, T. Hung, S. B. Cenko, et al. iPTF Discovery of the Rapid “Turn-on” of a Luminous Quasar. *ApJ*, 835:144, Feb. 2017. doi: 10.3847/1538-4357/835/2/144.
- O. González-Martín, & S. Vaughan. X-ray variability of 104 active galactic nuclei. XMM-Newton power-spectrum density profiles. *A&A*, 544:A80, Aug. 2012. doi: 10.1051/0004-6361/201219008.
- R. W. Goodrich. Dust in the broad-line regions of Seyfert galaxies. *ApJ*, 440:141–150, Feb. 1995. doi: 10.1086/175256.
- A. Goyal, W. Gopal-Krishna, Paul J., C. S. Stalin, & R. Sagar. Improved characterization of intranight optical variability of prominent AGN classes. *MNRAS*, 435:1300–1312, Oct. 2013. doi: 10.1093/mnras/stt1373.
- M. J. Graham, S. G. Djorgovski, D. Stern, et al. A systematic search for close supermassive black hole binaries in the Catalina Real-time Transient Survey. *MNRAS*, 453:1562–1576, Oct. 2015a. doi: 10.1093/mnras/stv1726.
- M. J. Graham, S. G. Djorgovski, D. Stern, et al. A possible close supermassive black-hole binary in a quasar with optical periodicity. *Nature*, 518:74–76, Feb. 2015b. doi: 10.1038/nature14143.
- M. J. Graham, S. G. Djorgovski, A. J. Drake, et al. Understanding extreme quasar optical variability with CRTS - I. Major AGN flares. *MNRAS*, 470:4112–4132, Oct. 2017. doi: 10.1093/mnras/stx1456.
- M. J. Graham, S. R. Kulkarni, E. C. Bellm, et al. The Zwicky Transient Facility: Science Objectives. *arXiv e-prints*, Feb. 2019a.

Bibliography

- M. J. Graham, N. P. Ross, D. Stern, et al. Understanding extreme quasar optical variability with CRTS: II. Changing-state quasars. *arXiv e-prints*, May 2019b.
- A. R. Green, I. M. McHardy, & H. J. Lehto. On the nature of rapid X-ray variability in active galactic nuclei. *MNRAS*, 265:664, Dec. 1993. doi: 10.1093/mnras/265.3.664.
- J. E. Greene, D. Pooley, N. L. Zakamska, J. M. Comerford, & A.-L. Sun. Extended X-ray Emission From a Quasar-Driven Superbubble. *ArXiv e-prints*, Apr. 2014.
- J. P. Grimes, T. Heckman, D. Strickland, & A. Ptak. A Chandra X-Ray Investigation of the Violent Interstellar Medium: From Dwarf Starbursts to Ultraluminous Infrared Galaxies. *ApJ*, 628:187–204, July 2005. doi: 10.1086/430692.
- F. Guo, & W. G. Mathews. The Fermi Bubbles. I. Possible Evidence for Recent AGN Jet Activity in the Galaxy. *ApJ*, 756:181, Sept. 2012. doi: 10.1088/0004-637X/756/2/181.
- H. Guo, J. Wang, Z. Cai, & M. Sun. How Far Is Quasar UV/Optical Variability from a Damped Random Walk at Low Frequency? *ApJ*, 847:132, Oct. 2017. doi: 10.3847/1538-4357/aa8d71.
- F. Haardt, & L. Maraschi. A two-phase model for the X-ray emission from Seyfert galaxies. *ApJ*, 380:L51–L54, Oct. 1991. doi: 10.1086/186171.
- K. Hada, A. Doi, H. Nagai, et al. Evidence for a Nuclear Radio Jet and its Structure down to 100 Schwarzschild Radii in the Center of the Sombrero Galaxy (M 104, NGC 4594). *ApJ*, 779:6, Dec. 2013. doi: 10.1088/0004-637X/779/1/6.
- K. N. Hainline, R. C. Hickox, J. E. Greene, et al. Gemini Long-slit Observations of Luminous Obscured Quasars: Further Evidence for an Upper Limit on the Size of the Narrow-line Region. *ApJ*, 787:65, May 2014. doi: 10.1088/0004-637X/787/1/65.
- C. M. Harrison, D. M. Alexander, A. M. Swinbank, et al. Energetic galaxy-wide outflows in high-redshift ultraluminous infrared galaxies hosting AGN activity. *MNRAS*, 426:1073–1096, Oct. 2012. doi: 10.1111/j.1365-2966.2012.21723.x.
- C. M. Harrison, A. P. Thomson, D. M. Alexander, et al. Storm in a "Teacup": a radio-quiet quasar with ~ 10 kpc radio-emitting bubbles and extreme gas kinematics. *ArXiv e-prints*, Oct. 2014.
- F. A. Harrison, W. W. Craig, F. E. Christensen, et al. The Nuclear Spectroscopic Telescope Array (NuSTAR) High-energy X-Ray Mission. *ApJ*, 770:103, June 2013. doi: 10.1088/0004-637X/770/2/103.
- M. R. S. Hawkins. Gravitational microlensing, quasar variability and missing matter. *Nature*, 366:242–245, Nov. 1993. doi: 10.1038/366242a0.

- T. M. Heckman, & P. N. Best. The Coevolution of Galaxies and Supermassive Black Holes: Insights from Surveys of the Contemporary Universe. *ARA&A*, 52:589–660, Aug. 2014. doi: 10.1146/annurev-astro-081913-035722.
- R. C. Hickox, J. R. Mullaney, D. M. Alexander, et al. Black Hole Variability and the Star Formation-Active Galactic Nucleus Connection: Do All Star-forming Galaxies Host an Active Galactic Nucleus? *ApJ*, 782:9, Feb. 2014. doi: 10.1088/0004-637X/782/1/9.
- L. C. Ho. Radiatively Inefficient Accretion in Nearby Galaxies. *ApJ*, 699:626–637, July 2009. doi: 10.1088/0004-637X/699/1/626.
- S. F. Hönig, & M. Kishimoto. The dusty heart of nearby active galaxies. II. From clumpy torus models to physical properties of dust around AGN. *aap*, 523:A27, Nov. 2010. doi: 10.1051/0004-6361/200912676.
- P. F. Hopkins, & L. Hernquist. Fueling Low-Level AGN Activity through Stochastic Accretion of Cold Gas. *ApJS*, 166:1–36, Sept. 2006. doi: 10.1086/505753.
- P. F. Hopkins, & E. Quataert. How do massive black holes get their gas? *MNRAS*, 407:1529–1564, Sept. 2010. doi: 10.1111/j.1365-2966.2010.17064.x.
- P. F. Hopkins, L. Hernquist, P. Martini, et al. A Physical Model for the Origin of Quasar Lifetimes. *ApJ*, 625:L71–L74, June 2005. doi: 10.1086/431146.
- F. Hoyle, & W. A. Fowler. Nature of Strong Radio Sources. *Nature*, 197:533–535, Feb. 1963. doi: 10.1038/197533a0.
- T. Hung, S. Gezari, N. Blagorodnova, et al. iPTF16axa: A Tidal Disruption Event at $z=0.108$. *ArXiv e-prints*, Mar. 2017.
- B. Husemann, T. Urrutia, G. R. Tremblay, et al. The Close AGN Reference Survey (CARS). What is causing Mrk 1018’s return to the shadows after 30 years? *A&A*, 593:L9, Sept. 2016. doi: 10.1051/0004-6361/201629245.
- Ž. Ivezić, J. A. Smith, G. Miknaitis, et al. Sloan Digital Sky Survey Standard Star Catalog for Stripe 82: The Dawn of Industrial 1% Optical Photometry. *AJ*, 134:973–998, Sept. 2007. doi: 10.1086/519976.
- Z. Ivezić, T. Axelrod, W. N. Brandt, et al. Large Synoptic Survey Telescope: From Science Drivers To Reference Design. *Serbian Astronomical Journal*, 176:1–13, June 2008. doi: 10.2298/SAJ0876001I.
- Ž. Ivezić, A. Connolly, J. Vanderplas, & A. Gray. *Statistics, Data Mining and Machine Learning in Astronomy*. Princeton University Press, 2014.
- K. Jahnke, & A. V. Macciò. The Non-causal Origin of the Black-hole-galaxy Scaling Relations. *ApJ*, 734:92, June 2011. doi: 10.1088/0004-637X/734/2/92.

Bibliography

- K. Jahnke, A. Bongiorno, M. Brusa, et al. Massive Galaxies in COSMOS: Evolution of Black Hole Versus Bulge Mass but not Versus Total Stellar Mass Over the Last 9 Gyr? *ApJ*, 706:L215–L220, Dec. 2009. doi: 10.1088/0004-637X/706/2/L215.
- T. H. Jarrett, M. Cohen, F. Masci, et al. The Spitzer-WISE Survey of the Ecliptic Poles. *ApJ*, 735:112, July 2011. doi: 10.1088/0004-637X/735/2/112.
- Y.-F. Jiang, S. W. Davis, & J. M. Stone. Iron Opacity Bump Changes the Stability and Structure of Accretion Disks in Active Galactic Nuclei. *ApJ*, 827:10, Aug. 2016. doi: 10.3847/0004-637X/827/1/10.
- M. L. Jones, R. C. Hickox, C. S. Black, et al. The Intrinsic Eddington Ratio Distribution of Active Galactic Nuclei in Star-forming Galaxies from the Sloan Digital Sky Survey. *ApJ*, 826:12, July 2016. doi: 10.3847/0004-637X/826/1/12.
- P. Jovanović, & L. Č. Popović. X-ray Emission From Accretion Disks of AGN: Signatures of Supermassive Black Holes. *arXiv e-prints*, Mar. 2009.
- G. I. G. Józsa, M. A. Garrett, T. A. Oosterloo, et al. Revealing Hanny’s Voorwerp: radio observations of IC 2497. *A&A*, 500:L33–L36, June 2009. doi: 10.1051/0004-6361/200912402.
- S. Juneau, M. Dickinson, F. Bournaud, et al. Widespread and Hidden Active Galactic Nuclei in Star-forming Galaxies at Redshift 0.3. *ApJ*, 764:176, Feb. 2013. doi: 10.1088/0004-637X/764/2/176.
- D. W. Just, W. N. Brandt, O. Shemmer, et al. The X-Ray Properties of the Most Luminous Quasars from the Sloan Digital Sky Survey. *ApJ*, 665:1004–1022, Aug. 2007. doi: 10.1086/519990.
- S. Kahn. The Large Synoptic Survey Telescope (LSST). In *42nd COSPAR Scientific Assembly*, volume 42 of *COSPAR Meeting*, pages E1.16–5–18, July 2018.
- V. P. Kasliwal, M. S. Vogeley, & G. T. Richards. Are the variability properties of the Kepler AGN light curves consistent with a damped random walk? *MNRAS*, 451: 4328–4345, Aug. 2015. doi: 10.1093/mnras/stv1230.
- R. Katebi, R. Chornock, E. Berger, et al. PS1-13cbe: The Rapid “Turn on” of a Seyfert 1. *ArXiv e-prints*, Nov. 2018.
- G. Kauffmann, & T. M. Heckman. Feast and Famine: regulation of black hole growth in low-redshift galaxies. *MNRAS*, 397:135–147, July 2009. doi: 10.1111/j.1365-2966.2009.14960.x.
- G. Kauffmann, T. M. Heckman, C. Tremonti, et al. The host galaxies of active galactic nuclei. *mnras*, 346:1055–1077, Dec. 2003. doi: 10.1111/j.1365-2966.2003.07154.x.

- T. Kawamuro, M. Schirmer, J. E. H. Turner, R. L. Davies, & K. Ichikawa. N uSTAR Hard X-Ray Data and Gemini 3D Spectra Reveal Powerful AGN and Outflow Histories in Two Low-redshift Ly α Blobs. *ApJ*, 848:42, Oct. 2017. doi: 10.3847/1538-4357/aa8e46.
- W. C. Keel, S. D. Chojnowski, V. N. Bennert, et al. The Galaxy Zoo survey for giant AGN-ionized clouds: past and present black hole accretion events. *mnras*, 420:878–900, Feb. 2012a. doi: 10.1111/j.1365-2966.2011.20101.x.
- W. C. Keel, C. J. Lintott, K. Schawinski, et al. The History and Environment of a Faded Quasar: Hubble Space Telescope Observations of Hanny’s Voorwerp and IC 2497. *AJ*, 144:66, Aug. 2012b. doi: 10.1088/0004-6256/144/2/66.
- W. C. Keel, W. P. Maksym, V. N. Bennert, et al. HST Imaging of Fading AGN Candidates I: Host-Galaxy Properties and Origin of the Extended Gas. *ArXiv e-prints*, Aug. 2014.
- W. C. Keel, W. P. Maksym, V. N. Bennert, et al. HST Imaging of Fading AGN Candidates. I. Host-galaxy Properties and Origin of the Extended Gas. *AJ*, 149:155, May 2015. doi: 10.1088/0004-6256/149/5/155.
- W. C. Keel, C. J. Lintott, W. P. Maksym, et al. Fading AGN Candidates: AGN Histories and Outflow Signatures. *ApJ*, 835:256, Feb. 2017. doi: 10.3847/1538-4357/835/2/256.
- B. C. Kelly, & Y. Shen. The Demographics of Broad-line Quasars in the Mass-Luminosity Plane. II. Black Hole Mass and Eddington Ratio Functions. *ApJ*, 764:45, Feb. 2013. doi: 10.1088/0004-637X/764/1/45.
- B. C. Kelly, J. Bechtold, & A. Siemiginowska. Are the Variations in Quasar Optical Flux Driven by Thermal Fluctuations? *ApJ*, 698:895–910, June 2009. doi: 10.1088/0004-637X/698/1/895.
- B. C. Kelly, M. Sobolewska, & A. Siemiginowska. A Stochastic Model for the Luminosity Fluctuations of Accreting Black Holes. *ApJ*, 730:52, Mar. 2011. doi: 10.1088/0004-637X/730/1/52.
- B. C. Kelly, A. C. Becker, M. Sobolewska, A. Siemiginowska, & P. Uttley. Flexible and Scalable Methods for Quantifying Stochastic Variability in the Era of Massive Time-domain Astronomical Data Sets. *ApJ*, 788:33, June 2014. doi: 10.1088/0004-637X/788/1/33.
- R. C. Kennicutt, Jr. The Global Schmidt Law in Star-forming Galaxies. *apj*, 498:541–552, May 1998. doi: 10.1086/305588.
- L. J. Kewley, M. A. Dopita, R. S. Sutherland, C. A. Heisler, & J. Trevena. Theoretical Modeling of Starburst Galaxies. *apj*, 556:121–140, July 2001. doi: 10.1086/321545.
- L. J. Kewley, C. Maier, K. Yabe, et al. The Cosmic BPT Diagram: Confronting Theory with Observations. *apjl*, 774:L10, Sept. 2013. doi: 10.1088/2041-8205/774/1/L10.

Bibliography

- E. Y. Khachikian, & D. W. Weedman. A New Cloud of Hydrogen Emission in a Bright Galactic Nucleus. *ApJ*, 164:L109, Mar. 1971. doi: 10.1086/180701.
- A. King. Black Holes, Galaxy Formation, and the M_{BH} - σ Relation. *ApJ*, 596:L27–L29, Oct. 2003. doi: 10.1086/379143.
- A. King, & C. Nixon. AGN flickering and chaotic accretion. *MNRAS*, 453:L46–L47, Oct. 2015. doi: 10.1093/mnras/slv098.
- A. R. King, & J. E. Pringle. Growing supermassive black holes by chaotic accretion. *MNRAS*, 373:L90–L92, Nov. 2006. doi: 10.1111/j.1745-3933.2006.00249.x.
- A. R. King, & J. E. Pringle. Fuelling active galactic nuclei. *MNRAS*, 377:L25–L28, May 2007. doi: 10.1111/j.1745-3933.2007.00296.x.
- M. Kishimoto, S. F. Hönig, R. Antonucci, et al. The innermost dusty structure in active galactic nuclei as probed by the Keck interferometer. *A&A*, 527:A121, Mar. 2011. doi: 10.1051/0004-6361/201016054.
- J. A. Kollmeier, C. A. Onken, C. S. Kochanek, et al. Black Hole Masses and Eddington Ratios at $0.3 < z < 4$. *ApJ*, 648:128–139, Sept. 2006. doi: 10.1086/505646.
- J. A. Kollmeier, G. Zasowski, H.-W. Rix, et al. SDSS-V: Pioneering Panoptic Spectroscopy. *arXiv e-prints*, Nov. 2017.
- E. G. Körtling, S. Jester, & R. Fender. Accretion states and radio loudness in active galactic nuclei: analogies with X-ray binaries. *mnras*, 372:1366–1378, Nov. 2006. doi: 10.1111/j.1365-2966.2006.10954.x.
- J. Kormendy. A critical review of stellar-dynamical evidence for black holes in galaxy nuclei. In J. Beckman, L. Colina, & H. Netzer, editors, *The Nearest Active Galaxies*, pages 197–218, Jan. 1993.
- J. Kormendy, & L. C. Ho. Coevolution (Or Not) of Supermassive Black Holes and Host Galaxies. *araa*, 51:511–653, Aug. 2013. doi: 10.1146/annurev-astro-082708-101811.
- J. Kormendy, & D. Richstone. Inward Bound—The Search For Supermassive Black Holes In Galactic Nuclei. *araa*, 33:581, 1995. doi: 10.1146/annurev.aa.33.090195.003053.
- M. Koss, B. Trakhtenbrot, C. Ricci, et al. BAT AGN Spectroscopic Survey. I. Spectral Measurements, Derived Quantities, and AGN Demographics. *ApJ*, 850:74, Nov. 2017. doi: 10.3847/1538-4357/aa8ec9.
- M. J. Koss, R. Assef, M. Baloković, et al. A New Population of Compton-thick AGNs Identified Using the Spectral Curvature above 10 keV. *ApJ*, 825:85, July 2016. doi: 10.3847/0004-637X/825/2/85.

- S. Kozłowski. Revisiting Stochastic Variability of AGNs with Structure Functions. *ApJ*, 826:118, Aug. 2016. doi: 10.3847/0004-637X/826/2/118.
- S. Kozłowski. Limitations on the recovery of the true AGN variability parameters using damped random walk modeling. *A&A*, 597:A128, Jan. 2017a. doi: 10.1051/0004-6361/201629890.
- S. Kozłowski. A Method to Measure the Unbiased Decorrelation Timescale of the AGN Variable Signal from Structure Functions. *ApJ*, 835:250, Feb. 2017b. doi: 10.3847/1538-4357/aa56c0.
- S. B. Kraemer, C.-C. Wu, D. M. Crenshaw, & J. P. Harrington. IUE Spectra and photoionization models of the Seyfert 2 galaxies NGC 7674 and I ZW 92. *ApJ*, 435: 171–180, Nov. 1994. doi: 10.1086/174803.
- S. B. Kraemer, M. L. Trippe, D. M. Crenshaw, et al. Physical Conditions in the Inner Narrow-Line Region of the Seyfert 2 Galaxy Markarian 573. *ApJ*, 698:106–114, June 2009. doi: 10.1088/0004-637X/698/1/106.
- H. A. Krimm, S. T. Holland, R. H. D. Corbet, et al. The Swift/BAT Hard X-Ray Transient Monitor. *ApJS*, 209:14, Nov. 2013. doi: 10.1088/0067-0049/209/1/14.
- J. H. Krolik, J. F. Hawley, & S. Hirose. Magnetically Driven Accretion Flows in the Kerr Metric. IV. Dynamical Properties of the Inner Disk. *ApJ*, 622:1008–1023, Apr. 2005. doi: 10.1086/427932.
- J. Labadie-Bartz, J. Pepper, M. V. McSwain, et al. Photometric Variability of the Be Star Population. *AJ*, 153:252, June 2017. doi: 10.3847/1538-3881/aa6396.
- S. M. LaMassa, S. Cales, E. C. Moran, et al. The Discovery of the First “Changing Look” Quasar: New Insights Into the Physics and Phenomenology of Active Galactic Nucleus. *ApJ*, 800:144, Feb. 2015. doi: 10.1088/0004-637X/800/2/144.
- I. Lamperti, M. Koss, B. Trakhtenbrot, et al. BAT AGN Spectroscopic Survey - IV: Near-Infrared Coronal Lines, Hidden Broad Lines, and Correlation with Hard X-ray Emission. *MNRAS*, 467:540–572, May 2017. doi: 10.1093/mnras/stx055.
- G. B. Lansbury, M. Jarvis, C. M. Harrison, et al. Storm in a Teacup: X-ray view of an obscured quasar and superbubble. *ArXiv e-prints*, Feb. 2018.
- N. M. Law, S. R. Kulkarni, R. G. Dekany, et al. The Palomar Transient Factory: System Overview, Performance, and First Results. *PASP*, 121:1395, Dec. 2009. doi: 10.1086/648598.
- J. Law-Smith, E. Ramirez-Ruiz, S. L. Ellison, & R. J. Foley. Tidal Disruption Event Host Galaxies in the Context of the Local Galaxy Population. *ApJ*, 850:22, Nov. 2017. doi: 10.3847/1538-4357/aa94c7.

Bibliography

- A. Lawrence. The relative frequency of broad-lined and narrow-lined active galactic nuclei - Implications for unified schemes. *MNRAS*, 252:586–592, Oct. 1991. doi: 10.1093/mnras/252.4.586.
- A. Lawrence. Clues to the Structure of AGN Through Massive Variability Surveys. In A. Mickaelian, A. Lawrence, & T. Magakian, editors, *Astronomical Surveys and Big Data*, volume 505 of *Astronomical Society of the Pacific Conference Series*, page 107, June 2016.
- A. Lawrence. Quasar viscosity crisis. *Nature Astronomy*, 2:102–103, Feb. 2018. doi: 10.1038/s41550-017-0372-1.
- A. Lawrence, & I. Papadakis. X-ray variability of active galactic nuclei - A universal power spectrum with luminosity-dependent amplitude. *ApJ*, 414:L85–L88, Sept. 1993. doi: 10.1086/187002.
- A. Lawrence, A. G. Bruce, C. MacLeod, et al. Slow-blue nuclear hypervariables in PanSTARRS-1. *MNRAS*, 463:296–331, Nov. 2016. doi: 10.1093/mnras/stw1963.
- J. C. Lee, A. Gil de Paz, C. Tremonti, et al. Comparison of $H\alpha$ and UV Star Formation Rates in the Local Volume: Systematic Discrepancies for Dwarf Galaxies. *ApJ*, 706:599–613, Nov. 2009. doi: 10.1088/0004-637X/706/1/599.
- B. D. Lehmer, A. R. Basu-Zych, S. Mineo, et al. The Evolution of Normal Galaxy X-Ray Emission through Cosmic History: Constraints from the 6 MS Chandra Deep Field-South. *ApJ*, 825:7, July 2016. doi: 10.3847/0004-637X/825/1/7.
- J. Li, J. H. Kastner, G. Y. Prigozhin, & N. S. Schulz. Refining Chandra/ACIS Subpixel Event Repositioning Using a Backside-illuminated CCD Model. *ApJ*, 590:586–592, June 2003. doi: 10.1086/374967.
- J. Li, J. H. Kastner, G. Y. Prigozhin, et al. Chandra ACIS Subpixel Event Repositioning: Further Refinements and Comparison between Backside- and Frontside-illuminated X-Ray CCDs. *ApJ*, 610:1204–1212, Aug. 2004. doi: 10.1086/421866.
- A. P. Lightman, & T. R. White. Effects of cold matter in active galactic nuclei - A broad hump in the X-ray spectra. *ApJ*, 335:57–66, Dec. 1988. doi: 10.1086/166905.
- C. J. Lintott, K. Schawinski, A. Slosar, et al. Galaxy Zoo: morphologies derived from visual inspection of galaxies from the Sloan Digital Sky Survey. *MNRAS*, 389:1179–1189, Sept. 2008. doi: 10.1111/j.1365-2966.2008.13689.x.
- C. J. Lintott, K. Schawinski, W. Keel, et al. Galaxy Zoo: ‘Hanny’s Voorwerp’, a quasar light echo? *MNRAS*, 399:129–140, Oct. 2009. doi: 10.1111/j.1365-2966.2009.15299.x.
- T. Liu, S. Gezari, S. Heinis, et al. A Periodically Varying Luminous Quasar at $z = 2$ from the Pan-STARRS1 Medium Deep Survey: A Candidate Supermassive Black

- Hole Binary in the Gravitational Wave-driven Regime. *ApJ*, 803:L16, Apr. 2015. doi: 10.1088/2041-8205/803/2/L16.
- J. M. Lotz, P. Jonsson, T. J. Cox, et al. The Major and Minor Galaxy Merger Rates at $z < 1.5$. *ApJ*, 742:103, Dec. 2011. doi: 10.1088/0004-637X/742/2/103.
- LSST Science Collaboration, P. A. Abell, J. Allison, et al. LSST Science Book, Version 2.0. *ArXiv e-prints*, Dec. 2009.
- D. Lynden-Bell. Gravity power. *Phys. Scr*, 17:185–191, Mar. 1978. doi: 10.1088/0031-8949/17/3/009.
- D. Lynden-Bell. On why discs generate magnetic towers and collimate jets. *MNRAS*, 341:1360–1372, June 2003. doi: 10.1046/j.1365-8711.2003.06506.x.
- T. J. Maccarone, E. Gallo, & R. Fender. The connection between radio-quiet active galactic nuclei and the high/soft state of X-ray binaries. *MNRAS*, 345:L19–L24, Oct. 2003. doi: 10.1046/j.1365-8711.2003.07161.x.
- C. L. MacLeod, Ž. Ivezić, C. S. Kochanek, et al. Modeling the Time Variability of SDSS Stripe 82 Quasars as a Damped Random Walk. *ApJ*, 721:1014–1033, Oct. 2010. doi: 10.1088/0004-637X/721/2/1014.
- C. L. MacLeod, Ž. Ivezić, B. Sesar, et al. A Description of Quasar Variability Measured Using Repeated SDSS and POSS Imaging. *ApJ*, 753:106, July 2012. doi: 10.1088/0004-637X/753/2/106.
- C. L. MacLeod, N. P. Ross, A. Lawrence, et al. A systematic search for changing-look quasars in SDSS. *MNRAS*, 457:389–404, Mar. 2016. doi: 10.1093/mnras/stv2997.
- C. L. MacLeod, P. J. Green, S. F. Anderson, et al. Changing-look Quasar Candidates: First Results from Follow-up Spectroscopy of Highly Optically Variable Quasars. *ApJ*, 874:8, Mar. 2019. doi: 10.3847/1538-4357/ab05e2.
- P. Madau, & M. Dickinson. Cosmic Star-Formation History. *ARA&A*, 52:415–486, Aug. 2014. doi: 10.1146/annurev-astro-081811-125615.
- P. Magdziarz, & A. A. Zdziarski. Angle-dependent Compton reflection of X-rays and gamma-rays. *MNRAS*, 273:837–848, Apr. 1995. doi: 10.1093/mnras/273.3.837.
- J. Magorrian, S. Tremaine, D. Richstone, et al. The Demography of Massive Dark Objects in Galaxy Centers. *AJ*, 115:2285–2305, June 1998. doi: 10.1086/300353.
- A. Mainzer, J. Bauer, T. Grav, et al. Preliminary Results from NEOWISE: An Enhancement to the Wide-field Infrared Survey Explorer for Solar System Science. *ApJ*, 731:53, Apr. 2011. doi: 10.1088/0004-637X/731/1/53.

Bibliography

- R. Maiolino, G. Risaliti, M. Salvati, et al. “Comets” orbiting a black hole. *A&A*, 517:A47, July 2010. doi: 10.1051/0004-6361/200913985.
- M. A. Malkan, & W. L. W. Sargent. The ultraviolet excess of Seyfert 1 galaxies and quasars. *ApJ*, 254:22–37, Mar. 1982. doi: 10.1086/159701.
- E. Marchese, V. Braitto, R. Della Ceca, A. Caccianiga, & P. Severgnini. NGC 454: unveiling a new ‘changing look’ active galactic nucleus. *MNRAS*, 421:1803–1812, Apr. 2012. doi: 10.1111/j.1365-2966.2012.20445.x.
- A. Marconi, & L. K. Hunt. The Relation between Black Hole Mass, Bulge Mass, and Near-Infrared Luminosity. *apjl*, 589:L21–L24, May 2003. doi: 10.1086/375804.
- A. Marconi, G. Risaliti, R. Gilli, et al. Local supermassive black holes, relics of active galactic nuclei and the X-ray background. *MNRAS*, 351:169–185, June 2004. doi: 10.1111/j.1365-2966.2004.07765.x.
- A. Marecki. Activity restart - a key to explaining the morphology of J1211+743. *A&A*, 544:L2, Aug. 2012a. doi: 10.1051/0004-6361/201219638.
- A. Marecki. Are 3C 249.1 and 3C 334 restarted quasars? *A&A*, 545:A132, Sept. 2012b. doi: 10.1051/0004-6361/201220010.
- F. Marin. Unveiling the physics behind the spectral variations of changing-look quasars with optical polarimetry. *A&A*, 607:A40, Nov. 2017. doi: 10.1051/0004-6361/201731726.
- A. Markowitz, R. Edelson, & S. Vaughan. Long-Term X-Ray Spectral Variability in Seyfert 1 Galaxies. *ApJ*, 598:935–955, Dec. 2003. doi: 10.1086/379103.
- P. Martini, & D. P. Schneider. Multiepoch Sky Surveys and the Lifetime of Quasars. *ApJ*, 597:L109–L112, Nov. 2003. doi: 10.1086/379888.
- S. Mathur, K. D. Denney, A. Gupta, et al. The Changing-look Quasar Mrk 590 Is Awakening. *ApJ*, 866:123, Oct. 2018. doi: 10.3847/1538-4357/aadd91.
- G. Matt, W. N. Brandt, & A. C. Fabian. The iron Kalpha line complex in Compton-thick Seyfert 2 galaxies. *MNRAS*, 280:823–834, June 1996. doi: 10.1093/mnras/280.3.823.
- G. Matt, M. Guainazzi, & R. Maiolino. Changing look: from Compton-thick to Compton-thin, or the rebirth of fossil active galactic nuclei. *MNRAS*, 342:422–426, June 2003. doi: 10.1046/j.1365-8711.2003.06539.x.
- T. A. Matthews, & A. R. Sandage. Optical Identification of 3C 48, 3C 196, and 3C 286 with Stellar Objects. *ApJ*, 138:30, July 1963. doi: 10.1086/147615.
- R. E. McElroy, B. Husemann, S. M. Croom, et al. The Close AGN Reference Survey (CARS). Mrk 1018 returns to the shadows after 30 years as a Seyfert 1. *A&A*, 593:L8, Sept. 2016. doi: 10.1051/0004-6361/201629102.

- I. M. McHardy, I. E. Papadakis, P. Uttley, M. J. Page, & K. O. Mason. Combined long and short time-scale X-ray variability of NGC 4051 with RXTE and XMM-Newton. *MNRAS*, 348:783–801, Mar. 2004. doi: 10.1111/j.1365-2966.2004.07376.x.
- I. M. McHardy, E. Koerding, C. Knigge, P. Uttley, & R. P. Fender. Active galactic nuclei as scaled-up Galactic black holes. *Nature*, 444:730–732, Dec. 2006. doi: 10.1038/nature05389.
- I. M. McHardy, P. Arévalo, P. Uttley, et al. Discovery of multiple Lorentzian components in the X-ray timing properties of the Narrow Line Seyfert 1 Ark 564. *MNRAS*, 382: 985–994, Dec. 2007. doi: 10.1111/j.1365-2966.2007.12411.x.
- B. McKernan, K. E. S. Ford, B. Kocsis, W. Lyra, & L. M. Winter. Intermediate-mass black holes in AGN discs - II. Model predictions and observational constraints. *MNRAS*, 441:900–909, June 2014. doi: 10.1093/mnras/stu553.
- B. R. McNamara, & P. E. J. Nulsen. Mechanical feedback from active galactic nuclei in galaxies, groups and clusters. *New Journal of Physics*, 14(5):055023, May 2012. doi: 10.1088/1367-2630/14/5/055023.
- J. E. Mejía-Restrepo, B. Trakhtenbrot, P. Lira, H. Netzer, & D. M. Capellupo. Active galactic nuclei at z 1.5 - II. Black hole mass estimation by means of broad emission lines. *MNRAS*, 460:187–211, July 2016. doi: 10.1093/mnras/stw568.
- R. B. Menezes, J. E. Steiner, & P. da Silva. The Off-centered Seyfert-like Compact Emission in the Nuclear Region of NGC 3621. *ApJ*, 817:150, Feb. 2016. doi: 10.3847/0004-637X/817/2/150.
- A. Merloni, P. Predehl, W. Becker, et al. eROSITA Science Book: Mapping the Structure of the Energetic Universe. *ArXiv e-prints*, Sept. 2012.
- A. Merloni, T. Dwelly, M. Salvato, et al. A tidal disruption flare in a massive galaxy? Implications for the fuelling mechanisms of nuclear black holes. *MNRAS*, 452:69–87, Sept. 2015. doi: 10.1093/mnras/stv1095.
- M. Mezcuca. Observational evidence for intermediate-mass black holes. *International Journal of Modern Physics D*, 26:1730021, 2017. doi: 10.1142/S021827181730021X.
- R. Middei, F. Vagnetti, S. Bianchi, et al. A long-term study of AGN X-ray variability . Structure function analysis on a ROSAT-XMM quasar sample. *A&A*, 599:A82, Mar. 2017. doi: 10.1051/0004-6361/201629940.
- R. L. Minkowski, & G. O. Abell. *The National Geographic Society-Palomar Observatory Sky Survey*, page 481. the University of Chicago Press, 1963.
- S. Miyamoto, K. Kimura, S. Kitamoto, T. Dotani, & K. Ebisawa. X-ray variability of GX 339 - 4 in its very high state. *ApJ*, 383:784–807, Dec. 1991. doi: 10.1086/170837.

Bibliography

- R. Moderski, M. Sikora, & J.-P. Lasota. On the spin paradigm and the radio dichotomy of quasars. *MNRAS*, 301:142–148, Nov. 1998. doi: 10.1046/j.1365-8711.1998.02009.x.
- R. Mor, H. Netzer, & M. Elitzur. Dusty Structure Around Type-I Active Galactic Nuclei: Clumpy Torus Narrow-line Region and Near-nucleus Hot Dust. *ApJ*, 705:298–313, Nov. 2009. doi: 10.1088/0004-637X/705/1/298.
- C. W. Morgan, C. S. Kochanek, N. D. Morgan, & E. E. Falco. The Quasar Accretion Disk Size-Black Hole Mass Relation. *ApJ*, 712:1129–1136, Apr. 2010. doi: 10.1088/0004-637X/712/2/1129.
- E. Morganson, W. S. Burgett, K. C. Chambers, et al. Measuring Quasar Variability with Pan-STARRS1 and SDSS. *ApJ*, 784:92, Apr. 2014. doi: 10.1088/0004-637X/784/2/92.
- E. Morganson, P. J. Green, S. F. Anderson, et al. The Time Domain Spectroscopic Survey: Variable Selection and Anticipated Results. *ApJ*, 806:244, June 2015. doi: 10.1088/0004-637X/806/2/244.
- R. Morganti. Archaeology of active galaxies across the electromagnetic spectrum. *Nature Astronomy*, 1:596–605, Sept. 2017. doi: 10.1038/s41550-017-0223-0.
- D. J. Mortlock, S. J. Warren, B. P. Venemans, et al. A luminous quasar at a redshift of $z = 7.085$. *nat*, 474:616–619, June 2011. doi: 10.1038/nature10159.
- C. A. Muller. De radiosterrenwacht Westerbork. *Hemel en Dampkring*, 67:56–62, 1969.
- K. D. Murphy, & T. Yaqoob. An X-ray spectral model for Compton-thick toroidal reprocessors. *MNRAS*, 397:1549–1562, Aug. 2009. doi: 10.1111/j.1365-2966.2009.15025.x.
- R. Mushotzky. How are AGN Found? In A. J. Barger, editor, *Supermassive Black Holes in the Distant Universe*, volume 308 of *Astrophysics and Space Science Library*, page 53, Aug. 2004.
- R. F. Mushotzky, R. Edelson, W. Baumgartner, & P. Gandhi. Kepler Observations of Rapid Optical Variability in Active Galactic Nuclei. *ApJ*, 743:L12, Dec. 2011. doi: 10.1088/2041-8205/743/1/L12.
- T. W. B. Muxlow. e-MERLIN - a Real-Time VLBI Array. In Y. C. Minh, editor, *New technologies in VLBI*, volume 306 of *Astronomical Society of the Pacific Conference Series*, page 245, 2003.
- K. Nandra. On the origin of the iron $K\alpha$ line cores in active galactic nuclei. *MNRAS*, 368:L62–L66, May 2006. doi: 10.1111/j.1745-3933.2006.00158.x.
- K. Nandra, & K. A. Pounds. GINGA Observations of the X-Ray Spectra of Seyfert Galaxies. *MNRAS*, 268:405, May 1994. doi: 10.1093/mnras/268.2.405.

- K. Nandra, I. M. George, R. F. Mushotzky, T. J. Turner, & T. Yaqoob. ASCA Observations of Seyfert 1 Galaxies. I. Data Analysis, Imaging, and Timing. *ApJ*, 476:70–82, Feb. 1997. doi: 10.1086/303600.
- R. Narayan, & I. Yi. Advection-dominated accretion: A self-similar solution. *ApJ*, 428: L13–L16, June 1994. doi: 10.1086/187381.
- R. Narayan, & I. Yi. Advection-dominated Accretion: Underfed Black Holes and Neutron Stars. *ApJ*, 452:710, Oct. 1995. doi: 10.1086/176343.
- R. Narayan, R. Mahadevan, & E. Quataert. Advection-dominated accretion around black holes. In M. A. Abramowicz, G. Björnsson, & J. E. Pringle, editors, *Theory of Black Hole Accretion Disks*, pages 148–182, 1998.
- R. M. Neal. Slice sampling. *Ann. Statist.*, 31(3):705–767, 06 2003. doi: 10.1214/aos/1056562461. URL <https://doi.org/10.1214/aos/1056562461>.
- A. Negri, & M. Volonteri. Black hole feeding and feedback: the physics inside the ‘sub-grid’. *MNRAS*, 467:3475–3492, May 2017. doi: 10.1093/mnras/stx362.
- M. Nenkova, M. M. Sirocky, Ž. Ivezić, & M. Elitzur. AGN Dusty Tori. I. Handling of Clumpy Media. *apj*, 685:147–159, Sept. 2008a. doi: 10.1086/590482.
- M. Nenkova, M. M. Sirocky, R. Nikutta, Ž. Ivezić, & M. Elitzur. AGN Dusty Tori. II. Observational Implications of Clumpiness. *apj*, 685:160–180, Sept. 2008b. doi: 10.1086/590483.
- H. Netzer. Active Galactic Nuclei: Basic Physics and Main Components. In D. Alloin, editor, *Physics of Active Galactic Nuclei at all Scales*, volume 693 of *Lecture Notes in Physics*, Berlin Springer Verlag, page 1, 2006. doi: 10.1007/3-540-34621-X_1.
- H. Netzer. *The Physics and Evolution of Active Galactic Nuclei*. Nov. 2013.
- H. Netzer. Revisiting the Unified Model of Active Galactic Nuclei. *ARA&A*, 53:365–408, Aug. 2015. doi: 10.1146/annurev-astro-082214-122302.
- H. Netzer, & B. Trakhtenbrot. Bolometric luminosity black hole growth time and slim accretion discs in active galactic nuclei. *MNRAS*, 438:672–679, Feb. 2014. doi: 10.1093/mnras/stt2238.
- H. Noda, & C. Done. Explaining changing-look AGN with state transition triggered by rapid mass accretion rate drop. *MNRAS*, 480:3898–3906, Nov. 2018. doi: 10.1093/mnras/sty2032.
- G. S. Novak, J. P. Ostriker, & L. Ciotti. Feedback from Central Black Holes in Elliptical Galaxies: Two-dimensional Models Compared to One-dimensional Models. *ApJ*, 737: 26, Aug. 2011. doi: 10.1088/0004-637X/737/1/26.

Bibliography

- K. Oh. *Improving spectral line strength measurements of SDSS galaxies and the demographics of nearby broad-line region active galaxies*. PhD thesis, The Graduate School Yonsei University, 2014.
- K. Oh, S. K. Yi, K. Schawinski, et al. A New Catalog of Type 1 AGNs and its Implications on the AGN Unified Model. *ApJS*, 219:1, July 2015. doi: 10.1088/0067-0049/219/1/1.
- K. Oh, M. Koss, C. B. Markwardt, et al. The 105-Month Swift-BAT All-sky Hard X-Ray Survey. *ApJS*, 235:4, Mar. 2018. doi: 10.3847/1538-4365/aaa7fd.
- J. P. Ostriker, & L. Ciotti. Active galaxies and radiative heating: One contribution of 13 to a Discussion Meeting 'The impact of active galaxies on the Universe at large'. *Philosophical Transactions of the Royal Society of London Series A*, 363:667, Mar. 2005. doi: 10.1098/rsta.2004.1521.
- P. Padovani, D. M. Alexander, R. J. Assef, et al. Active galactic nuclei: what's in a name? *A&A Rev.*, 25:2, Aug. 2017. doi: 10.1007/s00159-017-0102-9.
- M. W. Pakull, R. Soria, & C. Motch. A 300-parsec-long jet-inflated bubble around a powerful microquasar in the galaxy NGC 7793. *Nature*, 466:209–212, July 2010. doi: 10.1038/nature09168.
- F. Panessa, L. Bassani, M. Cappi, et al. On the X-ray, optical emission line and black hole mass properties of local Seyfert galaxies. *aap*, 455:173–185, Aug. 2006. doi: 10.1051/0004-6361:20064894.
- M. Paolillo, I. Papadakis, W. N. Brandt, et al. Tracing the accretion history of supermassive black holes through X-ray variability: results from the ChandraDeep Field-South. *MNRAS*, 471:4398–4411, Nov. 2017. doi: 10.1093/mnras/stx1761.
- M. L. Parker, N. Schartel, D. Grupe, et al. X-ray spectra reveal the reawakening of the repeat changing-look AGN NGC 1566. *MNRAS*, 483:L88–L92, Feb. 2019. doi: 10.1093/mnrasl/sly224.
- P. Parma, M. Murgia, H. R. de Ruiter, et al. In search of dying radio sources in the local universe. *A&A*, 470:875–888, Aug. 2007. doi: 10.1051/0004-6361:20077592.
- C. Y. Peng. How Mergers May Affect the Mass Scaling Relation between Gravitationally Bound Systems. *ApJ*, 671:1098–1107, Dec. 2007. doi: 10.1086/522774.
- M. V. Penston, & E. Perez. An evolutionary link between Seyfert I and II galaxies? *MNRAS*, 211:33P–39P, Nov. 1984. doi: 10.1093/mnras/211.1.33P.
- M. V. Penston, A. Robinson, D. Alloin, et al. The extended narrow line region of NGC 4151. I - Emission line ratios and their implications. *A&A*, 236:53–62, Sept. 1990.

- B. M. Peterson. The Broad-Line Region in Active Galactic Nuclei. In D. Alloin, editor, *Physics of Active Galactic Nuclei at all Scales*, volume 693 of *Lecture Notes in Physics*, Berlin Springer Verlag, page 77, 2006. doi: 10.1007/3-540-34621-X_3.
- B. M. Peterson. Measuring the Masses of Supermassive Black Holes. *Space Sci. Rev.*, 183:253–275, Sept. 2014. doi: 10.1007/s11214-013-9987-4.
- E. Piconcelli, E. Jimenez-Bailón, M. Guainazzi, et al. The XMM-Newton view of PG quasars. I. X-ray continuum and absorption. *A&A*, 432:15–30, Mar. 2005. doi: 10.1051/0004-6361:20041621.
- E. Piconcelli, F. Fiore, F. Nicastro, et al. The XMM-Newton view of IRAS 09104+4109: evidence for a changing-look Type 2 quasar? *A&A*, 473:85–89, Oct. 2007. doi: 10.1051/0004-6361:20077630.
- G. Ponti, R. Terrier, A. Goldwurm, G. Belanger, & G. Trap. Discovery of a Superluminal Fe K Echo at the Galactic Center: The Glorious Past of Sgr A* Preserved by Molecular Clouds. *ApJ*, 714:732–747, May 2010. doi: 10.1088/0004-637X/714/1/732.
- E. Pouliaxis, I. Georgantopoulos, A. Z. Bonanos, et al. Robust Identification of Active Galactic Nuclei through HST Optical Variability in GOODS-S: Comparison with the X-ray and mid-IR Selected Samples. *arXiv e-prints*, May 2019.
- K. A. Pounds, K. Nandra, G. C. Stewart, I. M. George, & A. C. Fabian. X-ray reflection from cold matter in the nuclei of active galaxies. *Nature*, 344:132, Mar. 1990. doi: 10.1038/344132a0.
- A. Ptak, Y. Terashima, L. C. Ho, & E. Quataert. Testing Radiatively Inefficient Accretion Flow Theory: An XMM-Newton Observation of NGC 3998. *ApJ*, 606:173–184, May 2004. doi: 10.1086/382940.
- J. T. Radomski, C. Packham, N. A. Levenson, et al. Gemini Imaging of Mid-Infrared Emission from the Nuclear Region of Centaurus A. *ApJ*, 681:141–150, July 2008. doi: 10.1086/587771.
- D. A. Rafferty, B. R. McNamara, P. E. J. Nulsen, & M. W. Wise. The Feedback-regulated Growth of Black Holes and Bulges through Gas Accretion and Starbursts in Cluster Central Dominant Galaxies. *ApJ*, 652:216–231, Nov. 2006. doi: 10.1086/507672.
- D. A. Rafferty, W. N. Brandt, D. M. Alexander, et al. Supermassive Black Hole Growth in Starburst Galaxies over Cosmic Time: Constraints from the Deepest Chandra Fields. *ApJ*, 742:3, Nov. 2011. doi: 10.1088/0004-637X/742/1/3.
- C. Ramos Almeida, & C. Ricci. Nuclear obscuration in active galactic nuclei. *Nature Astronomy*, 1:679–689, Oct. 2017. doi: 10.1038/s41550-017-0232-z.

Bibliography

- H. Rampadarath, M. A. Garrett, G. I. G. Józsa, et al. Hanny's Voorwerp . Evidence of AGN activity and a nuclear starburst in the central regions of IC 2497. *A&A*, 517:L8, July 2010. doi: 10.1051/0004-6361/201014782.
- P. Ranalli, A. Comastri, & G. Setti. The 2-10 keV luminosity as a Star Formation Rate indicator. *aap*, 399:39–50, Feb. 2003. doi: 10.1051/0004-6361:20021600.
- A. Rau, S. R. Kulkarni, N. M. Law, et al. Exploring the Optical Transient Sky with the Palomar Transient Factory. *PASP*, 121:1334, Dec. 2009. doi: 10.1086/605911.
- M. J. Rees. Tidal disruption of stars by black holes of 10 to the 6th-10 to the 8th solar masses in nearby galaxies. *Nature*, 333:523–528, June 1988. doi: 10.1038/333523a0.
- R. A. Remillard, & J. E. McClintock. X-Ray Properties of Black-Hole Binaries. *ARA&A*, 44:49–92, Sept. 2006. doi: 10.1146/annurev.astro.44.051905.092532.
- C. S. Reynolds, & M. C. Miller. The Time Variability of Geometrically Thin Black Hole Accretion Disks. I. The Search for Modes in Simulated Disks. *ApJ*, 692:869–886, Feb. 2009. doi: 10.1088/0004-637X/692/1/869.
- C. Ricci, R. Walter, T. J.-L. Courvoisier, & S. Paltani. Reflection in Seyfert galaxies and the unified model of AGN. *A&A*, 532:A102, Aug. 2011. doi: 10.1051/0004-6361/201016409.
- C. Ricci, Y. Ueda, S. Paltani, et al. Iron $K\alpha$ emission in type-I and type-II active galactic nuclei. *MNRAS*, 441:3622–3633, July 2014. doi: 10.1093/mnras/stu735.
- C. Ricci, Y. Ueda, M. J. Koss, et al. Compton-thick Accretion in the Local Universe. *ApJ*, 815:L13, Dec. 2015. doi: 10.1088/2041-8205/815/1/L13.
- C. Ricci, F. E. Bauer, P. Arevalo, et al. IC 751: A New Changing Look AGN Discovered by NuSTAR. *ApJ*, 820:5, Mar. 2016a. doi: 10.3847/0004-637X/820/1/5.
- C. Ricci, F. E. Bauer, E. Treister, et al. NUSTAR Unveils a Heavily Obscured Low-luminosity Active Galactic Nucleus in the Luminous Infrared Galaxy NGC 6286. *ApJ*, 819:4, Mar. 2016b. doi: 10.3847/0004-637X/819/1/4.
- C. Ricci, B. Trakhtenbrot, M. J. Koss, et al. BAT AGN Spectroscopic Survey. V. X-Ray Properties of the Swift/BAT 70-month AGN Catalog. *ApJS*, 233:17, Dec. 2017. doi: 10.3847/1538-4365/aa96ad.
- G. Richards, M. Lacy, L. Storrie-Lombardi, et al. Optical-IR SEDs of SDSS Quasars in the Spitzer First Look Survey. In L. Armus, & W. T. Reach, editors, *The Spitzer Space Telescope: New Views of the Cosmos*, volume 357 of *Astronomical Society of the Pacific Conference Series*, page 261, Dec. 2006.

- G. Risaliti, M. Elvis, G. Fabbiano, A. Baldi, & A. Zezas. Rapid Compton-thick/Compton-thin Transitions in the Seyfert 2 Galaxy NGC 1365. *ApJ*, 623:L93–L96, Apr. 2005. doi: 10.1086/430252.
- D. J. Rosario, P. Santini, D. Lutz, et al. The mean star formation rate of X-ray selected active galaxies and its evolution from $z \sim 2.5$: results from PEP-Herschel. *A&A*, 545:A45, Sept. 2012. doi: 10.1051/0004-6361/201219258.
- N. P. Ross, K. E. S. Ford, M. Graham, et al. A new physical interpretation of optical and infrared variability in quasars. *MNRAS*, 480:4468–4479, Nov. 2018. doi: 10.1093/mnras/sty2002.
- J. J. Ruan, S. F. Anderson, S. L. Cales, et al. Toward an Understanding of Changing-look Quasars: An Archival Spectroscopic Search in SDSS. *ApJ*, 826:188, Aug. 2016. doi: 10.3847/0004-637X/826/2/188.
- J. J. Ruan, S. F. Anderson, M. Eracleous, et al. The Analogous Structure of Accretion Flows in Supermassive and Stellar Mass Black Holes. *arXiv e-prints*, Mar. 2019.
- N. Rumbaugh, Y. Shen, E. Morganson, et al. Extreme Variability Quasars from the Sloan Digital Sky Survey and the Dark Energy Survey. *ApJ*, 854:160, Feb. 2018. doi: 10.3847/1538-4357/aaa9b6.
- J. C. Runnoe, S. Cales, J. J. Ruan, et al. Now you see it, now you don't: the disappearing central engine of the quasar J1011+5442. *MNRAS*, 455:1691–1701, Jan. 2016. doi: 10.1093/mnras/stv2385.
- E. E. Salpeter. Accretion of Interstellar Matter by Massive Objects. *ApJ*, 140:796–800, Aug. 1964. doi: 10.1086/147973.
- P. Sánchez-Sáez, P. Lira, J. Mejía-Restrepo, et al. The QUEST-La Silla AGN Variability Survey: Connection between AGN Variability and Black Hole Physical Properties. *ApJ*, 864:87, Sept. 2018. doi: 10.3847/1538-4357/aad7f9.
- P. Sánchez-Sáez, P. Lira, R. Cartier, et al. The QUEST-La Silla AGN Variability Survey: selection of AGN candidates through optical variability. *arXiv e-prints*, Apr. 2019.
- R. H. Sanders. Recurrent Seyfert activity in spiral galaxy nuclei. *Nature*, 294:427–429, Dec. 1981. doi: 10.1038/294427a0.
- L. F. Sartori, K. Schawinski, M. Koss, et al. Extended X-ray emission in the IC 2497 - Hanny's Voorwerp system: energy injection in the gas around a fading AGN. *MNRAS*, 457:3629–3636, Apr. 2016. doi: 10.1093/mnras/stw230.
- L. F. Sartori, K. Schawinski, M. J. Koss, et al. Joint NuSTAR and Chandra analysis of the obscured quasar in IC 2497 - Hanny's Voorwerp system. *MNRAS*, 474:2444–2451, Feb. 2018a. doi: 10.1093/mnras/stx2952.

Bibliography

- L. F. Sartori, K. Schawinski, B. Trakhtenbrot, et al. A model for AGN variability on multiple time-scales. *MNRAS*, 476:L34–L38, May 2018b. doi: 10.1093/mnrasl/sly025.
- L. F. Sartori, B. Trakhtenbrot, K. Schawinski, et al. A forward modelling approach to AGN variability – method description and early applications. Submitted to *ApJ*, 2019 submitted.
- K. Schawinski, D. Thomas, M. Sarzi, et al. Observational evidence for AGN feedback in early-type galaxies. *mnras*, 382:1415–1431, Dec. 2007. doi: 10.1111/j.1365-2966.2007.12487.x.
- K. Schawinski, D. A. Evans, S. Virani, et al. The Sudden Death of the Nearest Quasar. *ApJ*, 724:L30–L33, Nov. 2010a. doi: 10.1088/2041-8205/724/1/L30.
- K. Schawinski, C. M. Urry, S. Virani, et al. Galaxy Zoo: The Fundamentally Different Co-Evolution of Supermassive Black Holes and Their Early- and Late-Type Host Galaxies. *apj*, 711:284–302, Mar. 2010b. doi: 10.1088/0004-637X/711/1/284.
- K. Schawinski, M. Koss, S. Berney, & L. F. Sartori. Active galactic nuclei flicker: an observational estimate of the duration of black hole growth phases of $\sim 10^5$ yr. *MNRAS*, 451:2517–2523, Aug. 2015. doi: 10.1093/mnras/stv1136.
- M. Schirmer, R. Diaz, K. Holhjem, N. A. Levenson, & C. Winge. A Sample of Seyfert-2 Galaxies with Ultraluminous Galaxy-wide Narrow-line Regions: Quasar Light Echoes? *ApJ*, 763:60, Jan. 2013. doi: 10.1088/0004-637X/763/1/60.
- M. Schirmer, S. Malhotra, N. A. Levenson, et al. About AGN ionization echoes, thermal echoes, and ionization deficits in low redshift Lyman-alpha blobs. *ArXiv e-prints*, July 2016.
- M. Schmidt. 3C 273 : A Star-Like Object with Large Red-Shift. *Nature*, 197:1040, Mar. 1963. doi: 10.1038/1971040a0.
- R. Schödel, T. Ott, R. Genzel, et al. Stellar Dynamics in the Central Arcsecond of Our Galaxy. *apj*, 596:1015–1034, Oct. 2003. doi: 10.1086/378122.
- T. Schreiber, & A. Schmitz. Improved Surrogate Data for Nonlinearity Tests. *Physical Review Letters*, 77:635–638, July 1996. doi: 10.1103/PhysRevLett.77.635.
- A. Schulze, & L. Wisotzki. Low redshift AGN in the Hamburg/ESO Survey . II. The active black hole mass function and the distribution function of Eddington ratios. *A&A*, 516:A87, June 2010. doi: 10.1051/0004-6361/201014193.
- A. Schulze, A. Bongiorno, I. Gavignaud, et al. The cosmic growth of the active black hole population at $1 < z < 2$ in zCOSMOS, VVDS and SDSS. *MNRAS*, 447:2085–2111, Mar. 2015. doi: 10.1093/mnras/stu2549.

- K. Schwarzschild. Über das Gravitationsfeld eines Massenpunktes nach der Einsteinschen Theorie. *Sitzungsberichte der Königlich Preussischen Akademie der Wissenschaften (Berlin)*, 1916, Seite 189-196, 1916.
- F. Schweizer, P. Seitzer, D. D. Kelson, E. V. Villanueva, & G. L. Walth. The [O III] Nebula of the Merger Remnant NGC 7252: A Likely Faint Ionization Echo. *ApJ*, 773: 148, Aug. 2013. doi: 10.1088/0004-637X/773/2/148.
- B. Sesar, D. Svlković, Ž. Ivezić, et al. Variable Faint Optical Sources Discovered by Comparing the POSS and SDSS Catalogs. *AJ*, 131:2801–2825, June 2006. doi: 10.1086/503672.
- B. Sesar, Ž. Ivezić, R. H. Lupton, et al. Exploring the Variable Sky with the Sloan Digital Sky Survey. *AJ*, 134:2236–2251, Dec. 2007. doi: 10.1086/521819.
- R. O. Sexton, G. Canalizo, K. D. Hiner, et al. Stronger Constraints on the Evolution of the $M_{\text{BH}} - \sigma_*$ Relation up to $z \sim 0.6$. *arXiv e-prints*, May 2019.
- N. I. Shakura, & R. A. Sunyaev. Black holes in binary systems. Observational appearance. *A&A*, 24:337–355, 1973.
- L. Shao, D. Lutz, R. Nordon, et al. Star formation in AGN hosts in GOODS-N. *A&A*, 518:L26, July 2010. doi: 10.1051/0004-6361/201014606.
- B. J. Shappee, D. Grupe, S. Mathur, et al. Swift Monitoring of the AGN Outburst in NGC2617: Significant X-ray and UV Brightening. *The Astronomer's Telegram*, 5059, May 2013.
- B. J. Shappee, J. L. Prieto, D. Grupe, et al. The Man behind the Curtain: X-Rays Drive the UV through NIR Variability in the 2013 Active Galactic Nucleus Outburst in NGC 2617. *ApJ*, 788:48, June 2014. doi: 10.1088/0004-637X/788/1/48.
- Y. Shen. The mass of quasars. *Bulletin of the Astronomical Society of India*, 41:61–115, Mar. 2013.
- Y. Shen, G. T. Richards, M. A. Strauss, et al. A Catalog of Quasar Properties from Sloan Digital Sky Survey Data Release 7. *ApJS*, 194:45, June 2011. doi: 10.1088/0067-0049/194/2/45.
- Z. Sheng, T. Wang, N. Jiang, et al. Mid-infrared Variability of Changing-look AGNs. *ApJ*, 846:L7, Sept. 2017. doi: 10.3847/2041-8213/aa85de.
- G. A. Shields. Thermal continuum from accretion disks in quasars. *Nature*, 272:706–708, Apr. 1978. doi: 10.1038/272706a0.
- X. W. Shu, T. Yaqoob, & J. X. Wang. The Cores of the Fe $K\alpha$ Lines in Active Galactic Nuclei: An Extended Chandra High Energy Grating Sample. *ApJS*, 187:581–606, Apr. 2010. doi: 10.1088/0067-0049/187/2/581.

Bibliography

- A. Shulevski, R. Morganti, P. D. Barthel, et al. AGN duty cycle estimates for the ultra-steep spectrum radio relic VLSS J1431.8+1331. *A&A*, 583:A89, Nov. 2015a. doi: 10.1051/0004-6361/201525632.
- A. Shulevski, R. Morganti, P. D. Barthel, et al. The peculiar radio galaxy 4C 35.06: a case for recurrent AGN activity? *A&A*, 579:A27, July 2015b. doi: 10.1051/0004-6361/201425416.
- A. Shulevski, R. Morganti, J. J. Harwood, et al. Radiative age mapping of the remnant radio galaxy B2 0924+30: the LOFAR perspective. *A&A*, 600:A65, Apr. 2017. doi: 10.1051/0004-6361/201630008.
- A. Siemiginowska, & M. Elvis. Deriving the Quasar Luminosity Function from Accretion-Disk Instabilities. *ApJ*, 482:L9–L12, June 1997. doi: 10.1086/310673.
- D. Sijacki, M. Vogelsberger, S. Genel, et al. The Illustris simulation: the evolving population of black holes across cosmic time. *MNRAS*, 452:575–596, Sept. 2015. doi: 10.1093/mnras/stv1340.
- J. Silk, & M. J. Rees. Quasars and galaxy formation. *A&A*, 331:L1–L4, Mar. 1998.
- T. Simm, M. Salvato, R. Saglia, et al. Pan-STARRS1 variability of XMM-COSMOS AGN. II. Physical correlations and power spectrum analysis. *A&A*, 585:A129, Jan. 2016. doi: 10.1051/0004-6361/201527353.
- C. Simpson. The luminosity dependence of the type 1 active galactic nucleus fraction. *MNRAS*, 360:565–572, June 2005. doi: 10.1111/j.1365-2966.2005.09043.x.
- K. L. Smith, R. F. Mushotzky, P. T. Boyd, et al. The Kepler Light Curves of AGN: A Detailed Analysis. *ApJ*, 857:141, Apr. 2018. doi: 10.3847/1538-4357/aab88d.
- M. A. Sobolewska, A. Siemiginowska, & M. Gierliński. Simulated spectral states of active galactic nuclei and observational predictions. *MNRAS*, 413:2259–2268, May 2011. doi: 10.1111/j.1365-2966.2011.18302.x.
- D. I. Solovyov, & O. V. Verkhodanov. A search for faint giant radio galaxies in the NVSS survey. *Astrophysical Bulletin*, 66:416–423, Oct. 2011. doi: 10.1134/S1990341311040031.
- A. Soltan. Masses of quasars. *mnras*, 200:115–122, July 1982.
- V. Springel, T. Di Matteo, & L. Hernquist. Modelling feedback from stars and black holes in galaxy mergers. *MNRAS*, 361:776–794, Aug. 2005. doi: 10.1111/j.1365-2966.2005.09238.x.
- D. Stern, P. Eisenhardt, V. Gorjian, et al. Mid-Infrared Selection of Active Galaxies. *ApJ*, 631:163–168, Sept. 2005. doi: 10.1086/432523.

- D. Stern, R. J. Assef, D. J. Benford, et al. Mid-infrared Selection of Active Galactic Nuclei with the Wide-Field Infrared Survey Explorer. I. Characterizing WISE-selected Active Galactic Nuclei in COSMOS. *ApJ*, 753:30, July 2012. doi: 10.1088/0004-637X/753/1/30.
- D. Stern, B. McKernan, M. J. Graham, et al. A Mid-IR Selected Changing-Look Quasar and Physical Scenarios for Abrupt AGN Fading. *ArXiv e-prints*, May 2018.
- S. Stierwalt, L. Armus, J. A. Surace, et al. Mid-infrared Properties of Nearby Luminous Infrared Galaxies. I. Spitzer Infrared Spectrograph Spectra for the GOALS Sample. *ApJS*, 206:1, May 2013. doi: 10.1088/0067-0049/206/1/1.
- A. Stockton, H. Fu, & G. Canalizo. QSO extended emission-line regions. *New A Rev.*, 50:694–700, Nov. 2006. doi: 10.1016/j.newar.2006.06.024.
- M. Su, T. R. Slatyer, & D. P. Finkbeiner. Giant Gamma-ray Bubbles from Fermi-LAT: Active Galactic Nucleus Activity or Bipolar Galactic Wind? *ApJ*, 724:1044–1082, Dec. 2010. doi: 10.1088/0004-637X/724/2/1044.
- K. Suberlak, Ž. Ivezić, C. L. MacLeod, M. Graham, & B. Sesar. Solving the puzzle of discrepant quasar variability on monthly time-scales implied by SDSS and CRTS data sets. *MNRAS*, 472:4870–4877, Dec. 2017. doi: 10.1093/mnras/stx2310.
- M. Suganuma, Y. Yoshii, Y. Kobayashi, et al. Reverberation Measurements of the Inner Radius of the Dust Torus in Nearby Seyfert 1 Galaxies. *ApJ*, 639:46–63, Mar. 2006. doi: 10.1086/499326.
- R. A. Sunyaev, & L. G. Titarchuk. Comptonization of X-rays in plasma clouds - Typical radiation spectra. *A&A*, 86:121–138, June 1980.
- D. Syer, C. J. Clarke, & M. J. Rees. Star-disc interactions near a massive black hole. *MNRAS*, 250:505–512, June 1991. doi: 10.1093/mnras/250.3.505.
- Y. Terashima, N. Iyomoto, L. C. Ho, & A. F. Ptak. X-Ray Properties of LINERs and Low-Luminosity Seyfert Galaxies Observed with ASCA. I. Observations and Results. *ApJS*, 139:1–36, Mar. 2002. doi: 10.1086/324373.
- R. Teyssier. Cosmological hydrodynamics with adaptive mesh refinement. A new high resolution code called RAMSES. *A&A*, 385:337–364, Apr. 2002. doi: 10.1051/0004-6361:20011817.
- J. Timmer, & M. Koenig. On generating power law noise. *A&A*, 300:707, Aug. 1995.
- J. E. Tohline, & D. E. Osterbrock. Variation of the spectrum of the Seyfert galaxy NGC 7603. *ApJ*, 210:L117–L120, Dec. 1976. doi: 10.1086/182317.

Bibliography

- B. Trakhtenbrot, & H. Netzer. Black hole growth to $z = 2$ - I. Improved virial methods for measuring M_{BH} and L/L_{Edd} . *MNRAS*, 427:3081–3102, Dec. 2012. doi: 10.1111/j.1365-2966.2012.22056.x.
- B. Trakhtenbrot, F. Civano, C. M. Urry, et al. Faint COSMOS AGNs at z 3.3. I. Black Hole Properties and Constraints on Early Black Hole Growth. *ApJ*, 825:4, July 2016. doi: 10.3847/0004-637X/825/1/4.
- B. Trakhtenbrot, C. Ricci, M. J. Koss, et al. BAT AGN Spectroscopic Survey (BASS) - VI. The Γ_X - L/L_{Edd} relation. *MNRAS*, 470:800–814, Sept. 2017. doi: 10.1093/mnras/stx1117.
- B. Trakhtenbrot, I. Arcavi, C. L. MacLeod, et al. 1ES 1927+654: an AGN Caught Changing Look on a Timescale of Months. *arXiv e-prints*, Mar. 2019.
- E. Treister, & C. M. Urry. The Cosmic History of Black Hole Growth from Deep Multiwavelength Surveys. *Advances in Astronomy*, 2012:516193, 2012. doi: 10.1155/2012/516193.
- E. Treister, G. C. Privon, L. F. Sartori, et al. Optical, near-IR and sub-mm IFU Observations of the nearby dual AGN Mrk 463. *ArXiv e-prints*, Jan. 2018.
- D. Trevese, K. Boutsia, F. Vagnetti, E. Cappellaro, & S. Puccetti. Variability-selected active galactic nuclei from supernova search in the Chandra deep field south. *A&A*, 488:73–81, Sept. 2008. doi: 10.1051/0004-6361:200809884.
- H. Tsunemi, K. Mori, E. Miyata, et al. Improvement of the Spatial Resolution of the ACIS Using Split-Pixel Events. *ApJ*, 554:496–504, June 2001. doi: 10.1086/321338.
- G. E. Uhlenbeck, & L. S. Ornstein. On the Theory of the Brownian Motion. *Physical Review*, 36:823–841, Sept. 1930. doi: 10.1103/PhysRev.36.823.
- M.-H. Ulrich, L. Maraschi, & C. M. Urry. Variability of Active Galactic Nuclei. *ARA&A*, 35:445–502, 1997. doi: 10.1146/annurev.astro.35.1.445.
- C. M. Urry, & P. Padovani. Unified Schemes for Radio-Loud Active Galactic Nuclei. *pasph*, 107:803, Sept. 1995. doi: 10.1086/133630.
- P. Uttley, & I. M. McHardy. A Brief Review of Long-Term X-Ray and Optical Variability in Radio-Quiet AGN. *Progress of Theoretical Physics Supplement*, 155:170–177, 2004. doi: 10.1143/PTPS.155.170.
- P. Uttley, I. M. McHardy, & I. E. Papadakis. Measuring the broad-band power spectra of active galactic nuclei with RXTE. *MNRAS*, 332:231–250, May 2002. doi: 10.1046/j.1365-8711.2002.05298.x.

- P. Uttley, R. Edelson, I. M. McHardy, B. M. Peterson, & A. Markowitz. Correlated Long-Term Optical and X-Ray Variations in NGC 5548. *ApJ*, 584:L53–L56, Feb. 2003. doi: 10.1086/373887.
- M. van der Klis. Quantifying Rapid Variability in Accreting Compact Objects. In G. J. Babu, & E. D. Feigelson, editors, *Statistical Challenges in Modern Astronomy II*, page 321, 1997.
- S. van Velzen, G. R. Farrar, S. Gezari, et al. Optical Discovery of Probable Stellar Tidal Disruption Flares. *ApJ*, 741:73, Nov. 2011. doi: 10.1088/0004-637X/741/2/73.
- D. E. Vanden Berk, G. T. Richards, A. Bauer, et al. Composite Quasar Spectra from the Sloan Digital Sky Survey. *AJ*, 122:549–564, Aug. 2001. doi: 10.1086/321167.
- D. E. Vanden Berk, B. C. Wilhite, R. G. Kron, et al. The Ensemble Photometric Variability of $\sim 25,000$ Quasars in the Sloan Digital Sky Survey. *ApJ*, 601:692–714, Feb. 2004. doi: 10.1086/380563.
- J. Vanderplas, A. Connolly, Ž. Ivezić, & A. Gray. Introduction to astroml: Machine learning for astrophysics. In *Conference on Intelligent Data Understanding (CIDU)*, pages 47–54, oct. 2012. doi: 10.1109/CIDU.2012.6382200.
- A. N. Vantyghem, B. R. McNamara, H. R. Russell, et al. Cycling of the powerful AGN in MS 0735.6+7421 and the duty cycle of radio AGN in clusters. *MNRAS*, 442:3192–3205, Aug. 2014. doi: 10.1093/mnras/stu1030.
- R. V. Vasudevan, & A. C. Fabian. Simultaneous X-ray/optical/UV snapshots of active galactic nuclei from XMM-Newton: spectral energy distributions for the reverberation mapped sample. *MNRAS*, 392:1124–1140, Jan. 2009. doi: 10.1111/j.1365-2966.2008.14108.x.
- S. Vaughan, R. Edelson, R. S. Warwick, & P. Uttley. On characterizing the variability properties of X-ray light curves from active galaxies. *MNRAS*, 345:1271–1284, Nov. 2003. doi: 10.1046/j.1365-2966.2003.07042.x.
- S. Vaughan, P. Uttley, A. G. Markowitz, et al. False periodicities in quasar time-domain surveys. *MNRAS*, 461:3145–3152, Sept. 2016. doi: 10.1093/mnras/stw1412.
- M.-P. Véron-Cetty, & P. Véron. A catalogue of quasars and active nuclei: 13th edition. *A&A*, 518:A10, July 2010. doi: 10.1051/0004-6361/201014188.
- C. Vignali, W. N. Brandt, & D. P. Schneider. X-Ray Emission from Radio-Quiet Quasars in the Sloan Digital Sky Survey Early Data Release: The α_{ox} Dependence upon Ultraviolet Luminosity. *AJ*, 125:433–443, Feb. 2003. doi: 10.1086/345973.
- M. Villar-Martín, A. Cabrera-Lavers, A. Humphrey, et al. A 100 kpc nebula associated with the ‘Teacup’ fading quasar. *MNRAS*, 474:2302–2312, Feb. 2018. doi: 10.1093/mnras/stx2911.

Bibliography

- C. Villforth, A. M. Koekemoer, & N. A. Grogin. A New Extensive Catalog of Optically Variable Active Galactic Nuclei in the GOODS Fields and a New Statistical Approach to Variability Selection. *ApJ*, 723:737–754, Nov. 2010. doi: 10.1088/0004-637X/723/1/737.
- J. Wang, D. W. Xu, & J. Y. Wei. Identification of SDSS J141324.27+530527.0 as a New Changing-look Quasar with a Turn-on Transition. *ApJ*, 858:49, May 2018. doi: 10.3847/1538-4357/aab88b.
- A. K. Weigel, K. Schawinski, N. Caplar, et al. AGNs and Their Host Galaxies in the Local Universe: Two Mass-independent Eddington Ratio Distribution Functions Characterize Black Hole Growth. *ApJ*, 845:134, Aug. 2017. doi: 10.3847/1538-4357/aa803b.
- M. C. Weisskopf, H. D. Tananbaum, L. P. Van Speybroeck, & S. L. O’Dell. Chandra X-ray Observatory (CXO): overview. In J. E. Truemper, & B. Aschenbach, editors, *X-Ray Optics, Instruments, and Missions III*, volume 4012 of Proc. SPIE, pages 2–16, July 2000. doi: 10.1117/12.391545.
- R. L. White, R. H. Becker, M. D. Gregg, et al. The FIRST Bright Quasar Survey. II. 60 Nights and 1200 Spectra Later. *ApJS*, 126:133–207, Feb. 2000. doi: 10.1086/313300.
- D. R. Wik, A. Hornstrup, S. Molendi, et al. NuSTAR Observations of the Bullet Cluster: Constraints on Inverse Compton Emission. *ApJ*, 792:48, Sept. 2014. doi: 10.1088/0004-637X/792/1/48.
- B. C. Wilhite, R. J. Brunner, C. J. Grier, D. P. Schneider, & D. E. vanden Berk. On the variability of quasars: a link between the Eddington ratio and optical variability? *MNRAS*, 383:1232–1240, Jan. 2008. doi: 10.1111/j.1365-2966.2007.12655.x.
- E. L. Wright, P. R. M. Eisenhardt, A. K. Mainzer, et al. The Wide-field Infrared Survey Explorer (WISE): Mission Description and Initial On-orbit Performance. *AJ*, 140:1868, Dec. 2010. doi: 10.1088/0004-6256/140/6/1868.
- G. Yang, W. N. Brandt, D. M. Alexander, et al. Evident black hole-bulge coevolution in the distant universe. *MNRAS*, 485:3721–3737, May 2019. doi: 10.1093/mnras/stz611.
- Q. Yang, X.-B. Wu, X. Fan, et al. Discovery of 21 New Changing-look AGNs in the Northern Sky. *ApJ*, 862:109, Aug. 2018. doi: 10.3847/1538-4357/aaca3a.
- D. G. York, J. Adelman, J. E. Anderson, Jr., et al. The Sloan Digital Sky Survey: Technical Summary. *aj*, 120:1579–1587, Sept. 2000. doi: 10.1086/301513.
- Q. Yu, & S. Tremaine. Observational constraints on growth of massive black holes. *MNRAS*, 335:965–976, Oct. 2002. doi: 10.1046/j.1365-8711.2002.05532.x.
- F. Yuan, & R. Narayan. Hot Accretion Flows Around Black Holes. *ARA&A*, 52:529–588, Aug. 2014. doi: 10.1146/annurev-astro-082812-141003.

- A. A. Zdziarski. Hot accretion discs with thermal Comptonization and advection in luminous black hole sources. *MNRAS*, 296:L51–L55, June 1998. doi: 10.1046/j.1365-8711.1998.01682.x.
- M. Zetzl, W. Kollatschny, M. W. Oehmlich, et al. Long-term optical, UV, and X-ray continuum variations in the changing-look AGN HE 1136-2304. *A&A*, 618:A83, Oct. 2018. doi: 10.1051/0004-6361/201732506.
- S. Zhang, C. J. Hailey, K. Mori, et al. Hard X-Ray Morphological and Spectral Studies of the Galactic Center Molecular Cloud Sgr B2: Constraining Past Sgr A* Flaring Activity. *ApJ*, 815:132, Dec. 2015. doi: 10.1088/0004-637X/815/2/132.
- Y. Zu, C. S. Kochanek, S. Kozłowski, & A. Udalski. Is Quasar Optical Variability a Damped Random Walk? *ApJ*, 765:106, Mar. 2013. doi: 10.1088/0004-637X/765/2/106.
- K. Zubovas, & A. King. Clearing Out a Galaxy. *ApJ*, 745:L34, Feb. 2012. doi: 10.1088/2041-8205/745/2/L34.
- K. Zubovas, & A. R. King. The M - σ relation between supermassive black holes and their host galaxies. *General Relativity and Gravitation*, 51:65, May 2019. doi: 10.1007/s10714-019-2549-7.
- W. Zuo, X.-B. Wu, Y.-Q. Liu, & C.-L. Jiao. The Correlations between Optical Variability and Physical Parameters of Quasars in SDSS Stripe 82. *ApJ*, 758:104, Oct. 2012. doi: 10.1088/0004-637X/758/2/104.

List of symbols

\dot{m}_{BH}	Black hole accretion rate, usually measured in $M_{\odot} \text{ yr}^{-1}$
c	Speed of light, $\sim 2.99 \times 10^8 \text{ m s}^{-1}$
λ_{Edd}	Eddington ratio, also referred to as L/L_{Edd}
η	Radiative efficiency in SMBHs, usually ~ 0.1
Γ	Photon index
L_{bol}	Bolometric luminosity, usually in erg s^{-1}
L_{Edd}	Eddington luminosity, usually in erg s^{-1}
M_{BH}	Black hole mass, usually measured in M_{\odot}
M_{\odot}	Mass of the Sun, $\sim 1.9 \times 10^{30} \text{ kg}$

List of abbreviations

AGN	Active galactic nucleus
ASAS-SN	All-Sky Automated Survey for SuperNovae
BASS	Black hole
BAT	Burst Alert Telescope
BH	BAT AGN Spectroscopic Survey
BHARD	Black hole accretion rate density
BLR	Broad line region
BPT	Baldwin-Philipp-Terlevich diagram (Baldwin et al. 1981)
CL-AGN	Changing look AGN
CL-QSO	Changing look QSO
CRTS	Catalina Real-Time Transient Survey
DRW	Damped random walk
EELR	Extended emission line region
ER	Eddington ratio
ERDF	Eddington ratio distribution function
eROSITA	Extended ROentgen Survey with an Imaging Telescope Array
ETHZ	Eidgenössische Technische Hochschule Zürich
GPU	Graphics processing unit
HV	Hanny's Voorwerp
iPTF	Intermediate Palomar Transient Factory
LSST	Large Synoptic Survey Telescope
NLR	Narrow line region
NuSTAR	Nuclear Spectroscopic Telescope Array
PDF	Probability density function
POSS	Palomar Observatory Sky Survey
PSD	Power spectral density
PSF	Point spread function
PTF	Palomar Transient Factory

List of abbreviations

QSO	Quasi stellar object
SDSS	Sloan Digital Sky Survey
SF	Structure function
SFRD	Star formation rate density
SMBH	Supermassive black hole
TDSS	Time-Domain Spectroscopic Survey
VP	Voorwerp
XMM	X-ray Multi-Mirror Mission
ZTF	Zwicky Transient Facility

Acknowledgements

La vita è un'opportunità, coglila.

Madre Teresa di Calcutta

I would like to express my deep gratitude to my supervisor, Kevin Schawinski, for guiding me through my PhD journey. Thanks for the scientific supervision, the support and the many opportunities you gave me. As you once said, the PhD should not only be a period where you learn scientific notions, but also where you grow as a human being. During these years I discussed and collaborated with scientists all over the world, visited places I would probably never have seen, tried new foods, learned new languages, and much more. I am sure that all these experiences helped me growing as a scientist and also made me a different (probably better) person, with skills which will be extremely valuable for my future.

Gracias to Ezequiel Treister for mentoring and supporting me during the Master and the PhD, and for hosting me at the Pontificia Universidad Católica de Chile. I always enjoyed working with you, and our discussions about the different projects I was involved in, as well as academic life in general, taught me a lot about how to do science and how to present science. I am also very grateful for all what you and María José did to make me feel a bit at home in Chile.

I am grateful to Alexandre Refregier and Adam Amara for hosting me in the Cosmology Group. Students are very important for you, and I really appreciate this.

My deep gratitude goes to Benny Trakhtenbrot. Although you were never officially my supervisor, you have been a great mentor for me, from whom I've learned a lot about science and life. Thanks for teaching me how to be and how to behave like a scientist. And *toda* for making me discover Israel and your culture, and for making me better know and appreciate still more “my” Switzerland.

Through the years in the astronomy community many postdocs, fellows, senior scientists and professors were important for me in many ways. I would like to especially thank Mike Koss, Kyuseok Oh, Claudio Ricci, Sascha Quanz, Meg Urry, Ce Zhang, Masato

Acknowledgements

Onodera, Will Hartley, Kurt Soto, William Keel, Peter Maksym and Megan Argo. Each of you contributed a bit to my scientific growth and I am very grateful for this.

My ETH journey would not have been the same without the other past and present astro PhD students. *Danke* to my “black hole colleague” Anna Weigel for sharing with me a lot of adventures all over the world. *Grazie* to my officemate, Federica Tarsitano. I admire your attitude towards life and science, and I feel I’ve learned a lot from you. And clearly *grazie* to you and to our officemate Gabriele Cugno, who also had the “privilege” (or disadvantage?) to be my first student, for all the funny moments in our beautiful office. *Grazie* to Martina Fagioli for always being there when I needed. *Grazie* to Andrina Nicola for being a great friend and flatmate. *Grazie* to Luca Tortorelli for never letting us lose our smiles, even in difficult times. Your coffee for sure contributed to create a great atmosphere in our PhD corridor. *Hvala* to Neven Caplar for all the help and interesting discussions about AGN variability and science in general. *Grazie* to Claudio Bruderer for all the help with programming and installing, and for helping me explaining to everybody how nice Ticino is. Also, I want to thank you and Sabastian Seehars for providing the thesis template. *Danke* to Sandro Tacchella, I’ve always seen you as a role model and I’ve learned a lot from you about science and outreach. *Gracias* to Sofía Gallego for making me learn more about Chile even when I was not there. *Danke* to Rudolf Bär for being the most amazing “student” of our group and a model for all of us. And thanks to Tim Lichtenberg, Kyriakos Flouris, Andreas Faisst, Simon Birrer, Larry Sin, Jörg Herbel, Raphaël Sgier, Saeed Sarpas, Natalia Engler, Pawel Biernacki, Valentina Tamburello, Antonio Garufi, Maddalena Reggiani, Linda Baronchelli, Isabella Lamperti, Tamara Rahimi, Dennis Turp & Dominic Stark (but now I recognise you!), Quentin Pognan, Benjamin Strittmatter, Robin Petermann and all the other PhD, Master and Bachelor students for sharing part of your journey with me.

Research in academia would not be possible without the support of all the administrative and technical staff. I am very grateful to all the astronomy administrative assistants, in particular to Marianne Chiesi, Milena Ramirez-Barrero, Annie Agius and Esther Christen. We don’t know exactly everything what you do, but you always have an answer or a solution for every question, and I am sure that the institute would not survive without you. I want to thank the ISG staff, in particular Gürkan Myczko and Christian Herzog, for the technical support. My gratitude also goes to Catherine Arnold and Roland Munz from HR for helping me set up everything for my stay in Chile.

In addition to the astronomy professors, many physics professors had an important role during my time at ETH, and I am very grateful to all of them. In particular, I would like to thank Rainer Wallny for helping me “reorganise” my last year at ETH, and Leonardo Degiorgi. Since the first time I’ve met you during my high school exams I’ve seen how much you care about Ticino students (and students in general), and it was nice to see a “friendly known face” when I first arrived at ETH.

PhD life is not only work, and I wish to thank all the friends in and outside academia who shared with me this important part of my life. It would be impossible to name all of you here, but you all made this period special. A huge *grazie* goes to all the students who, for a long or short period, joined the “CLU family”, in particular to Clara Seitz, Zeno Antonini, Gioele Janett, Ilaria Affolter-Arigoni, Veronica Michel, Alberto Montefusco, Massimiliano Bertacchi, Ignazio Beghi, Maria Colombo, Simone Gatti, Claudia García, Fabiola Mattarelli and Bernardo Laffranchini. The dinners and all the moments I shared with you were fun and deep at the same moment, and I am grateful for the time we spent together. *Gracias* to all the PUC students, in particular to Diego Calderón, Rodrigo Carvajal, Felipe Gran, Gergely Hajdu, Camila Órdenes, Camila Navarrete, Ricardo Pantoja, Jonathan Quirola, Astor Sandoval, Andrés Scherer, Carolina Andonie, Katerine Joachimi, Julio Olivares, Dusán Tubín, Tianwen Cao, Vania Rodríguez and Nicolas Meza, for welcoming me in Santiago de Chile. *Grazie* to Demetra DeCicco, Federica Ricci, Fabio Vito, Giuseppe D’Ago, Giacomo Venturi, Chiara Mazzucchelli, Rosamaria Carraro, Lucia Guaita and the whole “Barrio Italia” for making me feel the Italian hospitality and cheerfulness also at the other side of the world. *Grazie* to Laura Tomatis for everything you are doing for us.

My sincere thanks go to Andrea (Ben) Soranno, Don Rolando Leo, Don Tomasz Tomczyk and Father David Brown SJ for showing me how religion, science and daily life are deeply interconnected and important one for the other. The discussions I had with all of you had a big impact on how I experienced my PhD journey.

A special thank you goes to Aleksandar Aleksandrović for being with me and supporting me in all the important decisions I had to take in the last year. Your attitude and your music make me appreciate what I have still more. *Hvala*.

My deepest gratitude goes to my Family: my parents Ivano and Gabriella and my siblings Gino and Zita. You supported and advised me during every and each step of my life and I could not have reached this achievement without you. *Grazie, Vargaltsgott*.

Curriculum Vitae

Lia Federica Sartori

Sentée dar Lagh
6945 Origlio, Switzerland
Phone: +41 79 266 71 57
E-Mail: sartori.lia@gmail.com

Born on October 26 1990, from Bosco/Gurin TI (Switzerland)

Education

- | | |
|-----------------|---|
| 09.2014–present | Ph.D. student, ETH Zurich, Galaxy and Black Hole Astrophysics Group |
| 10.2018–present | Research Internship at the Pontificia Universidad Católica, Santiago de Chile |
| 09.2012–07.2014 | M.Sc. in Physics, ETH Zurich (with distinction) |
| 03.2014–07.2014 | M.Sc. Thesis research project at Universidad de Concepción, Chile |
| 09.2009–08.2012 | B.Sc. in Physics, ETH Zurich |

Honors and awards

- | | |
|--------------|--|
| 2017 | MERAC Funding and Travel Award |
| 2015, 2017 | Swiss Society for Astrophysics and Astronomy travel support grant for young scientists |
| 2014 | Swiss Study Foundation Travel Grant |
| 2009–present | Fellow of the Swiss Study Foundation |
| 2009 | Wegelin & Co. Banchieri Privati Prize |

Curriculum Vitae

- 2009 Ezio Fioravanzo Prize, Tessin Astronomy Society
- 2009 National Contest Swiss Youth in Science: Excellence mention; Special Prize International Year of Astronomy 2009; Metrohm Foundation award

Mentoring

- 2017–2018 Robin Petermann, Undergraduate project, *An IFU analysis of switch-on AGN candidates in the BASS sample*
- 2015–2017 Rudolf Baer, Research project, *Active galactic nuclei from He II: a more complete census of AGN in SDSS galaxies yields a new population of low-luminosity AGN in highly star-forming galaxies*
- 2016 Dario Kermanschah, Undergraduate project, *Analysing IFU data of optically elusive AGN*
- 2015–2016 Andrea Scanzio, M.Sc. Thesis, *Constraining eLISA gravitational waves detection rate using recoil black holes found with citizen science*
- 2015–2016 Philipp Bernhard, M.Sc. Thesis, *Simulating the effect of AGN radiation on the gas ionisation in the host galaxy*
- 2015–2016 Gabriele Cugno, Undergraduate project, *XMM and Chandra analysis of nearby dwarf galaxies hosting AGN candidates with possible mid-IR deficit*

Teaching

- Fall 2014-2017 Observational Techniques in Astrophysics, graduate course, Teaching assistant & substitute lecturer
- Spring 2016, 2017 Black Hole Astrophysics, graduate course, Teaching assistant & substitute lecturer
- Fall 2015, 2016 Astroweek, Astronomy advanced physics lab for undergraduate students, Instructor
- Spring 2018 Physics I for Earth Sciences and Environmental System Science, undergraduate course, Teaching assistant
- Spring 2015 Physics III for Mechanical and Process Engineering, undergraduate course, Teaching assistant

Attended conferences and meetings

- March 2018 Local hard X-ray selected AGN across the multi-wavelength spectrum,

- invited talk, Santiago de Chile, Chile
- January 2018 231th American Astronomical Society meeting, poster & oral contribution for BASS special session, National Harbor, MD
- October 2017 Swiss Society for Astrophysics and Astronomy General Assembly 2017, participant, Zurich, Switzerland
- July 2017 Unveiling the physics behind extreme AGN variability, talk, St. Thomas, U.S. Virgin Islands
- October 2016 Swiss Society for Astrophysics and Astronomy General Assembly 2016, participant, Davos, Switzerland
- June 2016 AGN what's in a name, poster, Garching, Germany
- November 2016 2nd Young Astronomers on Galactic Nuclei, invited talk, Paris, France
- March 2016 X-ray view of BH activity in the local Universe, talk, Zurich, Switzerland
- October 2015 1st Young Astronomer on Galactic Nuclei, invited talk, Milano, Italy
- September 2015 Demography and environment of AGN from multiwavelength surveys, talk, Chania, Crete
- March 2014 Sociedad Chilena de Astronomía meeting 2014, poster, Puerto Varas, Chile
- March 2014 Unveiling the AGN - galaxy evolution connection, poster, Puerto Varas, Chile
- January 2015 225th American Astronomical Society meeting, poster, Seattle, WA

Other seminars and talks

- May 2019 Pontificia Universidad Católica de Chile, Santiago de Chile, Chile, *IA-PUC Seminar*
- September 2018 Space Telescope Science Institute, Baltimore, MD, *AGN Journal Club*
- September 2018 Space Telescope Science Institute, Baltimore, MD, *Galaxy Journal Club*
- September 2018 Princeton University, Princeton, NJ, *Galread extragalactic discussion group*
- September 2018 University of California Santa Cruz, Santa Cruz, CA, *FLASH talk*
- September 2018 Caltech, Pasadena, CA, *IPAC science talk*
- September 2018 University of California Los Angeles, Los Angeles, CA, *Lunch talk*

Curriculum Vitae

September 2018	University of Washington, Seattle, WA, <i>DIRAC seminar</i>
May 2018	Vatican Observatory, Castel Gandolfo, Italy, <i>special seminar</i>
January 2018	Pontificia Universidad Católica de Chile, Santiago de Chile, Chile, <i>AGN meeting</i>
December 2017	Kyoto University, Kyoto, Japan, <i>Kyoto - Zurich AGN workshop</i>
November 2017	Istituto Ricerche Solari Locarno, Locarno Monti, Switzerland, <i>special seminar</i>
December 2017	ETH Zurich, Zurich, Switzerland, <i>research seminar</i>
December 2016	Pontificia Universidad Católica de Chile, Santiago de Chile, Chile, <i>Galaxy evolution discussion group</i>
November 2016	Pontificia Universidad Católica de Chile, Santiago de Chile, Chile, <i>seminar</i>
September 2016	University of Bern, Bern, Switzerland, <i>Astronomy seminar</i>
June 2016	University of Manchester, Manchester, UK, <i>Group lunch</i>
March 2016	University of Yale, New Haven, CT, <i>Yale BH group meeting</i>
March 2016	University of Yale, New Haven, CT, <i>Yale Galaxy Journal Club</i>
March 2016	Harvard Center for Astrophysics, Cambridge, MA, <i>special seminar</i>
March 2016	University of Alabama, Tuscaloosa, AL, <i>Astronomy seminar</i>
October 2015	Università di Milano Bicocca, Milano, Italy, <i>Astronomy seminar</i>
April 2015	Università di Ferrara, Milano, Italy, <i>Astronomy seminar</i>
April 2015	INAF Bologna, Bologna, Italy, <i>Astronomy seminar</i>
March 2015	Gemini Observatory, La Serena, Chile, <i>AGN ionisation workshop</i>
November 2014	ETH Zurich, Zurich, Switzerland, <i>research seminar</i>

Publications

14. **Sartori, L.F.**; Trakhtenbrot, B.; Schawinski, K.; Caplar, N.; Treister, E.; Zhang, C.; *A forward modelling approach to AGN variability – method description and early applications*; submitted
13. Baer, R.E.; Trakhtenbrot, B.; Oh, K.; Koss, M.J.; Wong, O.I.; Ricci, C.; Schawinski, K.; Weigel, A.K.; **Sartori, L.F.**; Ichikawa, K.; Secrest, N.J.; Stern, D.; Pacucci, F.; Mushotzky, R.; Powell, M.C.; Ricci, F.; Sani, E.; Smith, K.L.; Harrison, F.A.;

- Lamperti, I.; Urry, M.C.; *BAT AGN Spectroscopic Survey – XIII. The nature of the most luminous obscured AGN in the low-redshift universe*; submitted
12. Buchner, J.; Treister, E.; Bauer, F.E.; **Sartori, L.F.**; Schawinski, K.; *On the Prevalence of Supermassive Black Holes over Cosmic Time*; ApJ, 874, 117 (2019)
 11. Koss, M.J.; Blecha, L.; Bernhard, P.; Hung, C.-L.; Lu J.R.; Trakhtenbrot, B.; Treister, E.; Weigel, A.; **Sartori, L.F.**; Mushotzki, R.; Schawinski, K.; Ricci, C.; Veilleux, S.; Sanders, D.B.; *A population of luminous accreting black holes with hidden mergers*; Nature, 563, 214 (2018)
 10. **Sartori, L.F.**; Schawinski, K.; Trakhtenbrot, B.; Caplar, N.; Treister, E.; Koss, M. J.; Urry, C. M.; Zhang, C. E.; *A model for AGN variability on multiple time-scales*; MNRAS, 476, 34L (2018)
 9. Stark, D.; Launet, B.; Schawinski, K.; Zhang, C. E.; Koss, M. K.; Turp, M. D.; **Sartori, L.F.**; Zhang, H.; Chen, Y.; Weigel, A. K.; *PSFGAN: a generative adversarial network system for separating quasar point sources and host galaxy light*; MNRAS, 477, 2513 (2018)
 8. **Sartori, L.F.**; Schawinski, K.; Koss, M. J.; Ricci, C.; Treister, E.; Stern, D.; Lansbury, G.; Maksym, W. P.; Baloković, M.; Gandhi, P.; Keel, W. C.; Ballantyne, D. R.; *Joint NuSTAR and Chandra analysis of the obscured quasar in IC 2497 - Hanny's Voorwerp system*; MNRAS, 474, 2444 (2018)
 7. Treister, E.; Privon, G. C.; **Sartori, L.F.**; Nagar, N.; Bauer, F. E.; Schawinski, K.; Messias, H.; Ricci, C.; U, V.; Casey, C.; Comerford, J. M.; Muller-Sanchez, F.; Evans, A. S.; Finlez, C.; Koss, M.; Sanders, D. B.; Urry, C. M. *Optical, Near-IR, and Sub-mm IFU Observations of the Nearby Dual Active Galactic Nuclei MRK 463*; ApJ, 854, 83 (2018)
 6. Koss, M.; Trakhtenbrot, B.; Ricci, C.; Lamperti, I.; Oh, K.; Berney, S.; Schawinski, K.; Baloković, M.; Baronchelli, L.; Crenshaw, D. M.; Fischer, T.; Gehrels, N.; Harrison, F.; Hashimoto, Y.; Hogg, D.; Ichikawa, K.; Masetti, N.; Mushotzky, R.; **Sartori, L.F.**; Stern, D.; Treister, E.; Ueda, Y.; Veilleux, S.; Winter, L.; *BAT AGN Spectroscopic Survey. I. Spectral measurements, derived quantities, and AGN demographics*; ApJ, 850, 74 (2017)
 5. Baer, R.E.; Weigel, A.K.; **Sartori, L.F.**; Oh, K.; Koss, M.J.; Schawinski, K.; *Active galactic nuclei from He II: a more complete census of AGN in SDSS galaxies yields a new population of low-luminosity AGN in highly star-forming galaxies*; MNRAS. 466, 2879 (2017)
 4. Keel, W. C.; Lintott, C. J.; Maksym, W. P.; Bennert, V. N.; Chojnowski, S. D.; Moiseev, A.; Smirnova, A.; Schawinski, K.; **Sartori, L.F.**; Urry, C. M.; *Fading AGN Candidates: AGN Histories and Outflow Signatures*; ApJ, 835, 256 (2017)

Curriculum Vitae

3. **Sartori, L.F.**; Schawinski, K.; Koss, M. J.; Treister, E.; Maksym, W. P.; Keel, W. C.; Urry, C. M.; Lintott, C. J.; Wong, O. I.; *Extended X-ray emission in the IC 2497 - Hanny's Voorwerp system: energy injection in the gas around a fading AGN*; MNRAS, 457 3629 (2016)
2. Schawinski, K.; Koss, M. J.; Berney, S.; **Sartori, L.F.**; *Active galactic nuclei flicker: an observational estimate of the duration of black hole growth phases of $\sim 10^5$ yr*; MNRAS, 451, 2517 (2015)
1. **Sartori, L.F.**; Schawinski, K.; Treister, E.; Trakhtenbrot, B.; Koss, M. J.; Shirazi, M.; Oh, K.; *The search for active black holes in nearby low-mass galaxies using optical and mid-IR data*, MNRAS, 454, 3722 (2015)

